Energy, Mines and Resources Canada
Énergie, Mines et Ressources Canada

CANMET
Canada Centre for Mineral and Energy Technology
Centre canadien de la technologie des minéraux et de l'énergie

DEVELOPMENT OF A ZIRCONIA ELECTROLYTE FOR USE IN A STEEL-MAKING OXYGEN PROBE

T. A. Wheat
Industrial Minerals Laboratory
Ceramic Section

November 1975

MINERALS RESEARCH PROGRAM
Mineral Sciences Laboratories
CANMET REPORT 76-13

Available by mail from

Printing and Publishing
Supply and Services Canada,
Ottawa, Canada K1A 0S9

and at Canadian Government Bookstores:

HALIFAX
1683 Barrington Street

MONTREAL
640 St. Catherine Street West

OTTAWA
171 Slater Street

TORONTO
221 Yonge Street

WINNIPEG
393 Portage Avenue

VANCOUVER
800 Granville Street

or through your bookseller

Catalogue No. M 38-13/76-13

Price: Canada: $5.00
Other countries: $6.00

Price subject to change without notice

En vente par la poste:

Imprimerie et Édition
Approvisionnements et Services Canada,
Ottawa, Canada K1A 0S9

et dans les Librairies du gouvernement du Canada:

HALIFAX
1683, rue Barrington

MONTRÉAL
640 ouest, rue Ste-Catherine

OTTAWA
171, rue Slater

TORONTO
221, rue Yonge

WINNIPEG
393, avenue Portage

VANCOUVER
800, rue Granville

ou chez votre libraire.

N° de catalogue M 38-13/76-13

Prix: Canada: $5.00
Autres pays: $6.00

Prix sujet à changement sans avis préalable

MINERAL SCIENCES LABORATORIES

MRP/MSL 75-233(R)

DEVELOPMENT OF A ZIRCONIA ELECTROLYTE FOR USE IN A STEEL-MAKING OXYGEN PROBE

by

T. A. Wheat*

- - -

ABSTRACT

A novel wet-chemical method has been developed to produce finely divided lime-stabilized zirconia from solutions of zirconyl chloride and calcium formate. The process involves the formation of a hydrated zirconium hydroxide precipitate and the adsorption of calcium ions onto the precipitate surface. The mixture is subsequently spray-frozen, freeze-dried and finally calcined to produce a reactive and homogeneous material. Using this technique, a series of materials was prepared containing between zero and sixteen mole per cent calcium oxide.

It was demonstrated that the single most important parameter that controls the development of a high-density body during subsequent processing is the degree of dispersion of the raw material prior to the initial fabrication stage. In order to develop an impermeable body, which is required for an oxygen probe application, the materials were first dispersed by ball-milling in alcohol containing a dissolved powder lubricant and binder. The resulting de-agglomerated and reactive material could then be processed into a 99% theoretically dense product at 1500°C using conventional cold pressing and sintering techniques.

It has been shown that the maximum thermal-shock resistance is developed in material having a composition of 7.6 mole per cent calcium oxide in the zirconia. The microstructure developed in this partially stabilized material is in contrast to that developed in either the pure or fully stabilized materials, both of which have a markedly inferior thermal shock resistance. X-ray and optical data have been obtained that support a recently proposed model in which the high thermal-shock resistance was attributed to the development of a microcrack network that is initiated during firing and extended during subsequent thermal cycling.

---

*Research Scientist, Mineral Sciences Laboratories, Canada Centre for Mineral and Energy Technology (CANMET), Department of Energy, Mines and Resources, Ottawa, Canada.

The use of partially stabilized material as the electrolyte in laboratory oxygen concentration cells demonstrated that a stable and reproducible emf output could be obtained. Subsequently, field trials showed that this particular material could be used successfully in commercial oxygen probe assemblies to reduce the scatter in the signal output to 2.9 mv. This performance exceeded the original design requirements for a standard deviation of not greater than 8 mv in a one-volt signal.

LABORATOIRES DES SCIENCES MINERALES

MRP/MSL 75-233(R)

DEVELOPPEMENT D'UN ELECTROLYTE DE ZIRCONE UTILISE DANS UNE SONDE A OXYGENE POUR LA FABRICATION DE L'ACIER

par

T. A. Wheat*

- - -

RESUME

Une nouvelle méthode chimique par voie humide a été développée afin de produire du zircone de chaux stabilisée finement divisé à partir de solutions de chlorure de zirconyle et de formate de calcium. Le processus implique la formation d'un précipité d'hydroxyde de zirconium hydraté et l'absorption d'ions de calcium sur la surface du précipité. Le mélange est ensuite gelé par vaporisation, séché à froid et finalement calciné afin de produire un matériau homogène et réactif. Avec cette technique, une série de matériaux a été préparée contenant entre zéro et seize pourcent de moles d'oxyde de calcium.

Il a été démontré que le paramètre simple le plus important contrôlant le développement d'un corps de haute densité pendant le traitement subséquent est le degré de dispersion du matériau brut avant l'étape initiale de fabrication. Afin de développer un corps imperméable, qui est nécessaire à l'application d'une sonde à oxygène, les matériaux ont été préalablement dispersés par broyage à boulets dans l'alcool contenant un lubrifiant à poudre dissous et un liant. Le matériau désagrégé et réactif qui en est résulté peut maintenant être transformé en produit théoriquement dense à 99% à 1500°C, en utilisant des techniques conventionnelles d'étampage à froid et d'agglutination.

Il a été démontré que la résistance maximale au choc thermique est développée dans les matériaux ayant une composition de 7.6% de moles d'oxyde de calcium dans la zircone. La microstructure développée dans le matériau partiellement stabilisé est

*Chercheur scientifique, Laboratoires des sciences minérales, Centre canadien de la technologie des minéraux et de l'énergie (CANMET), Ministère de l'Energie, des Mines et des Ressources, Ottawa, Canada.

en contradiction avec celle développée dans les matériaux purs ou totallement stabilisés, ces derniers ayant une résistance définitivement inférieure au choc thermique. Les données optiques obtenues ainsi que celles des rayons-x soutiennent la proposition récente d'un modèle dans lequel la forte résistance au choc thermique a été attribuée au développement d'un réseau de micro-fissure qui est amorçé pendant la cuisson et qui se poursuit durant le cycle thermique subséquent.

L'utilisation de matériau partiellement stabilisé comme électrolyte dans des cellules d'oxygène concentrées a démontré qu'un rendement emf stable et reproducible pouvait être obtenu. Subséquement, des essais sur le champ ont démontré que ce matériau particulier pouvait être utilisé avec succès dans des assemblages de sonde à oxygène commerciale afin de réduire la dispersion du débit de signal à 2.9 mv. Cette performance a exédé les spécifications originales du modèle qui demandaient une écart-type n'exédant pas 8 mv pour un signal d'un volt.

CONTENTS

FIGURES

TABLE

INTRODUCTION

In recent years, there has been a progressively increasing interest in the development and application of electrochemical cells for the measurement of elements in both gaseous and liquid systems at elevated temperatures. Irrespective of the system involved, the measurement of elemental concentrations depends on the formation of an electrochemical concentration cell having the general form:

Pt, X (activity 1)/ Electrolyte/ X (activity 2), Pt

where X is the element of interest. In such a cell, the ionic form of X 'flows' from one half-cell to the other (from high concentration to low) and an emf is generated across the platinum electrodes. This measured emf is then related to the activity, a_1 and a_2, of the element in each half-cell by the Nernst equation:

$$E = RT/nF \ln (a_1/a_2)$$

where E is the theoretical cell emf in volts, R is the gas constant = 1.9865 cal/mole/°K, T is the temperature, n is the number of electrons transferred per molecule of X, and F is the Faraday constant = 23.066 kcal/V/mole.

From this relationship, the activity (or concentration, if ideal gas behaviour is assumed) of the unknown may be calculated for a given reference activity (or concentration). Familiar examples, which employ this general principle, are the pH electrodes and the more recently developed specific-ion electrodes which are capable of measuring concentrations in liquid systems in parts per million.

In general, the use of concentration cells has been limited to near room-temperature applications due to the lack of a suitable high-temperature ionically conducting electrolyte. However, in 1957 Kiukkola and Wagner[1] demonstrated the feasibility of using a calcia-stabilized zirconia (CSZ) membrane in an electrochemical cell for the determination of the standard heats of formation of various sulphides and oxides. Calcia- and lanthana-stabilized thoria were also considered as potential membrane materials (solid electrolytes) but they were shown to have considerable electronic conductivity at 870°C. In contrast, the ac conductivity of CSZ was found to be virtually constant while the oxygen partial pressure (P_{O_2}) varied from 1 atm to 10^{-20} atm (10^{+5} to 10^{-15} N/m^2); this indicated that the electronic conductivity played only a minor role in the over all conductivity.

With this ionically conducting electrolyte available (CSZ), which is capable of withstanding temperatures well over 2000°C, the upper temperature limit of the oxygen concentration cell was raised considerably. Consequently, in the nineteen years since the work of Kiukkola and Wagner, the high temperature applications have covered diverse fields. In one case, a concentration cell has been used to analyse flue gases in order to optimize the combustion of fuel oil; in a second application the oxygen content of a furnace atmosphere was monitored in a furnace used to fire certain types of ferrite in which the ratio Fe^{2+}:Fe^{3+} is an important parameter for certain physical properties[2].

A similar device has recently been reported which is capable of measuring the water content of hydrogen gas as low as a few parts per billion[3]. This is of interest to the semiconductor industry where a minute amount of oxygen contamination significantly changes the properties of a semiconductor. In the metallurgical industry, oxygen sensors have been developed to monitor the oxygen content of liquid copper[4] and liquid steel[5-12]. Research efforts are also being directed to the continuous use of oxygen probes in a closed-loop control system in the copper industry[13].

In practice, the use of a concentration cell to measure the oxygen content of liquid metals can place a severe demand on the performance of the electrolyte material. The device must be capable of withstanding the extreme thermal shock which develops when the cell is placed directly into the molten metal (heating rate of approximately 300°C/sec when placed into steel). In addition, the electrolyte must remain impermeable to gaseous oxygen, e.g., any microcracks present must not propagate to form a continuous path for the flow of molecular oxygen which would disturb the electrode equilibrium; it must be stable in the presence of both liquid metal and slag and it must be chemically inert to the electrode because any reaction could either change the electrode activity or give rise to a new phase which would prevent the cell from operating at equilibrium. A final basic requirement for its use in liquid steel is that the electrolyte should remain an ionic conductor at oxygen partial pressures down to approximately 10^{-15} atm (10^{-10} N/m^2) in order that oxygen

concentrations down to about 1 ppm at 1600°C can be determined.

It appears to be tacitly assumed, in much of the recent research to develop a reliable oxygen sensor for use in liquid steel, that the zirconia acts only as a simple conductor and does not affect the emf developed in a cell. However, Kiukkola and Wagner[1], in an examination of the cell: Fe, Fe_xO/CSZ/Fe_yO, Fe_3O_4, noted on page 381 that some "...runs failed probably because of harmful impurities in the oxides used for the preparation of the electrolyte", and Kulkarni et al.[4] noted recently on page 18 that the "...systematic difference.....between the two investigations was probably caused by thermoelectric voltages arising from differences in sensor materials".

This problem of lack of reproducibility of emf output for a given oxygen concentration differential has continued to plague investigators including members of the Physical Metallurgy Research Laboratories of the Canada Centre for Mineral and Energy Technology. It was not known whether the differences observed were due to physical or chemical variations in each cell electrolyte. Consequently, a program was initiated to develop homogeneous zirconia, low in impurities, that would be suitable for fabricating an oxygen probe membrane for use in liquid steel.

EXPERIMENTAL PROCEDURE

In order to ensure homogeneity in the product, it was clear that some form of wet chemical processing was necessary instead of the usual method of mixing two oxides, or oxide pre-

cursors, in a ball-mill and subsequently calcining the mixture. In general, the methods available for producing a homogeneous ceramic raw material involve either co-precipitation from organic or inorganic precursors or, alternatively, spray-freezing and freeze-drying an aqueous mixture of inorganic salts by the method of Schnettler et al.[14].

The co-precipitation technique, using both inorganic[15] and organic[16] precursors, has been employed for some time on an industrial scale to produce homogeneous finely-divided ceramic raw materials for piezoelectric applications. However, a close control must be maintained to prevent significant segregation occurring due to widely differing precipitation rates. This problem does not arise in the spray-freeze and freeze-dry method. Consequently, the cryogenic technique was adopted in the present work.

Previous work[17] had shown that it was impossible to form pure or doped zirconia directly using the cryogenic process because a frozen zirconyl salt gradually melts at temperatures down to -40°C (the lower limit of a commercial freeze-drier). Consequently, the method was modified to that shown in Figure 1. In essence, the zirconyl ion was effectively removed from solution by precipitating a finely divided zirconium hydroxide. The precipitate was washed to remove soluble salts and subsequently doped with a known amount of calcium formate solution. The resulting slurry was rapidly frozen and successfully freeze-dried at -5°C without any of the previous difficulties.

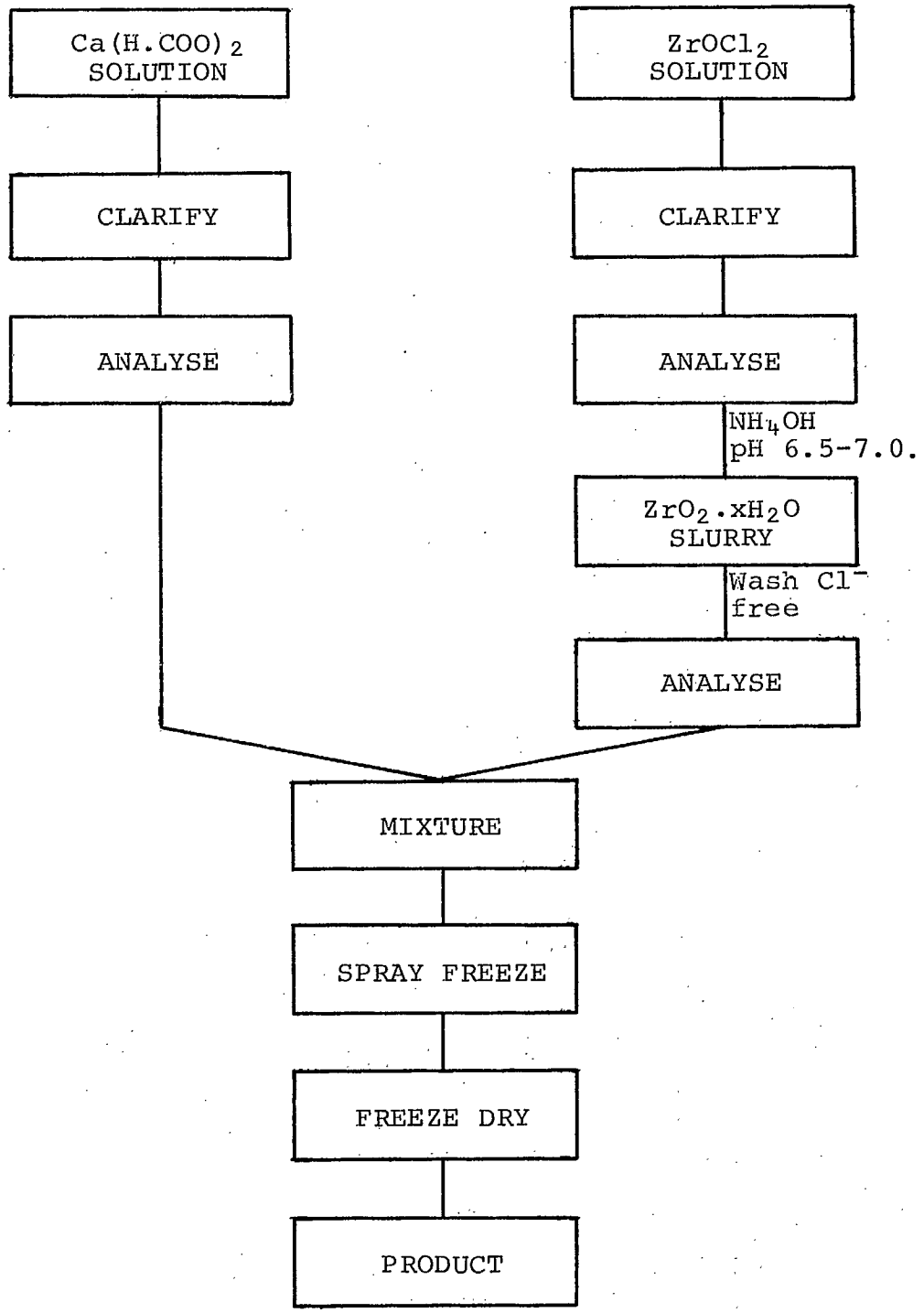

Figure 1. General flow sheet for the preparation of lime-stabilized zirconia.

Precipitation of Zirconium Hydroxide*

Initially, the as-received $ZrOCl_2$ solution obtained from Eldorado Nuclear Ltd was clarified to remove traces of insoluble material. The concentration of this solution was then determined by gravimetric analysis and found to be 301.15 g ZrO_2/litre $ZrOCl_2$.

The quantity of NH_4OH required to precipitate $Zr(OH)_4$ from the $ZrOCl_2$ was determined by a potentiometric titration (Figure 2). The data showed that 20 ml of chloride solution required 9.0 ml of NH_4OH to give a pH of 7.5 and to produce 6.0 g of ZrO_2 (on ignition to 1000°C). From these data, approximately 450 g of ZrO_2 would precipitate from 1.5 litres of $ZrOCl_2$ solution with 675 ml of concentrated NH_4OH.

To allow for possible error in scaling up the titration data from 20 ml to 1.5 litres and the variation in concentration of NH_4OH from batch to batch, the full amount of NH_4OH was not added directly. Instead, 600 ml of concentrated NH_4OH (sp gr 0.90) was diluted with 2.4 litres of distilled water and placed in a 40-litre container, and 1.5 litres of $ZrOCl_2$ stock solution, diluted with 3.0 litres of distilled water, was added. An additional 4.0 litres of water was used to wash down the containers and a further 15.0 litres of water was added to wash the precipitate. This gave a final volume of 26.5 litres and a pH, immediately after mixing, of 7.7.

*The exact composition of the hydrated oxide which is precipitated is unknown, but it is probably given by the formula $ZrO(OH)_2$, nH_2O. For brevity, the formula $Zr(OH)_4$ has been used throughout this report.

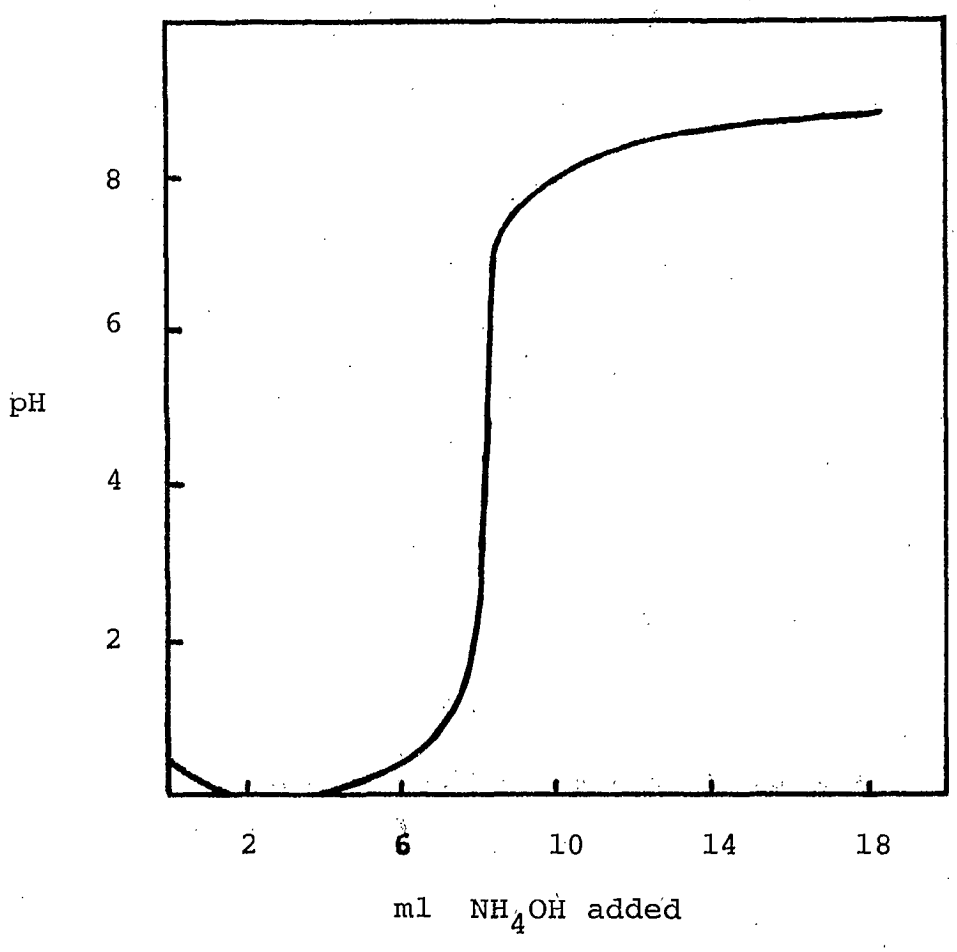

Figure 2. Potentiometric titration of 20 ml of as-received $ZrOCl_2$ solution

The mixture was allowed to stand and the precipitate settled to approximately 8.2 litres, giving a 5.5 wt % concentration of $Zr(OH)_4$ in the sediment. The clear supernatant liquor was discarded and the precipitate subsequently washed ten times to reduce the Cl^- content of the solution.

As the washing continued, the volume of the precipitate and the turbidity of the supernatant liquor increased, due to the progressive reduction in the pH of the liquor and the consequent deflocculation of the precipitate (the pH of distilled water is 5.8 due to dissolved CO_2). Therefore, a small quantity of NH_4OH

was added to the mixture at each washing to maintain the pH above 6 and to ensure that the precipitate was flocculated sufficiently to settle within three hours.

The concentration of Cl^- in the supernatant liquor was measured after each washing using a specific-ion electrode. It was found that the Cl^- concentration ($[Cl^-]$) was reduced by a factor of 2.2 at each washing instead of the expected value of 5.0 based on the relative volumes of the settled precipitate and added water. This suggested that the Cl^- was adsorbed onto the surface of the precipitate. Further evidence of this adsorption, obtained from earlier trial experiments, is shown in Figure 3. The concentration of free Cl^- in solution is seen to increase with the addition of NH_4OH from a relatively low value of 8 ppm to nearly 60 ppm. In addition, the supernatant liquor was always found to have a lower $[Cl^-]$ than a slurry of the settled precipitate. Consequently, all subsequent batches of doped zirconia were prepared from a precipitate having a $[Cl^-]$ less than 20 ppm in the supernatant liquor at a pH between 6.5 and 7.0.

After washing, the supernatant liquor was decanted from the settled precipitate to leave 10.0 litres of slurry which was stirred vigorously for 2 hours and subsequently split into weighed batches. A small quantity of the slurry was retained to determine the zirconia concentration so that the amount of calcia required for each batch could be calculated prior to doping with calcium formate solution.

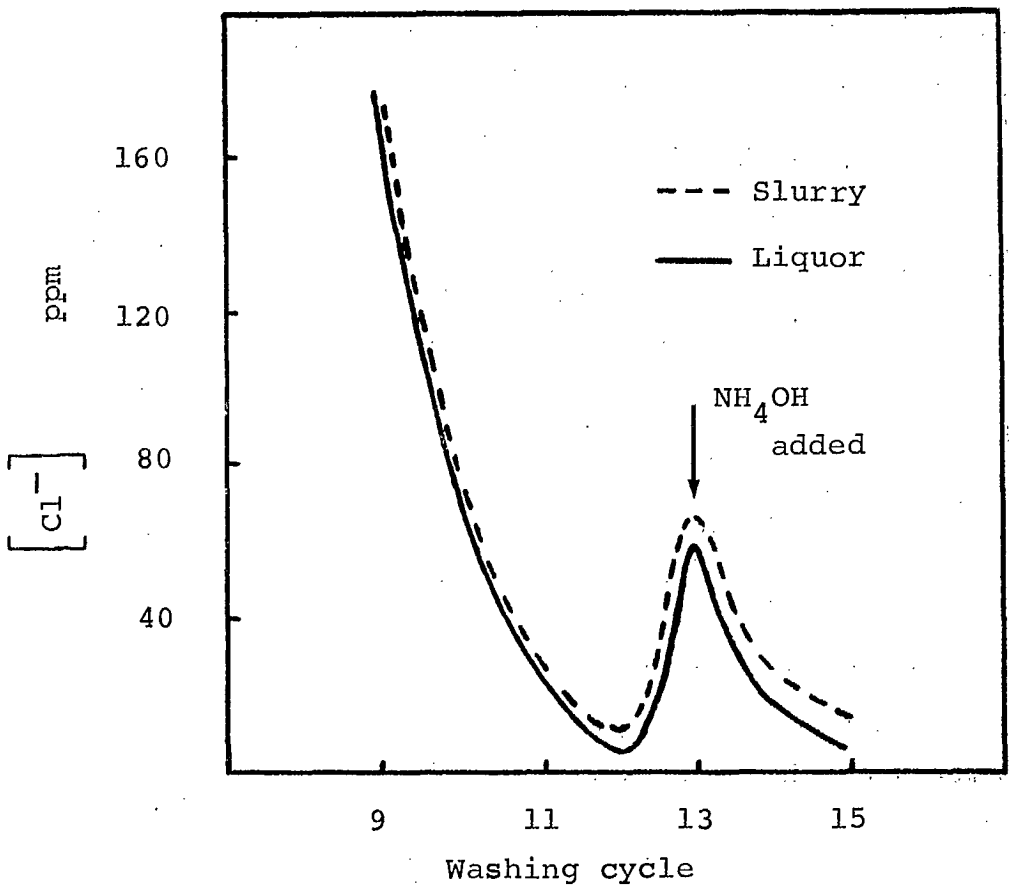

Figure 3. Variation of Cl^- concentration in liquor and slurry with progressive washing.

Preparation of Doped Zirconia

Initially, a solution of calcium formate in water (∿32 g/l) was prepared, clarified, and the concentration determined accurately by gravimetric analysis. The weight loss of the formate on ignition to 1000°C was also determined. These data, together with the concentration of zirconia in each batch of precipitate, were used to determine the volume of formate solution required to give a specific mole ratio of $CaO:ZrO_2$ in the dried product after calcination to 1000°C as shown in Appendix A.

With the required amount of formate solution added, the batches were stirred for one hour prior to being spray-frozen and freeze-dried by a method described elsewhere[18]. The slurry was agitated throughout the spraying process to prevent settling, which would allow the spray to be initially rich in zirconia and finally rich in formate. Thermogravimetric analyses of the dried products from the initial and final spraying showed the same concentration of formate; this confirmed that homogeneity had been maintained during the spraying stage.

Using this method, a series of CSZ raw materials was prepared which contained 16.0, 13.8, 11.5, 9.0, 7.6, 6.0, 4.0, and 2.0 mole % CaO. The data which follow in Parts I to III were obtained mainly from samples containing 16.0, 13.8, 11.5, and 7.6 mole % CaO.

RESULTS AND DISCUSSION

PART I

CHARACTERIZATION OF RAW MATERIALS

The as-prepared materials were all bulky, free-flowing white powders with a tap density of approximately 0.15 g/cc. In all cases, X-ray diffraction analyses indicated that the materials were amorphous immediately after leaving the freeze-drier.

Differential Thermal Analyses

Differential thermal analyses (DTA) and thermogravimetric analyses (TGA) were obtained on all materials at tempera-

tures up to 1150°C in air. The characteristic DTA curves are given in Figures 4 and 5 and show that the doped precipitated materials pass through three regions of activity with increasing temperature.

A broad endothermic peak is generated by a reaction at approximately 170°C and it is accompanied by a considerable weight loss. A second endothermic peak at 350°C (in samples containing greater than 7.6 mole % CaO) is also associated with a weight loss. In all cases, the samples remain amorphous after both these reactions. Hence, the peaks have been tentatively ascribed to the loss of physi-sorbed and subsequently chemi-sorbed water from the surface of the material as the temperature is increased.

At higher temperature, the materials undergo an exothermic reaction over a narrow temperature range. X-ray diffraction analysis (XRD) confirmed that this was accompanied by the rapid crystallization of the samples. It can be seen that the temperature of this crystallization is dependent on the CaO content of the material and it may be significant that the greatest increase in the crystallization temperature occurs between 9.0 and 11.5 mole % CaO - the composition range in which the partially stabilized zirconia (cubic + monoclinic at 9.0 mole % CaO) is transformed to fully stabilized material (cubic only at 11.5 mole % CaO).

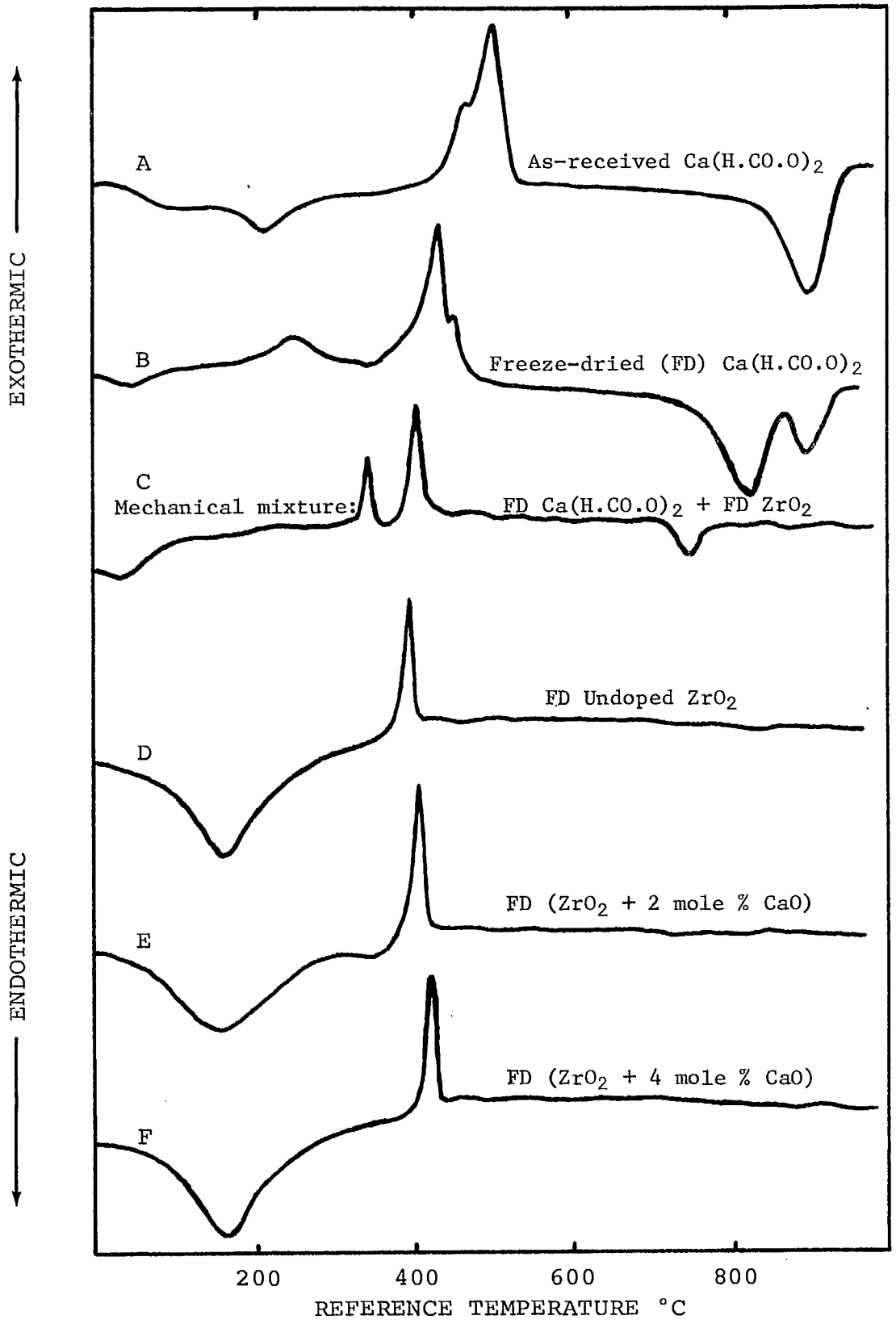

Figure 4. DTA curves of calcium formate and as-prepared zirconia samples heated at 12°C/min.

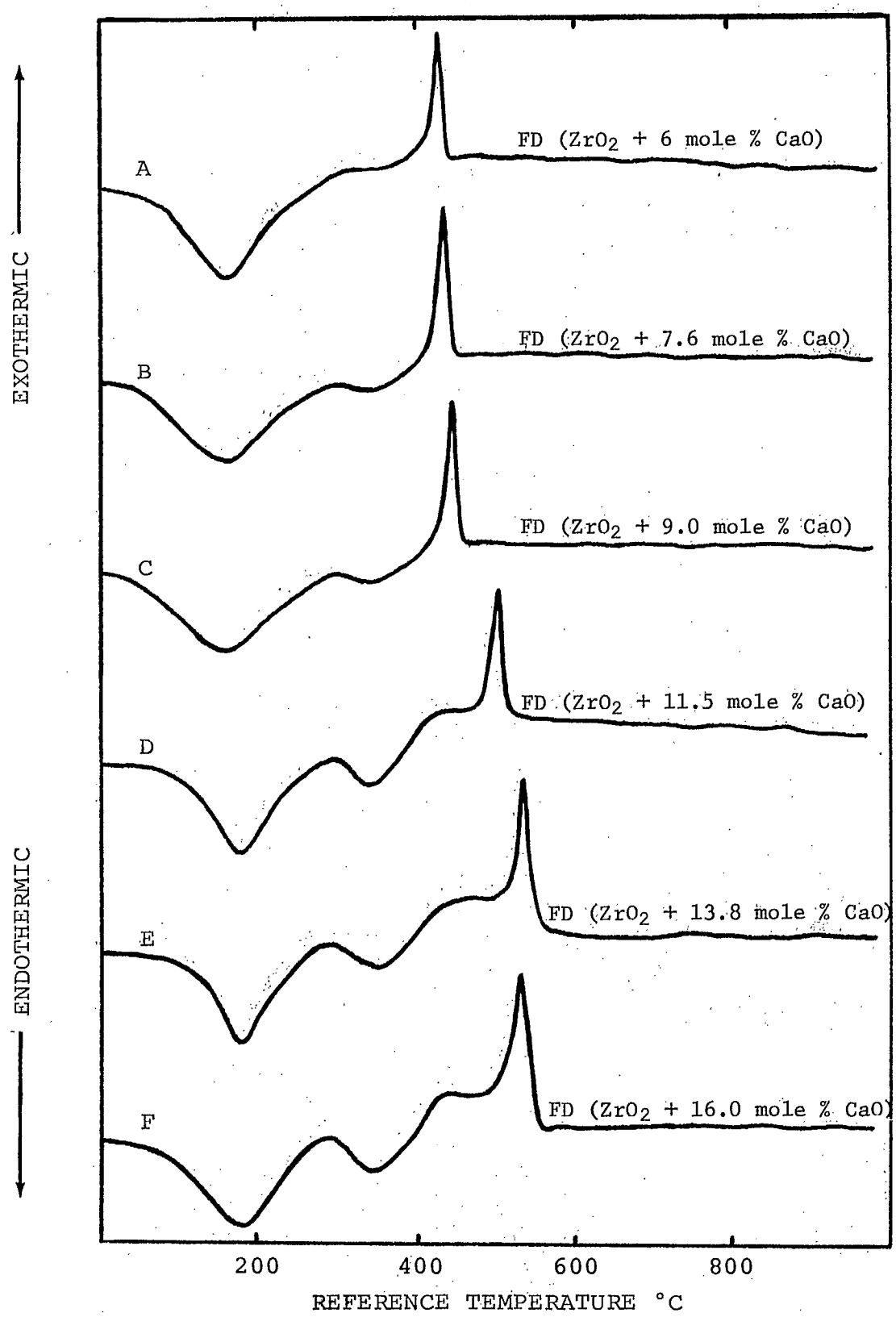

Figure 5. DTA curves of as-prepared zirconia samples heated at 12°C/min.

The DTA curves of the doped materials (D to F in Figure 4 and A to F in Figure 5) do not show the decomposition of the formate and the TGA curves likewise differ little from that of an undoped sample. This initially suggested that the formate was completely decomposed during the freeze-drying process. However, X-ray analysis and TGA showed that the unadulterated freeze-dried formate suffered only a minor structural change during the drying process. In addition, the DTA curve (B in Figure 4) was basically similar to that for the as-received material (Curve A in Figure 4) which further demonstrated that the formate was largely unaltered during drying.

In order to verify that the concentration of formate present in the doped materials was sufficient so that DTA and XRD could detect free formate, particularly at low concentrations, mechanical mixtures of freeze-dried formate and freeze-dried zirconium hydroxide were prepared and examined. A typical DTA trace for such a mixture is shown in Figure 4, Curve C (the exothermic reaction at approximately 330°C was not investigated and remains unidentified). Examination of a series of such mixtures showed that DTA was the more sensitive technique for the detection of free formate. The lower detection limit was less than 2 weight % (approximately 2 mole %) whereas the lower limit for XRD was greater than 4 weight %. It should be noted that the presence of formate could be detected in DTA only by the endothermic peak for the reaction $CaCO_3 \rightarrow CaO$ which occurs between 700 and 900°C. The main exothermic peak at approximately 400°C coincided with that for the crystallization of the ZrO_2 component

in the mixture and hence this much stronger peak could not be unambiguously ascribed to formate alone.

Thus, it was demonstrated that XRD would detect free formate in compositions containing 6 mole % and above, whereas DTA would detect free formate in compositions containing 2 mole % and above. However, the DTA curves shown in Figure 4 (D to F) and Figure 5 fail to show the presence of formate even at high doping levels and XRD likewise failed to indicate any formate in the materials prepared by the solution route (Figure 1). Consequently, it was assumed that the formate had been removed from solution during the preparation of the doped materials and adsorbed onto the surface of the freshly precipitated $Zr(OH)_4$. Such an adsorption would explain the absence of free formate in these materials as indicated by both the DTA and XRD results.

Adsorption of Calcium Ions by Zirconium Hydroxide

Following the indirect evidence of the adsorption of calcium formate onto the surface of $Zr(OH)_4$ gained from the DTA and XRD results above, an attempt was made to determine qualitatively the extent of this adsorption using a divalent-ion selective electrode. Initially, the electrode assembly was calibrated (Appendix B) using the standard formate solution (∿32 g/l) that was employed previously to dope the various batches of material. Subsequently, the concentration of free Ca^{2+} ions in the supernatant liquor taken from a batch of washed and settled $Zr(OH)_4$ precipitate was determined and the change in this concentration with time was recorded following the addition of a known amount

of formate solution. The result is shown as Curve A in Figure 6. The initial concentration of 3.5×10^{-5} moles/litre increased rapidly to an equilibrium value of 2.4×10^{-2} moles/litre after 25 seconds. This determination was then repeated using the same volume of $Zr(OH)_4$ slurry and the same amount of formate solution. The results obtained at pH 8 and pH 6 are shown as Curves B and C respectively in Figure 6.

The adsorption data indicates that the change in pH does not affect the degree of adsorption. In both cases, the final equilibrium concentration of free Ca^{2+} ions in solution was established after approximately 10 minutes and found to be 1.1×10^{-2} moles/litre. However, as expected, the rate of adsorption at pH 8 (fully flocculated $Zr(OH)_4$) was confirmed to be slower than that at pH 6 where the precipitate is partially defloccu-lated.

Comparison of Curves B and C with Curve A show that the free Ca^{2+} ion concentration does not increase rapidly when the formate is added to the $Zr(OH)_4$ slurry as it does when added to the $Zr(OH)_4$-free liquor. This suggests that the calcium formate is nearly completely adsorbed onto the precipitate surface ini-tially and subsequently is slowly desorbed over a period of 10 minutes allowing the concentration of free Ca^{2+} ions to increase and reach its equilibrium value as shown. The possibility that the slower response of the specific-ion electrode in the slurry (Curves B and C, Figure 6) was due to the increased viscosity of the $Zr(OH)_4$ suspension was discounted because similar traces for the adsorption of Cl^- ion onto the precipitate did not display

any measurable lag. It was therefore assumed that the added ion was rapidly and uniformly distributed throughout the slurry and that the slower response was due to a very rapid adsorption by the slurry rather than the increased viscosity impeding the uniform distribution of the added calcium formate solution.

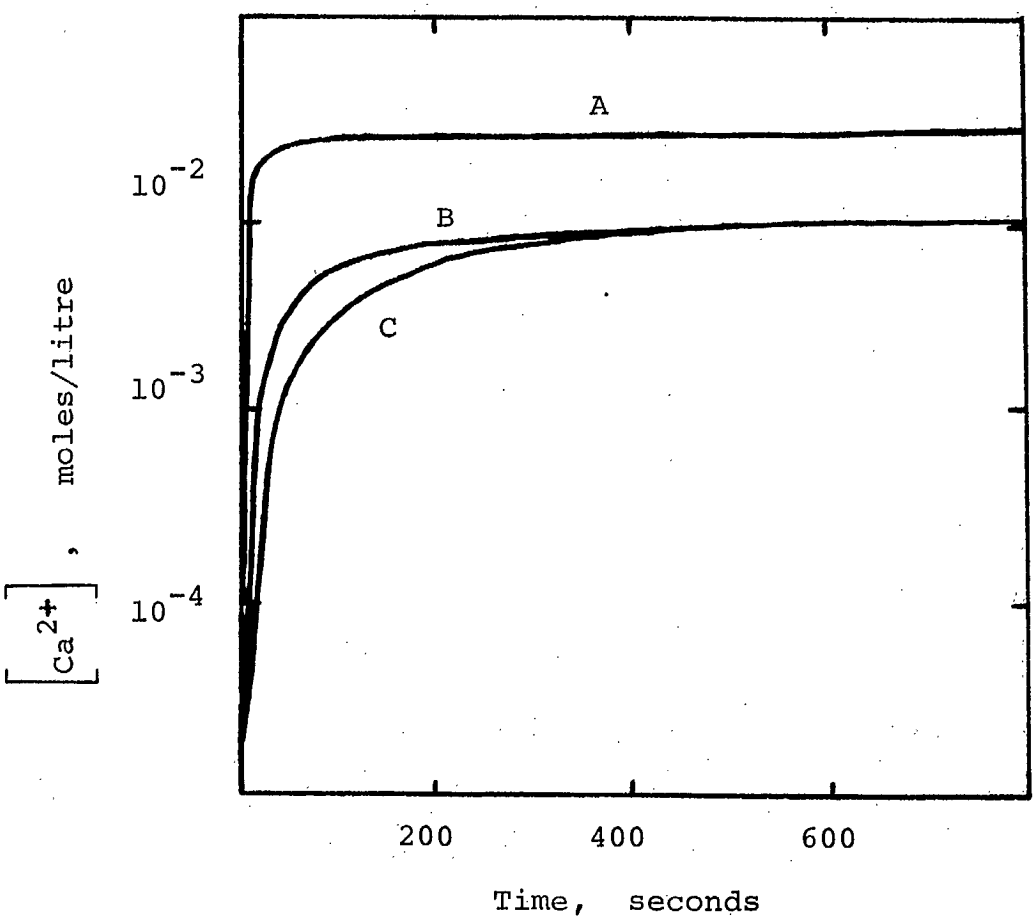

Figure 6. Increase in calcium ion concentration in solutions to which calcium formate was added.

A. $Zr(OH)_4$-free supernatant liquor
B. $Zr(OH)_4$ slurry at pH 8 (NH_4OH added)
C. $Zr(OH)_4$ slurry at pH 6.

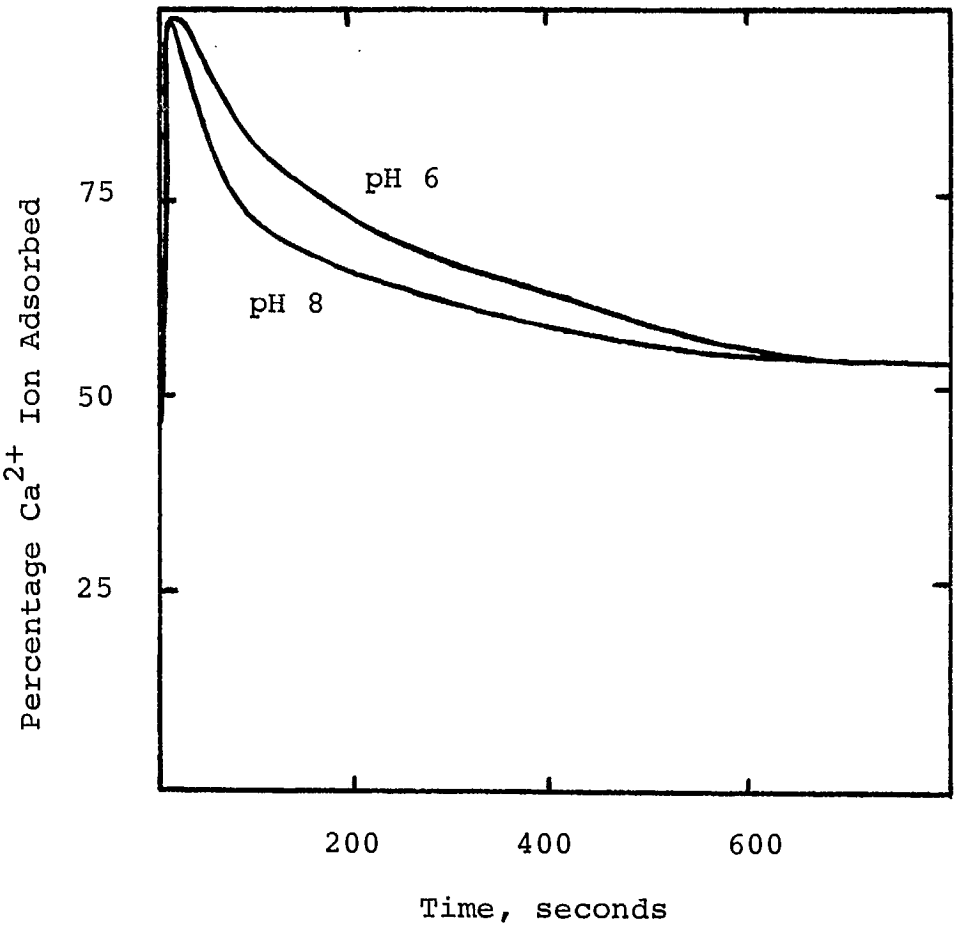

Figure 7. Percentage of Ca^{2+} adsorbed onto $Zr(OH)_4$ slurry at pH 6 and pH 8 following the addition of a low concentration of calcium formate.

The percentage of the free calcium ions in solution which was adsorbed by the $Zr(OH)_4$ precipitate was calculated from the data in Figure 6 (see also Appendix B). The results, given in Figure 7, show that there is essentially a total adsorption of calcium in the first minute following the addition of the formate solution. Thereafter, a progressive desorption takes place and the final equilibrium value is established after approximately 10 minutes. With greater concentrations of $Ca(H.CO.O)_2$,

a greater adsorption would be expected. However, increasing the formate concentration threefold from 6.5 mole % to 19.5 mole % only increased the amount of adsorbed calcium from 54% to 64% (Appendix B).

Adsorption of Chloride Ions by Zirconium Hydroxide

Attempts to re-adsorb Cl^- ions onto the $Zr(OH)_4$ surface were unsuccessful. The difference between the measured free Cl^- concentration developed in both $Zr(OH)_4$-free liquor and the $Zr(OH)_4$ slurry following the addition of 2 ml of 0.1 molar NaCl solution was within the limits of experimental error and hence not significant, i.e., little or no Cl^- can be re-adsorbed onto the precipitate surface under these conditions.

At first, this appears to contradict the evidence for Cl^- adsorption presented in Figure 3. However, it is still feasible for the $Zr(OH)_4$ to adsorb Cl^- initially during its precipitation, and then slowly release the Cl^- during the washing stages replacing it with OH^- (ionic radius of Cl^- 1.81 Å and of O^{1-} 1.76 Å - radius of O^{1-} assumed to be similar to that of OH^-)[19]. Subsequently, any attempt to re-adsorb the Cl^- onto the $Zr(OH)_4$ would be complicated by the competition between the OH^- and Cl^- ions. Because the amount of OH^- and Cl^- in 21.5 ml of slurry + 2 ml of 0.1 molar NaCl is approximately 1.3 moles and 2×10^{-4} moles respectively, i.e., a concentration ratio of OH^-/Cl^- of 6500/1, and because the ionic radii are very similar, it would be expected that the OH^- would be retained on the $Zr(OH)_4$ surface by a mass action effect.

From the above, it has been shown that the precipitate will adsorb approximately 60% of the added formate, leaving 40% free in solution. It was initially assumed that this ratio was retained during the drying stages and that about 40% free formate would be present in the dried powder. This would mean that XRD should be able to detect formate in compositions containing greater than approximately 10 mole % total formate and DTA should detect formate in compositions containing greater than 5 mole % total formate (see limits of detection on page 15). However, as shown in Figure 5, the more sensitive technique was unable to detect any free formate in compositions containing up to 16 mole % total formate. This suggested that the ratio of adsorbed:free formate of 60:40, which is developed in solution during the preparation of doped material, changes during the drying stage so that much more material becomes adsorbed onto the $Zr(OH)_4$ surface.

Determination of the Free Formate in Freeze-Dried Material

The quantity of free (recoverable) formate which was present in the dried materials was determined by re-slurrying the powder in water and subsequently measuring the concentration of Ca^{2+} ions using a divalent-ion selective electrode. This experiment was performed using a one-gram sample of zirconia containing 7.6 mole % CaO which was slurried in 100 ml of distilled water. Results were obtained for four different batches of 7.6 mole % material which had been prepared in essentially the same manner (Appendix C). The experiment demonstrated the variable nature of the different batches and showed that the amount of

free formate present varied from 17% to 27% with an average of 22%.

Hence, with only 22% of that present acting as free formate in the dry powders, XRD and DTA would only be able to detect the presence of formate in compositions containing approximately 25 mole % and 10 mole % formate respectively (see limits of detection on pages 14 and 15). Consequently, the presence of free formate in compositions containing up to 16 mole % formate would remain undetected in X-ray diffraction patterns of the powder. However, DTA should be able to show the presence of formate in compositions containing greater than 10 mole %, yet, as shown in Figure 5, the formate component was not detected in compositions containing up to 16 mole %.

One possible reason for this lack of formate peaks in the DTA traces could be that most of the formate present in the sample is completely decomposed (i.e., to oxide rather than carbonate) at approximately 400°C coincidentally with the very strong exothermic peak due to the crystallization of the ZrO_2. In this manner, little or no carbonate would be retained to be detected in DTA by the endothermic reaction at 900°C as the carbonate decomposes to oxide. The amount of formate that decomposes at 400°C and subsequently the amount of carbonate at ∿900°C was determined directly from the TGA data.

Thermogravimetric Analyses

One-gram samples of material ranging in composition from undoped to fully doped zirconia were heated in air at 6°C/min

in an automatically controlled Stanton thermobalance. The percentage weight loss recorded for some of the materials is shown in Figure 8. For the purposes of clarity, the traces for the extreme compositions only have been presented. All other compositions (2 mole % to 13.8 mole % CaO) were found to produce weight loss curves which were intermediate between the two end members and which showed a progressively increasing total weight loss as the amount of formate dopant was increased.

The TGA curves for undoped material showed a progressive loss of weight at temperatures up to 400°C. The loss of 17.0 weight % to 400°C was only marginally increased on further heating; the toal weight loss at 1000°C was 18.3%. With progressively increasing amounts of calcium formate in the sample, the form of the TGA curve is retained but the weight loss to 400°C and the overall loss to 1000°C is increased. In 11.5 mole % material, the weight loss to 400°C is 23.7% and the total loss to 1000°C is 27.0%.

In materials containing 13.8 and 16.0 mole % CaO, the form of the TGA curve is slightly modified by the development of two points of inflection occurring at approximately 300°C and 720°C (shown by arrows in Figure 8). It is assumed that these two additional minor weight losses are due to the formate-to-carbonate decomposition and the carbonate-to-oxide transition respectively.

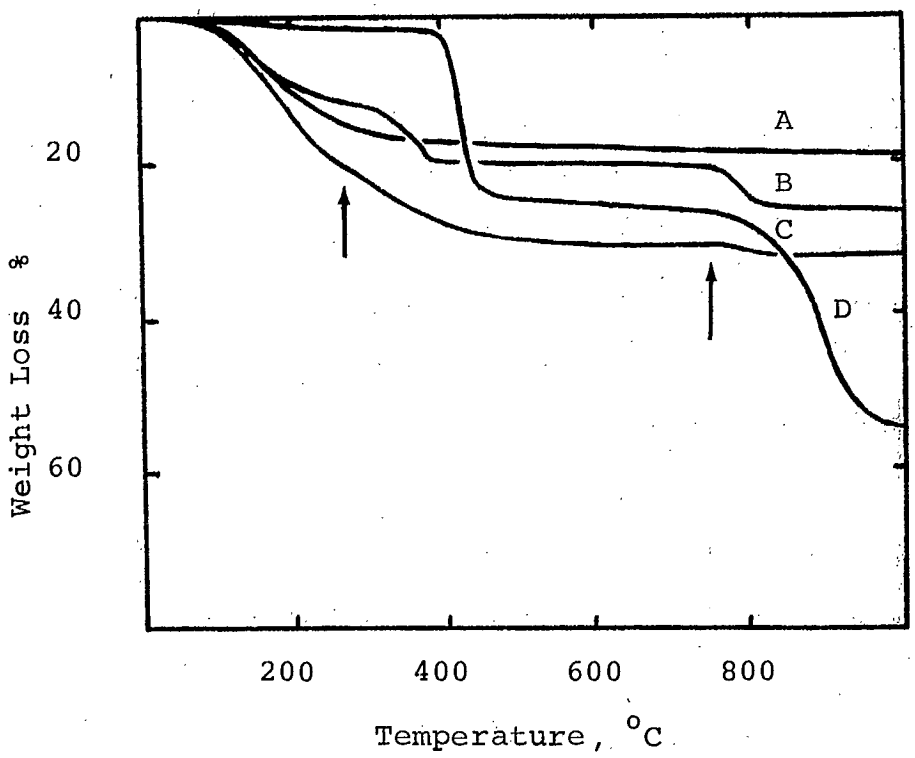

Figure 8. TGA curves for material heated at 6°C/min.

A. Undoped freeze-dried zirconia
B. Mechanical mixture of undoped freeze-dried zirconia and 16 mole % calcium formate
C. Freeze-dried zirconia containing 16 mole % calcium formate prepared via route in Figure 1
D. Freeze-dried calcium formate

Comparison of Curves C and D in Figure 8 shows that the decomposition temperatures are higher in the pure formate (D) than in a mixture with zirconia (C). This may be due to a mass action effect in which the concentration of CO and CO_2 increases sufficiently above the surface of the reactant to suppress further decomposition and hence higher temperatures are required to complete the reaction. This temperature discrepancy could also be

due to a particle size effect; smaller sized material is known to decompose at lower temperatures. However, comparison of Curves D (pure formate) and B (same pure formate diluted with zirconia) shows that the reaction temperatures are lowered in the diluted material suggesting that the lowering is due to a mass effect and not to a particle size effect.

The lack of any discontinuity in the TGA curve at approximately 720°C in all compositions up to 11.5 mole % CaO demonstrates the absence of any intermediate carbonate phase. Even in the more highly doped materials, the weight loss is minimal; at 720°C the loss is 0.3% and 0.4% for the 13.8 and 16.0 mole % materials respectively. This is contrary to expection. Assuming that all the formate in the 16.0 mole % materials were to form an intermediate carbonate, then a weight loss of 5.7% would occur, which agrees well with the experimental value of 5.8% obtained with a mechanical mixture (Curve B). Alternatively, if only the free formate were to act in this manner, i.e., only 22% of the total, then a weight loss of 1.25% would occur, which is well outside the limit of 0.1% that can be recorded by the thermobalance.

The much lower-than-expected weight loss that developed in the doped materials suggests that very little carbonate is formed during heating. This, in turn, suggests that the majority of the formate present decomposes directly to the oxide rather than first forming an intermediate carbonate. A weight loss of 0.4% for the doped 16.0 mole % material compared to 5.8% for a mechanical mixture of the same composition indicates that only

7% (0.4/5.8) of the maximum amount of carbonate that could be formed actually develops in the doped material. For the 13.8 mole % material, this figure is reduced to 5% (± 1%). The TGA curve of the 11.5 mole % material at 720°C implies that less than 2.5% (± 2.5%) carbonate was formed.

The decomposition of most of the formate directly to the oxide is unusual, yet well over 90% follows this reaction route for which TGA fails to show any specific decomposition temperature. The absence of a sharp weight loss between 300°C and 400°C (except in 13.8 and 16.0 mole % material) such as is developed in mechanical mixtures (which contain crystalline formate) suggests that the formate is present in an amorphous state and hence the decomposition is slow and occurs over a wide temperature range. Even in the two compositions where an inflection is developed in the TGA curves, the additional weight loss is only approximately 34% of that required for the direct conversion of formate to oxide. Hence, the remaining 60% (difference between the 34% decomposed at the inflection temperature and the approximately 94% decomposed up to 720°C) must break down outside the temperature limits of the inflection and the associated weight loss must also occur above and/or below the inflection temperature.

This behaviour is consistent with the formate being adsorbed on the zirconia surface. It is unlikely that the adsorbed formate would exist as a stable crystalline layer which would decompose sharply at a critical temperature. Rather, it would be present in a random structure, particularly when the

substrate itself is amorphous, and would be expected to decompose slowly over a wide temperature range.

The endothermic reaction at 350°C in DTA, due to the loss of chemi-sorbed water, was discussed earlier. The coincidence of this DTA peak with the inflection recorded in the TGA of the 13.8 and 16.0 mole % materials suggests that the endotherm may be more reasonably attributed to the decomposition of the formate to, mostly, oxide. It is seen in Figure 5 that the magnitude of this 350°C endotherm increases with increasing formate content. It is also a relatively broad peak as would be expected for the decomposition of an adsorbed amorphous phase.

Unfortunately, it was not possible to gain quantitative data on the amount of formate decomposed at approximately 350°C because part of the weight loss recorded was also due to the loss of some water from the precipitate itself, c.f. the loss of 2.1 weight % from undoped zirconia between 275°C and 400°C - the temperature range for the 350°C endotherm in doped material. However, on a qualitative basis, if it is assumed that the weight loss from the zirconia is always 2.1%, then any additional loss would be due to the decomposition of the formate. Using this approach, it may be shown that approximately 70 ± 10% of the total formate present in the 13.8 and 16.0 mole % materials is completely decomposed. The discrepancy between this figure and the over 90% determined above from the weight loss at 720°C is presumably due to the invalid assumption that <u>exactly</u> the same weight loss occurs from the zirconia component of the undoped material as in the different doped batches. However, the data do show qualitatively

that essentially all the formate present is decomposed directly to the oxide at approximately 350°C. These results are summarized in Figure 9.

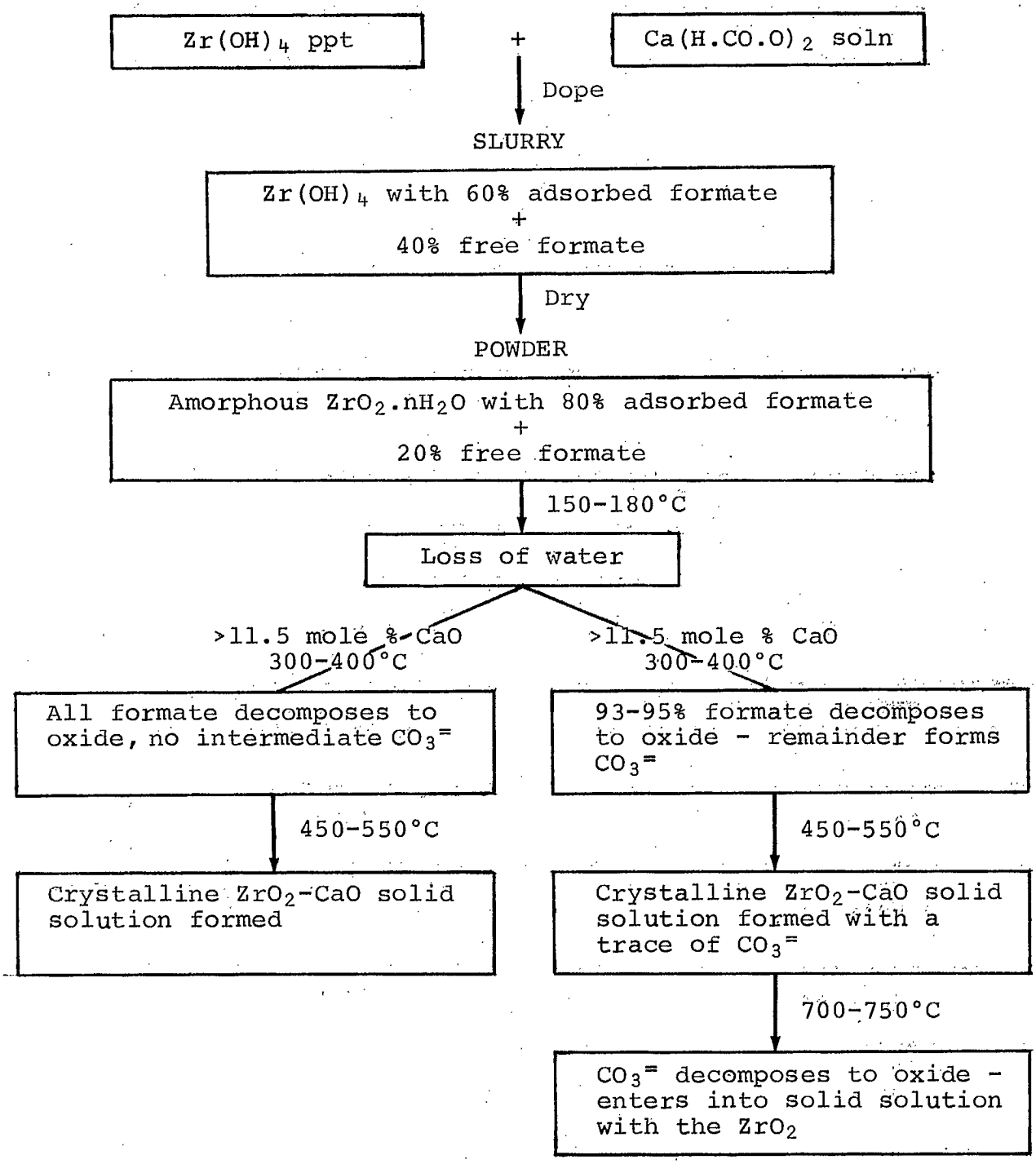

Figure 9. Summary of reactions occurring during the preparation and calcination of doped zirconia.

X-ray Diffraction Analyses

Initially, the powder samples were examined using a North American Philips X-Ray Diffractometer in order to identify the phases formed in both the as-prepared and calcined materials. However, the equipment was found to be too insensitive to detect low concentrations of crystalline material which may be present under certain conditions, e.g., the products formed immediately after the reactions shown by DTA. Consequently, all analyses were conducted using a Guinier-DeWolff focussing camera which is inherently more sensitive than a diffractometer yet retains approximately the same angular dispersion (1° 2θ/4 mm of film for the camera; slightly less for the diffractometer).

The main disadvantage in the use of a Guinier camera is that it does not record diffraction data at 2θ angles greater than approximately 90° using Co K-alpha radiation. Hence, no information can be obtained from the 'back-reflection' region, i.e., 2θ angles greater than 90°, where minor changes in lattice spacings due to either compositional changes or strain effects are more readily observed. As a result, samples were examined with a Guinier focussing camera to identify the phases present and with a non-focussing Debye-Scherrer camera (which essentially records all the diffraction data between 2θ angles of zero and 180° with a dispersion of 1° 2θ/mm of film) to obtain data on changes in the high-angle 'back-reflection' region.

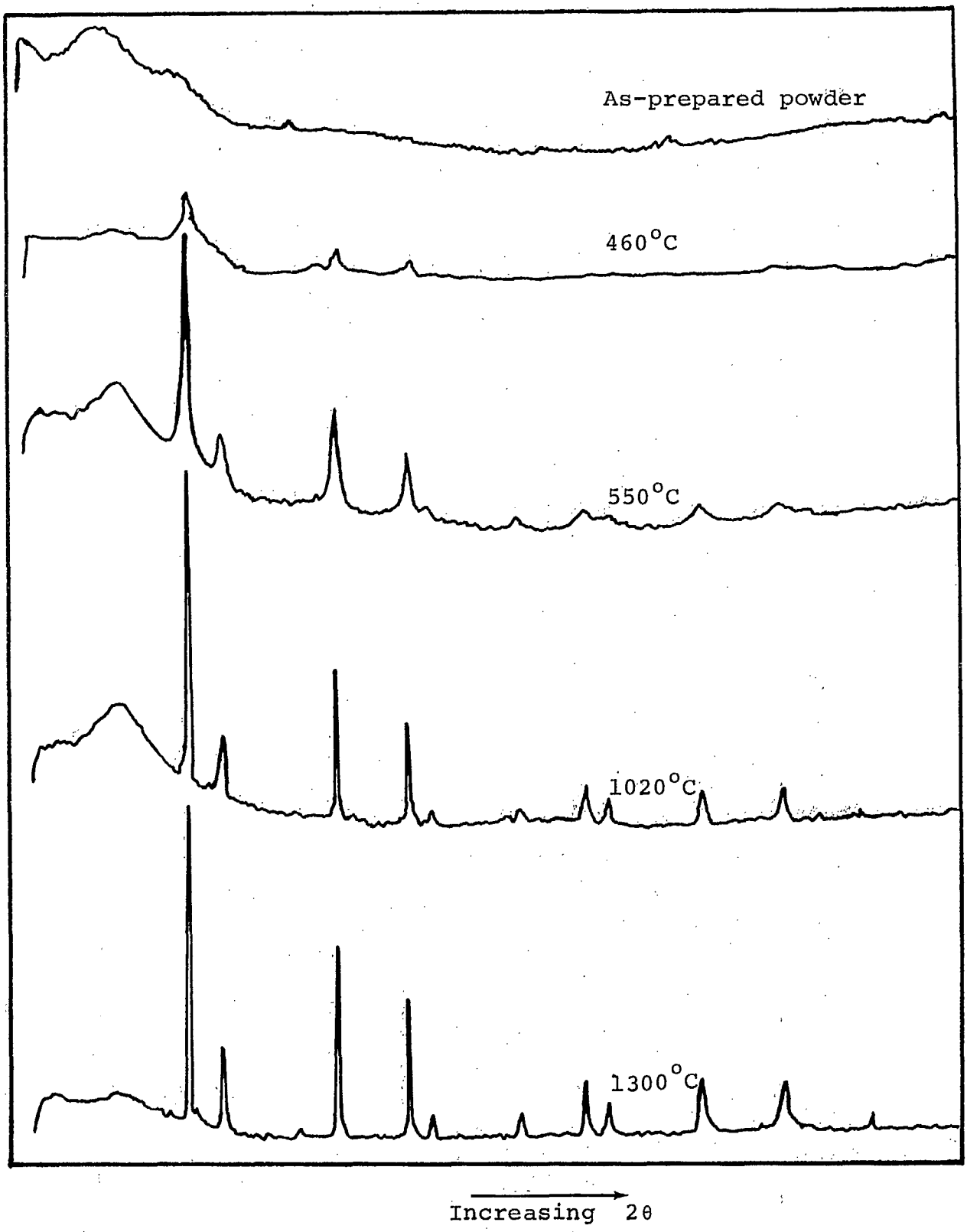

Figure 10. X-ray diffraction patterns of zirconia containing 16.0 mole % CaO. Samples heated for 1 hour at temperatures indicated, allowing the cubic phase to develop above 550°C.

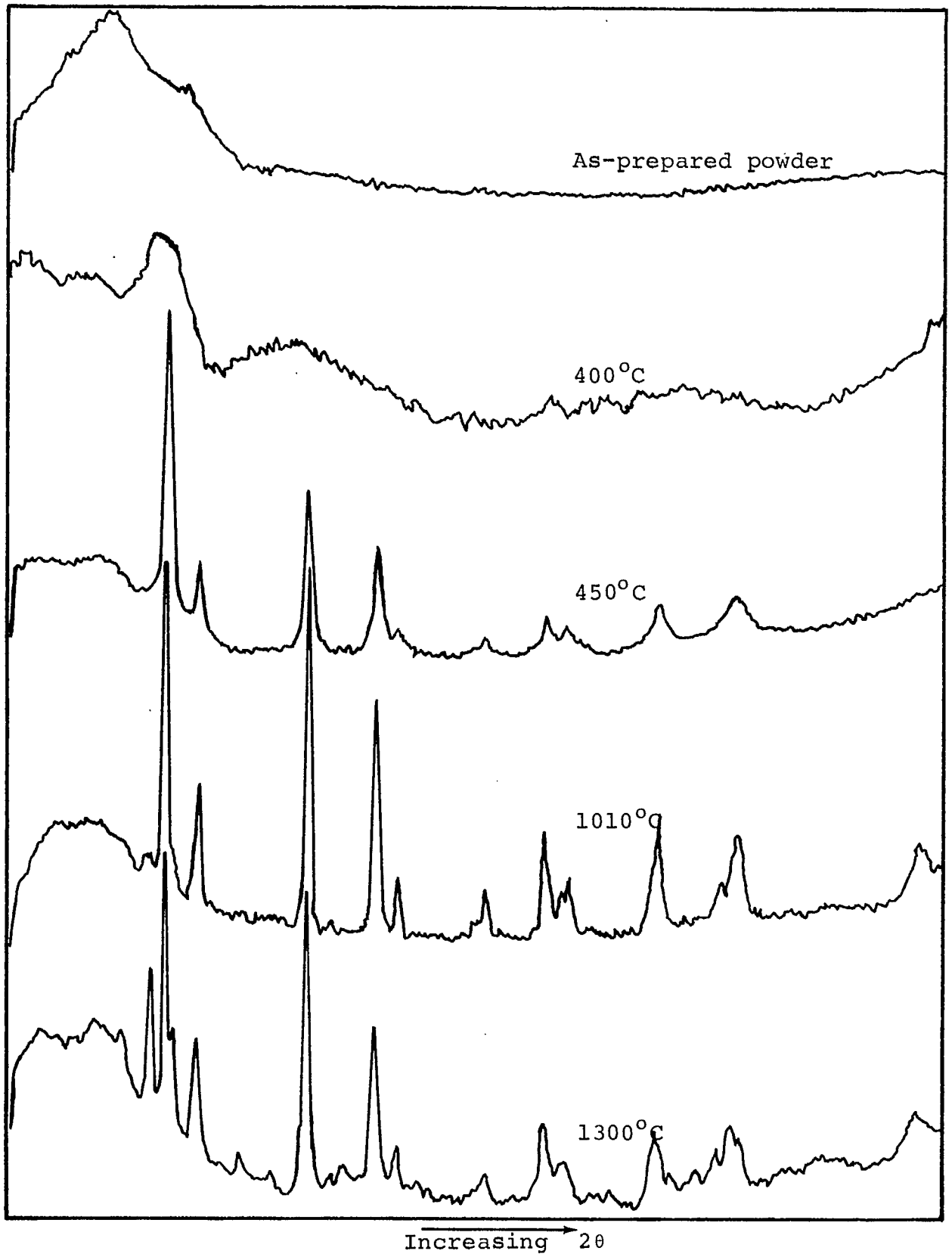

Figure 11. X-ray diffraction patterns of zirconia containing 7.6 mole % CaO. Samples heated for 1 hour at temperatures indicated, allowing the cubic phase to develop above 450°C and cubic + monoclinic above 1010°C.

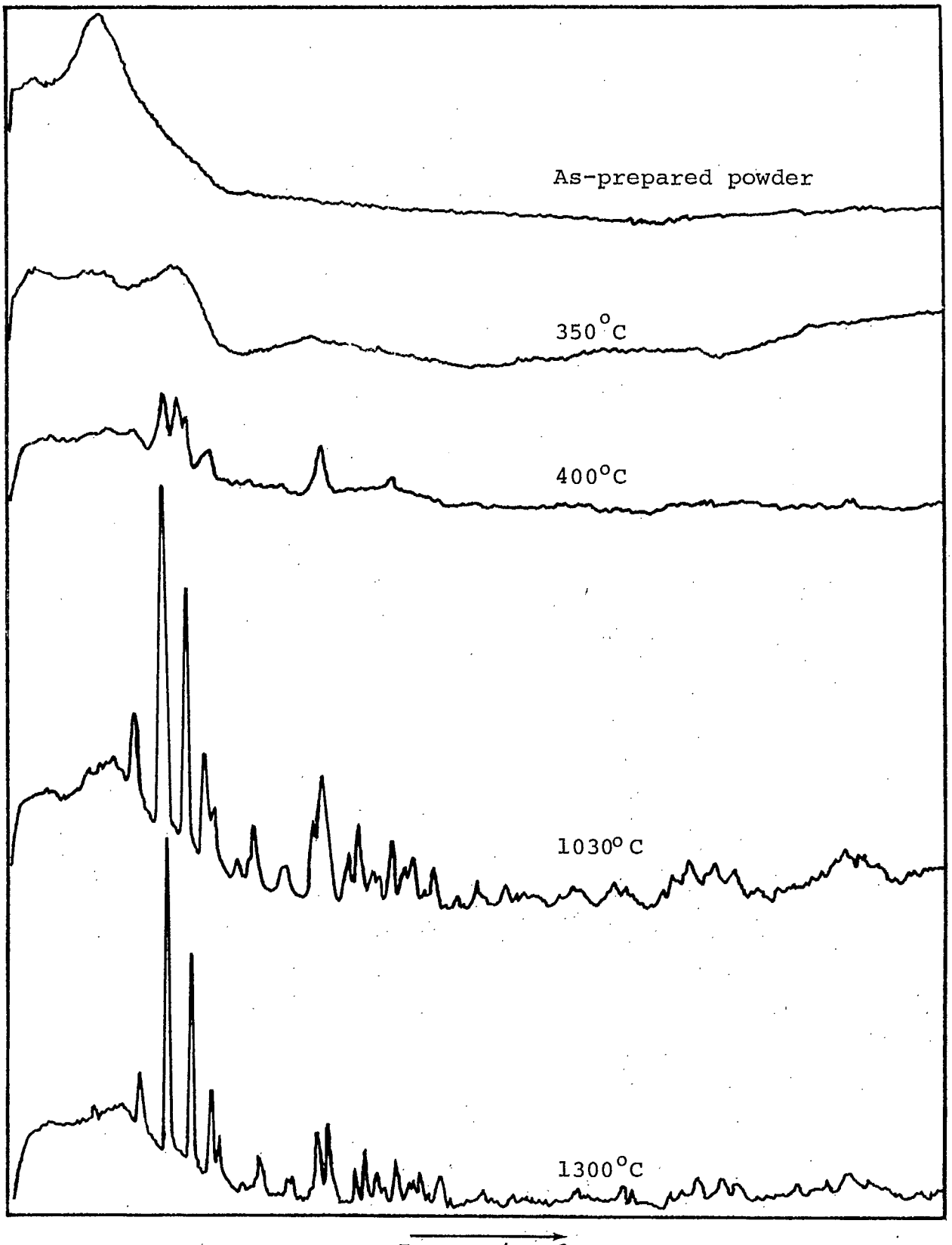

Figure 12. X-ray diffraction patterns of undoped zirconia. Samples heated for 1 hour at temperatures indicated, allowing a trace of cubic and monoclinic phases to develop at 400°C. At higher temperatures only the monoclinic phase is retained.

Minor differences in the diffraction patterns were readily shown in the derived diffractograms produced by microdensitometer scans of the photographic film. Initially, diffractograms were produced using maximum sensitivity because this allowed accurate intensity ratios to be obtained, which proved to be valuable in examining the internal strain developed in fired, partially stabilized materials. However, for the purposes of presentation in this report, the operating conditions of the double beam microdensitometer were changed to give maximum attenuation of the recorded peak height (Appendix D). Typical results obtained in this manner are shown in Figures 10, 11 and 12 in which the data were obtained from a 1:1 scan of film exposed in a 57.3-mm diameter Debye-Scherrer camera that has a dispersion of 2° 2θ/mm of film.

The results can be divided into three groups in which the material is either undoped, partially stabilized or fully stabilized zirconia. Consequently, data is presented for only the three groups rather than for each individual composition. All samples were shown to be completely amorphous in the as-prepared state and to become progressively more crystalline as the calcination temperature is increased.

Figure 10 illustrates the typical diffraction patterns produced by fully stabilized materials after calcination to the temperatures indicated. In the example given, it can be seen that the sample contains a very low concentration of crystalline material. On heating to 550°C, i.e., just above the strong exothermic reaction at about 535°C (Figure 5, Curve F), the sample

develops a significant amount of cubic crystalline material having a very small crystallite size - all the diffraction peaks are broadened and consequently there is no resolution of the back-reflection doublets.

As the temperature is progressively increased, the line-broadening effects are reduced and consequently the recorded peak-heights are increased indicating that the crystal size is gradually increased. Although not shown in Figure 10, this reduction in peak-width allowed the back-reflection doublets to be resolved in the diffraction patterns of material heated above 1200°C. It can be shown[20] that this resolution occurs for Co k-alpha radiation when the size of the coherent diffracting domain (assumed to be the crystal size) exceeds about 400 Å (Appendix D). Hence, the resolution of the doublets demonstrated that the fully stabilized materials have a crystal size of approximately 400 Å at 1200°C.

The diffraction patterns developed on heating the partially stabilized compositions are slightly more complex. Initially, the material crystallized as a cubic solid solution. With progressively increasing temperature the peak widths are reduced suggesting that a gradual crystal growth process occurs. Above 1000°C the system becomes two phase as the amount of cubic material is reduced and the amount of monoclinic material is increased. It was not possible to distinguish the cubic from the tetragonal phase in these materials after heating to moderate temperatures because the intrinsically similar patterns have broadened diffraction peaks due to either small crystal size and/or strain effects.

It should be noted that these results are in apparent conflict with the reported phase equilibrium data for the $CaO-ZrO_2$ system[21] which indicates that the compositions between 2 mole % and 12 mole % CaO are composed of monoclinic solid solution and cubic solid solution below 900°C, while at higher temperatures the system is reported to be a single phase tetragonal solid solution.

This discrepancy between the reported data and the present results is probably due to the invalid comparison of true equilibrium data with those obtained under dynamic conditions. It is probable that the cubic phase that developed initially in the PSZ compositions at about 450°C (Figure 11) is in metastable equilibrium and the system would probably become two-phase on extended annealing.

The absence of any tetragonal phase in the partially stabilized zirconia (PSZ) samples heated above 900°C may be due to the very rapid decomposition of this phase on cooling or even quenching. The fact that the tetragonal phase is only developed in finely divided zirconia has led to the suggestion that the stability of this phase is dependent on the crystallite size. It has been reported that the tetragonal phase becomes unstable when the crystallite size exceeds 300 Å[22]. This is suggested to be the reason why tetragonal ZrO_2 can not be retained on quenching from high temperatures, yet it may be prepared by the low temperature calcination of salts such as the chloride or nitrate. Assuming similar behaviour to that for the fully stabilized materials, it would be expected that the crystallite size

of the PSZ materials would exceed 400 Å in material calcined at 1200°C, i.e., an unstable tetragonal phase would be expected to form at temperatures less than 1200°C. Consequently, the diffraction patterns obtained for material heated to 1010°C and 1300°C, Figure 11, show the presence of cubic + monoclinic ZrO_2 rather than a tetragonal solid solution.

More recent data[23] suggest that the stable phase above 900°C for PSZ materials is a cubic solid solution rather than tetragonal. It is reported that the phase field between 0 mole % and 20 mole % CaO may be regarded as a continuous solid solution between pure monoclinic ZrO_2 and the cubic compound $CaZr_4O_9$. The supersaturation of the compound that occurs on cooling from the firing temperature allows the precipitation of fine-grained monoclinic pure zirconia in grains which had previously been entirely cubic. This mechanism results in a structure in which the grains are composed of alternating cubic and monoclinic domains of approximately 1000 Å. This fine-textured microstructure has recently been shown to be responsible for the very good thermomechanical properties of the partially stabilized materials[24].

In addition to identifying the phases formed in these materials, X-ray powder diffraction patterns were also used to determine the unit-cell edge of each annealed material. The lattice parameter would be expected to change with composition between the limits of approximately 10 mole % and 20 mole % CaO, i.e., the limits of the cubic phase field. Hence, only samples having the composition: 7.6 mole %, 11.5 mole %, 13.8 mole % and

16.0 mole % CaO in ZrO_2 were examined. The materials were first annealed at 1600°C in air for 1 hr prior to examination.

Powder diffraction patterns were obtained of each material using Fe-filtered Co K-alpha radiation and a Debye-Scherrer camera (114.6-mm diameter) having a dispersion of 1° 2θ/mm. Using the Straumanis technique[25], a series of unit-cell edge values was first computed for each (hkl) plane. These values were in error due to the systematic errors of adsorption and divergence of the beam - the errors are greatest at low angle and least at high angle and become zero at 2θ = 180°. Consequently, a least-squares analysis was obtained for a plot of the unit-cell edge values ($a_{(hkl)}$) versus the Nelson & Riley function[26] (an angular function proportional to the systematic errors) from which extrapolation to 2θ = 180° gave the true a_o value. The a_o values were determined separately by two individuals A and B using the same films in order to estimate the subjective error in reading the film. The unit-cell edge values together with the calculated single crystal density of the cubic phase for each composition were determined to be:

Composition	Determined by 'A'		Determined by 'B'	
mole % CaO	a_o Å	density g/cc	a_o Å	density g/cc
7.6	5.1273	6.071	5.1289	6.066
11.5	5.1301	6.059	5.1304	6.060
13.8	5.1308	6.059	5.1306	6.060
16.0	5.1389	6.030	5.1385	6.032

It can be seen that the data for the fully stabilized materials (11.5 mole % and above) are in close agreement for each composition; the a_o values lie within ±0.0002 Å of the mean. The greater difference between the a_o values for the 7.6 mole % material was expected as the diffraction pattern was diffuse due to lattice strain effects; the back-reflection doublets were just resolved. It has been estimated that the precision of the unit-cell edge value is about ±0.2% when the doublets are not resolved and approximately ±0.1% when the doublets are clearly resolved[27]. Hence, the precision of the a_o value for the 7.6 mole % material is only about ±0.0051 Å (±0.1%) and for the fully stabilized materials it is ±0.0005 Å (±0.01%). This leads to a precision of ±0.018 g/cc in the density of the cubic phase in the partially stabilized material and to a precision to ±0.002 g/cc in the density of the fully stabilized materials.

The variation of the a_o values with the CaO content indicated that the lower limit of the cubic phase field lies at 13.8 mole % CaO; this is in very good agreement with the reported value of 13.4 mole %[28].

Infrared Spectroscopy

The powder transmission spectrum of selected materials was examined in an attempt to further characterize the structure of the precipitated zirconia and also to examine the state of the adsorbed formate on the surface of the precipitate after drying to a powder. For this purpose, samples of 7.6, 11.5, 13.8 and 16.0 mole % CaO and also samples of these materials calcined

at 1000°C for 1 hour were examined.

The spectra were obtained from KBr pellets containing 0.5 to 5.0 wt % of the dispersed powdered sample. Particle size distribution analyses (Figure 19, page 56) of the powders indicated that the mean agglomerate size could be as high as 25 μm and hence a small effect of particle size on the spectra could be expected[29]. Consequently, all the samples were first dry-ground in an alumina mortar and pestle to disperse the agglomerates. The sample was dispersed in the KBr by stirring and subsequently screening the mixture prior to vacuum pressing in a ½ in. diameter die at 90,000 psi. A Perkin-Elmer double beam grating spectrophotometer (Model 457) was used to obtain spectra in the region 4000 to 250 cm^{-1}. The results are given in Figures 13 to 16.

The spectra of the as-prepared materials (Figure 13) are relatively uninformative. The three strong absorption bands at approximately 3400, 1595 and 1335 cm^{-1} have been reported recently in the literature for the lime-stabilized zirconia materials[30] and were attributed to the presence of OH groups (3400 cm^{-1}) and to impurities formed by the adsorption of atmospheric CO_2 (1595 and 1335 cm^{-1}). These assignments are probably valid for the present work.

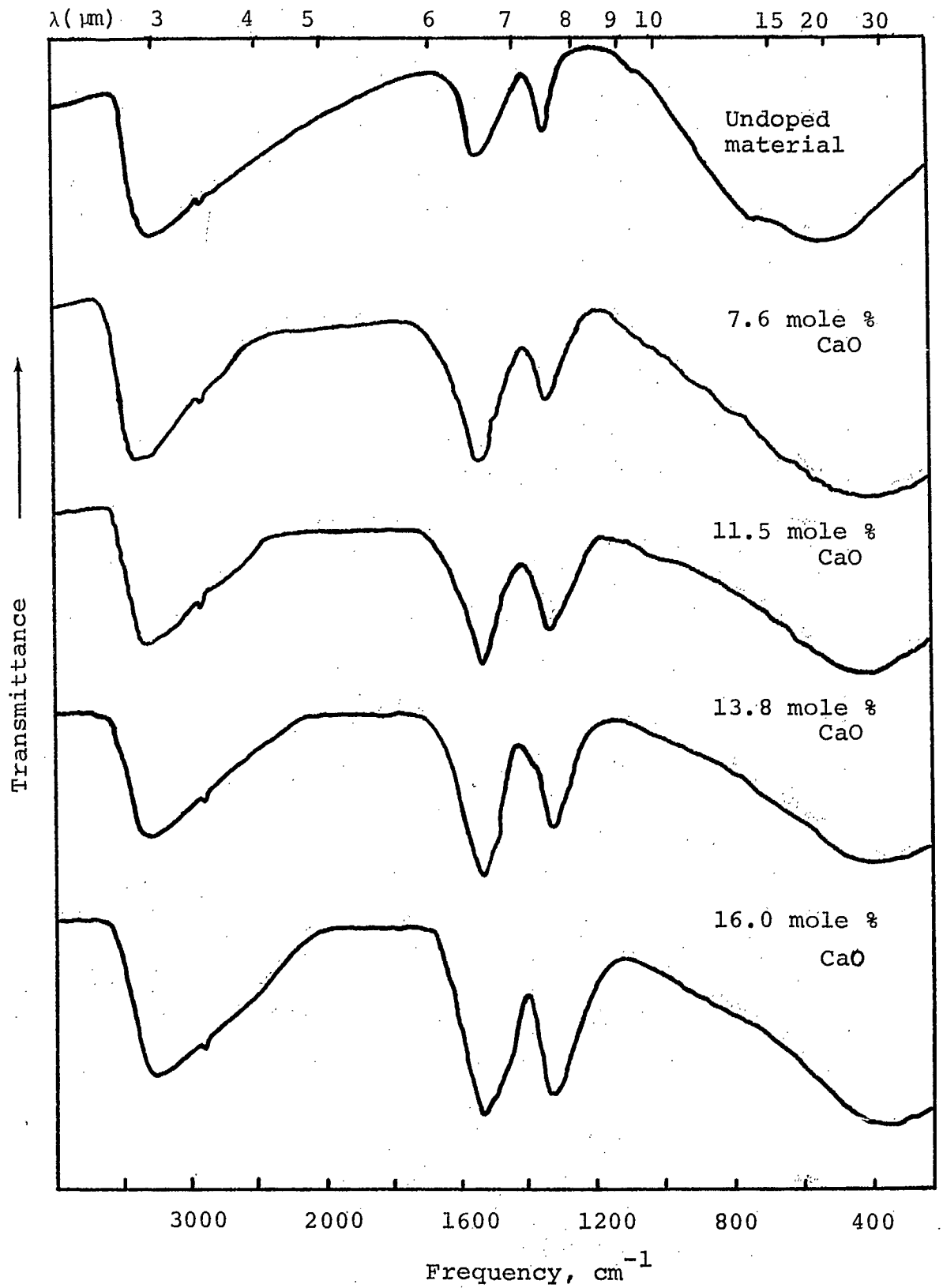

Figure 13. Infrared transmission spectra of as-prepared zirconia powders.

The broad absorption band at 3400 cm^{-1} is the fundamental stretch frequency of the O-H bond. The peak is broadened and asymmetric due to a varying degree of hydrogen bonding, i.e., the peak shape is indicative of surface heterogeneity. The presence of absorbed molecular water is suggested by the band at 1595 cm^{-1} which is the fundamental bend frequency for the H-O-H structure. The peak is slightly asymmetric due to some interaction between the water and the zirconia substrate (possibly heterogeneous hydrogen bonding) or due to partial overlap with a 'carbonate' peak. No assignment is suggested for the minor absorption peak at approximately 2900 cm^{-1}.

The adsorption of CO_2 onto a surface containing metal ions, oxygen ions and hydroxyl groups would be expected to produce one or more of the structures below:

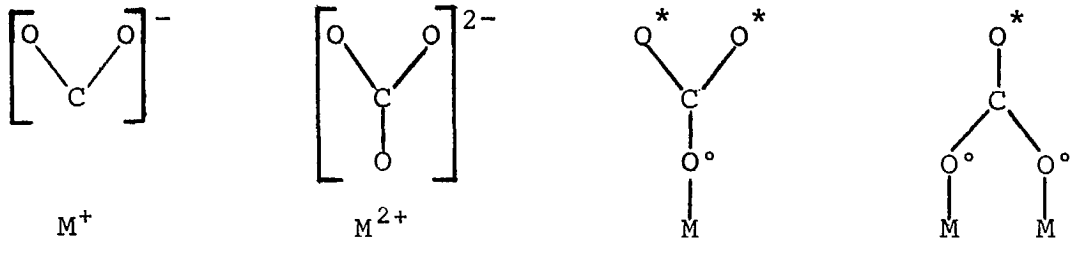

carboxylate (A) | carbonate (B) | monodentate carbonate (C) | bidentate carbonate (D)

Structure A, formed by the direct adsorption of CO_2 onto a metal ion by the transfer of an electron from the adsorbent to the adsorbate, is essentially the same as the structure of an ionized salt of a carboxylic acid, c.f. $(H.CO.O)_2Ca$. Having an XY_2 structure, it will give rise to both symmetric and asymmetric C-O stretching vibrations occurring in the region 1350 to

1400 and 1560 to 1580 cm^{-1}. The torsional vibration of the $O_{\diagdown C \diagup O}$ group occurs at about 650 cm^{-1}. The important feature of this structure is that it does not give rise to any absorption bands in the region 1000 cm^{-1}.

In the case of the carbonate species that may be formed (B, C and D), the structures are based on the planar CO_3 group which, due to degeneracy, only allows four of the possible six vibration modes to be observed. Of these four, the symmetrical C-O stretch frequency is inactive in the infrared (no change in the dipole moment) and can only be observed in the Raman spectrum (due to the change in polarizability). Consequently, the ionic carbonate Structure B gives rise to three absorption bands; one at 1440 cm^{-1} and two below 900 cm^{-1}. Again no absorption occurs in the region of 1000 cm^{-1}.

Modification of the ionic Structure B to the covalent monodentate or bidentate carbonates (C and D) introduces a degree of asymmetry into the structure which thus allows the fundamental C-O stretch frequency (1080 cm^{-1}) to become infrared active. In addition, the symmetric doubly degenerate vibration becomes split into its components due to the slight difference in the C-O° and C-O^{*} force constants. This splitting is greater in the bidentate than the monodentate complexes and typically is of the order 300 cm^{-1} and 100 cm^{-1} respectively.

From the foregoing, it will be appreciated that there are various structures which may be formed by the adsorption of CO_2 onto a hydrated metal oxide surface. In principle, the different structures should be distinguished by their infrared

spectra. For example, the carboxylate Structure A does not have an absorption at about 1070 cm^{-1} whereas the carbonate structures (B, C and D) absorb in this region. The ionic carbonate (B) will have a single absorption in the range 1370-1430 cm^{-1} whereas the covalent structures (C and D) will have two peaks near this frequency range separated by 100 cm^{-1} (monodentate) to 300 cm^{-1} (bidentate?). On this basis, it would appear straightforward to identify the species present in a sample.

However, the situation is further complicated by the fact that absorption bands at 1570 and 1330 cm^{-1} and also at 1630 and 1220 cm^{-1} have all been shown to arise from a bidentate structure (page 208, Reference 29). It is possible that the structures involved are either D or E:

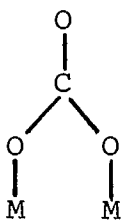

(D)

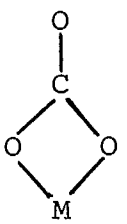

(E)

On the intuitive assumption that the two metal atoms in Structure D will exert a greater influence on the degenerate C-O stretching vibrations than the single metal atom in E, the bands at 1630 and 1220 cm^{-1} are attributed to Structure D and those at 1570 and 1330 cm^{-1} to E.

As shown in Figure 13, the as-prepared materials contain both adsorbed water and CO_2. Comparison of the spectrum of undoped material with that for material containing 16 mole %

formate shows little or no difference which suggests that the adsorbed CO_2 has formed a carboxylate structure on the surface of the undoped material. This possibility is further supported by the spectra developed by all the materials investigated, which, after calcining to 1000°C and equilibrating with the ambient atmosphere for one year, showed strong absorption bands at 3400, 1595, 1375, 1350 cm^{-1} (which are essentially the same as the as-prepared materials, Figure 13) together with a minor absorption band at 785 cm^{-1}. The low frequency vibration agrees well with the strongest absorption in the spectrum of pure calcium formate, Figure 14. Consequently, it is probable that CO_2 is adsorbed onto the surface of all the precipitated zirconia materials to form a free carboxylate structure.

One of the main features of the spectra of the as-prepared doped materials is that they do not have the strong absorption bands at 1350-1400 cm^{-1} and at about 800 cm^{-1}, typical of pure free formate. Because of the tenuous nature of the evidence for the formation of a carboxylate structure on the surface of aged calcined materials (the evidence resting on a single very weak absorption at 785 cm^{-1}), the spectra of mechanical mixtures of undoped zirconia and freeze-dried pure calcium formate were examined in order to determine the limits below which the presence of free formate cannot be detected in the infrared transmission spectrum. The results indicated that the limit was below 8 wt % formate (using the unambiguous absorption bands close to 800 cm^{-1}, Figure 14). In this particular mixture, the weight fraction and the mole fraction are nearly equal and hence the lower limit for

the detection of formate can be regarded as lying below 8 mole %, yet no characteristic formate absorption bands were detected in doped zirconia materials containing up to 16 mole % formate. Consequently, it is assumed that the majority (over 80% - Appendix C) of the formate in the doped samples is adsorbed onto the surface of the zirconia substrate in such a way that the usual torsional vibration of the $O\diagdown C\diagup O$ group is effectively prevented. This could occur if the oxygen atoms of the carbonyl and former hydroxyl groups of the formate structure were covalently bonded to metal atoms. Such a direct bond would also explain the very low recovery of free dopant in slurries of doped zirconia samples (Appendix C).

It will be recalled that the DTA data suggested that the broad endothermic peak at 350°C in the doped materials was due to the decomposition of the adsorbed formate (TGA data suggests this to be over 90% of the total present - see page 26) directly to the oxide. The remaining free formate (less than 10% in the 16 mole % material) was assumed to decompose at a higher temperature (possibly coincidentally with crystallization of the zirconia component at 400°C to 550°C) to form carbonate which subsequently decomposes to oxide at 720°C. Assuming that this reaction scheme is correct, then the 10% free formate present in the 16 mole % material would be expected to react as the pure formate and to decompose to carbonate in the range 400°C to 550°C (Curves A and B, Figure 4). Consequently, samples of the 16 mole % material were calcined at various temperatures and the infrared spectra of the products were examined in an attempt to determine the

temperature limits of the intermediate carbonate phase. The spectra obtained are shown in Figure 15.

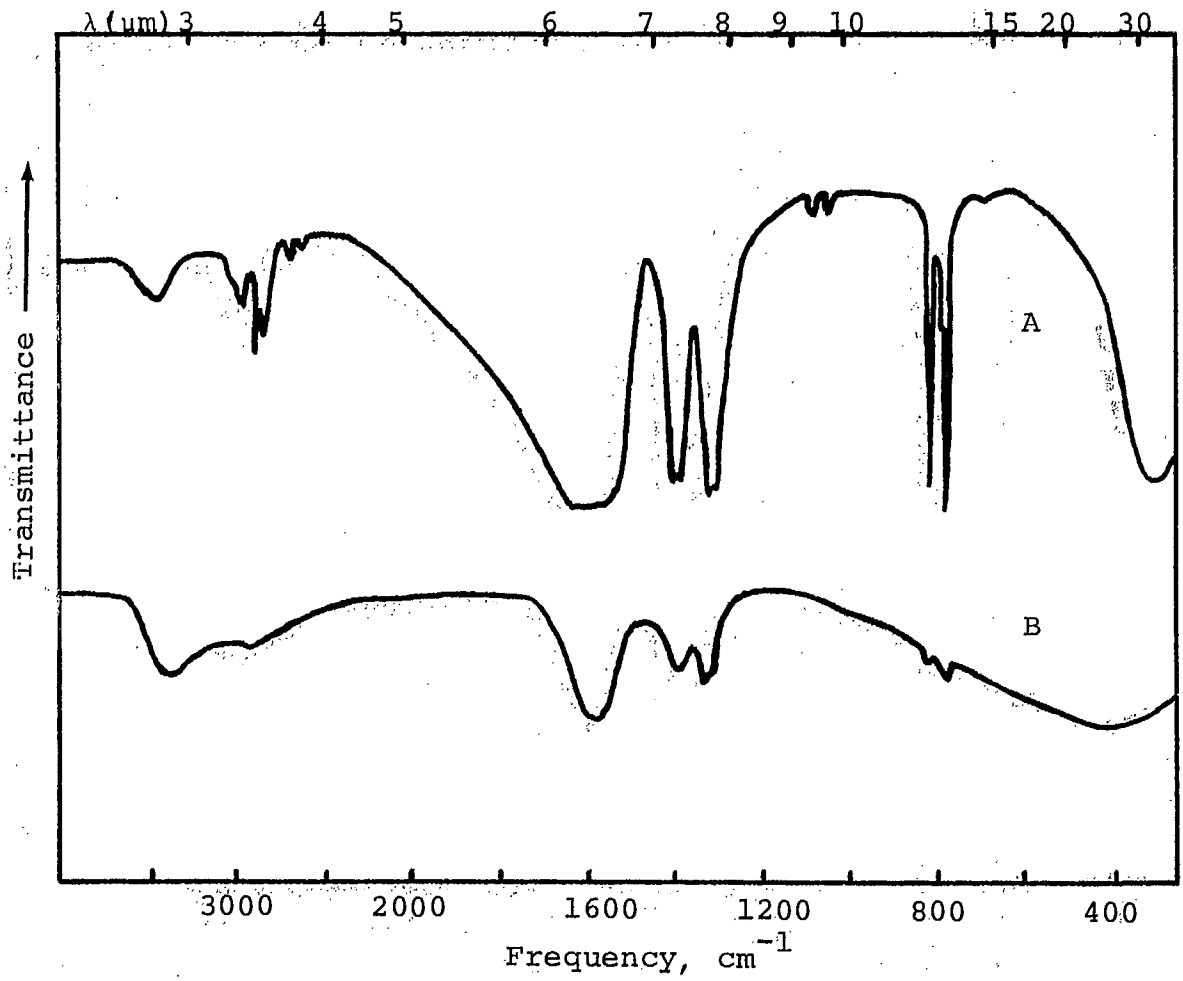

Figure 14. Infrared transmission spectra.

A. Freeze-dried calcium formate aged one year in a normal atmosphere
B. Mechanical mixture of freeze-dried undoped zirconia containing 8 wt% of A

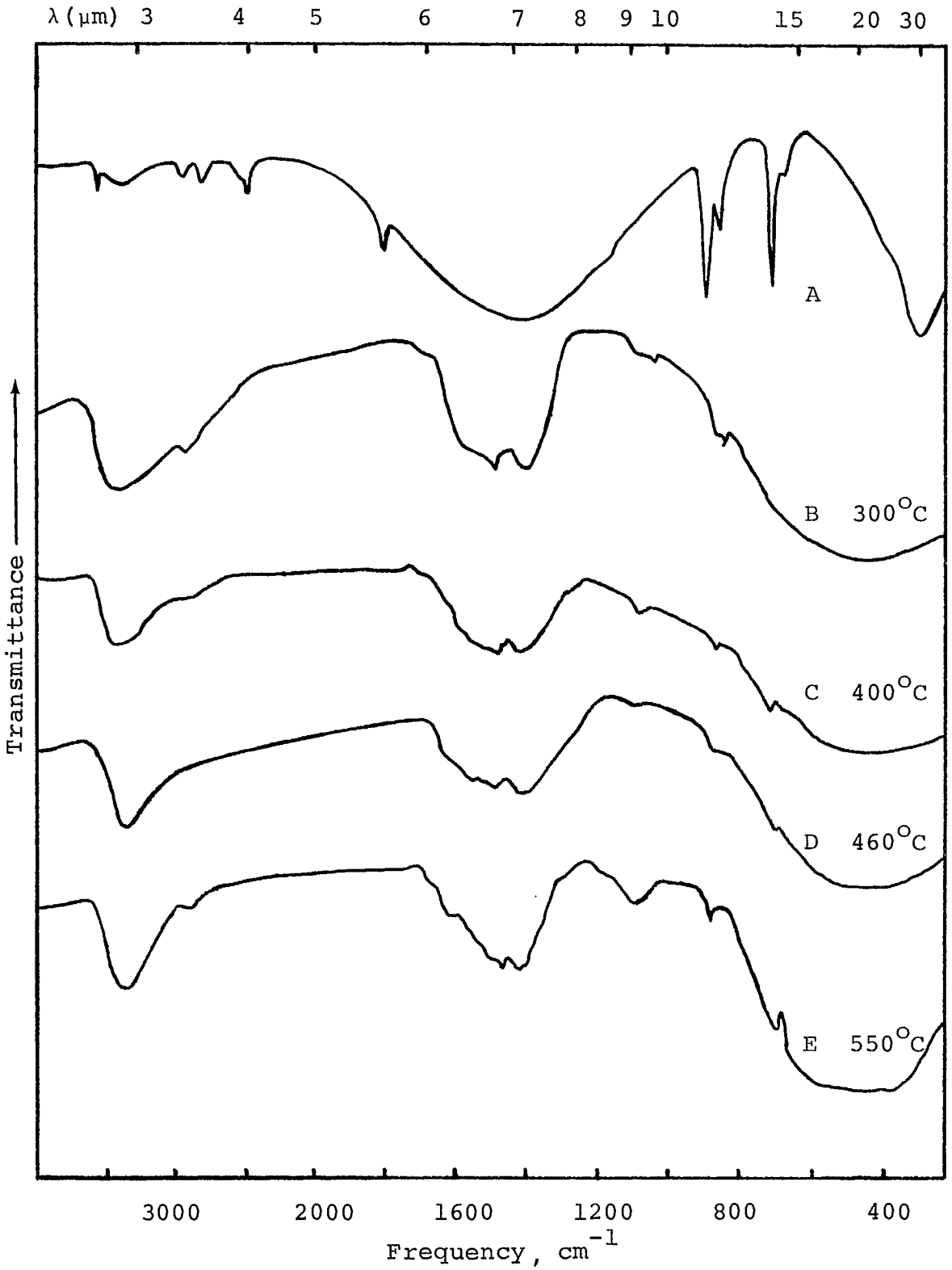

Figure 15. Infrared transmission spectra of materials calcined in air for 15 minutes.
A. Calcium formate calcined to 550°C
B to E. Zirconia containing 16 mole % CaO

It can be seen that there is a gradual change in the spectrum of the 16 mole % material as the calcination temperature is increased. The broad absorption between 1350 and 1650 cm^{-1} develops a progressively greater transmittance at the higher frequency with increasing temperature. In addition, the absorption at 1630 cm^{-1} is enhanced sufficiently to become a distinct peak in the spectrum of material calcined at 550°C. The weak absorptions at about 700 and 870 cm^{-1} also become progressively stronger with increasing temperature.

Comparison with the spectrum of calcium formate calcined at 550°C, Curve A, which is typical of an ionic carbonate (Structure B, page 41), suggests that the absorption bands at 700 and 870 cm^{-1} in the spectra of doped calcined zirconia are due to the presence of an ionic carbonate. Presumably this is just free calcium carbonate which has formed from the free formate present.

The absorption in the range 1350 to 1650 cm^{-1} suggests the development of a covalent carbonate phase. This is further supported by an absorption at 1080 cm^{-1}. Because this 1080 cm^{-1} band was not observed in the spectra of the as-prepared materials (Figure 13), and because the absorption increases in magnitude with calcination temperature, this band further supports the view that the covalent carbonate present in the partially calcined doped zirconia is developed intrinsically rather than by CO_2 pick-up after calcination.

The lack of clearly defined absorption peaks in the region 1350 to 1650 cm^{-1} suggests a considerable heterogeneity in the nature of the covalent carbonate formed. Assuming that

this phase is formed by the partial decomposition of covalently bonded formate on the surface of the amorphous zirconia, then it would be expected that the covalent carbonate would form over a wide temperature range. This is shown in the spectra by the gradual development of the 1080 cm^{-1} absorption between 300 and 550°C.

The spectra also suggest that the amount of covalent carbonate is much greater than the amount of ionic carbonate, because the intensity of the 1350 to 1650 cm^{-1} absorption is much greater than the 700 and 870 cm^{-1} absorption (yet both groups are the strongest bands in the spectrum of the pure phase). This indirectly supports the data in Appendix C which showed that the amount of adsorbed (covalently bonded) formate was about 80% of the total present.

At temperatures above about 750°C, the carbonate phase(s) could no longer be detected in the transmission spectra. However, the tenacity of the OH groups present was shown by the continued presence of the 3400 cm^{-1} absorption in the spectra of materials calcined at temperatures up to 1000°C for 15 minutes, Figure 16.

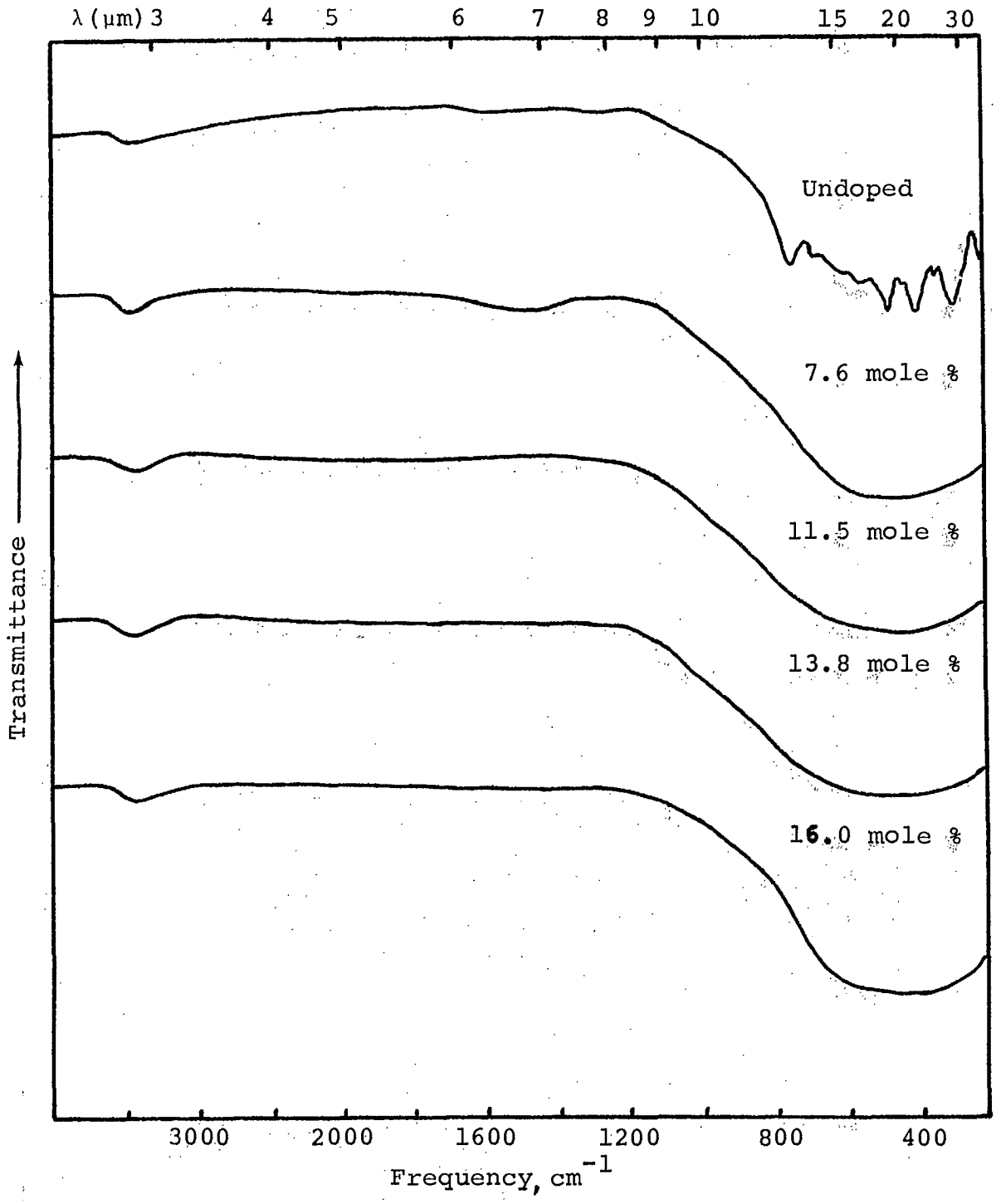

Figure 16. Infrared transmission spectra of zirconia samples calcined in air at 1000°C for 15 minutes.

As shown, the spectra for the fully stabilized compositions (11.5 mole % CaO and above) are essentially featureless and display a single broad absorption band between 800 and 300 cm^{-1}. This is in contrast to the spectrum for the partially stabilized material (7.6 mole % CaO) which has absorptions at 760, 610, 580, 490, 450, 410, 340 and 265 cm^{-1}. This marked difference between the spectra of the cubic and monoclinic zirconia phases has been reported earlier[31], where it was suggested that the absorption at 760 cm^{-1}, which is specific for the monoclinic phase, could be used in an analytical procedure for the determination of monoclinic zirconia.

Surface Area

In order to reduce the considerable shrinkage (and hence reduce the possibility of cracking) during the firing of these extremely bulky materials (typically 45% shrinkage on firing to 1600°C), it was necessary to precalcine prior to fabricating and firing. Hence, to determine the appropriate calcination conditions, a series of samples was calcined at 50°C intervals between 600 and 1300°C and the surface areas measured using a Perkin-Elmer Shell sorptometer. The results are given in Appendix E and for some of the compositions the data is presented graphically in Figure 17.

It can be seen that the doped materials have higher surface areas than the undoped zirconia throughout this temperature range and at any given temperature there is a trend for the surface area to increase with the amount of dopant. The surface

area is seen to fall quite sharply between 600 and 1000°C and this decrease is associated with an increasing sharpness of all diffraction lines in the powder patterns (c.f. Figures 10 to 12) which suggests a progressive increase in crystal size within the powder agglomerates.

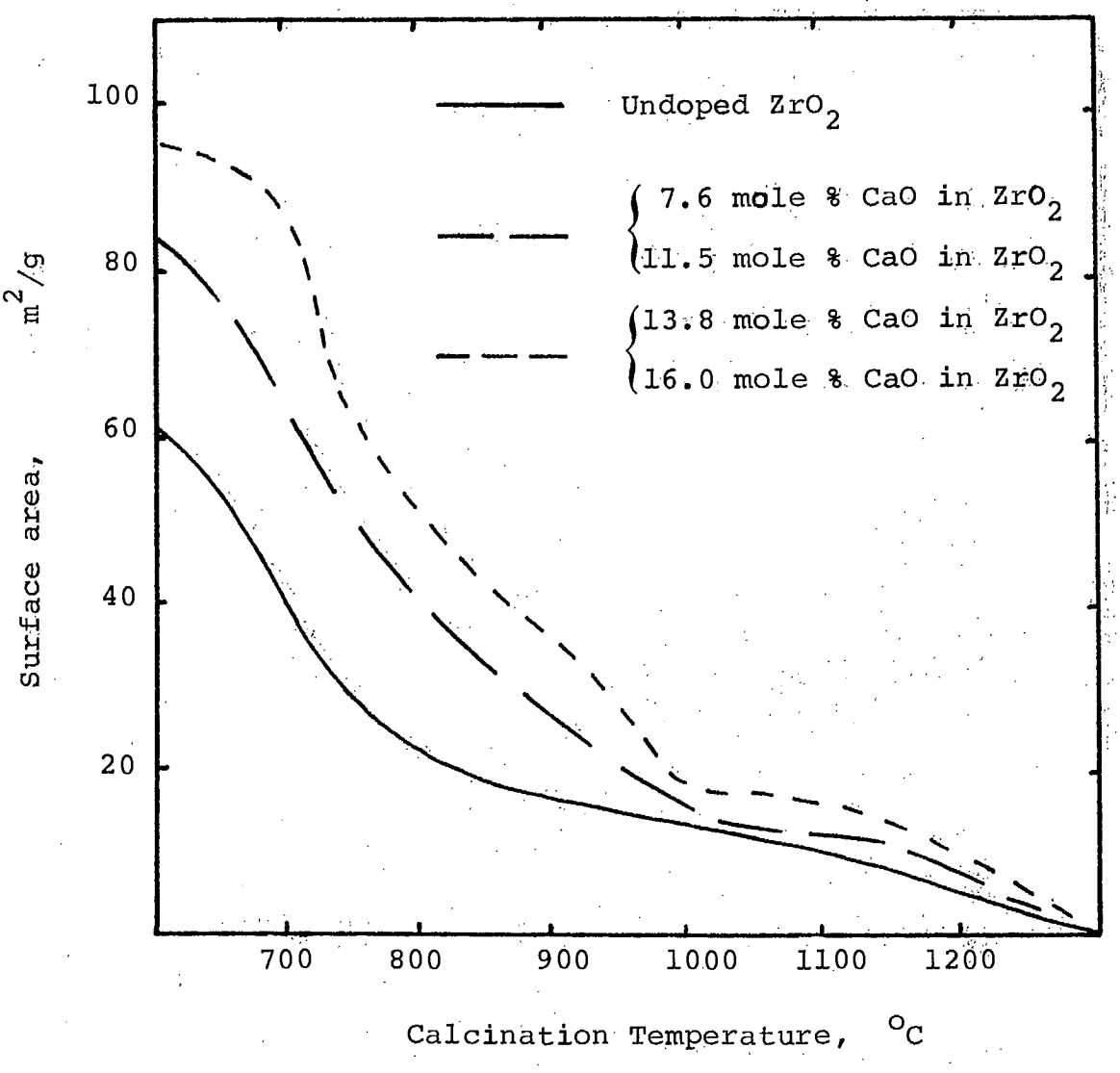

Figure 17. Variation of surface area with temperature for undoped and lime-doped zirconia raw materials.

Using the simplifying assumption that all the particles present in a sample have a perfect cubic morphology, then it may be shown that for zirconia a particle edge length of 400 Å will produce powder having a surface area of 25 m^2/g (Appendix E). From Figure 17, it can be seen that this surface area is developed in the temperature range of approximately 950 to 1000°C. Hence, it should be possible to resolve the X-ray back-reflection doublets in the powder pattern of material calcined above ∿1000°C (Appendix D). However, this assumes that the materials will consist of perfect crystals whereas, in practice, domains will be present and mosaic crystals will be formed. Consequently, it is not surprising that a temperature of 1200°C and above is found necessary to resolve the doublets (page 34). The discrepancy between the X-ray data which suggests a 'crystal' size of 400 Å at 1200°C and the surface area data which give a calculated 'crystal' size of 1250 Å (assuming an average surface area of 8 m^2/g at the same temperature) is good evidence that the crystals within the agglomerates possess a mosaic structure at low temperatures (below 1100°C) (Figure 18).

Between 1000°C and 1100°C the surface area remains essentially constant with increasing temperature as the intra-agglomerate growth ceases. At higher temperatures, the surface area again decreases slowly with increasing temperature as inter-agglomerate growth commences and the samples start to sinter (see sintering curve, Figure 25).

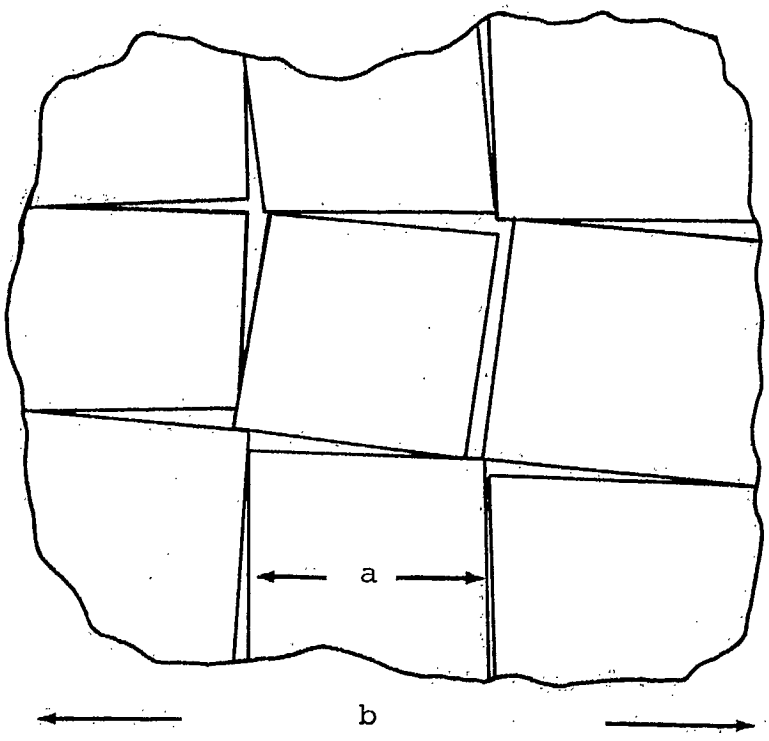

Figure 18. Schematic of mosaic structure developed in powders below 1100°C.

a. X-ray crystal size
b. Surface area crystal size

In order to minimize surface area differences between batches of the same material due to possible temperature fluctuations during successive calcinations, the materials were all calcined at a given temperature between 1000°C and 1100°C, the range in which the rate of change of surface area with temperature is a minimum.

Particle Size Distribution

Immediately after leaving the freeze drier, the materials were composed of perfectly spherical agglomerates. Particle

size analysis obtained from optical micrographs and a Zeiss-Endter analyser showed that the freshly prepared materials had a mean size (m) between 100 μm and 200 μm depending on the batch. This variation was subsequently related to the critical setting of the atomizing gas flow rate and the liquid feed rate used in the spray-freezing operation. However, this variation in m for the freshly prepared materials was found to be unimportant because the spherical agglomerates were extremely friable and broke up readily on normal handling such that m was reduced to approximately 20 μm and the standard deviation (s) was reduced from 3.2 μm to 2.8 μm. The size distribution produced by such handling is shown in Figure 19, Curve A. The data were obtained using a Coulter Counter particle size analyser in which a 4 wt % solution of $Na_4P_2O_7$ was used as both the electrolyte and sample deflocculant.

Prior to size analysis, the samples are usually exposed to an ultrasonic beam in water containing a deflocculant. This treatment further emphasizes the weak nature of these materials, for within 15 seconds the mean size is reduced to 4 μm and s is reduced to 1.9 μm (Curve B). Although material having this size distribution would probably be satisfactory for the production of high-density fabricated bodies, the ultrasonic equipment available was only capable of dealing with very small batches of material (approximately 4 g) and consequently larger batches of material were dispersed by ball-milling.

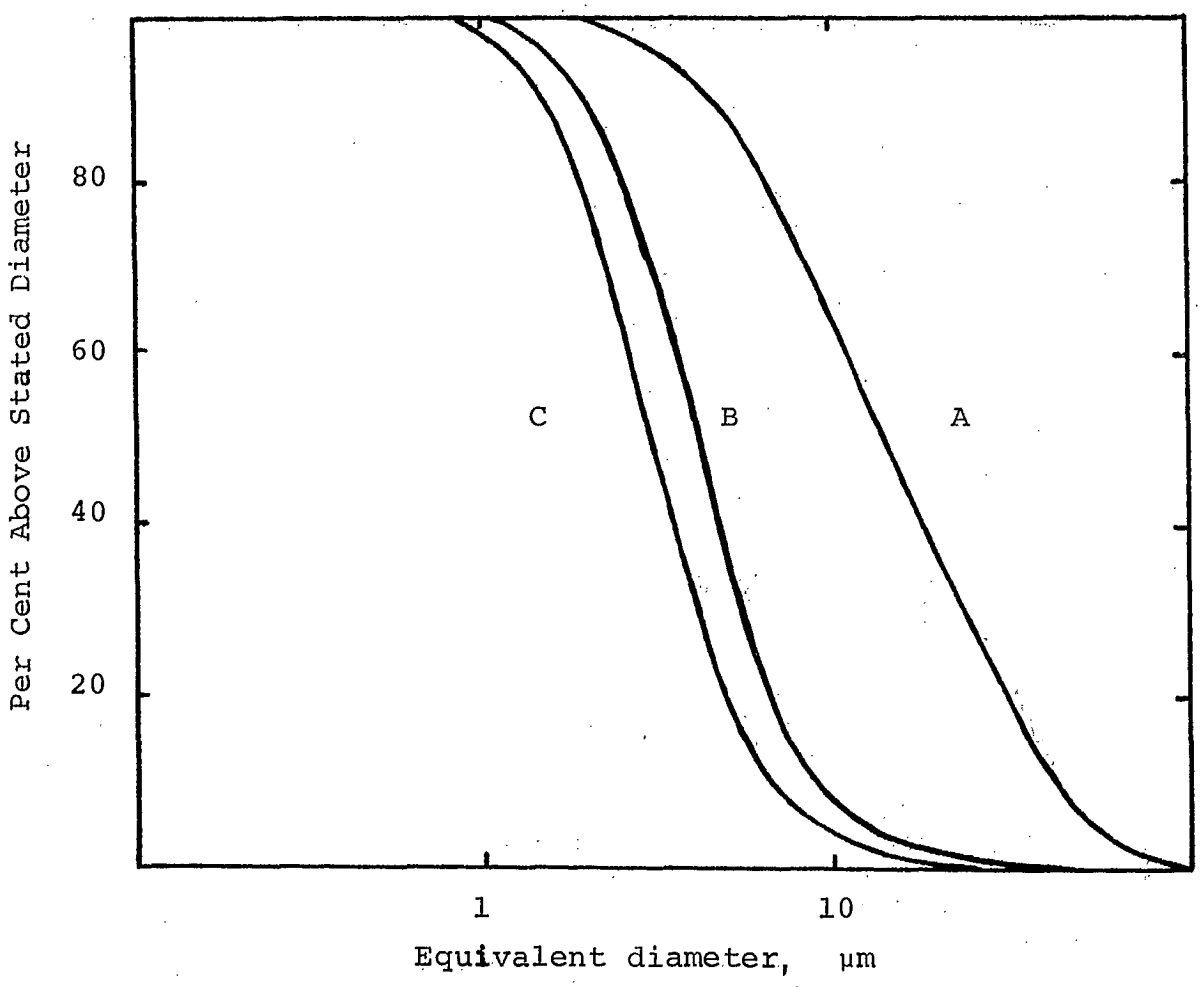

Figure 19. Particle size distribution of 16 mole % material.
A. Typical distribution developed in the as-prepared material after normal handling
B. Typical size distribution observed after treating A with ultrasonics in water
C. Size distribution developed after ball-milling A in alcohol for 1 hour

Attempts to disperse these materials by dry-milling failed; the mill became packed with 15 minutes of operation. No attempt was made to examine the effects of dry milling defloccu-

lants such as the stearates or the aliphatic amines because wet milling proved to be very satisfactory without the use of any deflocculants. In addition to adequately dispersing the zirconia, wet milling also allowed a lubricant and binder to be uniformly dispersed throughout the material. Because de-agglomeration was found to be the single most important parameter to be controlled in order to develop a uniform microstructure and a high fired density, the wet milling process was carried out in isopropyl alcohol rather than water as this not only acted as a solvent for the binder and lubricant but also acted as a desiccant and removed water absorbed on the surface of the powders.

A typical distribution of material wet-milled in alcohol for 1 hour is given in Figure 19, Curve C. The mean size and distribution for all the lime-stabilized zirconia compositions prepared was found to be independent of the composition, mill charge and grinding medium geometry. In all cases, the mean size was approximately 2 μm and the distribution was narrowed slightly from that for the ultrasonically treated material, with s being reduced to 1.7 μm.

Extended milling did not reduce the mean size any further, which suggests that the agglomerates in the powder are being formed as fast as they are broken down. The agglomerate size was also found to be independent of the ultimate crystal size of the material. Calcination of material at 850°C and 1000°C (surface area data gives a crystal size of 220 Å and 550 Å respectively) followed by 1 hour ball-milling in alcohol produced materials having essentially the same particle size distribution as the

uncalcined raw material.

Optical Microscopy

The shape of the particles in the freeze-dried powder would be expected to copy the shape of the liquid droplets directly as they meet the liquid nitrogen surface during the spray freezing process. High speed photography has established that the form of a liquid droplet in free flight is not static but pulsates from a doughnut shape through spherical to a dumb-bell shape and back. Because the surface of the droplets freezes first and the thin solid shell so formed captures the particle shape, a variety of shapes would be expected in the dried powder Examination of powders produced by spray-freezing aqueous solutions (Al^{3+}, Cr^{3+}, and Mg^{2+} sulphates; also mixtures which produce ruby and spinel) has confirmed that a wide range of shapes does exist[18].

In the zirconia materials, the freeze-dried particles tend to be spherical immediately after leaving the freeze drier. This basic difference in shape between the zirconia and the sulphate-based materials above is probably due to the considerable difference in the viscosity of the liquids during spraying. On the one hand, the sulphate systems of Reference 18 were true solutions whereas the zirconia materials were aqueous suspensions and hence much more viscous. With an increased viscosity, the free-flight pulsation would be severely reduced and the particles would very rapidly assume a spherical form.

Optical examination of all the zirconia batches con-

firmed the spherical form of the particles. However, even after the minimum of handling, some of the particles readily break down and hence the remainder become coated with a layer of debris (Figure 20). With further handling, the size distribution approaches that given in Figure 19 but even with this breakdown occurring some particles are sufficiently stable to retain the underlying spherical form. In fact, it will be seen later that some of the agglomerates survive not only the calcination stage but are also retained through the forming stage to be incorporated as very dense spherical regions in a fired microstructure.

This stability of some of the agglomerates through the various processing stages is in marked contrast to their behaviour in the immersion oil of a thin section (Figure 21). It can be seen that no spherical agglomerates are retained in either the as-prepared or calcined materials. This is the result of the high shear forces which act on the particles during the preparation of the section. Under these conditions, the as-prepared material is seen to have a much wider particle size distribution than the calcined product which suggests that the agglomerate strength is reduced during calcination. The much narrower size distribution of the calcined material is not immediately obvious in the micrograph due to the development of a chain-like structure from the nearly mono-sized particles. This effect is due to the retention of a high electrostatic charge and the resultant attraction of the particles. During subsequent processing (wet milling) this charge is dissipated and hence does not contribute to any handling difficulties.

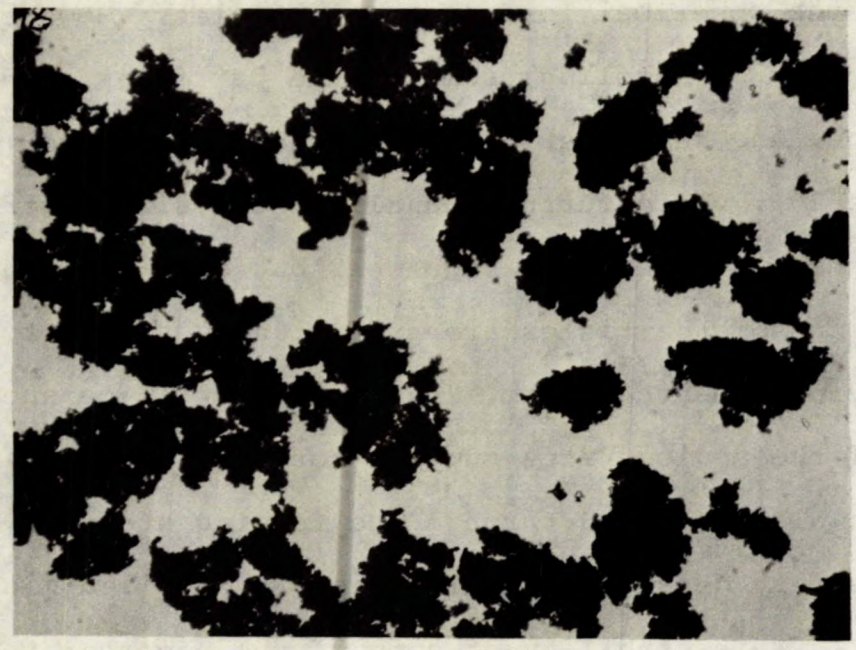

Figure 20. As-prepared material viewed in transmitted light.

Examination of the calcined powders (1000°C) in transmitted light under crossed polars shows the presence of birefringent material in both the partially- and fully-stabilized compositions. The presence of anisotropic material in the fully-stabilized zirconias is in apparent disagreement with the X-ray data of Figure 10 which shows the presence of cubic phase material (isotropic). This discrepancy suggests either severe inhomogeneity in the batches (zones of monoclinic and cubic material due to considerable CaO concentration variations) or the presence of strain within the particles. If the birefringence were due to inhomogeneity giving rise to cubic and monoclinic regions, then it would be expected that the birefringent areas would be

equal to the crystal size of the material. In the present case, the crystal size has been shown to be ∿400 Å at 1000°C (p 53) which is two orders of magnitude less than the observed particle size. Under these circumstances, a single-phase (monoclinic) or two-phase (cubic + monoclinic) polycrystalline particle would be expected to display the non-coherent birefringence typical of anisotropic material in random orientation. However, this was not the case. Each particle was observed to display the nearly coherent birefringence characteristic of strained materials (compared to the complete coherence of a single crystal or the non-coherence of randomly oriented material). The presence of strain in these materials was further demonstrated by the observation of birefringence in all the as-prepared (non-crystalline) materials.

In transmitted light, the particles of all the as-prepared and calcined batches appeared brown whereas in reflected light they were white indicating the microporous nature of the agglomerates. This was confirmed during an examination of the materials using a scanning electron microscope.

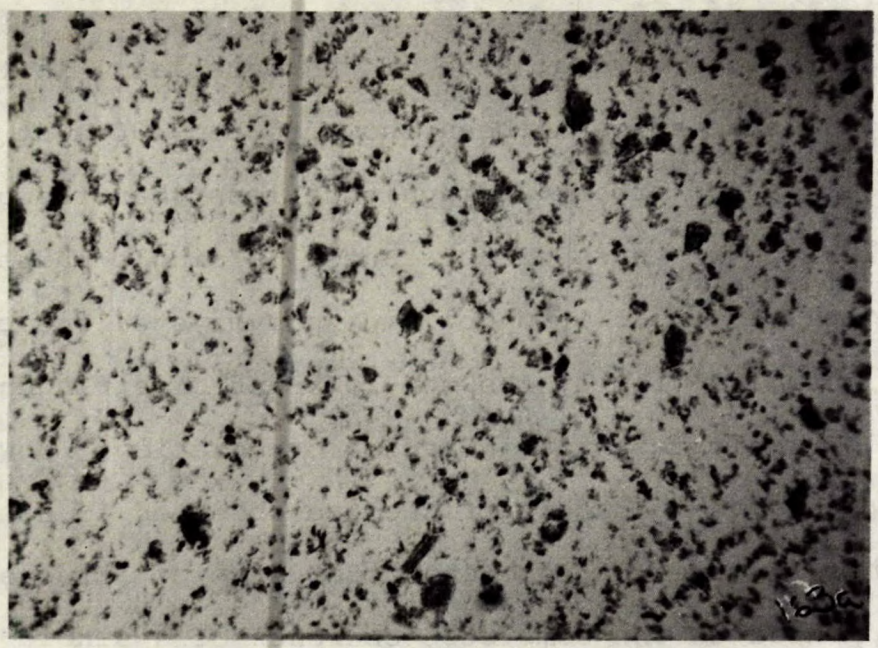

(a) 400 μm

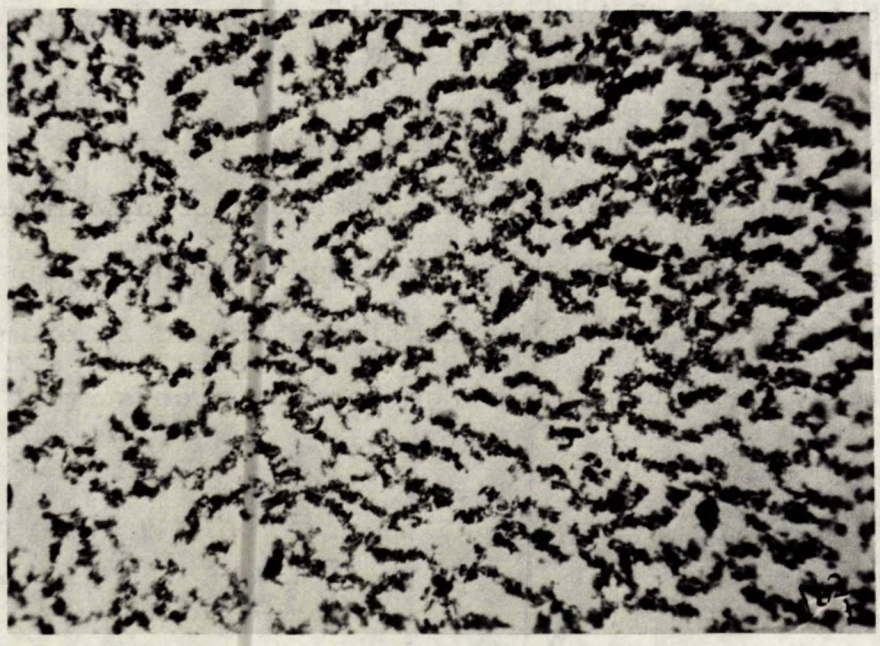

(b) 400 μm

Figure 21. Particles of 7.6 mole % material viewed in transmitted light. Large agglomerates broken down by shearing the immersion oil between the cover slip and microscope slide.

(a) As-prepared (b) Calcined 1000°C 1 hr

Scanning Electron Microscopy

All the as-prepared batches and their 1000°C calcines were examined in the scanning electron microscope (SEM). Conventional sample preparation techniques were used in which the samples were held on the specimen stubs by conducting silver paste and subsequently coated with carbon using a vacuum evaporator. Despite these precautions, it was still difficult to prepare specimens having a continuous electrically conducting surface. This is necessary to avoid the build-up of an electrical charge which would otherwise be dissipated in an erratic fashion with the consequent disruption of the photographic record. This difficulty was probably due to the intrinsically microporous character of the agglomerates and also due to their spherical form making it difficult to ensure a continuous carbon film between the sphere base and the silver substrate.

The morphology typical of all the as-prepared materials is shown in Figure 22 which confirms the spherical form of the agglomerates and also their considerable microporosity. Pores several micrometers in diameter are common, as shown in Figure 22b. Examination of a section through a sphere confirmed that the larger pores were oriented along the sphere radii. This radial texture has been observed in a number of materials and is typical of spray-frozen and freeze-dried powders formed from both solutions and suspensions.

It was impossible to resolve individual crystals in materials calcined to temperatures below 1100°C. The form of the agglomerate constituents was essentially the same as that shown

in Figure 22 for the majority of the compositions prepared. However, in the case of 11.5 mole % CaO material the form was somewhat atypical as even the as-prepared material appeared to have discrete crystallites present (Figure 23). On calcination to 1000°C for 1 hr, the size and form of the small 0.5 to 1 μm particles is unchanged, as shown in Figure 23b. However, the X-ray data of Figures 10 to 12 have already shown that the as-prepared materials were amorphous whereas the 1000°C calcines were crystalline. Consequently, the particles seen in the as-prepared material are probably the remnants of the flocs which were present in the zirconia suspension prior to spray-freezing. On heating, these flocs crystallize above approximately 500°C (actual temperature given by the DTA data of Figures 4 and 5) and the crystallites produced undergo a progressive growth with increasing temperature. The considerable discrepancy between the surface-area crystal size of 725 Å (calculated from data in Appendix E) and the SEM particle size of 0.5 to 1.0 μm indicated by Figure 23 for the 1000°C calcine is evidence that the small particles shown in the micrograph are themselves agglomerates of very small crystallites which are too small to be resolved in practice by the microscope (the Cambridge Instruments Stereoscan Mark IIA SEM used in this examination has a claimed resolution of 250 Å). Hence, it is probable that the mosaically structured particles shown in Figure 18 are agglomerated to form the discrete 0.5 to 1.0 μm particles, which themselves are agglomerated to form the approximately 200 μm particles shown in Figure 20.

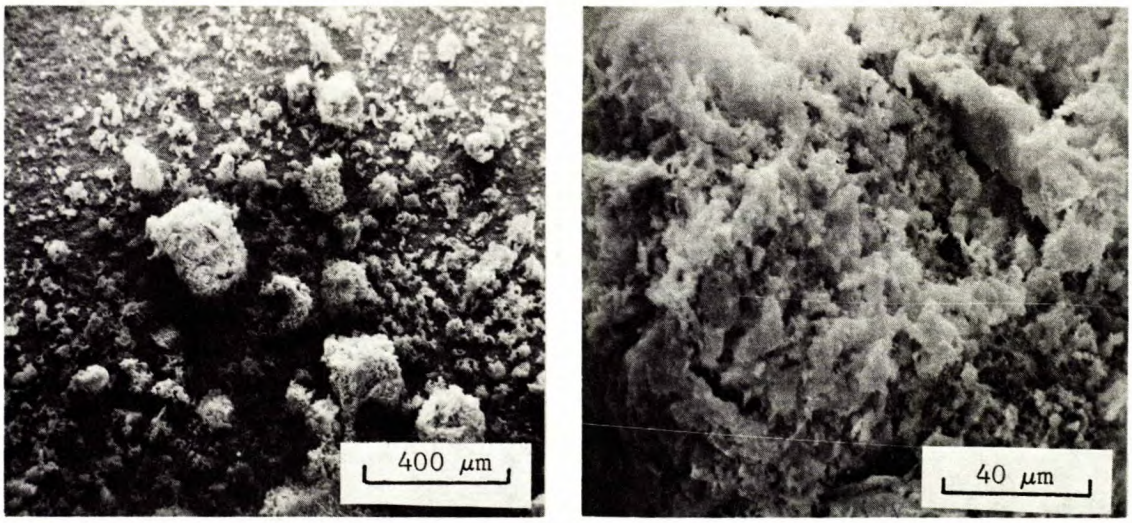

(a) (b)

Figure 22. SEM micrographs of as-prepared undoped zirconia.

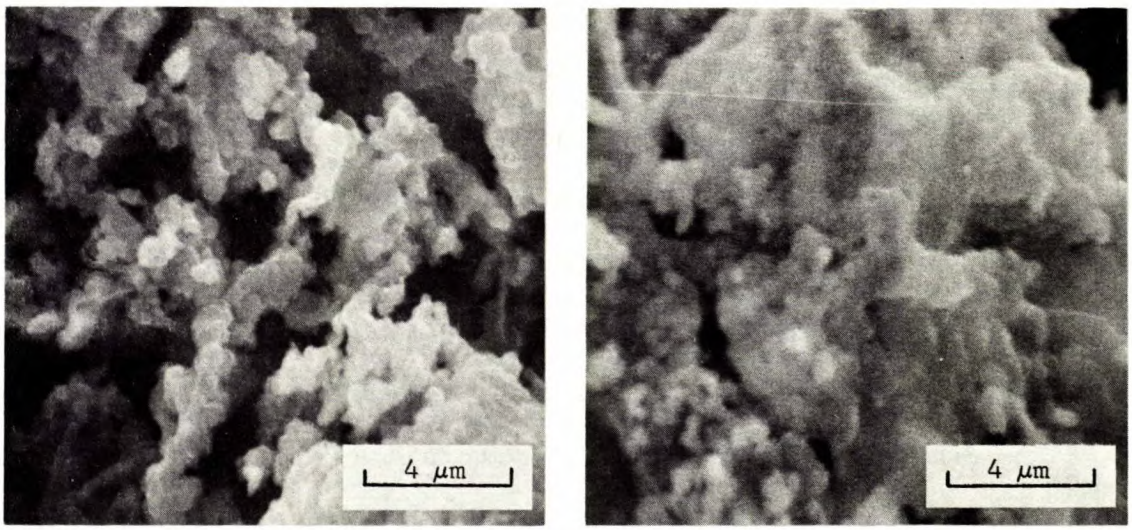

(a) (b)

Figure 23. SEM micrographs of 11.5 mole % material. (a) As-prepared (b) Calcined 1000°C 1 hr

The highly agglomerated structure of these materials is thought to be responsible for the low pressed density and consequently the high firing-shrinkage developed by the as-prepared materials. These sintering data were most conveniently obtained using a hot-stage microscope.

Hot-Stage Optical Microscopy

Initial experiments showed that a considerable firing shrinkage is developed in the as-prepared materials when fired to 1400°C and above. This is partly due to the very low pressed density (∿25% of theoretical density) of the compacted material, which is the result of particle bridging in these highly agglomerated materials. In addition, the high firing-shrinkage is also due to the loss of CO and CO_2 from the adsorbed formate and the loss of H_2O from the zirconia itself. In order to determine the progressive shrinkage of both the as-prepared and calcined materials with increasing temperature, a series of samples was examined using a Leitz Heating Microscope type IIA-P, which is capable of operating in air up to 1750°C. The construction and operation of this equipment has been described elsewhere[32].

Small samples of each material were formed into cylinders 3 mm in diameter by 4 mm long and heated at 6°C/min in the microscope. The projected image of the sample was photographed at 100°C intervals as the temperature was raised to 1600°C. In this manner, a series of photographs was obtained showing the progressive shrinkage of the samples with increasing temperature. Typical results are shown in Figure 24.

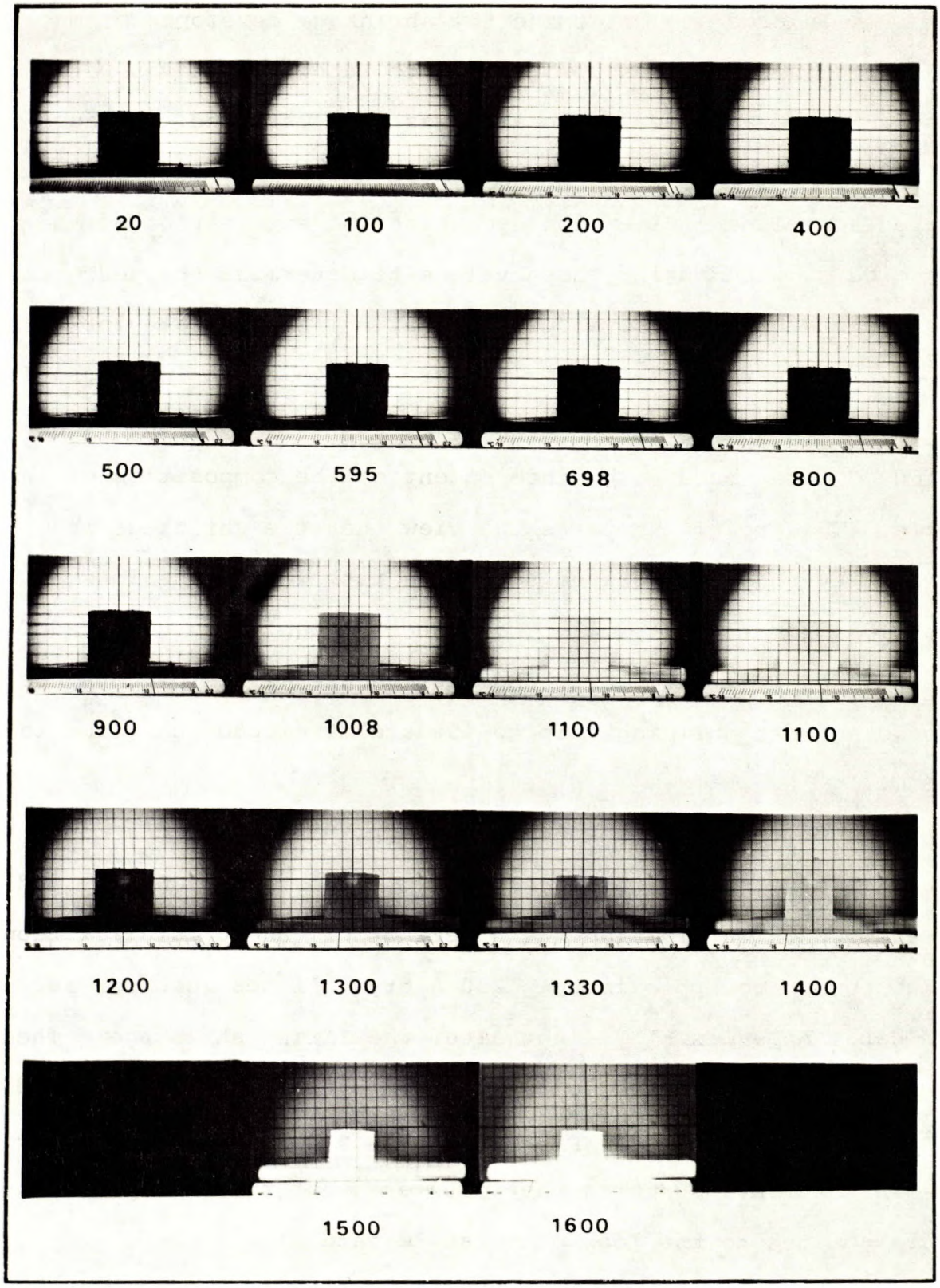

Figure 24. Sample of 13.8 mole % material viewed in Leitz Heating Microscope during heating to 1600°C in air.

In order to determine the shrinkage developed by materials fired in the microscope, the photographic negatives were first enlarged and the sample area was then measured. Because the sample silhouette is approximately square, the area was related to a linear dimension by taking the square root of the projected area and using these values to determine the percentage length change that is developed on heating. A typical plot of these values versus the firing temperature is given in Figure 25. Both the form of the curves and the magnitude of the shrinkage at 1600°C were found to be independent of the composition of the sample. This result supports the view that the shrinkage is dictated by the agglomerated structure rather than the loss of volatiles from the material. With such a highly agglomerated structure on both the macro- and micro-scale, it is perhaps not surprising that shrinkages up to 45% are developed on firing to 1600°C.

Calcination of the materials to 850°C with the consequent removal of approximately 25 wt % volatiles (CO, CO_2 and H_2O adsorbed after leaving the freeze drier) and crystallization of the powder to approximately 250 Å crystallites (see surface area data, Appendix E) did not alter the firing shrinkage. The curves obtained deviated so little from that of the as-prepared material that the two are presented as a single curve in Figure 25. This further supports the postulate that the firing shrinkage is not due to the loss of volatile material.

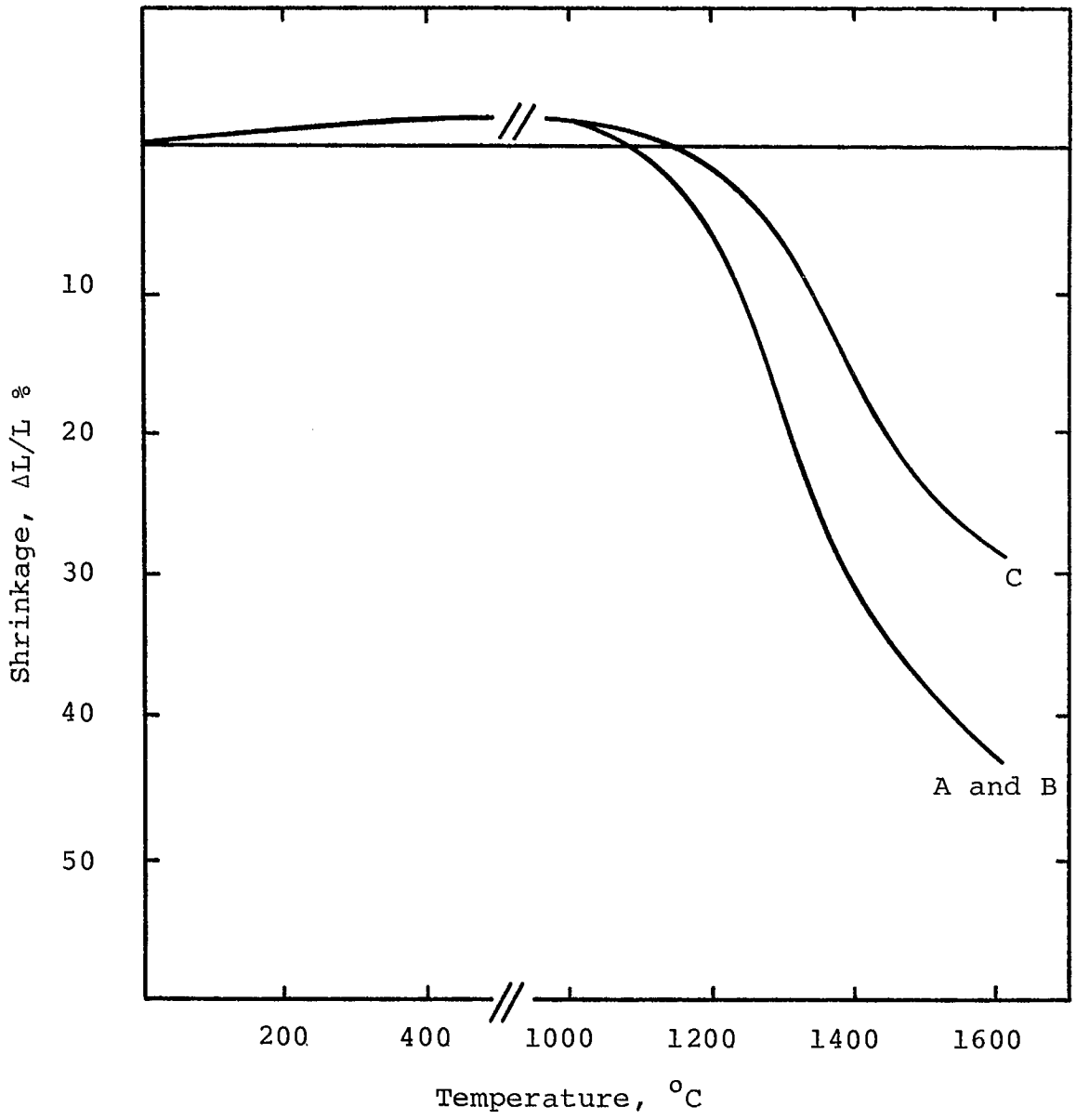

Figure 25. Shrinkage curves for 13.8 mole % material.
A and B. As-prepared material and also material calcined at 850°C for 1 hour
C. Calcined at 1000°C for 1 hour

Calcination to 1000°C, which incurs an additional 0.3 wt % loss to that at 850°C, produces material which undergoes a much smaller firing shrinkage (Curve C, Figure 25). The crystallite size of this material is approximately 750 Å and the shrinkage to 1600°C is about 25%. Although this figure is high compared to that of other ceramic raw materials, these calcines can be satisfactorily fabricated without developing cracks during firing. In every case, it was found that the materials started sintering at approximately 1100°C, which agrees well with the surface area data of Figure 17.

Ball-milling the 1000°C calcined materials did not appreciably alter the firing shrinkage. The curves obtained were very similar to those of the unmilled calcined powders (Curve C). The fact that similar firing curves are produced by materials having agglomerates approximately 10 times larger than the mean particle size of the milled materials (Figure 19), suggests either that the agglomerates break down during the fabrication stage to produce particles smaller than those present originally in the finer materials or that the particle size distribution is little altered during fabrication and the shrinkage is entirely due to intra-agglomerate sintering. Examination of the fired microstructure developed by the as-prepared materials confirmed that the shrinkage was due to intra-agglomerate sintering and this in turn suggested that the particle size distribution was little altered during the fabrication stages. This is discussed further in Part II of this report.

PART II

FABRICATION AND CHARACTERIZATION OF SINTERED MATERIALS

One of the requirements for the successful operation of an oxygen probe in any environment is that the integrity of the concentration cell be maintained throughout the measurement period. In practical terms, this means that the cell must not develop a short circuit due to the passage of oxygen from one half-cell to the other. Consequently, the membrane separating the two half-cells must be impermeable to prevent the direct transfer of molecular oxygen from one side to the other. In addition, the membrane must remain impermeable throughout the measurement and therefore it must have extremely good thermal shock resistance in order to survive the very rapid heating rate of approximately 350°C/sec and thus avoid developing a continuous crack network which would render it permeable.

The development of a thermally shock resistant zirconia in the refractories industry is achieved by using a blend of the monoclinic and cubic phases. This mixture, which has approximately 30% monoclinic material[33], has a much greater shock resistance than either of the component phases. Because of this practice, it was thought that satisfactory performance would be found for the present materials if the composition closely matched that of a commercial blend. On this basis, it was expected that one of the partially stabilized materials would have an adequate shock resistance and hence this requirement was not thought to present a particular difficulty in the programme. On the other

hand, the main difficulty at this stage of the project was the development of an impermeable fired body at as low a temperature as possible, and consequently, this aspect occupied a major portion of the programme.

The development of an impermeable body generally requires that a high fired density be obtained. It is not possible to predict the relative density at which the open porosity is eliminated and only closed porosity remains. In most of the common single-phase oxide ceramics, an impermeable body is usually formed at a relative density of approximately 90%. However, cases have been reported where a body having a relative density of 95% was still found to be permeable. Consequently, the objective at this stage was to develop as high a density as possible.

Development of High-Density Fired Material

Initially, samples of as-prepared doped material were vacuum cold-pressed at 10 ksi* using a 0.5-in. diameter floating die assembly, Thin samples (0.050 to 0.090 in.) were used to avoid significant die-wall effects.. In addition, samples of each composition which had been calcined at 850°C and 1050°C were similarly fabricated. The densities developed by these materials after firing to 1600°C for 1 hour in a gas-fired furnace are given in Table I of Appendix F. In general, the samples developed a relative density in the range 80-87% and were crack-free.

Use of lower firing temperatures and an increased soaking time did not significantly alter the fired density. The results,

*ksi: thousand pounds per square inch

given in Table II of Appendix F, show that for these particular materials, the green density is not necessarily related to the fired density. For example, the 11.5 mole % material developed the lowest fired density (4.92 g/cc) from a compact that initially had the highest green density.

The development of low-density fired samples was to be expected in view of the highly agglomerated structure retained throughout the precipitation and freeze-drying stages. Examination of the microstructure developed in these fired samples showed the presence of a non-linear porosity distribution. Figure 26 shows a typical example of the microstructure observed in reflected light. It can be seen that the section is composed of circular dense areas surrounded by regions of considerable porosity. At higher magnification, the presence of fine porosity within the dense areas is confirmed.

The microstructure shown in Figure 26(a) suggests that the spherical agglomerates, present in both the as-prepared and calcined powders, retain their integrity throughout the forming stage and so form the dense circular areas seen in the section.

Effect of Agglomeration on Microstructure

In order to establish that these dense areas were the fired remnants of the original spherical particles, a series of samples was fired using both the original as-prepared powder and also the -325 m fraction (<44 μm). The samples were vacuum cold-pressed between 10 ksi and 50 ksi (in increments of 10 ksi) and fired in air to 1485°C without any soaking period. In this manner,

it was hoped to show that polished sections of the fired materials would not have dense circular areas exceeding 44 μm in diameter. In addition, it was anticipated that the higher forming pressures would tend to collapse the larger spherical particles and thus promote a more uniform microstructure.

Typical microstructures developed in these fired compacts are shown in Figures 27 and 28. At low forming pressures (10 ksi), the microstructure of the fabricated as-prepared material clearly showed the retention of dense circular areas within a porous matrix (Figure 27). On the other hand, the use of -325 m material produced a much more linear porosity distribution. Unfortunately, the relative density was only marginally increased and the product still possessed considerable open porosity.

At high forming pressures (50 ksi), dense circular areas were still present although they were not as clearly defined as at low pressures. Comparison of the microstructures developed in the as-prepared and -325 m samples showed that they became similar as the forming pressure was increased. However, even the compacts formed at 50 ksi still had 15% porosity and impregnation with an aniline dye - toluene mixture showed the samples to be permeable. In part, this permeability could have been due to the formation of microcracks within samples formed at pressures of 30 ksi and above. Microcracking at these higher pressures was extensive and frequently led to the lamination of the compacts.

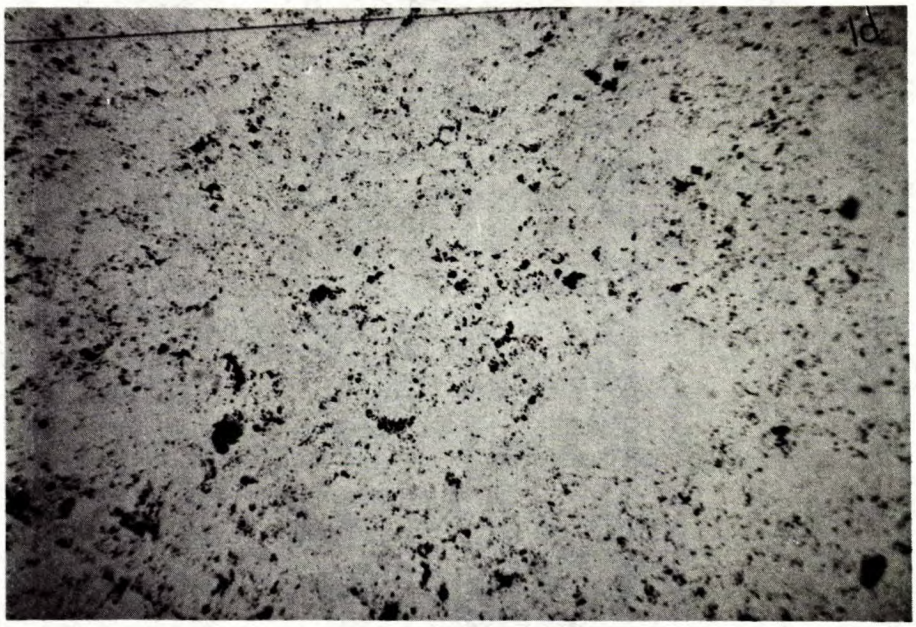

(a) 400 μm

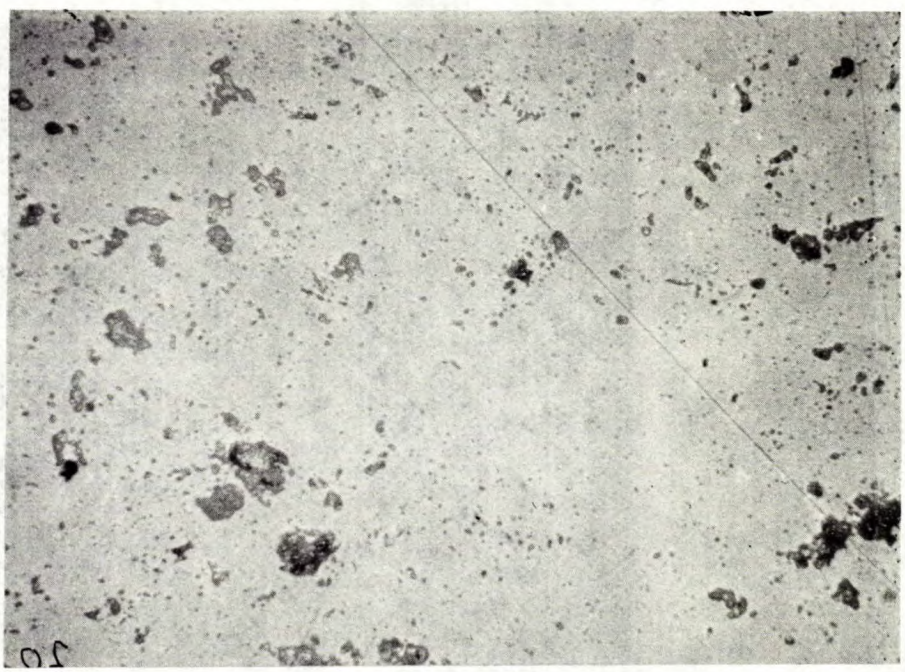

(b) 50 μm

Figure 26. Microstructure developed by as-prepared 16.0 mole % material after firing in air to 1600°C for 1 hour.

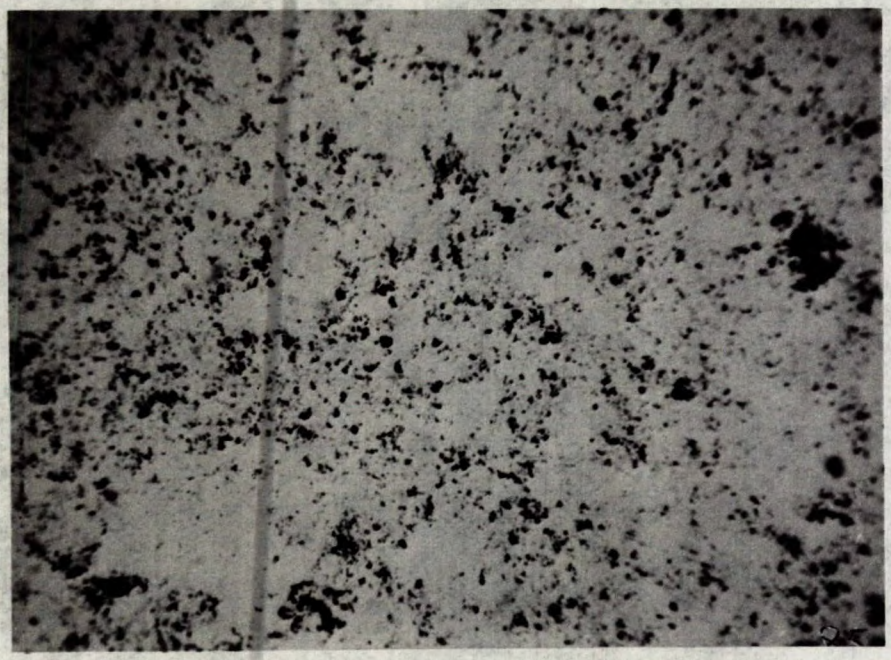

(a) 400 μm

(b) 400 μm

Figure 27. Microstructure developed in 16.0 mole % material after forming at 10 ksi and firing to 1485°C without any soaking period.

(a) As-prepared material (b) -325 m fraction

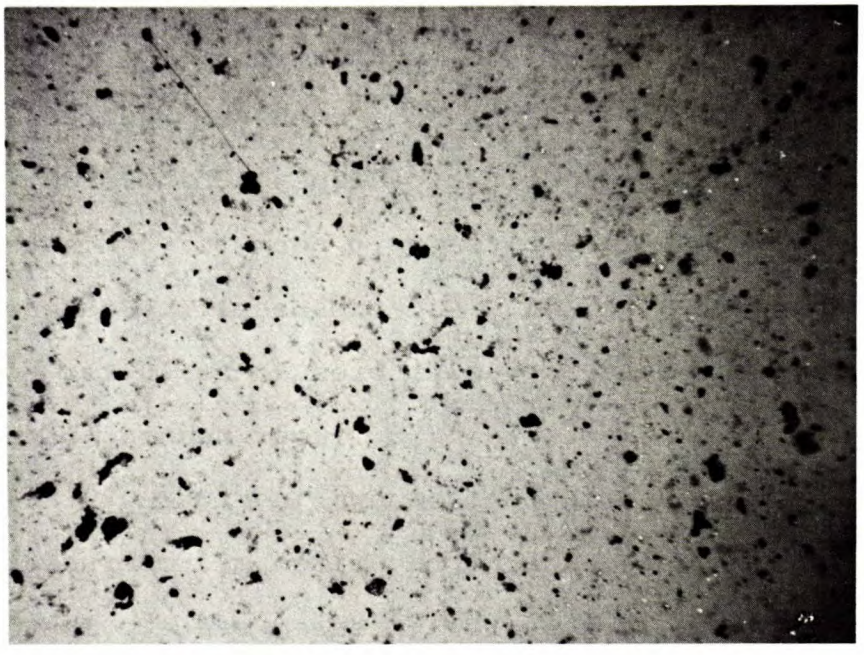

(a) 400 μm

(b) 400 μm

Figure 28. Microstructure developed in 16.0 mole % material after forming at 50 ksi and firing to 1485°C without any soaking period.

(a) As-prepared material (b) -325 m fraction

Subsequently, ultrasonics were used in an attempt to disperse the powders prior to pressing in order to develop a more uniform microstructure. Samples of both as-prepared and calcined material (1000°C for 1 hour) were dispersed in $Pr^{i}OH$ (isopropyl alcohol) using a 400-watt ultrasonic beam for 2 minutes. The slurry was air dried at 110°C and the resulting cake was broken up in a mortar and pestle, vacuum pressed at 10 ksi and fired in air to 1485°C with no soak using a linear heating rate of 3°C/min. The microstructure developed is shown in Figure 29 and clearly shows the strong dependence of the fired microstructure on the structure developed in the green-pressed state. The density increase in samples treated with ultrasonics prior to pressing was only 1% on firing to 1485°C. Increasing the temperature to 1550°C and soaking at that temperature for a 4-hour period produced samples in which the relative density was only 4% greater than that developed in the compacts formed from as-prepared material.

These experiments demonstrated that the limitation to high density is the persistence of the agglomerate structure through the forming and firing stages. Consequently, several techniques other than the somewhat impractical ultrasonic treatment were examined to determine their effectiveness in providing a suitably well dispersed powder.

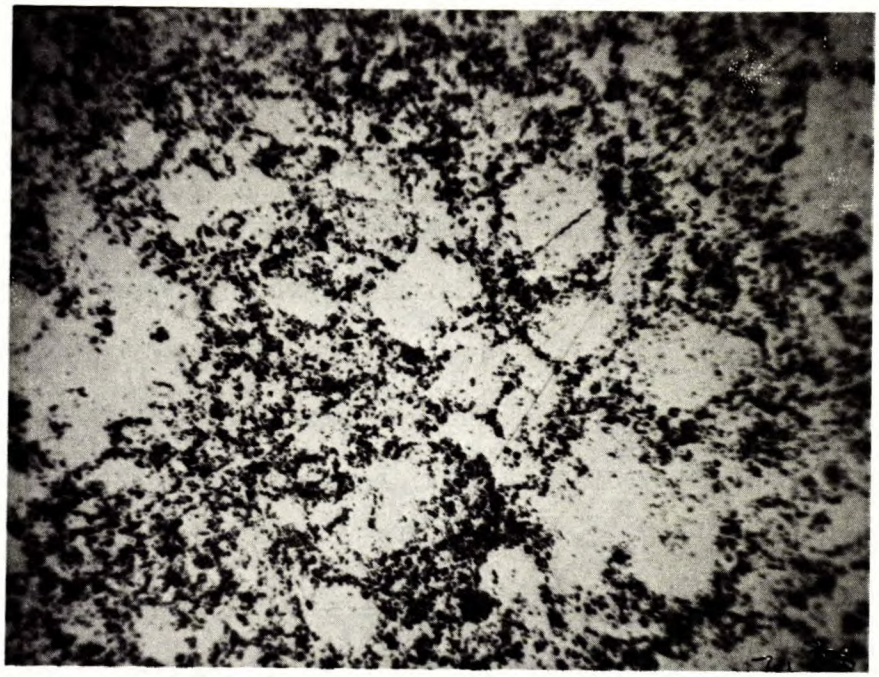

(a) 400 μm

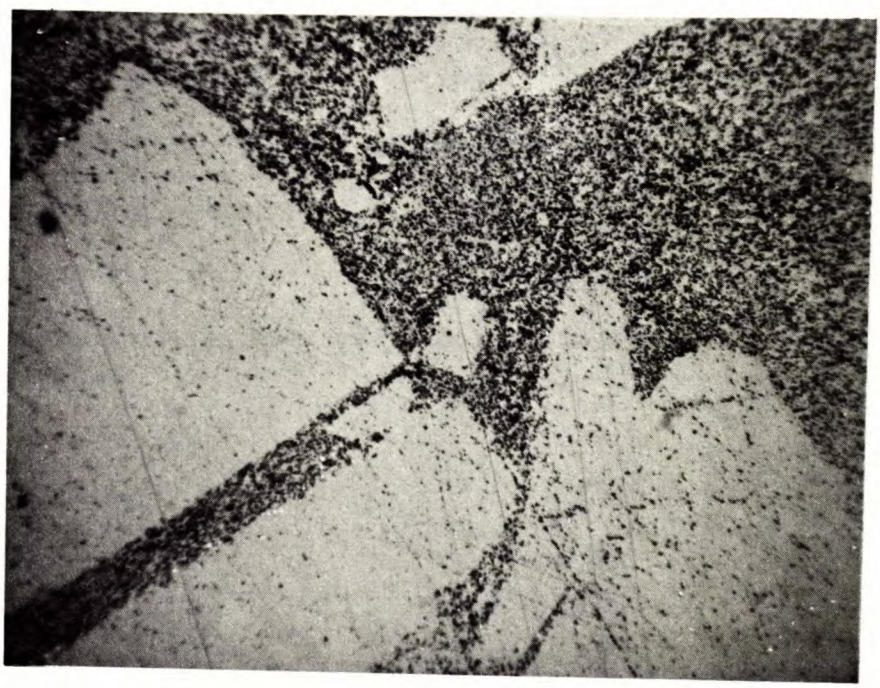

(b) 400 μm

Figure 29. Microstructure developed in 16.0 mole % material after forming at 10 ksi and firing to 1485°C without any soaking period.

(a) As-prepared material
(b) As-prepared material initially dispersed in alcohol using ultrasonics.

Initially, dry dispersion techniques were used. Dry ball-milling was found to be valueless because the mill packed badly even after limited operation. Consequently, fluid-energy milling (a dry impact process) was subsequently used in an attempt to deagglomerate the raw material. This dry grinding process produced material which, on firing, developed a much more uniform porosity distribution but unfortunately the relative density was 85% after firing to 1500°C with no soak and the samples were still permeable.

Subsequently, wet dispersion methods were examined. It has already been shown that material ball-milled in alcohol for 1 hour has a smaller mean size than material dispersed in alcohol using ultrasonics (Figure 19). Also the micrograph of Figure 29b shows that the green structure developed in the unbroken cake pieces is suitable to form a dense fired microstructure. Consequently, ball-milled material should be adequately dispersed to form high-density fired compacts from sedimented material. This was not verified by experiment because it is difficult to visualize a forming process based on sedimentation which could be as rapid as the conventional pressing process. However, it was shown that an inferior product resulted from the use of ball-milled material which had been formed by pressing. Hence, in order to increase the fired density and reduce the permeability, it was clear that the milled materials would have to be modified by a suitable powder lubricant which would allow particle rearrangement to occur during the forming stage and so lead to a more uniform green microstructure.

Stearic acid could not be used as a lubricant because its melting point (70.1°C) is too low to allow an isopropyl alcohol (b.p. 82.4°C) slurry to be spray dried easily as a drier exit-temperature greater than about 85°C would be necessary to ensure the complete removal of the alcohol and such a temperature would melt the stearic acid component and render the powder sticky. Consequently the acid amide* (m.p. 109°C) was used in the expectation that it would promote the development of a pressed green microstructure from ball-milled material which would be as dense and uniform as that developed in the sedimented ultrasonically treated compacts.

Initially, the minimum concentration of lubricant which allowed the maximum green density to be obtained in pressed compacts was determined. Calculation showed this value to vary from 1 wt % to 10 wt % depending on the assumed orientation of the unit cell on the powder surface; in practice a concentration of 7 wt % was found necessary. This high concentration was required because the surface area of these materials was approximately an order of magnitude greater than that of typical commercial zirconias.

The stearamide was added to the powder by first dissolving in warmed alcohol (40°C) and subsequently adding the powder to give a 12.5 wt/vol % slurry which was ball-milled in a polyethylene jar with 0.5-in. high-alumina cylinders for 1 hour. The suspension was then spray dried using a Nerco-Niro spray drier operated with an inlet temperature of 200°C and an outlet

*Matheson Coleman and Bell, East Rutherford, N.J.

temperature of 95°C. The spinner was operated with an air pressure of 6 kg/cm^2. A slurry feed rate of 40 ml/min was chosen so that the air-alcohol ratio for the maximum fan speed (80 cu ft/min displacement) was well below the lower explosion limit of 2.6% for the air-isopropanol system. All the powders sprayed well under these conditions to produce material having a typical tap density of 0.33 g/cc.

The presence of the stearamide in the ball-milled powders resulted in an increase in the relative green density from approximately 26% to 38% (Figure 30). However, the density developed on firing to 1500°C was only marginally increased from 84% to 87% and increasing the forming pressure from 10 to 30 ksi resulted in a further slight increase to 89%. The microstructure developed by the lubricated material shows essentially a linear porosity distribution (Figure 31). However, isolated pockets of quite coarse porosity are still retained. Increasing the firing temperature to 1525°C and soaking at that temperature for 3 hours resulted in only a marginal improvement in the density. Etched sections showed that the greatest change was the increase in the average grain size from 9 μm (1500°C) to 15 μm (Figure 32).

Examination of the etched section of Figure 32 shows that part of the remaining porosity is trapped within the centre of the grains. In addition, grain-boundary pinning by the pores is frequently observed. This suggests that the heating rate during firing was too rapid for these materials, i.e., the grain boundaries sweep through the porous regions too rapidly and were thus prevented from acting as vacancy sinks. Hence the pores

remain trapped within the centre of each grain. The heating rate in these cases was 3°C/min up to the maximum firing temperature.

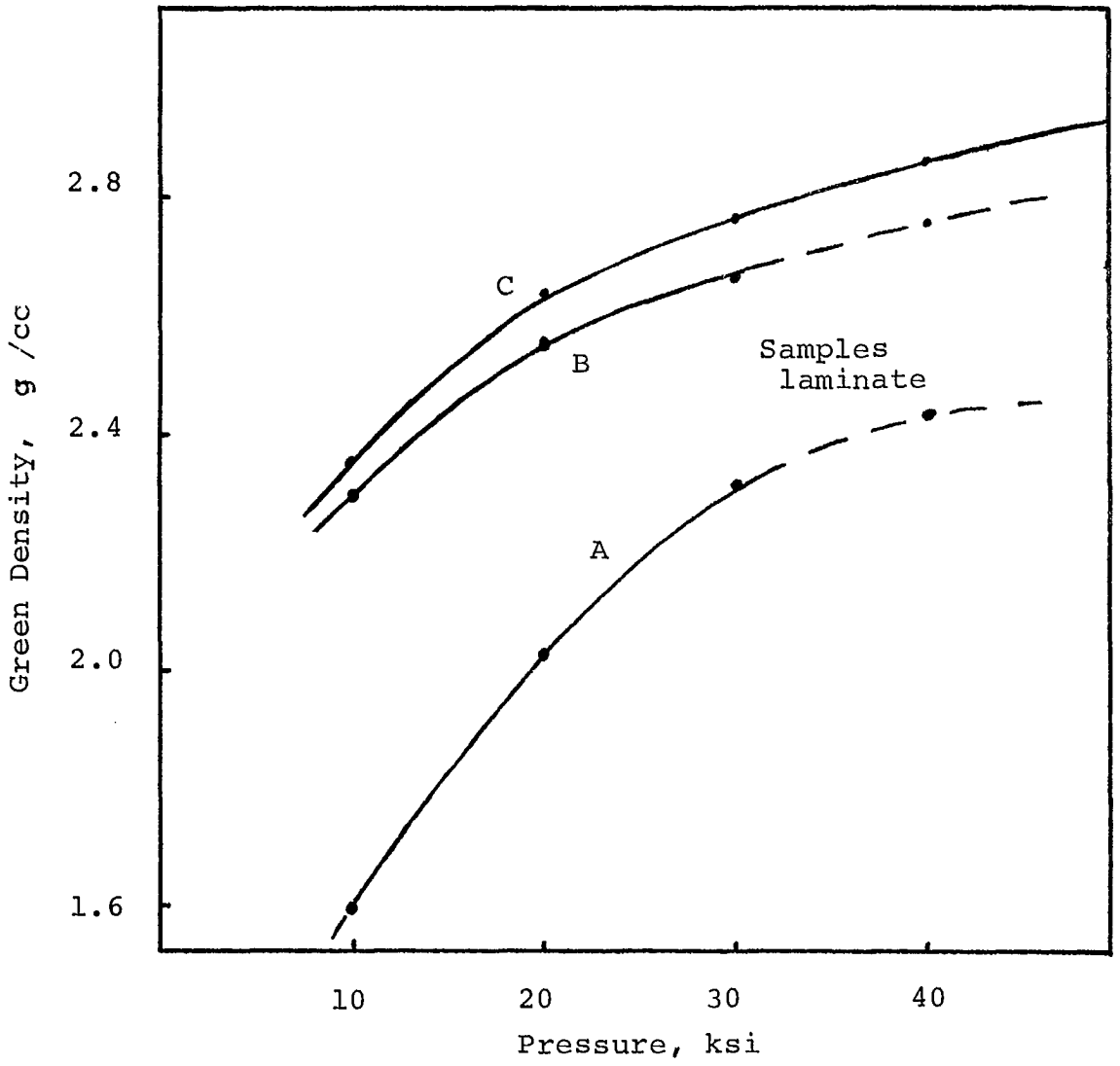

Figure 30. Effect of applied pressure on the green density of 16.0 mole % material.

A. As-prepared material
B. Ball-milled and spray dried with stearamide
C. Ball-milled and spray dried with polyvinyl acetate and polyethylene glycol

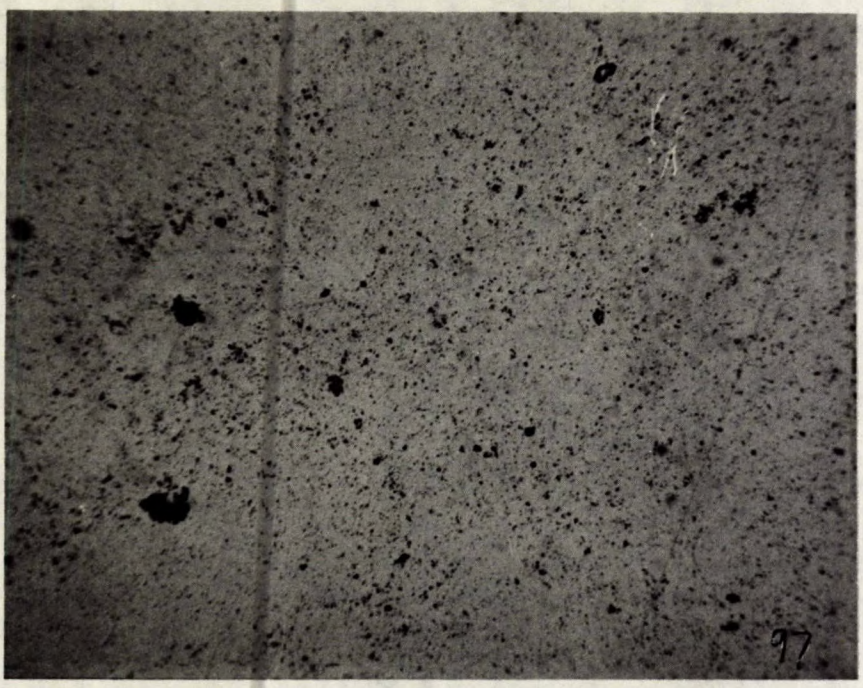

(a) 400 μm

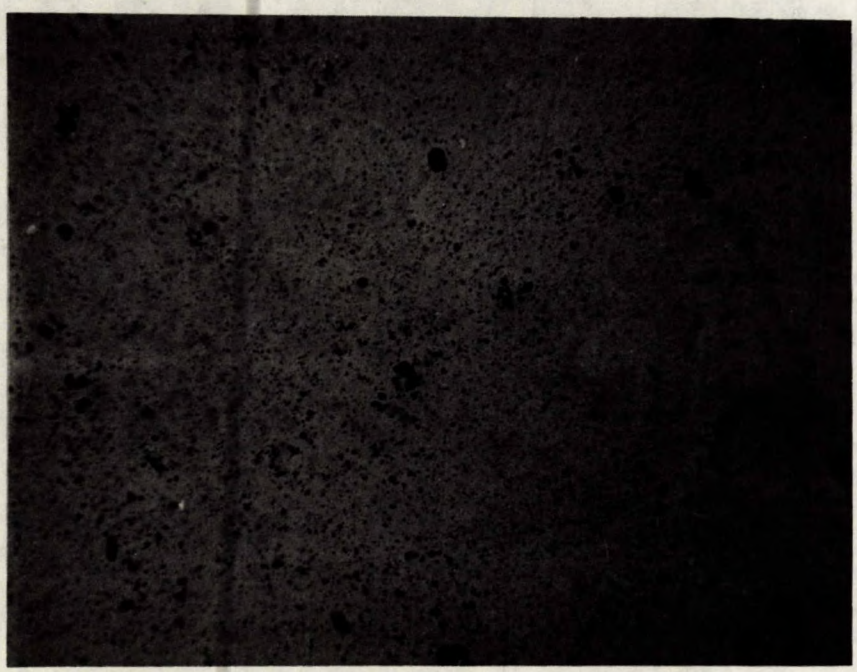

(b) 400 μm

Figure 31. Effect of forming pressure on the microstructure developed by stearamide-containing material. 16.0 mole % material fired at 3°C/min to 1500°C with no soak.

(a) Pressed at 10 ksi (b) Pressed at 40 ksi

(a) 400 μm

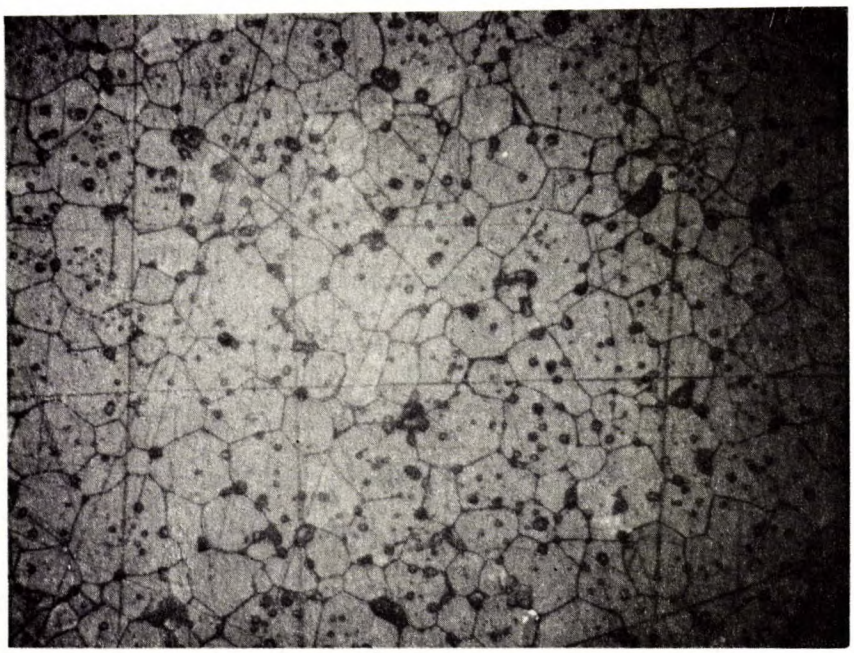

(b) 50 μm

Figure 32. Microstructure developed in stearamide-containing, 16 mole % material after firing to 1525°C for 3 hours.

(a) Polished (b) Etched

Subsequently, a series of experiments was conducted to determine the grain size developed on heating to a given temperature at 3°C/min. The purpose was to find the maximum temperature to which these materials could be heated at 3°C/min and yet avoid the development of trapped porosity. At higher temperatures a much slower heating rate would be necessary. In this manner, it was hoped that the grain-boundary migration would be slow enough to allow the complete elimination of the porosity.

On the basis of the sintering data of Figure 25, a number of samples were fired at 100°C intervals between 1100°C and 1500°C and the fracture surface of each examined using the SEM. The results indicated that significant crystal growth occurs between 1300°C and 1400°C (Figure 33). The crystal size at 1200°C is approximately 0.2 μm and increases to 0.4 μm at 1300°C. At 1400°C the material has sintered extensively and has a general crystal size of 6 μm. At this stage, trapped porosity is seen within the crystals. Measurement of the relative density of these samples indicated that densification begins between 1100°C and 1200°C and becomes considerable in the range 1200°C to 1300°C (Figure 34). These density data, together with the SEM micrographs, show that a relative density increase from 40% to 58% (Figure 34) between 1200°C and 1300°C over a period of 33 minutes (100°C at 3°C/min) gives a densification rate of 0.54%/min, which is too rapid to eliminate porosity at the grain boundaries. This porosity, which eventually becomes trapped within the grains, clearly sets an upper limit to the fired density.

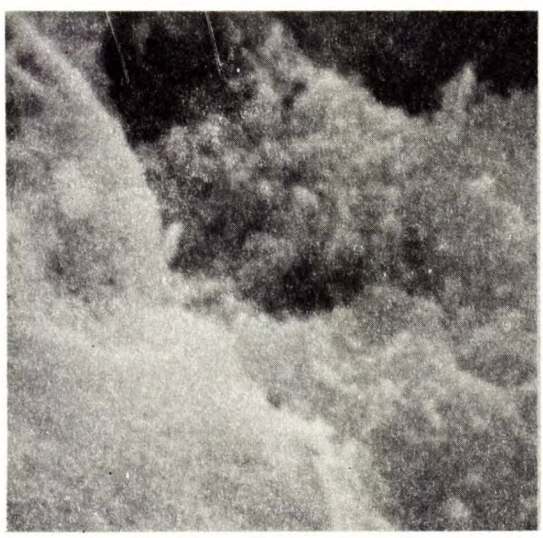

1100°C

1200°C

1300°C

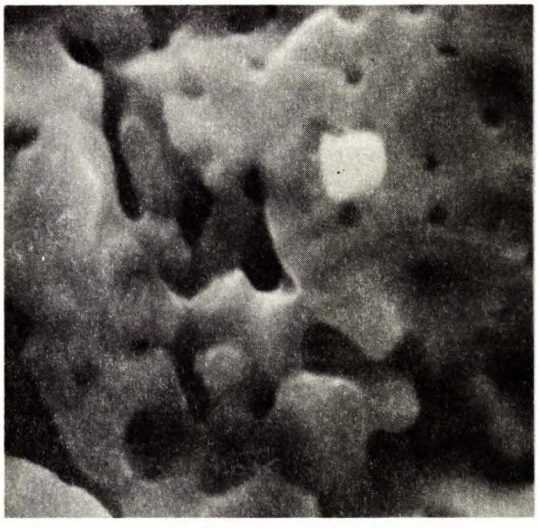

1400°C

2 μm

Figure 33. Microstructure developed in stearamide-containing, 16.0 mole % material with increasing temperature.

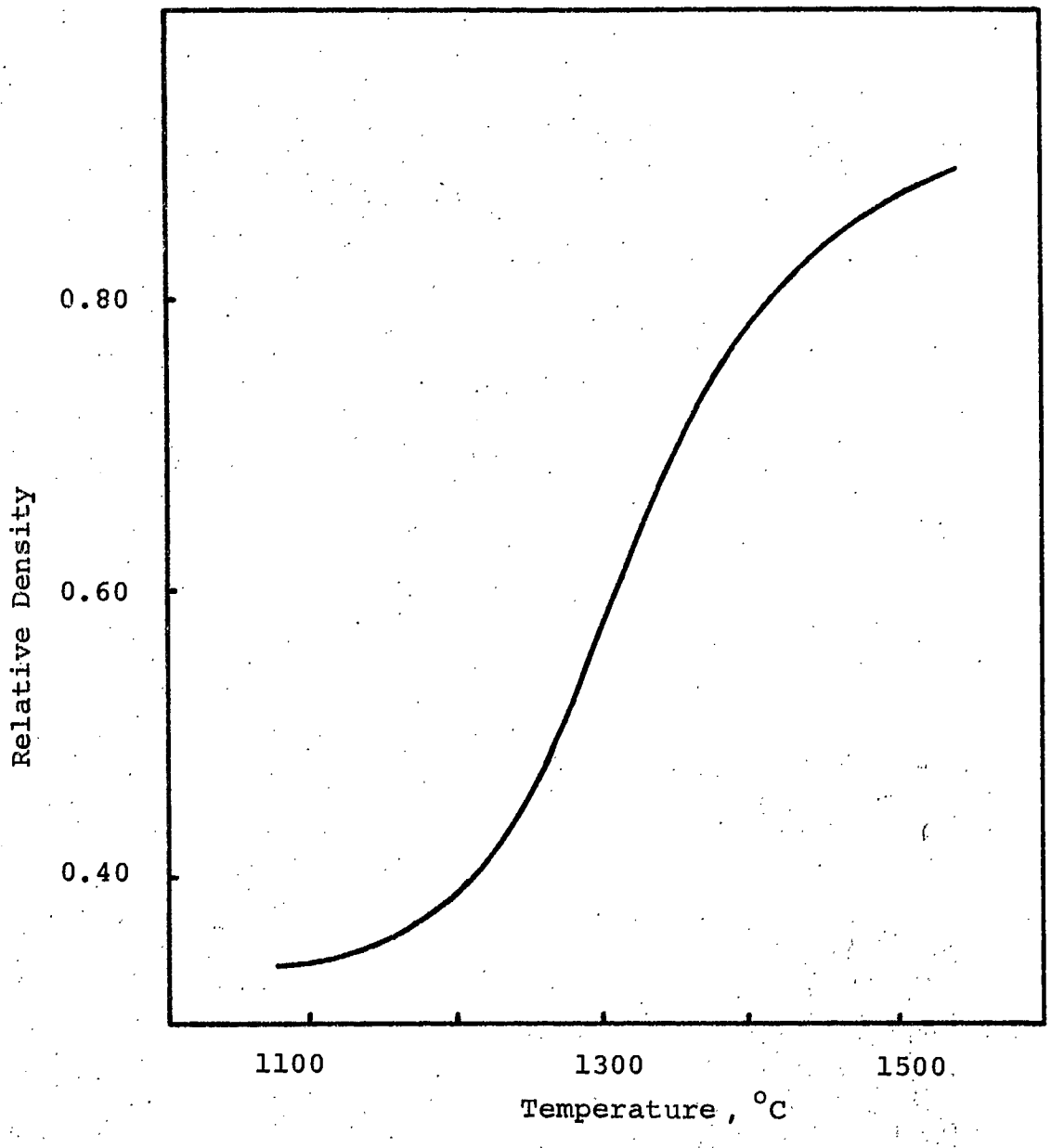

Figure 34. Increase in relative density of stearamide-containing, 16.0 mole % material during firing at 3°C/min.

In an attempt to reduce the amount of trapped porosity within the grains and also to eliminate the open porosity that was retained in the above samples and rendered them permeable, a series of samples was fired using a linear heating rate of

15°C/min up to 1000°C and thereafter slowing down to a rate of 0.5°C/min from 1200°C to 1500°C. However, this slower firing schedule only resulted in a 1% lower porosity product with a mean grain size of 8 μm and, as suggested by this porosity value, the samples remained permeable to a toluene-aniline dye mixture.

In order to eliminate the permeability of these samples, and in particular to avoid the retention of the large pore pockets shown in Figure 31, it appeared desirable to develop a more uniform green structure than was possible with the stearamide materials. In part, this should be achieved by the use of a mixture of both a lubricant and binder in the powders which would allow the use of high forming pressures and yet avoid the development of laminations characteristic of the stearamide material above 30 ksi (Figure 30). In addition, with an effective lubricant it should be possible to avoid the retention of the large pore pockets shown in Figure 31, which are thought to be the result of particle bridging occurring during the forming process, i.e., the stearamide did not lubricate the powders sufficiently to allow particle sliding to occur during compaction and hence reduce or eliminate these pockets.

In an earlier project it had been experimentally shown that a mixture of 5.5 wt % polyvinyl acetate* and 1.5 wt % polyethylene glycol** will enhance the development of very uniform and dense green microstructures in a variety of raw materials. Consequently, a series of experiments was conducted to evaluate

---

* Gelva V-7, Monsanto Canada Ltd., Montreal.
**Carbowax 400, Union Carbide Canada Ltd., Toronto.

the possible advantages of using this mixture in the present zirconia materials.

These additives were dispersed in the same manner as the stearamide, but using methyl alcohol as the solvent. The zirconia slurry was ball-milled and subsequently spray dried, using an inlet temperature of 150°C and an exit temperature of 75°C, to produce a nearly free-flowing material which had extremely good pressing properties. With the polyvinyl acetate binder, compacts were readily formed at pressures up to 50 ksi without developing the laminations or microcracks typical of the stearamide materials.

As shown in Figure 30, the Gelva-Carbowax material developed higher density green compacts than the stearamide-containing materials; the relative density ranged from 42% at 10 ksi to 50% at 40 ksi and, as a result, higher fired densities were obtained. The microstructure formed on firing to 1500°C with no soak (Figure 35) indicates that the isolated large pores which were present in the stearamide material have been eliminated and only a uniformly distributed fine-pore system remains. The relative density of these fired samples ranged from 91 to 95%; the highest density was developed in samples compacted at 40 ksi.

Examination of an etched section (Figure 35b) shows that the remaining porosity is in part retained within the individual grains. In addition, grain boundary pinning by pores is frequently observed in samples which were fired using a linear 3°C/min heating schedule (Figure 36). Consequently, samples were subsequently fired using the 0.5°C/min schedule that was employed

(a) 400 μm

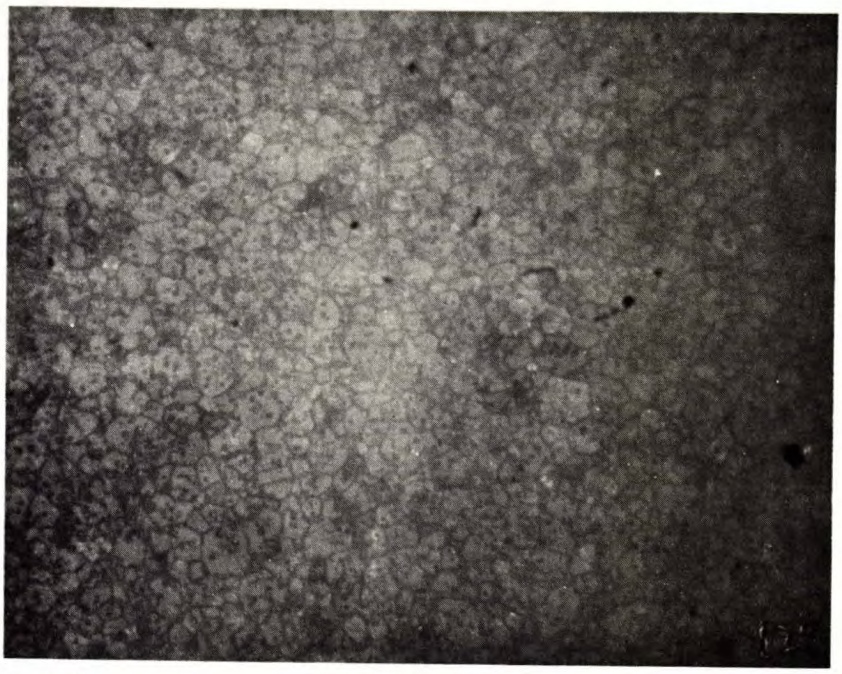

(b) 50 μm

Figure 35. Microstructure developed by Gelva-Carbowax 13.8 mole % material fired at 3°C/min to 1500°C with no soak

(a) Polished (b) Etched

for the stearamide materials. However, this slower heating rate did not significantly alter the microstructure or fired density from that developed by the stearamide materials; pores were trapped within the grains suggesting that the heating rate was still too rapid.

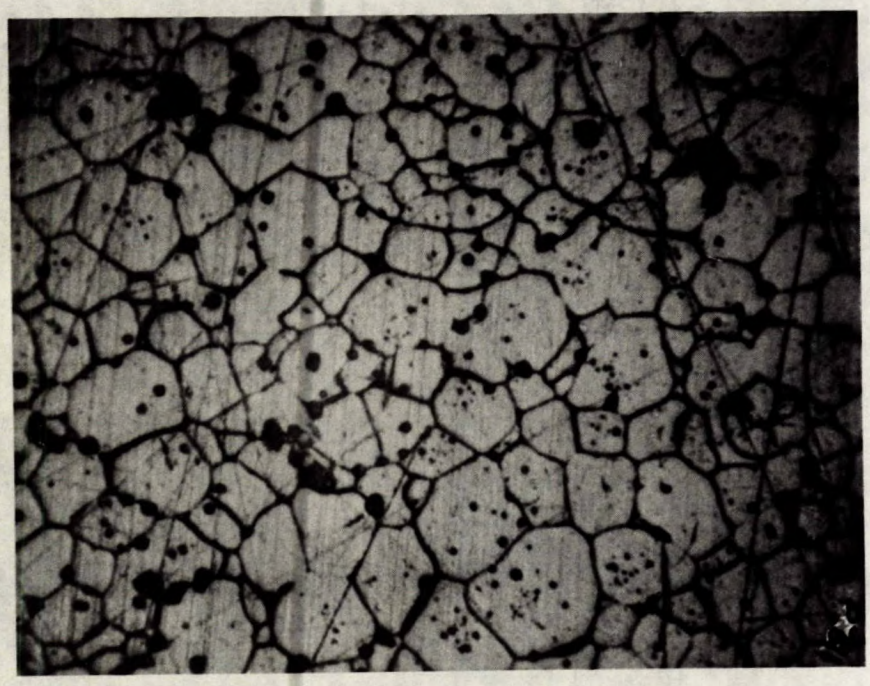

Figure 36. Microstructure developed in 16 mole % material which originally contained Gelva V-7 and Carbowax 400 prior to firing to 1525°C and soaking for 3 hours.

Subsequently, the rate was reduced by extending the time base of the programmer* by four times to give a 3.75°C/min rate up to 1000°C and 0.125°C/min between 1200°C and 1500°C. This extremely slow schedule produced compacts which had relative

*DataTrak programmer, Model 5500, R.I. Controls, Minneapolis, Minn.

densities ranging from 93% to 99% as the original forming pressure increased from 10 ksi to 40 ksi. However, despite this very slow schedule, the remaining porosity was found in part to be retained within the grains.

In order to establish that this persistent porosity was not due to the use of an air atmosphere during firing and the trapping of insoluble N_2 gas, a series of samples was also fired to 1500°C in oxygen using the very slow schedule. Other than a reduction in the average grain size from 14 μm to 9 μm, neither the porosity nor its distribution was altered from that developed on firing in a normal atmosphere. Consequently, it was assumed that this trapped porosity was present within the crystallites of each agglomerate prior to forming and firing. Because the crystallites were much smaller than approximately 2 μm (the lower limit of particle size which can be milled in a ball-mill), this porosity would not be released during the milling process. This very finely divided porosity within the crystallite could have been generated due to the lack of control during the calcination of the as-prepared materials to 1000°C. In all cases, the powders were heated to this temperature and soaked for 5 min, however, the rate at which the powders were heated was not controlled. The equipment used in this case had a heating rate of 20°C to 25°C/min which could well be sufficient to trap microporosity within the rapidly growing crystallites in the temperature range 600°C to 1000°C. Once this porosity is trapped, subsequent reheating through the 600°C to 1000°C temperature range during the firing cycle cannot eliminate all the pores

irrespective of the heating rate, because the grain boundaries will be moving away from some pores and hence they become permanently trapped.

Dye impregnation of the high-density samples formed by pressing the Gelva-Carbowax materials at pressures up to 40 ksi and subsequent firing using a very slow schedule showed that they were impermeable when the relative density exceeded approximately 94%. Consequently, from this point of view, these samples should be satisfactory for use as the membrane in the oxygen probe assembly. The fact that about 5% porosity could be retained within the impermeable samples is not deleterious and may help to impart greater thermal-shock resistance than the theoretically dense samples would show.

Development of Thermal-Shock Resistant Material

The actual use of an oxygen probe in a steel-making furnace demands that it be inserted directly into the molten metal, which is typically at 1600°C. Consequently, the probe assembly, which is not preheated, suffers a considerable thermal shock as the heating rate is of the order of 350°C/sec. Under such a severe thermal stress many ceramic materials would disintegrate. However, the zirconia membrane in the oxygen probe assembly has not only to resist spalling but also to avoid the development of a continuous crack network which would otherwise allow the passage of molecular oxygen from one side of the cell to the other and thus short circuit the cell.

It has been stated earlier that commercial applications

for shock-resistant zirconia generally depend on a composition of approximately 30% monoclinic and 70% cubic zirconia. This two-phase system has been found by trial and error to offer much greater shock resistance than is possible in either of the single-phase compositions, even with the use of grog to promote the formation of microcracks that would act as 'crack-stoppers' by blunting the crack-tip radius of any propagating macrocracks. Consequently, it was expected that the greatest thermal-shock resistance would be developed by the composition which most closely matched that of the commercial products, i.e., 7.6 mole % CaO in ZrO_2. In addition to the composition, other parameters were examined for their possible influence on shock resistance.

The thermal-shock resistance of small cylinders (0.125-in. diameter x 0.250-in. long) and thin discs (0.500-in. diameter x 0.040-in. thick) was determined by inserting them rapidly into a furnace at 1575°C for one minute followed by rapid withdrawal and cooling for one minute. This cycle was repeated until the samples spalled. In this manner, qualitative results were obtained of the effect of composition, grain size (6 to 15 μm), porosity (32% to 1%) and geometry (aspect ratio* from 2 to 0.1) on the thermal-shock resistance.

The results showed that thermal-shock resistance was independent of grain size, marginally dependent on the porosity and geometry, and very dependent on the composition. For example, the single-phase cubic materials (11.5, 13.8 and 16.0 mole % CaO materials) had very poor shock resistance and failed after a

*aspect ratio - the ratio of height (or length) to diameter for a cylinder.

maximum of two cycles to 1575°C; the discs failed after one cycle whereas the small cylinders failed after two cycles. This difference is presumably due to differing geometry in each case. The greater the radius, the greater will be the strain on the outer annulus of material. Hence, although the small cylinders have a greater minimum thickness through which the heat has to penetrate to achieve thermal equilibrium, the outer circumferential layer of material does not suffer as great a stress as that in the 0.5-in. diameter disc and therefore it tends to be more shock resistant.

This behaviour is in contrast to that found for the two-phase PSZ materials. The 7.6 mole % materials was taken through thirty-five cycles to 1575°C and back again without spalling. The discs showed some deterioration after ten cycles, with the development of one or two cracks within the surface. In addition, a progressive surface roughening was also observed. However, after the 35 cycles (the limit of the experiment) the samples were still strong and could only be broken with difficulty. The only visible change in the small cylinders was the gradual surface roughening; no macro-cracking was observed. In view of the considerable thermal-shock resistance of the PSZ materials, the microstructure was examined before, during, and after the 35 thermal-shock cycles to 1575°C in an attempt to identify the stress-relief mechanism.

Microstructure of Thermally Shocked Partially Stabilized Zirconia

Examination of partially stabilized material in reflected light failed to show the two-phase nature indicated by X-ray diffraction patterns (Figure 11). A typical microstructure is shown in Figure 37 and confirms that the PSZ microstructure is essentially the same as that of the fully stabilized materials. This suggests that either the reflectivity of the two phases is identical or that they are uniformly dispersed and smaller than the resolution of the optical microscope, i.e., each single phase grain is less than 1 μm. The possibility that the reflectivities were identical is very remote, for this would require the birefringent phase (monoclinic zirconia) to be in preferred orientation with respect to the surface of the section so that its reflectivity (which varies with the orientation of the crystal and optic axes) could match that of the isotropic phase (cubic zirconia). However, this remote possibility of identical reflectivities was indirectly discounted on examination of these materials in transmitted light. The thin sections failed to show the component phases - the samples remained uniformly isotropic under crossed polars which suggested that the single phase areas were too small to be resolved optically. However, the thin sections did show the presence of radial strain in the fabricated tablets. This indicated that the very fine-grained matrix of cubic and monoclinic zirconia had retained (from the forming stage) or had developed (during firing) fabrication stresses.

(a) 400 μm

(b) 50 μm

Figure 37. Microstructure developed by 7.6 mole % material which originally contained Gelva-Carbowax additives. Fired at 3°C/min to 1500°C with no soak.

During thermal cycling to 1575°C, the PSZ samples suffered an irreversible expansion which continued with each cycle for the first 20 cycles (Figure 38). This effect, which is known as 'ratchetting', has been reported recently and related to the 3% volume change associated with the monoclinic - tetragonal inversion which normally occurs at approximately 1100°C[24]. However, the authors showed that ratchetting will occur at temperatures down to 400°C and they postulate that this is due to the transition occurring at subnormal temperatures as a result of fabrication and thermal-shock stresses. Consequently, during thermal-shock cycling, PSZ undergoes an expansion on cooling (due to the conversion of the high-temperature tetragonal phase to the monoclinic phase) and the authors have shown that this creates a considerable microcrack density.

Elsewhere, it has been shown that the critical temperature difference ΔT_c required for crack instability is given by:

$$\Delta T_c = \left(\pi \frac{2G}{1\alpha^2 E}\right)^{\frac{1}{2}} (1 + 2\pi N l^2)$$

where G is the shear modulus, α is the thermal expansion coefficient, E the modulus of elasticity, N the crack density, and l tne crack half-length[34]. A plot of the critical temperature difference ΔT_c against the crack half-length is concave upwards passing through a minimum at $l_{min} = (6\pi N)^{-\frac{1}{2}}$. For very small cracks (less than l_{min}) the slope is negative, indicating that there is more than enough stored elastic energy to drive the cracks. When ΔT_c is attained, the cracks propagate very rapidly resulting in a sudden catastrophic loss in strength. On the other hand, for large cracks where the crack half-length is greater

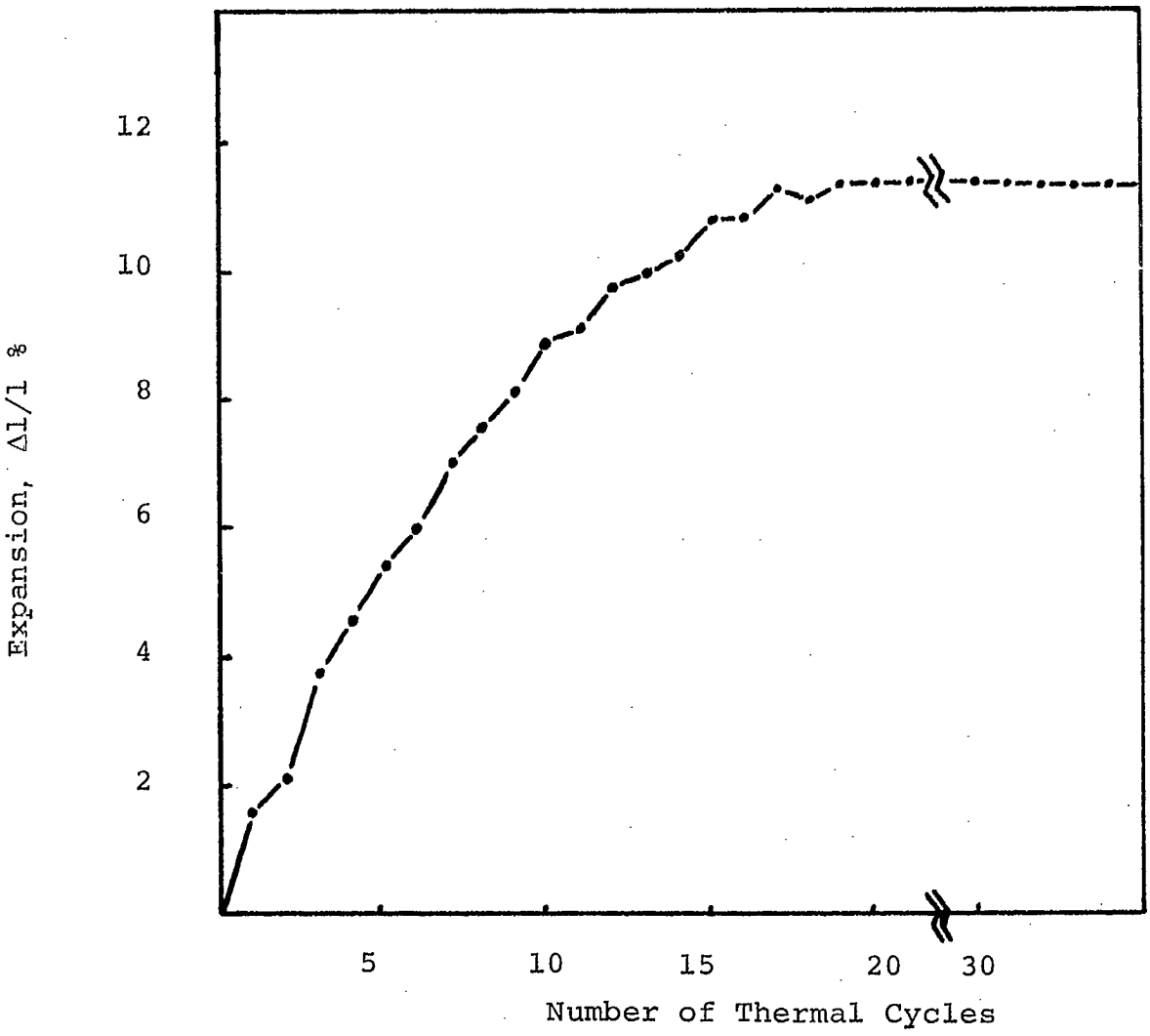

Figure 38. Permanent expansion developed in PSZ after thermally cycling to 1575°C followed by air quenching.

than l_{min}, the slope is positive, which implies that when the crack density N and the crack half-length l satisfy a given ΔT_c no further crack propagation occurs. For the cracks to progress further, the degree of under-cooling must be increased. This

situation, which Hasselman[34] has described in terms of a quasi-static propagation, is very desirable in all high-temperature materials for it avoids the sudden loss of strength during thermal cycling.

Indirect evidence for the presence of fabrication stresses (postulated to energetically favour the occurrence of the monoclinic-tetragonal transition at subnormal temperatures) was obtained from an examination of polished and etched surfaces of both as-fired and thermally cycled material. Figure 39 shows an etched section of PSZ before and after thermal-shock treatment. It can be seen that the etchant has developed a very fine microstructure consisting of zones 2-3 μm in diameter for the thermally shocked material and about 1 μm in diameter for the as-fired material. Such areas cannot be of a single phase, i.e., the etchant has not revealed a grain boundary network, otherwise the phases would be resolved in thin sections - particularly the monoclinic phase under crossed polars.

Although an etchant is most commonly used to reveal a grain boundary network, it must be realised that it will attack all the sample, but with particular emphasis on the high-energy regions such as lattice defects, regions of high strain energy, and high-energy crystal surfaces as well as grain boundaries. The thin section data eliminate the latter two possibilities and the irregular nature of the 'boundaries' eliminates lattice defects such as dislocations giving a polygonized structure. The possibility that strain fields have been etched is also suggested by the apparent increase in zone size after thermal-shock treat-

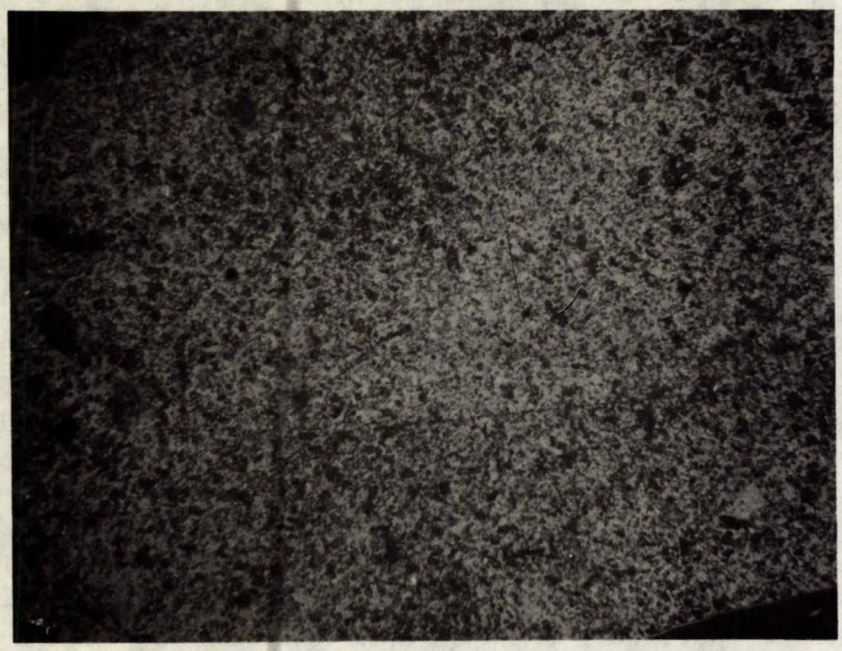

(a) 100 μm

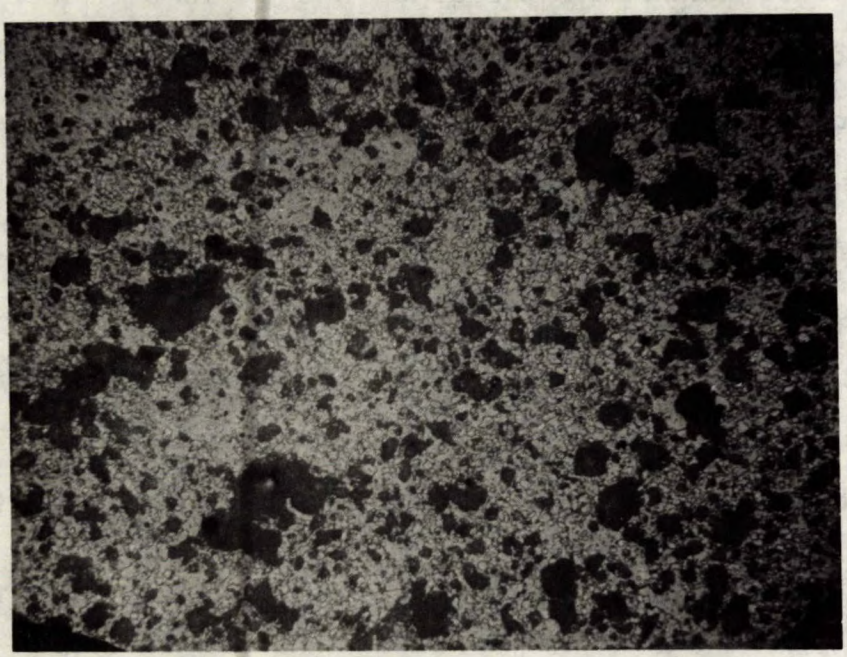

(b) 100 μm

Figure 39. Microstructure developed after firing 7.6 mole % material to 1500°C at 3°C/min without any soak. Polished and etched.

(a) As-fired material
(b) As (a) but with an additional 35 thermal-shock cycles to 1575°C

ment - the strain is partially released and consequently less 'boundaries' are revealed.

Direct evidence for the presence of strain in these compacts was obtained from X-ray diffraction data. Debye-Scherrer powder patterns were obtained using an 114.6-mm diameter camera and Fe-filtered Co radiation. The patterns were subsequently examined using a double beam microdensitometer operated under the conditions given in Appendix D. The traces of the high-angle regions of these patterns are shown in Figure 40.

The low-angle region was examined using a Guinier focussing camera as this has a four times greater dispersion than the 114.6-mm diameter Debye-Scherrer camera. The densitometer traces of these patterns are shown in Figure 41.

Examination of Figures 40 and 41 shows that there is a progressive change in the diffraction pattern as the as-fired 7.6 mole % material is taken through successive thermal-shock cycles. The most obvious change is the gradual increase in the intensity of the diffraction pattern with thermal cycling. In addition, the intensity of the background in the low-angle region decreases. These results, in isolation, suggest that there has been an increase in the amount of crystalline material and a reduction in the amount of amorphous material. The gradual increase in the intensity ratio of the cubic (111)/monoclinic ($11\bar{1}$) from 1.25 to 1.76 further suggests that the cubic phase is formed preferentially. However, comparison of the trace obtained from the pattern of the as-fired compact with that from the as-fired powder suggests that the compact is apparently less crystalline

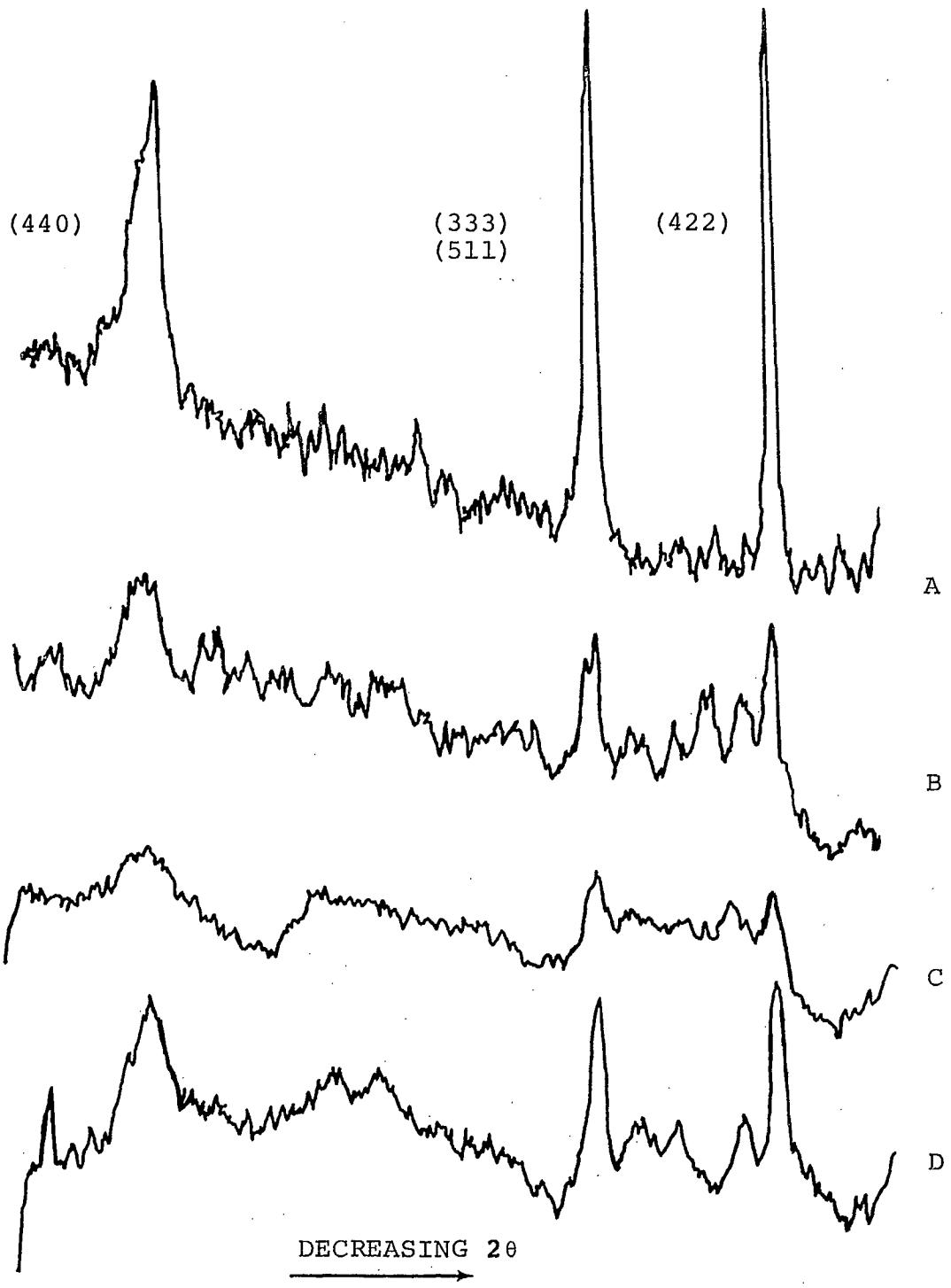

Figure 40. Microdensitometer traces of the back-reflection region of Debye-Scherrer X-ray powder patterns:

A. 11.5 mole % material fired to 1600°C for 1 hour
B. 7.6 mole % powder fired to 1600°C for 1 hour
C. Material B compacted and fired to 1500°C with no soak
D. Sample C thermally shocked 35 times to 1575°C

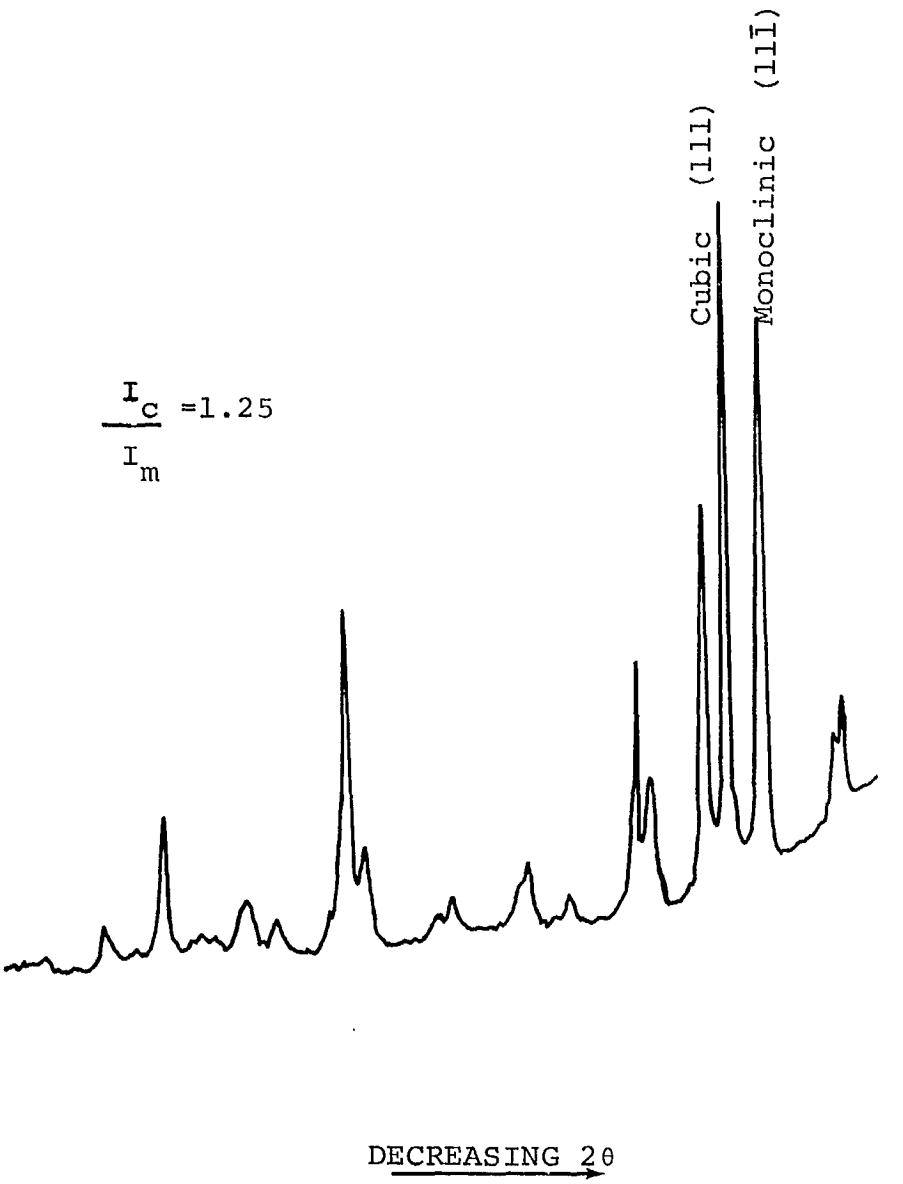

Figure 41a. Microdensitometer trace of the low-angle region of a Guinier X-ray diffraction pattern. 7.6 mole % material compacted and fired to 1500°C with no soak. As-fired sample.

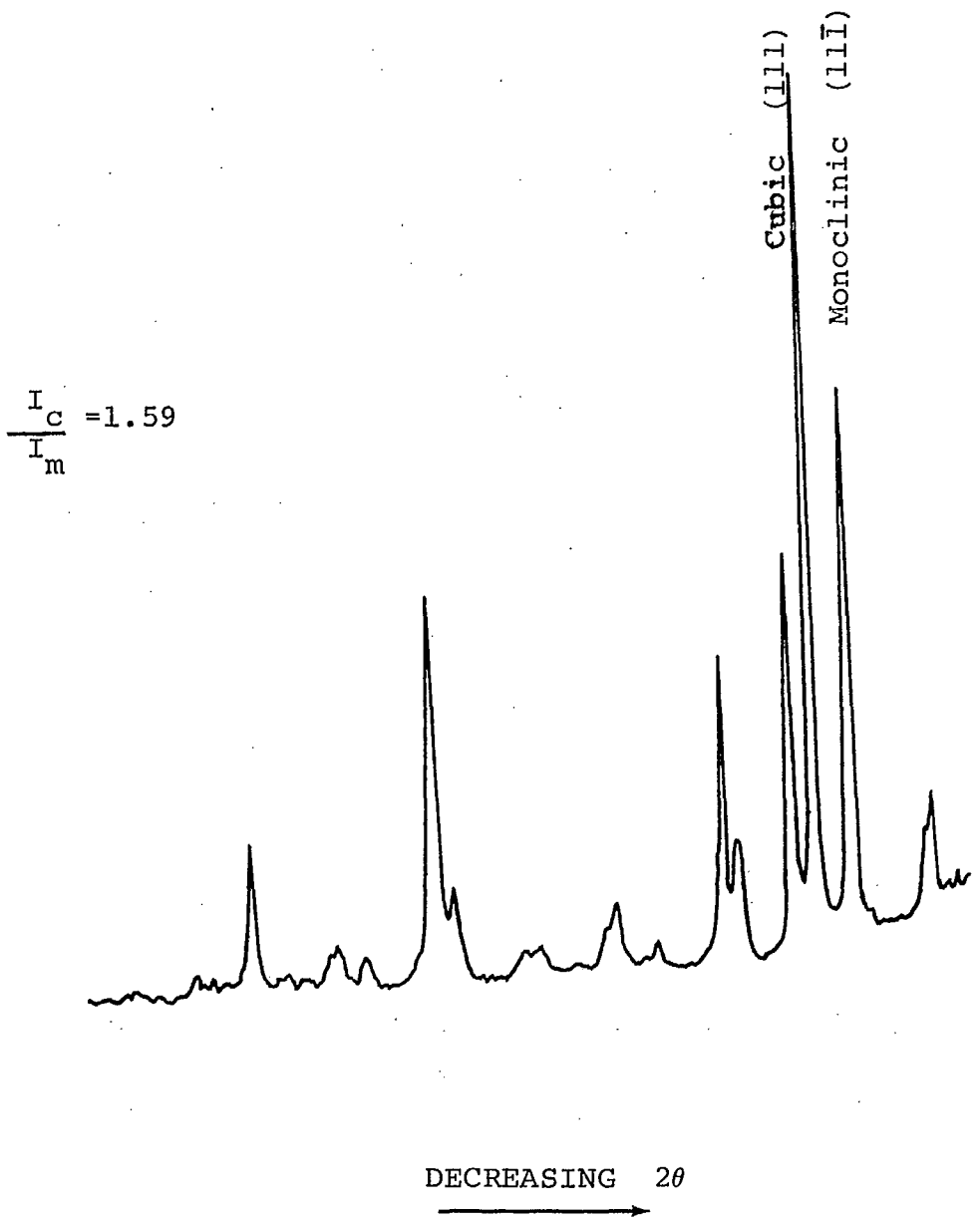

Figure 41b. 7.6 mole % material compacted and fired to 1500°C with no soak. Compact thermally shocked once to 1575°C.

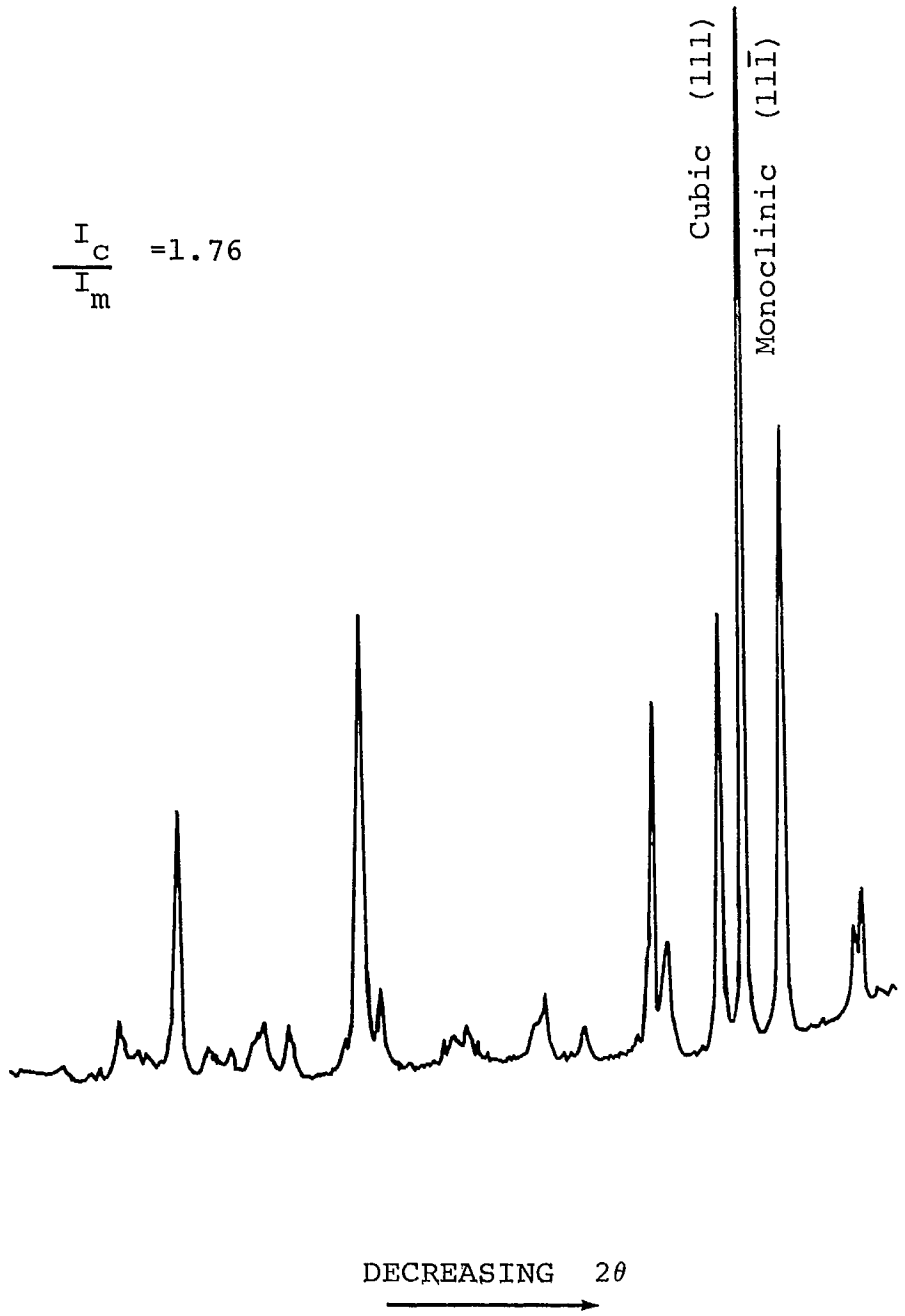

Figure 41c. 7.6 mole % material compacted and fired to 1500°C with no soak. Compact thermally shocked 35 times to 1575°C

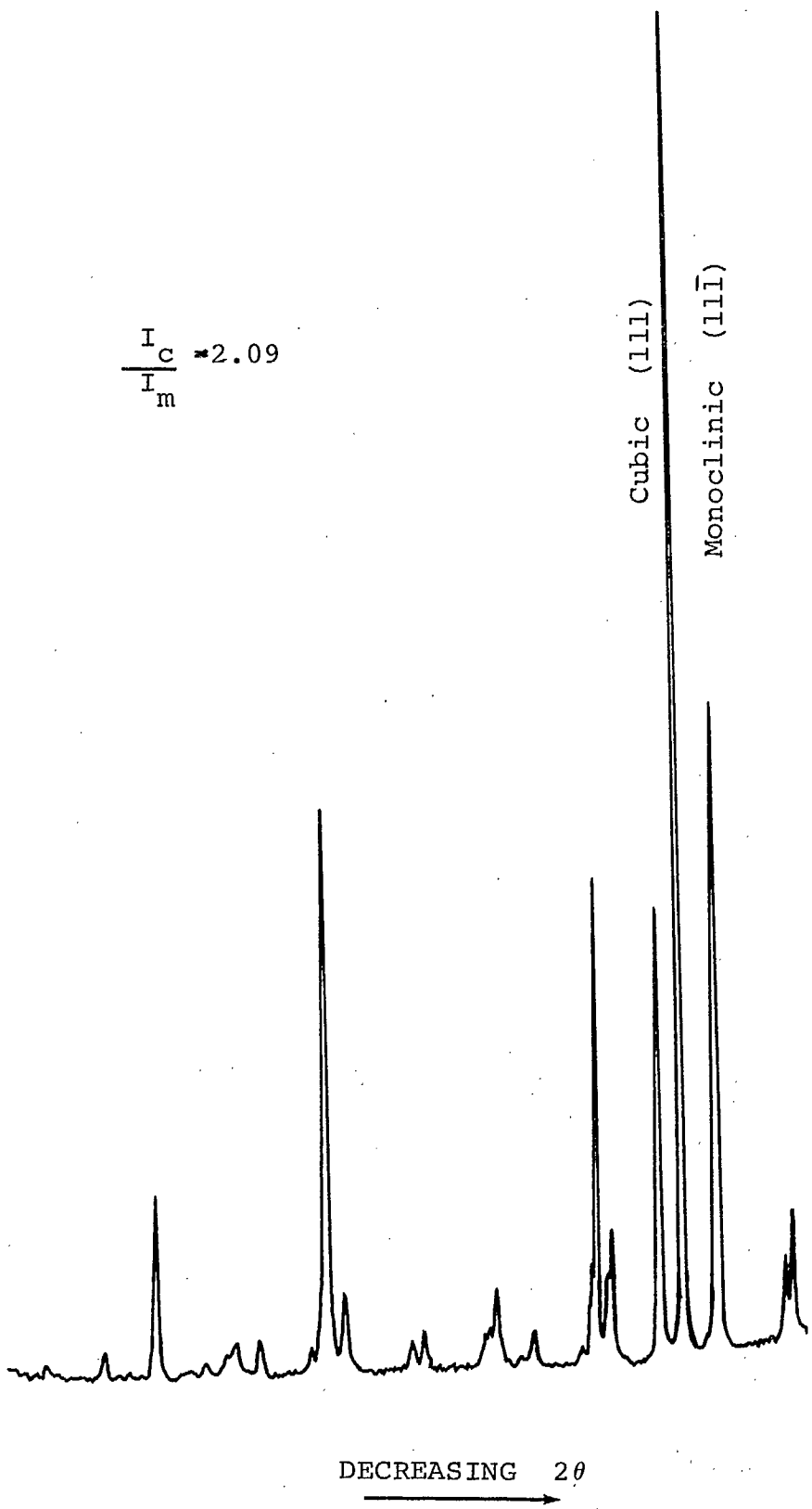

Figure 41d. 7.6 mole % <u>powder</u> fired to 1500°C with no soak

and has less cubic phase. It would be expected that each sample would have the same ratio of monoclinic to cubic material and that both would be entirely crystalline. Consequently, these results are not interpreted as showing a change in either the phase ratio or crystallinity with continuing thermal cycling.

Additional changes were also observed in the diffraction patterns although they are not all obvious in the figures due to the scale used for the presentation. With progressive cycling, gradual reduction in peak width was found and also an increase in the resolution of the back-reflection doublets. In addition, the back-reflection diffraction lines of the cubic phase were shifted to a higher angle. These results could be interpreted to mean that a greater crystal size had developed (line broadening effect due to the size of the coherent diffracting unit) and also that the amount of CaO in solid solution had been reduced (line shifts due to solute concentration changes). However, if this were valid it would be expected that these effects (reduction in line broadening and line shifting to higher angle) would be observed in the pattern of powder fired to 1600°C for 1 hour (Trace B, Figure 40). On the contrary, this trace shows well resolved doublets, narrow peak widths and line positions which agree very closely with those of fully shocked samples. In addition, chemical analysis confirmed that the CaO concentration had remained unaltered during firing.

The changes in the diffraction patterns can be satisfactorily explained in terms of the residual strain retained in the as-fired compact, which is subsequently partially released

during each thermal-shock cycle. In this fashion, it can be seen that the pattern of a fired compact should progressively approach that of a fired powder as the compact suffers continuing thermal shock and the gradual release of strain.

The effect of microstructural stresses on the position and width of a diffracted beam is shown qualitatively in Figure 42. Essentially, two conditions will exist in which the lattice experiences either a uniform or non-uniform strain distribution. Due to the presence of neighbouring grains around a given crystal lattice and the random orientation of each lattice it would be expected that a non-uniform strain situation would develop. Consequently, the diffraction lines will be broadened and displaced from their strain-free positions. With excess broadening, the pattern in the back-reflection region of the as-fired PSZ compacts becomes so diffuse that it is barely resolved from the background (Trace C, Figure 40).

With progressive thermal cycling and the partial release of strain, the lines become much sharper and, in order to maintain the area of the diffraction profile, the intensity is increased. This release of strain also accounts for the improved resolution of the doublets, the reduction in the low-angle background, and the shift of the diffraction lines of the cubic phase to higher angle as this component was originally under tension. However, changes in strain alone would not account for the progressive increase in the intensity ratio of the cubic (111)/monoclinic ($11\bar{1}$) diffraction lines. The intensities of the major peaks in Figure 41 are given in Appendix G.

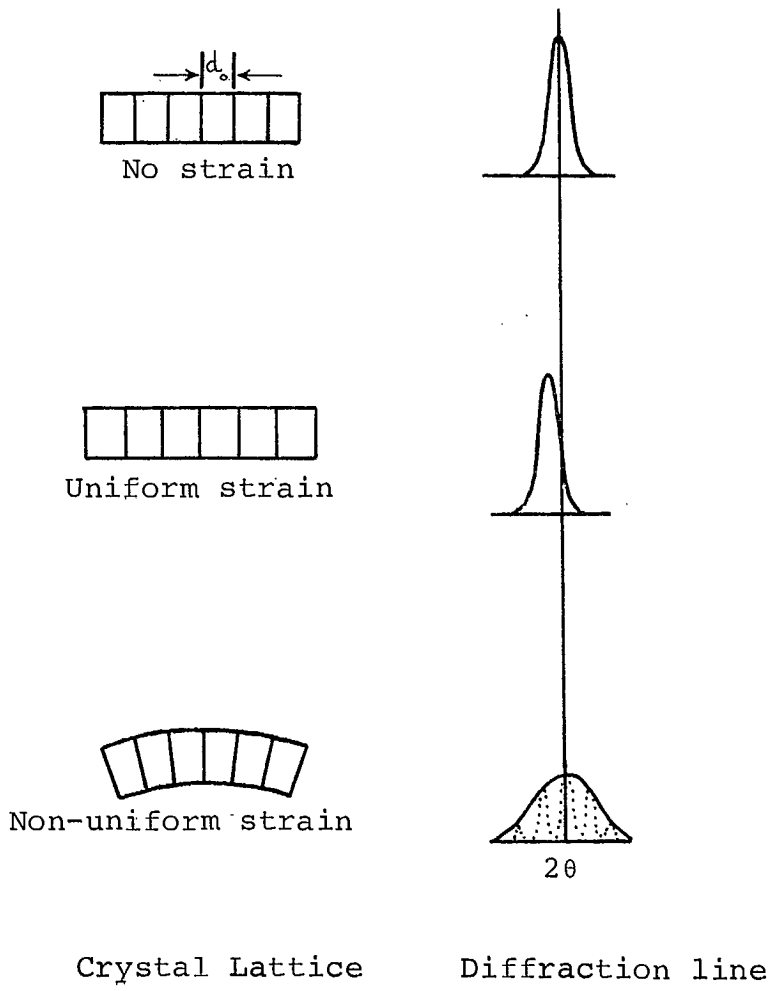

Figure 42. Effect of lattice strain on the diffracted beam width and position. After B.D. Cullity, 'Elements of X-ray Diffraction', Addison-Wesley, (1956).

The data confirm that there is a gradual increase in the intensity of the cubic pattern with progressive thermal cycling, whereas the intensity of the monoclinic phase is nearly constant. This could be due to the cubic phase having essentially a perfect crystal lattice under strain whereas the monoclinic phase consists of a defect lattice having a mosaic structure under strain. As the strain is reduced during cycling, the

diffraction intensity will be increased and this will occur for both phases. However, the presence of a mosaic structure would retain part of the line broadening effect found initially and hence the intensity of the monoclinic pattern would not increase as rapidly. This structural difference between the two phases could account for the change in the intensity ratio (cubic (111)/ monoclinic ($11\bar{1}$)) with progressive thermal shock.

With continuing thermal cycling to 1575°C, the PSZ compacts undergo an irreversible expansion (ratchetting) as the stresses are slowly released (Figure 38). This behaviour gives rise to a progressive roughening of the surface as shown in Figure 43. The correlation between the surface projections and subsurface porosity was demonstrated by carefully lapping the rough surface; a one-to-one correlation was found between the prominences and pores. This increase in porosity is not confined to the surface layers only, but distributed throughout the bulk of the sample.

Figure 39 shows a considerable increase in porosity in the thermally shocked sample. A point count analysis of the porosity in this and other polished sections of thermally shocked material indicated an increase in the total porosity from approximately 10% to 38% after cycling to equilibrium. This figure agrees well with the increase in volume suggested by the ratchetting data of Figure 38. A linear increase of 11.2% implies a volume increase of 40.3% approximately. This close agreement between the two sets of figures discounts the possibility that the pores in the micrographs 'pull-outs'. However, this evidence

(a) 750 μm

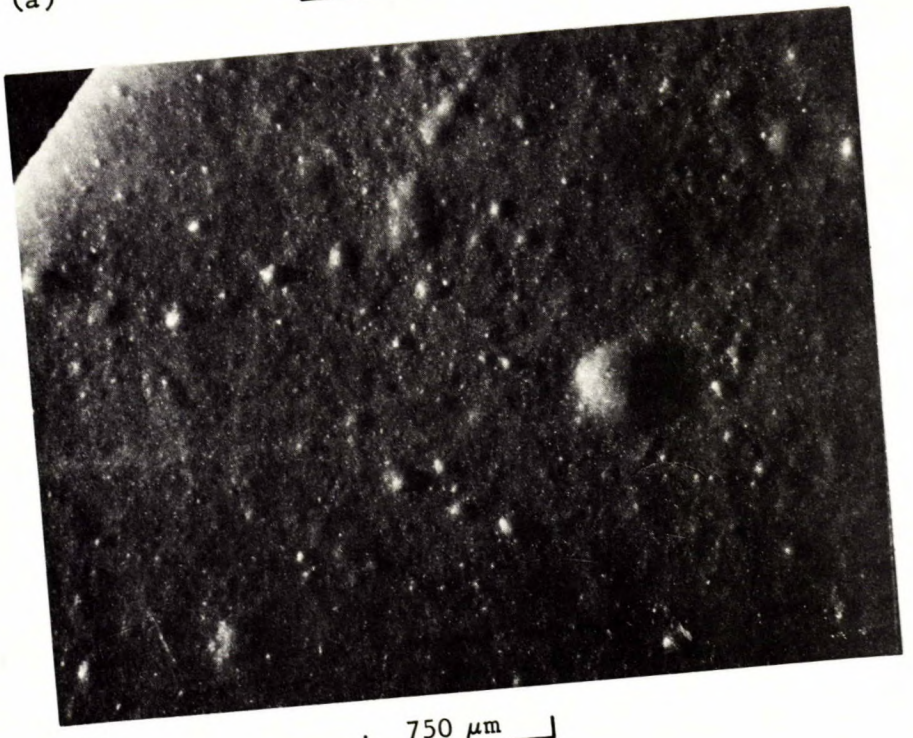

(b) 750 μm

Figure 43. Surface of PSZ compact viewed in oblique light.
(a) As-fired surface
(b) After 35 thermal shock cycles to 1575°C

does not indicate whether the pores present in the original body are genuine voids or whether they contain loose material which has separated from the matrix. Intuitively, it would be expected that these features were originally filled with loose material which had been lost during the preparation of either polished or fractured surfaces.

Evidence in support of a limited microcrack propagation mechanism which could be responsible for the formation of these pores is shown in the SEM micrograph of material thermally shocked once to 1575°C (Figure 44a(b)). The features indicated by the arrows could well be material that has gradually separated from the matrix due to ratchetting occurring at each cycle. With continued thermal shock, more microcracks will propagate and unite to release a greater volume of material from the bulk of the sample. Consequently, the resulting 'pore' size is increased.

Examination of the fine-structure of PSZ shows that the grain size is essentially constant during cycling (Figure 44). In the as-fired materials the grain size is approximately 2000 Å and increases to about 3000 Å after 35 cycles. This confirms the supposition made from an optical examination of the material that the individual single-phase regions are too small to be resolved using the optical microscope. In addition, the fact that the pores observed in the fracture surfaces increased in size with cycling whereas the grain size remained nearly constant, further supports the hypothesis that the pores are created by a microcrack mechanism rather than by pulling out.

(a) 200 μm

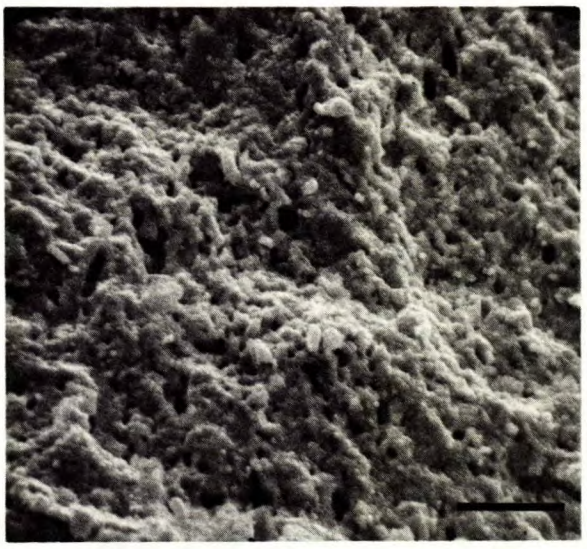

5 μm

(b) 200 μm

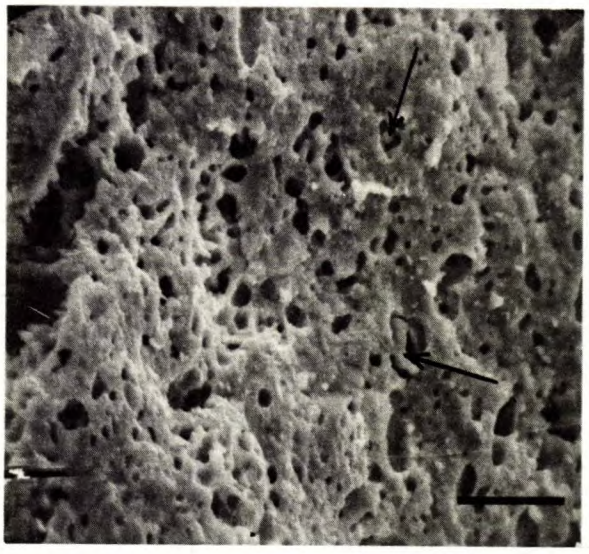

5 μm

Figure 44a. SEM micrographs of the fracture surface of PSZ.
(a) As-fired
(b) Thermally shocked once to 1575°C

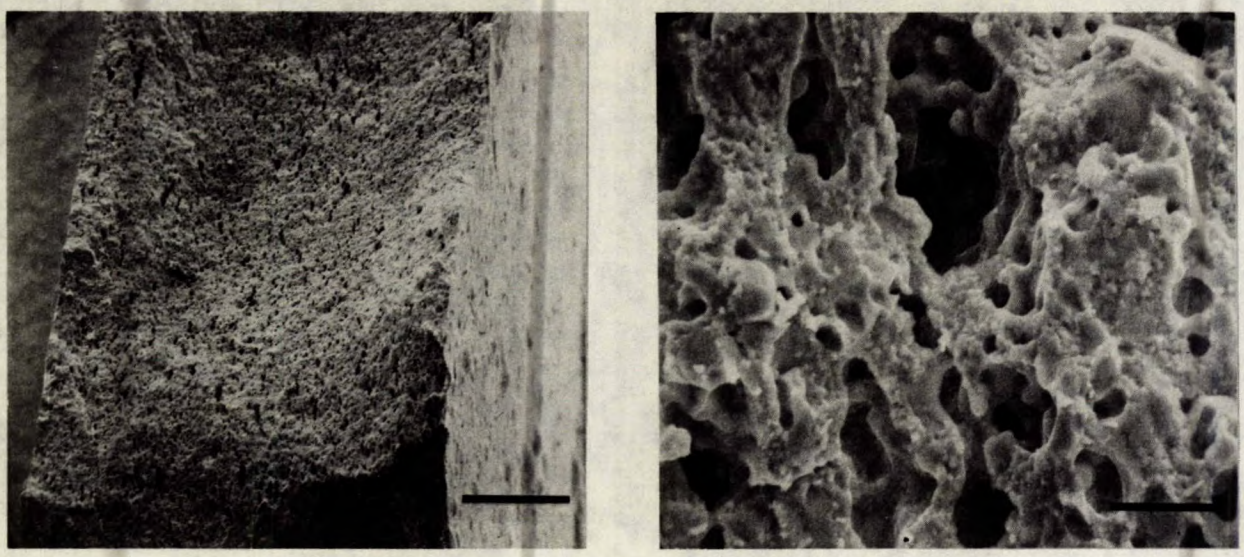

200 µm 5 µm

Figure 44b. SEM micrographs of the fracture surface of PSZ after thermal cycling 35 times to 1575°C.

The internal fine-grain structure observed in this material at all stages of thermal cycling contrasts with the surface microstructure developed with progressive cycling (Figure 45). Initially, the surface shows the fine structure characteristics of the interior. However, with progressive thermal shock the surface appears to develop a bimodal grain-size distribution with the smaller grains having a mean size of approximately 0.5 µm while the larger grains have a mean size of approximately 6 µm. This apparent contradiction between the interpretation of the micrographs of the surface and interior of PSZ has been explained by the nature of the cubic phase field in the CaO-ZrO_2 system[23]. It has been suggested that the field may be regarded as a continuous solid-solution series between pure ZrO_2 and the cubic

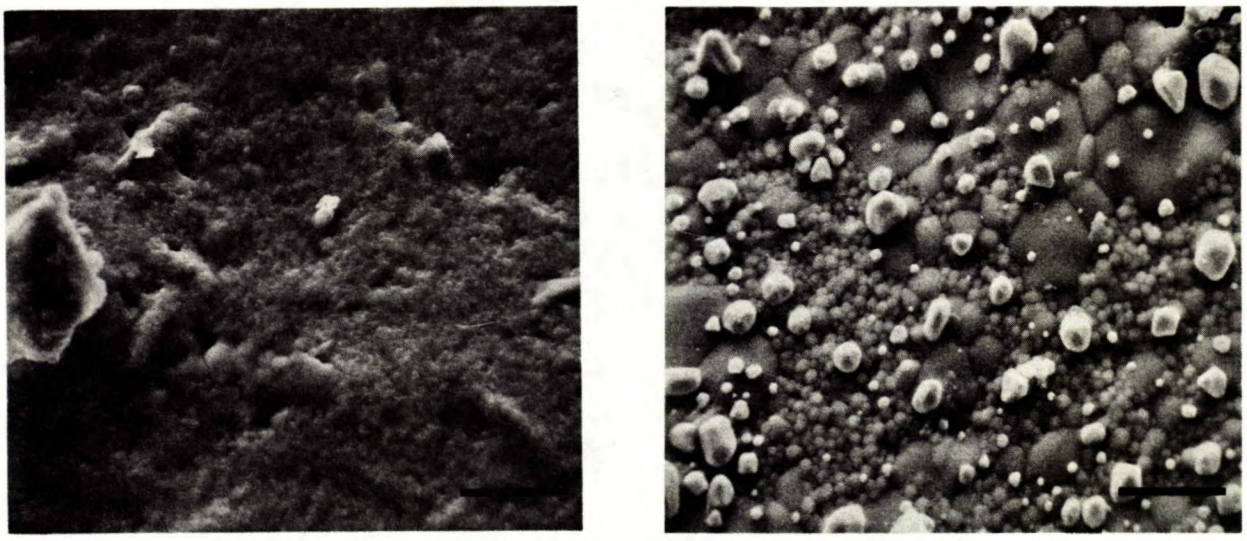

(a) 5 μm (b) 5 μm

Figure 45. SEM micrographs of the surface of PSZ material.
(a) As-fired
(b) Thermally cycled 35 times to 1575°C - white features are Pt single crystals formed by evaporation and condensation of sample container

compound $CaZr_4O_9$. The supersaturation of the cubic phase with pure ZrO_2, which results when the material is cooled from the firing temperature, leads to the precipitation of pure fine-grained ZrO_2 in grains that had been entirely cubic. This may explain the existence of the large grains shown in Figure 45; their boundaries are actually the relics of a high-temperature structure. Consequently, the fracture surfaces only show the presence of a fine-grained material and fail to substantiate the existence of a relatively coarse-grained phase.

From the X-ray, optical and SEM data it is concluded that the microstructure of PSZ is composed of 2000 Å domains of

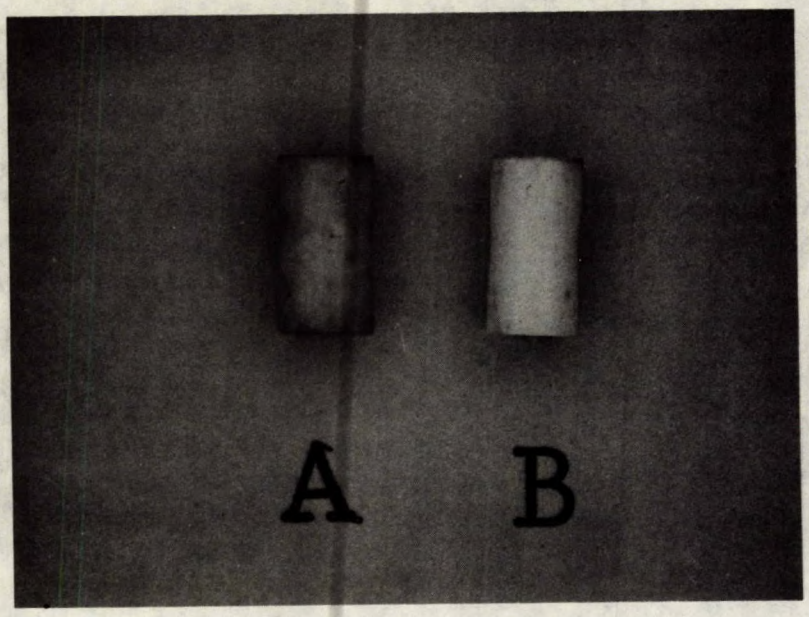

Figure 46. Oxygen-probe membranes made from PSZ showing the very high thermal-shock resistance of this material.

A. Membrane thermally cycled 35 times from room temperature to 1575°C and back to room temperature again with a heating rate of approximately 400°C/sec
B. As-fired membrane

cubic and monoclinic zirconia held in a matrix which contains considerable fabrication and firing stresses which, during severe thermal cycling, are gradually released as a stable network of microcracks is established. During further thermal shock, the microcrack network is extended through the matrix as the precipitated 2000 Å domains of pure zirconia continue to expand against a contracting cubic matrix during each cooling cycle. The catastrophic propagation of these cracks is restricted because the stored elastic energy is dissipated among the many cracks which are formed; to propagate further, the severity of the thermal

shock must be increased. Because of the high density of micro-cracks, the material develops a considerable thermal-shock resistance such that it can withstand heating and cooling rates up to 400°C/sec without suffering gross mechanical damage (Figure 46).

Electrical Properties of Thermal-Shock Resistant Zirconia

Having established the procedure by which impermeable, thermal-shock resistant zirconia may be produced, it was desirable to examine the ionic conductivity of this material under controlled laboratory conditions. This was necessary in order to establish the reproducibility of the emf output on a cell-to-cell basis and hence to allow a distinction to be drawn between the scatter in the emf data contributed by the electrolyte itself and that contributed by the whole probe assembly when used in an environment which contains stray electrical fields.

In essence, the reproducibility is determined by measuring the emf developed across a number of zirconia electrolytes when they are used in oxygen concentration cells operating at a given temperature and with a given oxygen gradient. The actual oxygen concentration that is required on each side of the electrolyte can be obtained using either gas mixtures of known P_{O_2} or alternatively metal-metal oxide composites for which the equilibrium: Metal Oxide $\leftrightharpoons$ Metal + Oxygen, will furnish a fixed P_{O_2} at a given temperature.

The use of gas mixtures requires an effective high-temperature seal to prevent the passage of molecular oxygen across the zirconia membrane. In addition, such a seal would be pre-

ferably demountable to allow different membranes to be used in an oxygen concentration cell that retained a constant geometry. Because of the practical difficulties in developing a seal with these characteristics, the much simpler open-cell design was used which employs metal-metal oxide reference electrodes operating in an argon atmosphere (Figure 47).

The two reference electrodes and the PSZ compact were held in contact by spring-loaded Pt electrodes. The emf developed across the cell was determined using a high-impedance digital voltmeter* as the cell equilibrium temperature was progressively raised from 700°C to 1200°C and subsequently cooled over the same temperature interval. The argon atmosphere used in the apparatus was initially purified by passing over $CaCl_2$ and $Mg(ClO_4)_2$ desiccants followed by a CO_2 absorbent** and finally Zr metal at 800°C to remove O_2; the last traces of O_2 were removed by a Ti-foil getter which surrounded the cell assembly.

The reference electrodes were prepared by mixing equal weights of metal (99.9% pure, -200 mesh) and oxide (99.5% pure, -200 mesh) and subsequently blending in a dental amalgamator for 5 minutes. The mixture was uniaxially pressed at 10,000 psi in a steel die and sintered in vacuum for 5 hours at 1000°C. The composites were fabricated to produce discs 7 to 10 mm in diameter and 3 to 5 mm thick after firing. Using this procedure, pellets of Fe-FeO (Fe_2O_3 actually used), Ni-NiO, and Co-CoO were made which sintered well and developed an adequate fired strength.

---

* Model 801 Digital pH meter, Orion Research Inc., Cambridge Mass. having an input impedance of 10^{13} ohms

**Ascarite supplied by Arthur H. Thomas Co., Philadelphia Pa.

On the other hand, composites of $Cr-Cr_2O_3$ barely sintered and hence were extremely fragile after firing under the above conditions.

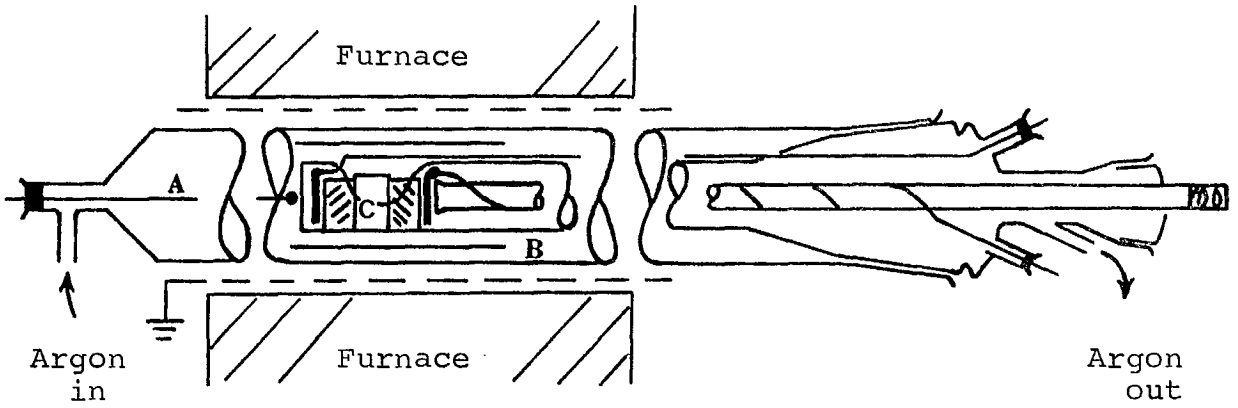

Figure 47. Schematic of oxygen concentration cell.

A. Pt, Pt-10% Rh thermocouple
B. Ti-foil oxygen getter
C. Concentration cell consisting of ZrO_2 sample held between metal-metal oxide composites and Pt electrodes

Initially, it was intended to measure, as a function of temperature, the emf of the following cells:

Pt, $Ni-NiO/ZrO_2/Fe-FeO$, Pt (1)

Pt, $Ni-NiO/ZrO_2/Co-CoO$, Pt (2)

Pt, $Ni-NiO/ZrO_2/Cr-Cr_2O_3$, Pt (3)

However, the emf of cell (3) was found to deviate markedly from the theoretical value given by the Nernst equation (page 1) and to be unstable with time which suggests that the zirconia developed electronic conductivity at the P_{O_2} levels associated with the chromium-chromia equilibrium (Figure 48, data from Appendix H).

Similar behaviour has been reported using fully stabilized zirconia as the electrolyte[36].

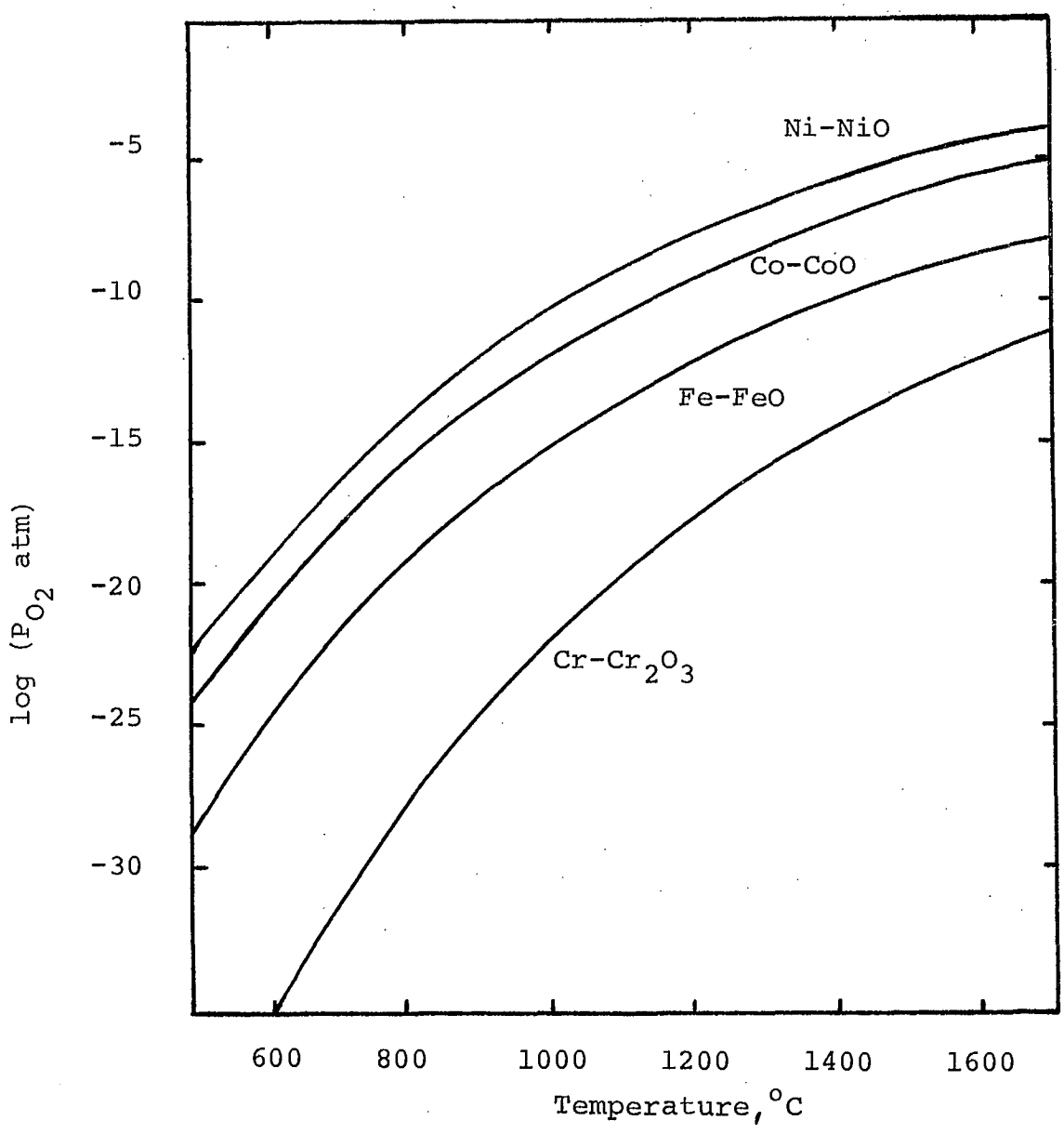

Figure 48. Variation of oxygen partial pressure in equilibrium with different metal-metal oxide systems as a function of increasing temperature.

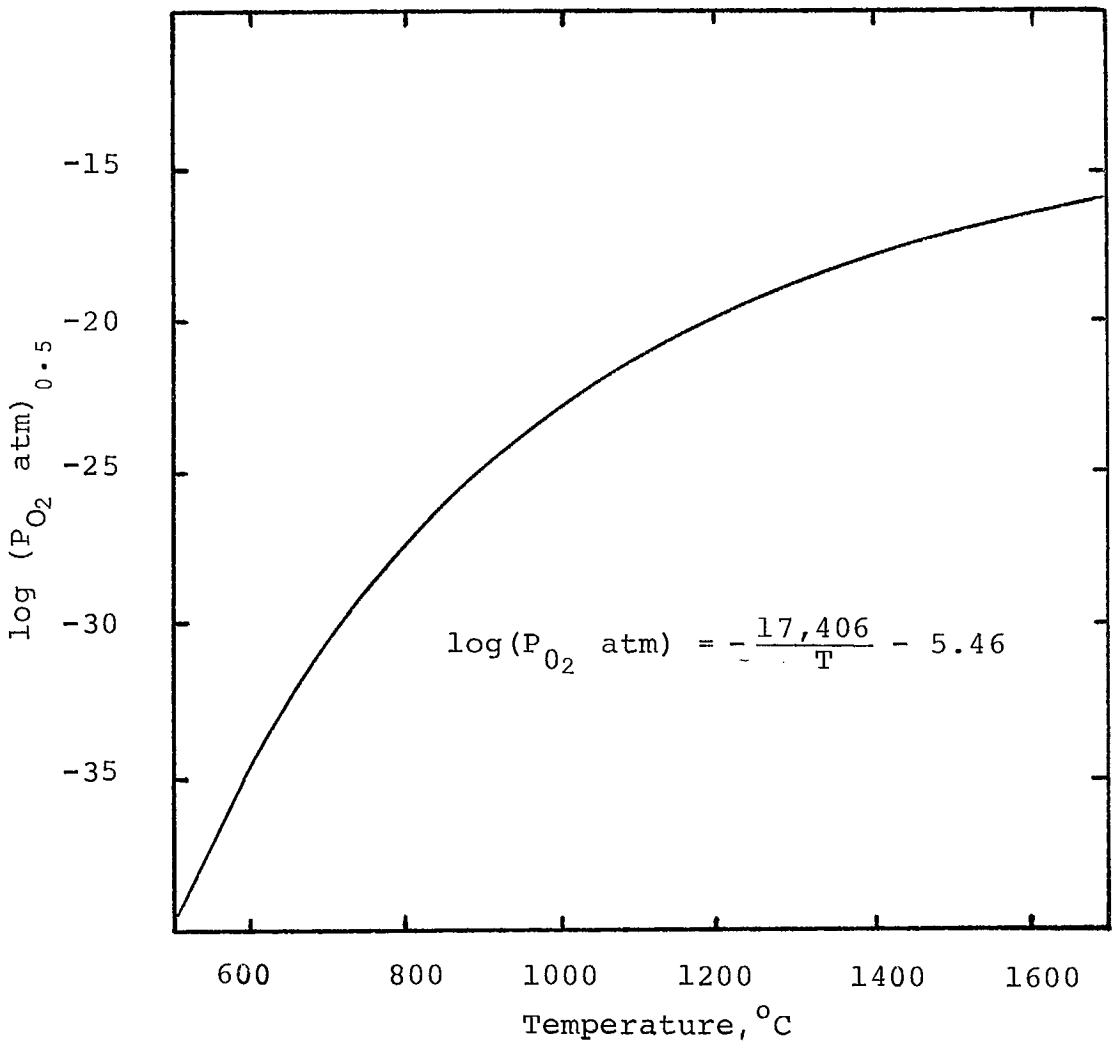

Figure 49. Variation of oxygen partial pressure with temperature at which the ionic and electronic conductivities of zirconia are equal.

The temperature and P_{O_2} values at which significant electronic conductivity is developed in lime-stabilized zirconia have been widely examined[5,12,37-41]. Unfortunately, there is wide disagreement in the data presented. The oxygen partial pressure $(P_{O_2})_{0.5}$ at which the electronic and ionic conductivities are equal, i.e., the transport numbers $t_i = t_e = 0.5$, has been

variously reported between 10^{-22} and 10^{-28} atmospheres at 1000°C[37,40]. These discrepancies are probably due to the differing homogeneity and impurity levels present in the electrolyte. It is perhaps fortuitous that silica is one of the main impurities in commercially available zirconias (principal mineral is zircon, $ZrSiO_4$) because recent data has indicated that this impurity exhibits an ionic conductivity which is approximately 80% of the total SiO_2 conductivity[11], otherwise the discrepancies in the reported $(P_{O_2})_{0.5}$ values could be much greater if the major impurity in commercial oxygen probes had a high electronic conductivity.

One of the more conservative estimates of the variation of $(P_{O_2})_{0.5}$ with temperature has been given for the temperature range 500°C to 1000°C[42]. The equation for the curve was determined and extrapolated to cover the range from 500°C to 1700°C (Figure 49). The data show that at 1000°C the ionic and electronic conductivities become equal at an oxygen partial pressure of 1.4×10^{-23} atmospheres which is very close to the equilibrium P_{O_2} of 9.4×10^{-23} atmospheres developed by $Cr\text{-}Cr_2O_3$ mixtures at the same temperature (Appendix H). Consequently, any oxygen concentration cell that incorporates a $Cr\text{-}Cr_2O_3$ reference electrode cannot develop the theoretical Nernst emf because the cell will be partially shorted by the development of a significant electronic conductivity in the ZrO_2 membrane.

The gradual development of an increasing electronic conductivity with decreasing oxygen pressure is of importance to the ultimate use of ZrO_2 in oxygen probe assemblies. However,

contrary to suggestions in the literature on this aspect of an oxygen probe, it is not necessary that the zirconia electrolyte be a perfect ionic conductor having zero electronic conductivity under steel-making conditions. An electrolyte which possessed mixed ionic and electronic conductivity would not allow the full Nernst emf to be developed, but if the ratio of ionic to electronic conductivity (σ_i/σ_e) were constant on a probe-to-probe basis then a constant readout would be obtained using successive probes. Hence, the introduction of an 'instrumental factor' to the observed emf reading would allow the actual oxygen content of the steel to be determined. Although this takes a purely practical view of the use of zirconia probes, it may be shown theoretically that this material is predominantly an ionic conductor under steel-making conditions and hence the theoretical emf output should be obtained in practice.

The variation of the ionic transport number t_i with changes in P_{O_2} may be estimated from the relationship:

$$t_i = \sigma_i/(\sigma_i + \sigma_e) = 1/(1 + \sigma_e/\sigma_i)$$

Assuming that σ_i is constant whereas σ_e is proportional to $P_{O_2}^{-\frac{1}{4}}$ (37) and using the $(P_{O_2})_{0.5}$ values from Figure 49 of 10^{-16} and 10^{-23} atmospheres at 1600°C and 1000°C respectively, the curves relating t_i to P_{O_2} may be calculated as shown in Appendix I.

The data is presented in Figure 50 and shows that, irrespective of temperature, a ten decade change in P_{O_2} is necessary for the reduction of t_i from 0.95 to 0.05. However, of more significance to the use of zirconia in a probe is the result that approximately a three decade change in P_{O_2} is required for

the lowering of t_i from 0.99 to 0.95 and, as shown in Figure 50, such a reduction in t_i occurs over the range of P_{O_2} values measured in commercial steel-making practice. Consequently, a progressive reduction in the output would be expected as the measured emf is gradually depressed from the theoretical value as the oxygen content of the steel is reduced from 830 ppm (10^{-9} atmospheres) to 26 ppm (10^{-12} atmospheres)*.

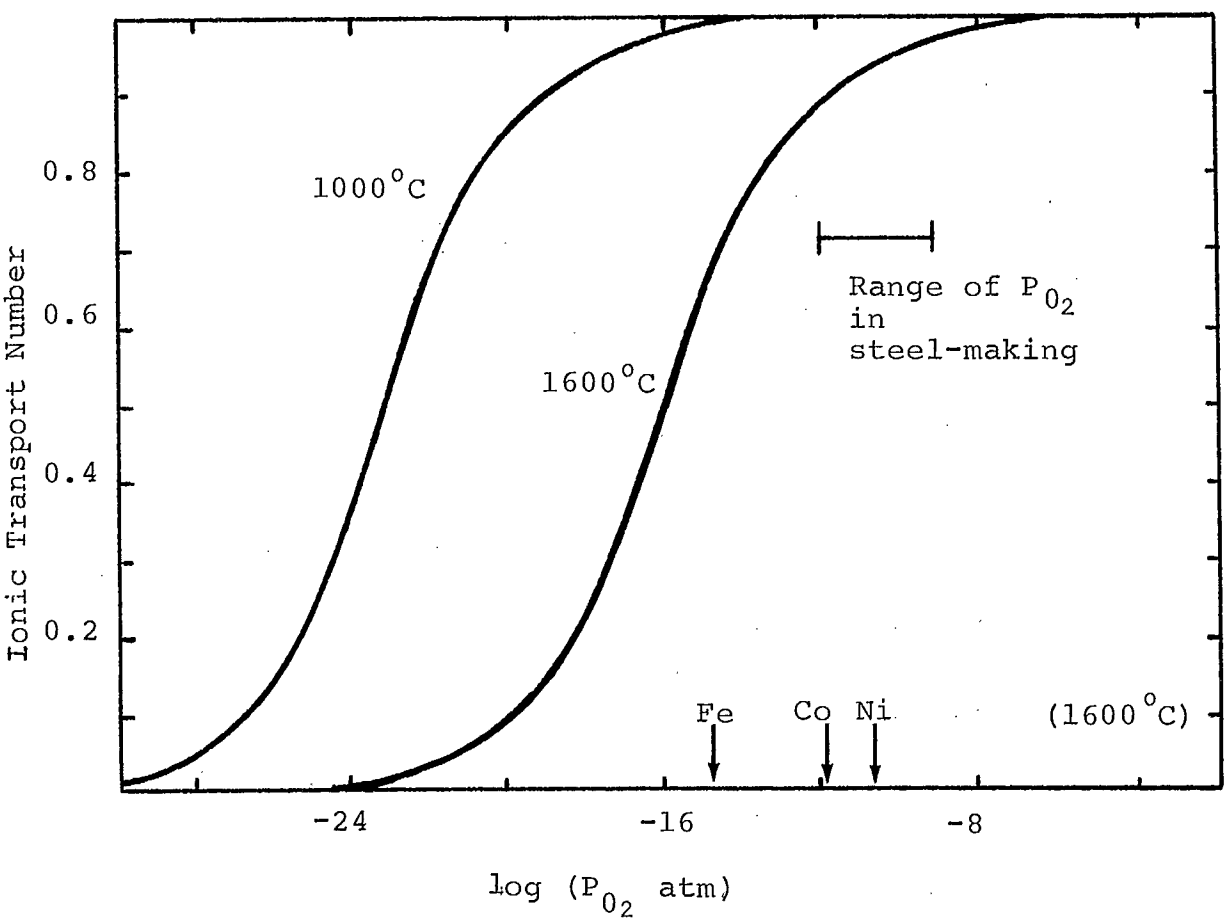

Figure 50. Variation of ionic transport number with oxygen partial pressure for zirconia at 1000°C and 1600°C. Arrows indicate the P_{O_2} developed by metal-metal oxide composites at 1600°C.

*It may be shown[12] that: $(O)_{ppm} = P^{\frac{1}{2}}(\exp(14100/T + 9.557))$

This depression in the emf due to the development of a significant electronic conductivity may be determined from the basic equation for the emf developed in a concentration cell:

$$E = -\frac{RT}{4F}\int_{P_1}^{P_2} t_i \, d\ln P$$

Integration leads to the Nernst equation for those cases where the cell operates in a purely ionic mode, i.e., $t_i = 1$.

$$E_{th} = -\frac{RT}{4F} \ln \left(\frac{P_2}{P_1}\right)$$

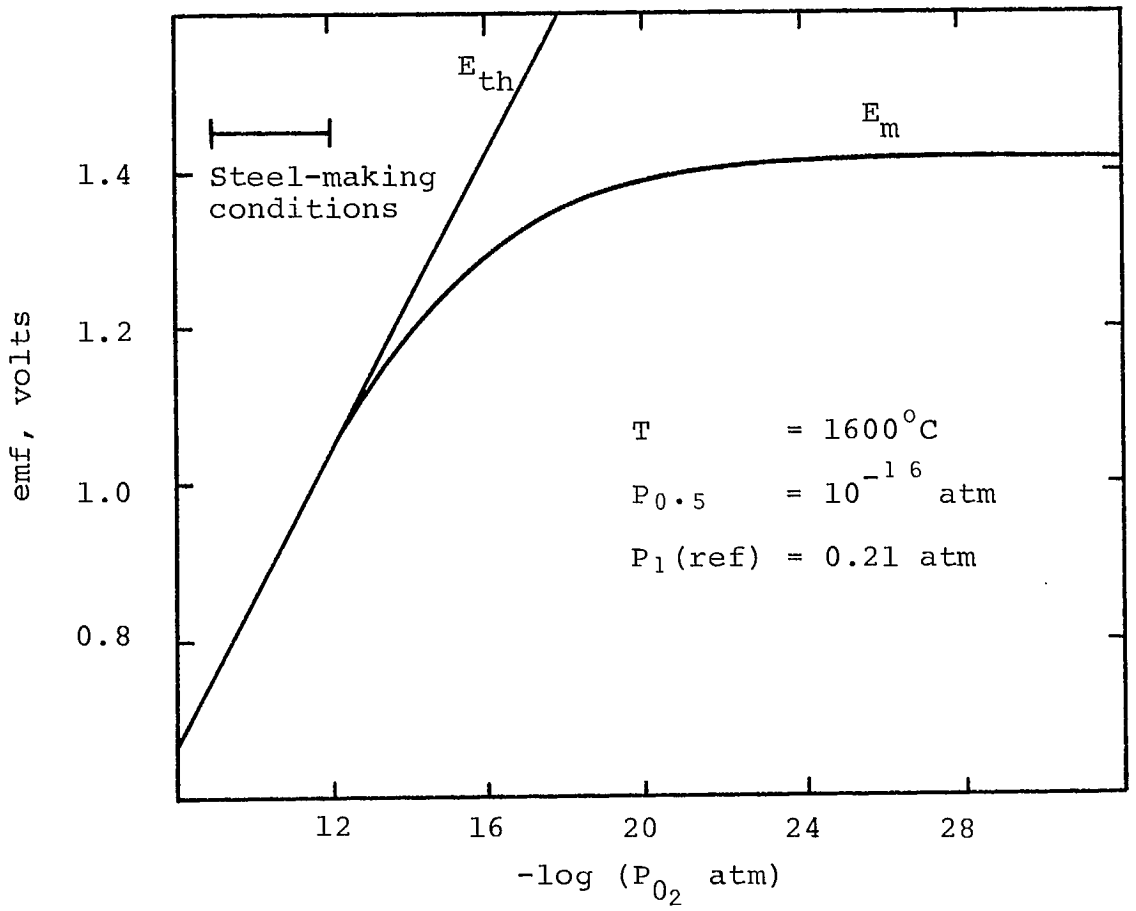

Figure 51. Variation of emf output with oxygen partial pressure for a concentration cell operating in a purely ionic mode (E_{th}) or with mixed ionic and electronic conductivity (E_m).

However, $t_i \neq 1$ under steel-making conditions and hence integration leads to[43]:

$$E_m = -\frac{RT}{F} \ln \frac{(P_{0.5}^{1/4} + P_2^{1/4})}{(P_{0.5}^{1/4} + P_1^{1/4})}$$

when t_i is assumed to be a function of ln P_{O_2} as shown in Figure 50[12,42]. A plot of the above equations for E_{th} and E_m as a function of P_{O_2} is given in Figure 51. Although it is not apparent from the figure, the minor contribution of σ_e to the total conductivity that occurs under steel-making conditions, Figure 50, results in a significant reduction in the emf developed, particularly at the lower P_{O_2} values. For example, when P_2 is 10^{-12} atm, the Nernst value E_{th} of 1.052 volts is reduced to a measured value E_m of 1.036 volts. Provided this difference of 16 mv in the emf output is maintained on a probe-to-probe basis and is truly an intrinsic property of the zirconia, then reliable data would be obtained.

It may be shown that the reduction of the emf signal is not only dependent on the absolute magnitude of P_2 but is also dependent on the oxygen concentration gradient across the electrolyte. The leakage current (i_e which flows in the electrolyte when some electronic conductivity is present is given by:

$$i_e = \frac{RT\sigma_i}{LF}\left(\frac{P_{0.5}^{1/4}}{P_2^{1/4}}\right)\left(\frac{P_2^{1/4} - P_1^{1/4}}{P_{0.5}^{1/4} - P_1^{1/4}}\right)$$

where L is the length of the electrolyte[12].

Clearly, the magnitude of $i_e \rightarrow 0$ and hence $E_m \rightarrow E_{th}$ as $P_{0.5} \rightarrow 0$ and also as $P_1 \rightarrow P_2$ so that $(P_2^{1/4} - P_1^{1/4}) \rightarrow 0$. Consequently, the attenuation of the emf will be minimized by having

$P_1 \simeq P_2$, i.e., for application in a steel-making furnace a reference oxygen pressure in the range 10^{-9} to 10^{-12} atm at 1600°C would be desirable.

Because the electronic conductivity in zirconia is developed due to either electron formation (resulting from oxygen vacancy formation and ionization or zirconium interstitial formation) or positive hole formation (resulting from zirconium vacancy formation and ionization or oxygen interstitial formation), σ_e would be expected to depend on the ZrO_2 solid-solution composition for both di- and tri-valent stabilizers[44]. However, this 'intrinsic' behaviour of the zirconia itself is probably of minor significance to the performance of the electrolyte as a whole compared to the 'extrinsic' variability which can be introduced by the presence of a second phase that may vary in concentration, identity or distribution within the zirconia microstructure.

Figure 52 shows a typical microstructure of a commercially available zirconia oxygen probe membrane. The rounded grains of zirconia are seen to be coated with a layer of $CaSiO_3$ as the grain-boundary phase. In such a structure it is difficult to determine whether the silicate or the zirconia forms the continuous phase. Taking two extreme cases, it would be possible to have a zirconia electrolyte containing a $CaSiO_3$ impurity or, with a slight increase in the silicate content to allow it to form the continuous phase, one could unwittingly be using a $CaSiO_3$ probe which contains a major quantity of zirconia as the impurity phase. If the electronic and ionic conductivities of these two phases differ to any significant extent then it can be

appreciated that a considerable scatter in the electrical properties could easily be developed.

Figure 52. Microstructure of a commercially available oxygen-probe zirconia membrane. Light grey - zirconia; dark grey - calcium silicate; black - pores.

Many commercially available zirconia raw materials typically contain between 0.5 and 1 wt % SiO_2 that, on firing, reacts with the CaO to remove it from solid solution with the zirconia and so form $CaSiO_3$ which develops as a grain-boundary phase. The presence of 0.5 to 1 wt % SiO_2 in zirconia will produce approximately 1 to 2 wt % $CaSiO_3$ assuming all the SiO_2 is reacted. The potential for just 1 wt % $CaSiO_3$ to significantly alter the electrical properties of a zirconia probe would be

realised if the impurity were uniformly distributed throughout the microstructure so as to coat each grain. For example, it can be shown that 1 wt % silicate in a zirconia matrix consisting of spherical grains 20 μm in diameter will cover each grain with a layer 336 Å thick and this quantity has been shown to greatly aid in the sintering of these relatively coarse-grained materials[45]. However, as shown in Figure 52, the silicate is not uniformly distributed but tends to collect in pockets leaving areas where the zirconia-zirconia bond is formed. Consequently, the possibility of a continuous electronically conducting phase existing across the zirconia membrane is prevented and hence the Nernst emf is developed in full (or slightly attenuated due to the intrinsic electronic conductivity of the zirconia itself).

Ionic Conductivity of Partially Stabilized Zirconia

Because of the difficulty in obtaining stable readings from oxygen concentration cells which used $Cr-Cr_2O_3$ reference electrodes, subsequent data were obtained using Fe-FeO and Ni-NiO electrodes. In essence, the assembled cell was heated in an argon atmosphere between 700 and 1200°C and the emf developed was recorded as a function of temperature.

A typical set of results together with the Nernst emf curve calculated from the tabulated thermodynamic data[35] (Appendix J) are given in Figure 53. The data were obtained on both the heating and cooling cycles and the emf was found to be stable over long periods; no drift was observed. At the lower temperatures, i.e., below 900°C, a change in the cell operating

temperature results in a very sluggish response in the emf output and may require up to two hours to establish electrical equilibrium; at 800°C up to ten hours was found necessary. Several cells were operated in equilibrium for periods of up to 36 hours confirming that there was no degredation in the emf output.

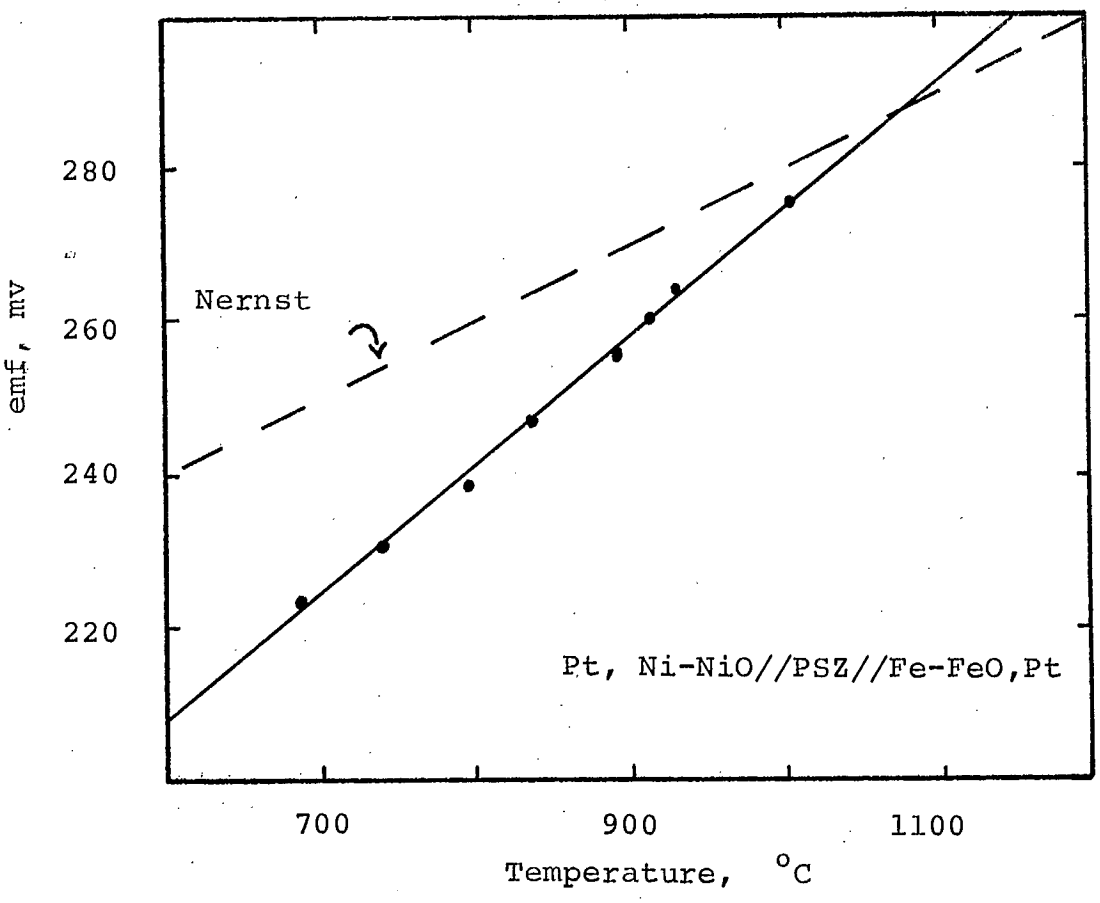

Figure 53. Variation of emf with temperature for a concentration cell employing a PSZ electrolyte.

With extended use, i.e., over 10 hours at temperatures over 1000°C, the reference electrodes were degraded as the surfaces became progressively more metallic and poorly defined emf readings were obtained. Consequently, because most experiments

were conducted to temperatures over 1000°C, the reference electrodes were changed after every cycle from room temperature to high temperature and back. The cells were shown to be reversible[46] by passing a small current through the cell in each direction; the cell emf always returned to the original value.

The deviation of the data from the theoretical curve is difficult to explain; it has been observed[47] and reported[48] elsewhere. It is possible that the minor impurities present in the reference electrode materials give rise to this effect. However, this discrepancy between the theoretical and experimental curves was not investigated because the prime concern of this part of the programme was the examination of the linearity of the emf - temperature relationship and, more importantly, the reproducibility of the data on a cell-to-cell basis.

It has been reported that ferrous oxide penetrates zirconia electrolytes at temperatures greater than 1050°C, but that this penetration does not interfere with the cell emf even at temperatures up to 1250°C[48]. In general, this was found to be true in the present work, however, in some cases a curve of the form shown in Figure 54 was obtained. The deviation of the slope and intercept on the heating cycle between 900 and 950°C may be the result of a reaction occurring between the ZrO_2 and the FeO resulting in a compound formation and hence mixed potentials. In addition to these anomolous results, an unacceptable scatter in the data was also obtained on a cell-to-cell basis (Appendix K), resulting in a correlation coefficient of only 0.90 (Figure 55). Consequently, all subsequent data were

obtained using only Ni-NiO and Co-CoO reference electrodes because, unlike the Fe-FeO based cells, only a simple linear relationship between emf and temperature was observed on both the heating and cooling cycles (c.f. Figure 54) and no degredation of the PSZ electrolyte was observed at temperatures up to 1200°C.

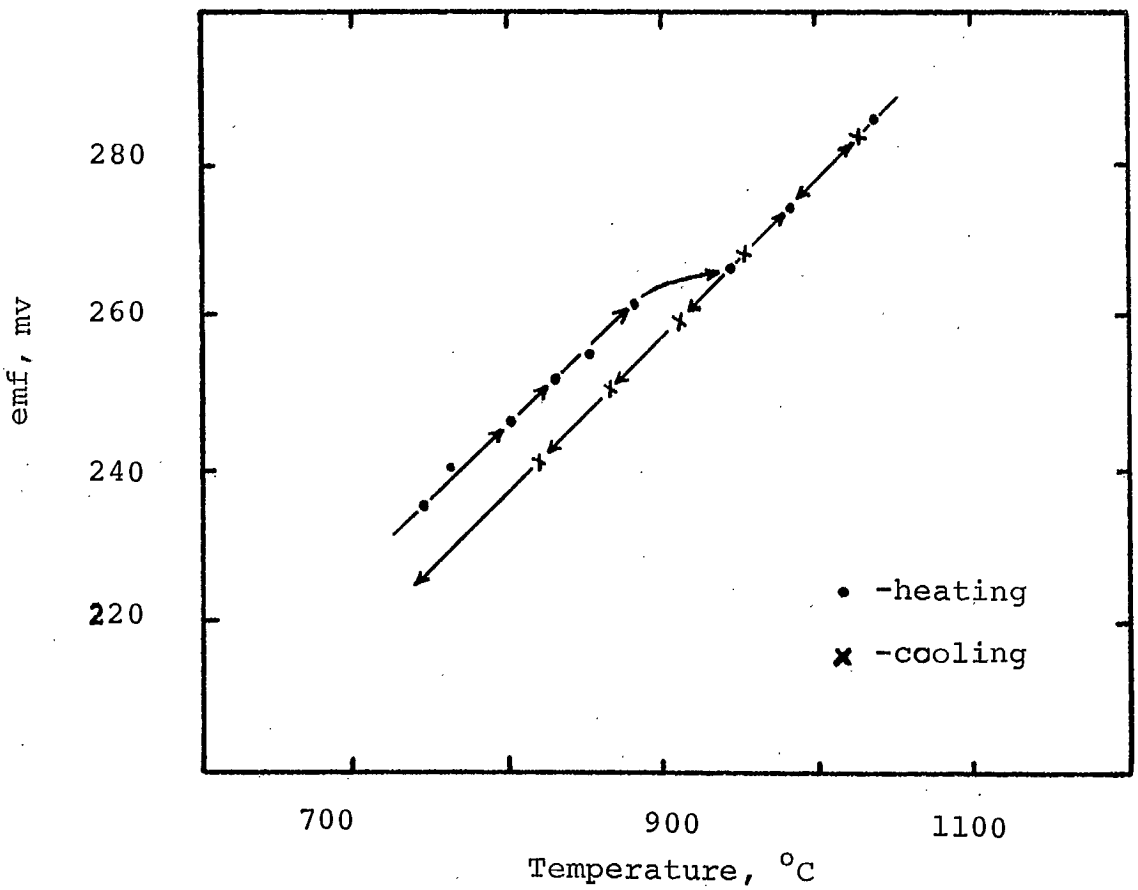

Figure 54. Typical emf versus temperature data obtained with some of the concentration cells which employed Fe-FeO and Ni-NiO reference electrodes and PSZ electrolyte.

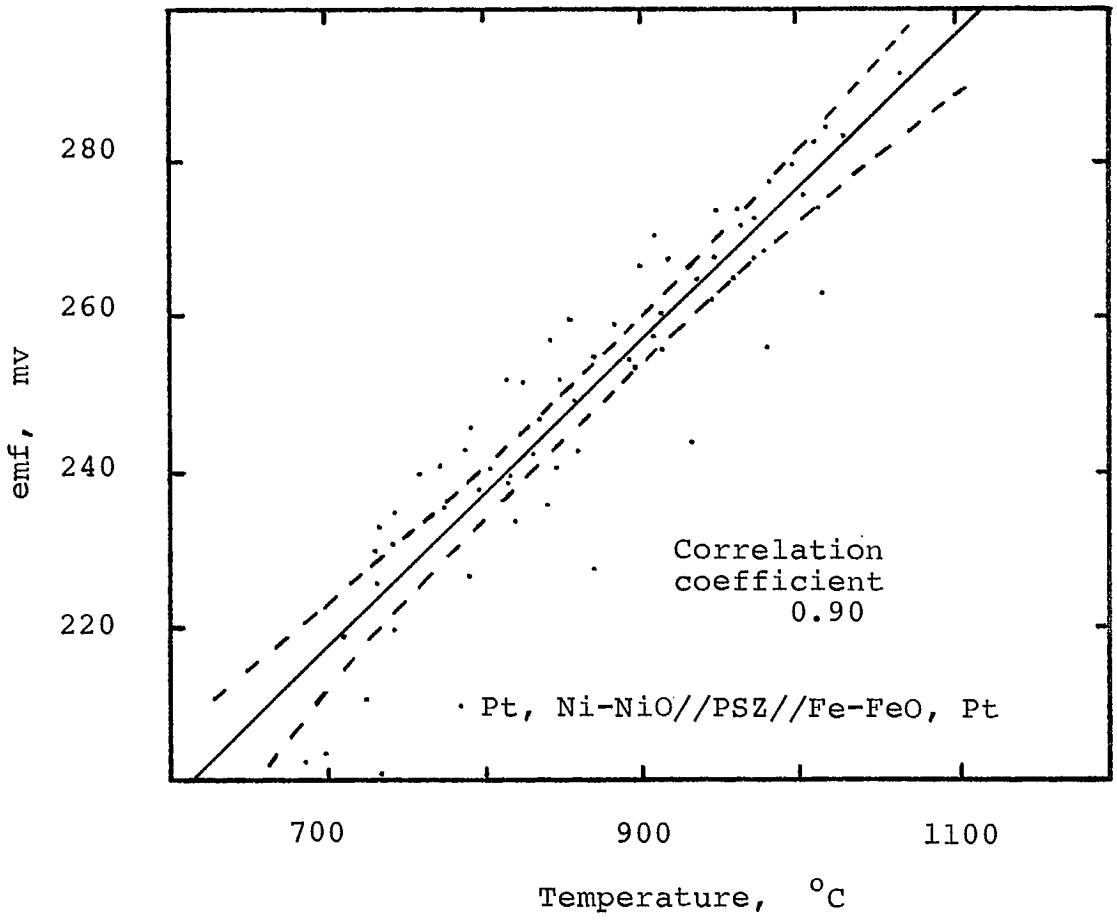

Figure 55. Emf versus temperature data for all the Fe - Ni concentration cells examined, together with the line of best fit and the 95% confidence band.

The data for the Co - Ni concentration cells are shown in Figure 56 and given in Appendix K. It can be seen that the substitution of the Co-CoO for the Fe-FeO electrodes results in a much smaller scatter in the data, such that the correlation coefficient is increased to 0.98. This improvement in the data further suggests that there was probably some interaction between the Fe-FeO electrode and the PSZ in the results of Figure 55.

It should be noted that the scatter in the above data is probably as much due to the variability in the reference

electrodes as it is due to the variability of the electrolyte samples under test. In many cases, data were obtained which exhibited a non-linear relationship between the emf and temperature; in some tests, this deviation from the theoretical curve was so marked that the line of best fit was parabolic with the minimum value of emf occurring at some intermediate temperature. However, in every case, the basic linear relationship was restored by replacing the reference electrodes. In none of the experiments could the non-linearity be related to the PSZ electrolyte itself.

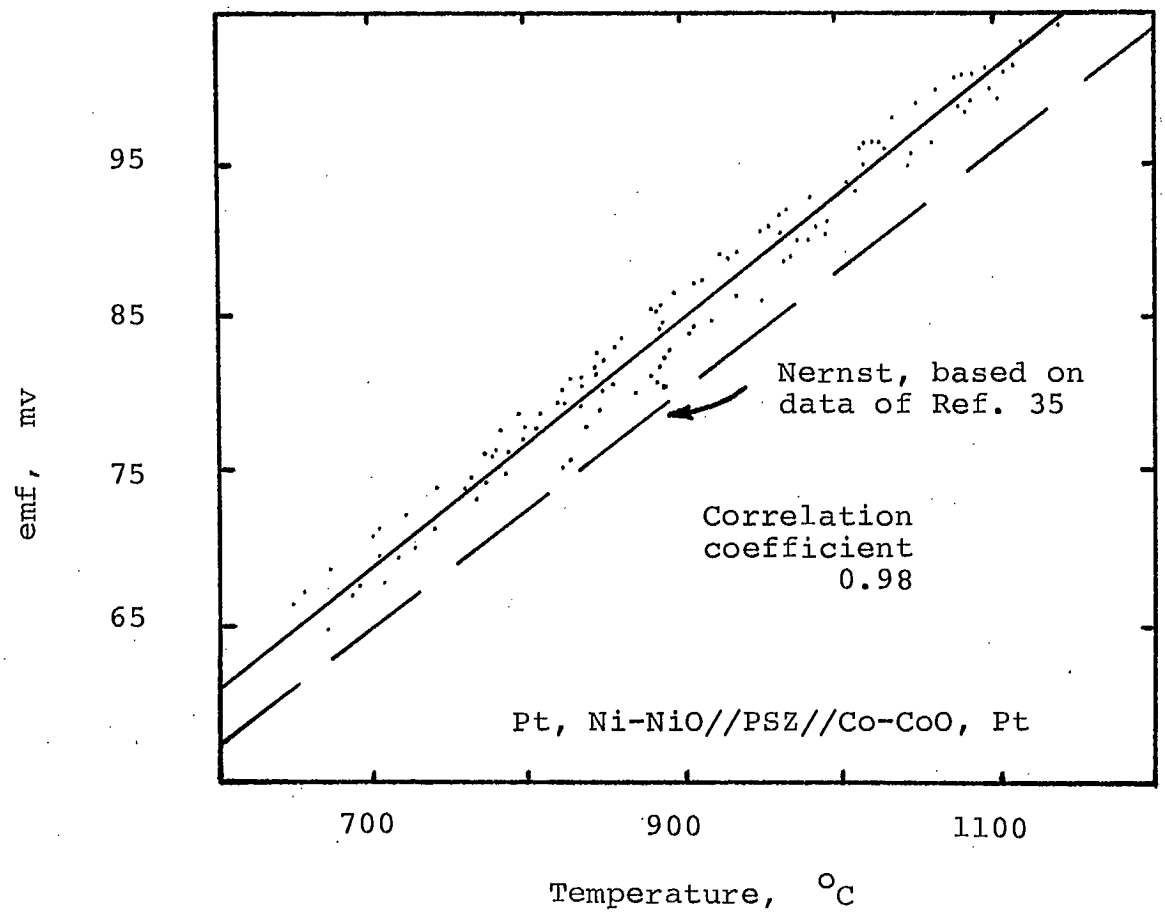

Figure 56. Emf versus temperature data for all the Co - Ni concentration cells examined, together with the line of best fit. The very small 95% confidence band is omitted from this figure in order to retain clarity.

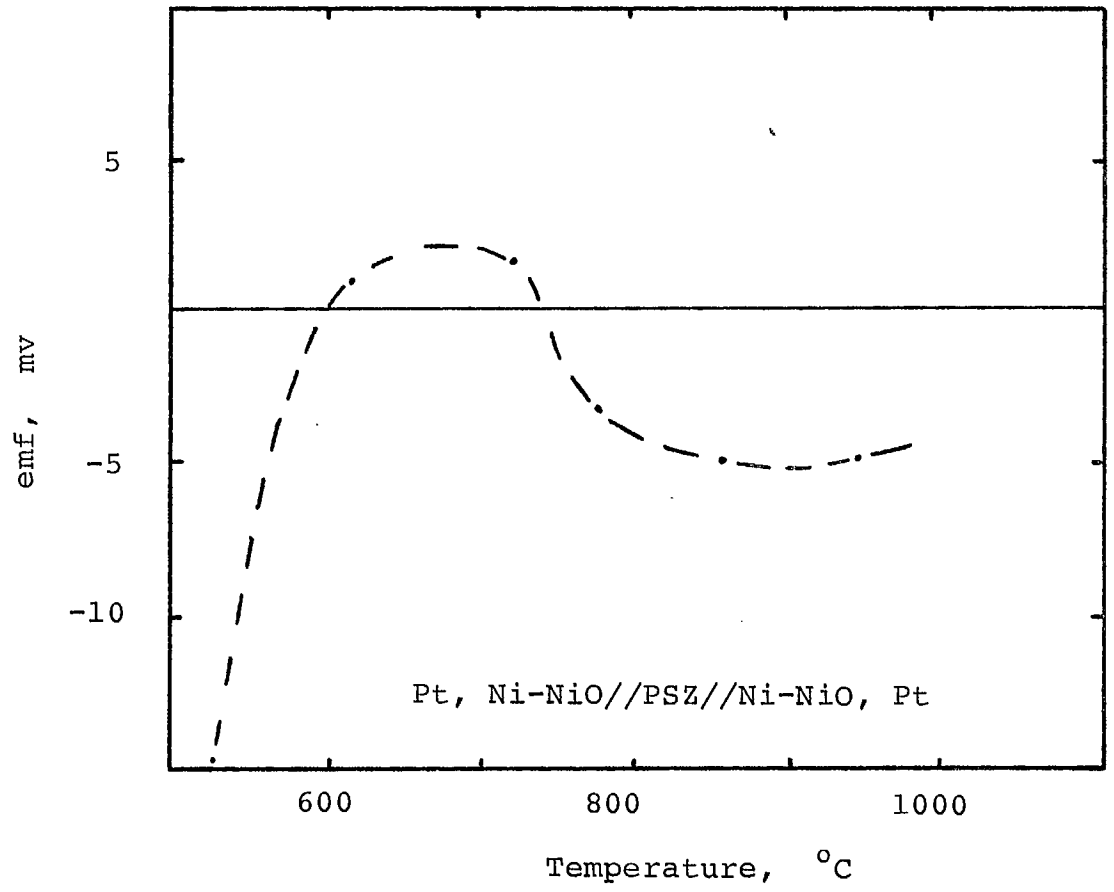

Figure 57. Emf versus temperature characteristics of a concentration cell formed between two Ni-NiO half-cells.

This lack of reproducibility between the individual reference electrodes was demonstrated by connecting two Ni-NiO half-cells in opposition and recording the emf output as a function of temperature. Assuming the two electrodes were indistinguishable, then there would be no oxygen gradient across the electrolyte and hence no emf output irrespective of the temperature. The data obtained from a cell of this type is shown in Figure 57 and demonstrates that an error of typically 4 mv may be obtained from a cell composed of supposedly two similar Ni-NiO

half-cells that had been prepared from the same batch of material and fired in the same furnace charge. Consequently, it is probable that most of the scatter in the results of Figures 55 and 56 arises from variations in the reference electrode materials rather than the electrolyte itself.

Despite this particular difficulty in the laboratory testing of the zirconia, it appeared probable that the electrolyte would be suitable for use in an oxygen probe assembly and would possibly allow the standard deviation of the output to be less than the originally specified maximum of 8 mv in one volt on a cell-to-cell basis when operated in liquid steel at 1600°C. Consequently, having established the behaviour of PSZ under the closely controlled conditions of laboratory testing, it was necessary to conduct a series of field trials under steel-making conditions in order to prove the system and to allow an estimate to be made of the intrinsic scatter (due to the electrolyte and reference electrodes) and extrinsic scatter (due to the noisy electrical environment of a steel plant) in the data. This pilot-plant testing of complete oxygen probe assemblies is discussed in Part III of this report.

PART III

PRODUCTION AND FIELD TRIALS OF OXYGEN PROBE ASSEMBLIES

The purpose of this final stage of the programme was (a) to prepare a 500 g batch of partially stabilized zirconia and to produce sufficient probe assemblies for pilot-plant testing, and (b) to determine the limits of the more important processing parameters. The first objective was met by preparing a batch of material having optimum properties and that was suitable for processing into cell membranes. Following the fabrication and firing stages, the membranes were incorporated into probes and tested under steel-making conditions. This procedure allowed the electrical properties of the complete assembly to be determined under operating conditions and the results could be compared with the data produced under laboratory conditions.

The second objective required an examination of the more important parameters in the precipitation and fabrication stages to determine the latitude which may be taken in the various processing steps by a commercial production facility without significantly compromising the properties of the final product. For example, referring to the flow sheet of Figure 1, is it necessary to hold the pH during the initial precipitation of the $Zr(OH)_4$ to the limits 6.5 to 7.0? Is there any relationship between the floc size of the precipitate and the concentration of the reactants - does a changing size have any effect on the sintering of the product and hence the operation of the probe assembly? These and other questions were answered by preparing six batches of

material, designated A to F, each of which was initially processed in a different way, however, the final fabrication and firing stages were the same for all six materials.

The various papameters that were examined concerned either the precipitation and washing stages or the drying stage. During precipitation, the floc size may be significantly altered by a change in pH. For example, a well dispersed suspension at pH 5 becomes fully flocculated at pH 8. A smaller floc size is also developed if the $ZrOCl_2$ and NH_4OH reactants are first diluted prior to mixing and precipitating the $Zr(OH)_4$. Although the dried zirconia powders were all ball-milled for an hour to disperse the binder and lubricant necessary for the fabrication stage, this process was unable to eliminate the floc size differences which were dictated by either pH or concentration effects. These differences were sufficient to significantly alter the sintering characteristics of the dried product.

A variable which could be of significance to the properties of the final product is the degree of washing used to free the precipitate of Cl^- and NH_4^+ ions. If the precipitate were not washed at all, then NH_4Cl would be retained throughout all the subsequent processing. In an undoped material, where the mole ratio of NH_4Cl to ZrO_2 is 1:1, it can be shown that a body compacted to 50% porosity will have a solid volume composed of 32.1% NH_4Cl and 17.9% ZrO_2. On firing, the NH_4Cl sublimes from the material at 337°C which would then leave a compact having a porosity of approximately 82%. Such a very porous green structure would not be expected to fire to high density. On the other hand,

if the NH_4Cl were completely removed the compact would retain its original porosity of 50% and should sinter to a much higher density. It can be appreciated, therefore, that the concentration of NH_4Cl remaining in the final powder could be the critical factor that controls the development, or otherwise, of an impermeable sintered material.

The final variable that was examined, and which is known to significantly affect the characteristics of a powder, was the method of drying. Although feasibility studies have shown that ceramic materials may be freeze-dried commercially for a cost of 60¢/lb[50], this process is still not used in the ceramic industry. More importantly, none of the engineering organizations offer a service for freeze-drying customers' materials - whereas it is possible to have ceramic slurries spray-dried on a contract basis. Because of the relatively high capital investment of $250,000 necessary to develop a freeze-drying facility, it was clear that the fairly common method of spray drying should be examined as the commercially acceptable drying technique. Consequently, some of the materials were spray-dried rather than freeze-dried in order to assess how the markedly different agglomerate morphology developed by these two drying techniques would influence the sintering characteristics and hence the performance of the final product. A summary of these basic processing variables is given in Table 1.

TABLE 1

Processing Variables Examined During the Preparation of Batches A to F

Batch	pH[a]	Mix & then Dilute	Low in Cl^-	Dilute & then Mix	High in Cl^-	Spray-Freeze & Freeze-Dry	Spray-Dry
A	6.80	*	*			*	
B	7.80	*	*			*	
C	6.02		*	*			*
D	7.99		*	*		*	
E	6.67			*	*	*	
F	6.67			*	*		*

a - pH of slurry after washing stage and prior to drying.

From the Table, it can be seen that differences in the products made from Batches A and B could be related to the variation in pH at the completion of the washing stage. Comparison of C with D would show the difference between spray-dried and freeze-dried materials at low chloride concentrations, whereas comparison of E and F would show any differences at high chloride concentrations. D and E allow comparison to be made between freeze-dried materials having low and high chloride concentrations respectively, whereas C and F compare the properties of spray-dried materials also having low and high chloride concentrations.

Preparation of Batches A to F

(a) Batches A and B

These two batches were prepared using the same quantity and concentration of reactants as given in the Experimental Procedure section of this report. However, the precipitate of Batch A was washed sixteen times whereas that of Batch B was washed thirty times so that at the completion of washing the stirred slurry of A had a pH of 6.80 and a $[Cl^-]$ of 3 ppm while that of B had a pH of 7.80 and a $[Cl^-]$ of 4 ppm. Subsequently, the two batches were doped with calcium formate and freeze dried to produce the basic raw material.

(b) Batches C and D

The same basic procedure was used as for A and B above, but in this case, the reactants were further diluted prior to mixing and precipitating $Zr(OH)_4$. It was anticipated that the dilution would lead to a smaller floc size of the precipitate

and this might affect the fired microstructure of the finished product. Consequently, 1.5 litres of stock $ZrOCl_2$ solution (301.15 g ZrO_2/litre $ZrOCl_2$) was diluted with 10 litres of distilled water prior to slowly adding to the 600 ml of NH_4OH which had also been diluted with 10 litres of distilled water. The equipment was washed down with an additional 2.9 litres of distilled water to bring the total volume to 25 litres. After washing both batches a total of seventeen times, the pH of Slurry C was 6.02 and the [Cl^-] was 4 ppm, whereas the pH of Slurry D was 7.99 and the [Cl^-] was 5 ppm. After doping with calcium formate, the washed precipitate of Batch D was finally freeze-dried while that of Batch C was spray-dried using a Nerco-Niro drier operated with an inlet temperature of 250°C and an outlet temperature of 125°C.

(c) Batches E and F

The same initial procedure was followed as for C and D above in which the reactants were diluted prior to mixing and forming the $Zr(OH)_4$ precipitate. However, these two batches were initially formed as one, which was washed once and stirred vigorously prior to splitting into the two Batches E and F which had a pH of 6.67 and a [Cl^-] of 3200 ppm. After the doping stage, Batch E was freeze dried while Batch F was spray-dried.

Characterization of Batches A to F

Despite some major changes in the preparation of the freeze-dried materials: A, B, D and E, they were all bulky and nearly free flowing. On the other hand, the spray-dried materials:

C and F tended to 'set' in a container if left to stand undisturbed for more than a day. This behaviour was most noticeable in F which contained a relatively high concentration of NH_4Cl. This division of the materials into two groups dependent of the method of drying was further substantiated by the tap density data which showed that the spray-dried materials were at least three times more dense than the freeze-dried materials (Appendix L). The difference in density between the washed (C) and unwashed (F) spray-dried materials was due to the different composition of the dried powders. In C, only doped zirconia was present whereas in F, NH_4Cl was also present. Although all the materials at this stage are completely amorphous, the presence of a considerable quantity of NH_4Cl (single crystal density 1.527 g/cc) would be expected to lower the tap density of the much denser zirconia (single-crystal density 6.069 g/cc when stabilized with 7.6 mole % CaO).

The difference between the washed and unwashed materials was demonstrated by the loss-on-ignition data (Appendix L). The loss on ignition for the washed materials (A, B, C and D) was in the range of approximately 13% to 24% on heating to 1000°C. This contrasts with the much higher loss of between 36% and 39% for the high chloride unwashed materials E and F.

The compositional differences between E and F and the remainder was also shown by the concentration of chloride that was released into solution when a powder sample was reslurried in distilled water. In general, the washed and dried Samples A to D contained a Cl^- concentration of just over 1 wt % whereas

the unwashed batches contained over 20 wt % chloride (Appendix L). This same trend was also exhibited by the divalent ions (principally Ca^{2+}, ZrO^{2+}, and $ZrCl_2{}^{2+}$) present in the materials. The approximately one order of magnitude greater concentration of M^{2+} ions in Batches E and F is due to the residual ZrO^{2+} and $ZrCl_2{}^{2+}$ ions, whereas the data for Batches A to D (page 21 and Appendix C) indicate the presence of essentially Ca^{2+} alone. Calcination of these materials results in a lowering of both the Cl^- and divalent ion concentrations, which is due to the volatilization of NH_4Cl at low temperature (337°C) followed by the subsequent decomposition of the calcium formate dopant and the rapid entry of the calcia into solid solution with the zirconia.

The great discrepancy between the concentration of Cl^- remaining in the liquor over a fully washed material and that recovered into solution on reslurrying the dried powder is difficult to understand. It was shown earlier in Figure 3 that the $[Cl^-]$ of the slurry is always greater than that of the liquor and further that the addition of NH_4OH would always greatly increase the $[Cl^-]$ of both the slurry and liquor. These and other observations lead to the conclusion that the Cl^- ion is strongly adsorbed onto the surface of the precipitate even at the completion of washing when the $[Cl^-]$ is reduced to a few ppm in the liquor. The fact that reslurrying the dried powder produces a solution rich in Cl^- under conditions where the concentration ratio of $OH^-:Cl^-$ is approximately 20,000:1 indicates that the materials have aged, i.e., the drying process (either

spray-drying or freeze-drying) drastically alters the energetics of the adsorption sites on the surface of the precipitate. Unfortunately, it was not possible to follow this drastic change using infrared spectroscopy as the spectra of all the as-prepared materials were essentially featureless (Figure 13). This retention of a relatively high Cl^- concentration of approximately 1 wt % at the completion of the washing process further explains the failure of earlier experiments to measure the amount of Cl^- which could be re-adsorbed onto the precipitate surface (page 20).

The particle size distribution of all the materials was monitored throughout the various processing stages. In general, all the materials had the same distribution at each stage and consequently only the changes produced by a particular process are shown in Figure 58. As expected, the size distribution of the as-precipitated slurry was quite wide and typically had a mean particle size (m) of 8 μm and a standard deviation (s) of 2.6 μm (Curve A, Figure 58). After drying and calcining to form the partially stabilized material, the zirconia was ball-milled for 1 hour in methanol to disperse the pressing aids: Gelva V-7 and Carbowax 400, which were added (Curve B, Figure 58). The size distribution developed after milling in alcohol was much narrower (s = 1.2 μm) and the mean size was significantly reduced (m = 2.8 μm). Following the final spray-drying of the alcohol slurry and the development of small spheres of plasticized material, the distribution remained narrow (s = 1.2 μm) but the mean size was increased to 8 μm (Curve C, Figure 58).

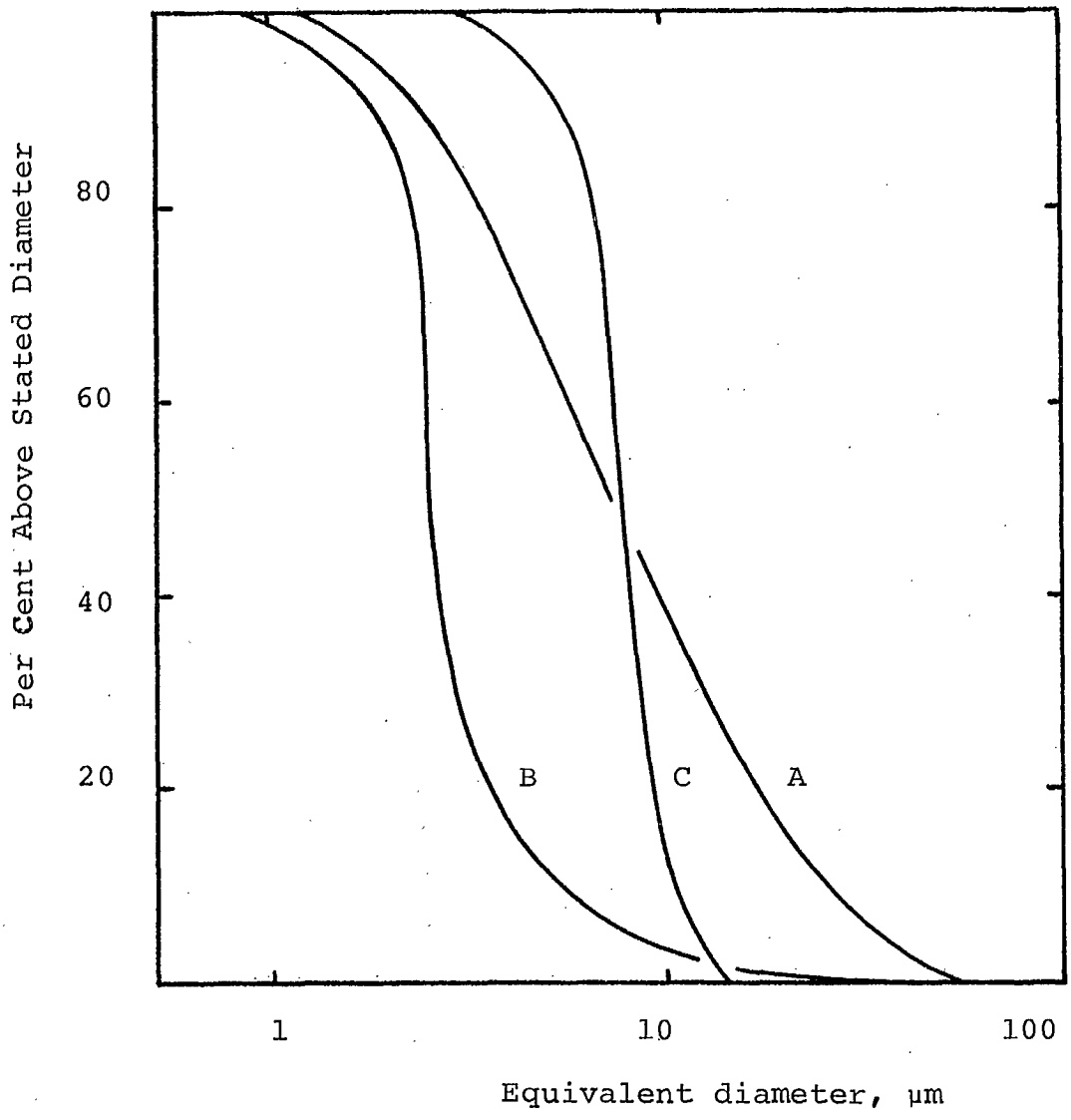

Figure 58. General particle size distribution curves for Materials A to F.

A. As-prepared $Zr(OH)_4$ precipitate
B. Dried precipitate ball-milled 1 hour in alcohol
C. Spray-dried slurry from B

In order to develop a surface area of approximately 20 m^2/g it was clear that the different batches would have to be calcined at approximately 1000°C for 1 hour (Figure 17). However, to guard against the possibility that the different batches of

material had different calcination characteristics and did not conform to the data presented in Figure 17, a series of calcinations was made and the surface areas were determined in order to locate the plateau for each material at approximately 1000°C (Appendix L). From this preliminary data it was decided to calcine the batches in air for 1 hour at 935°C (Batches E and F), 975°C (Batches B and C) and 1000°C (Batches A and D) in an attempt to develop a surface area of 20 m^2/g in every batch. However, as shown in the data of Appendix L, the area developed on calcination of the main batches did not always agree with the predicted value and values ranging from 15 m^2/g (F) to 26 m^2/g (B) were obtained.

As a check on the impurity pick-up which could occur after the precipitation stage, a series of samples was analysed for a wide range of elements. Comparison of the analyses for the undoped material with those for the various doped samples shows that the doping, drying, calcining, ball-milling and final spray-drying operations do not significantly alter the concentration of the major impurities: Mg, Si and Cu, nor do they raise the concentration of another 30 elements sufficiently for their spectrographic detection (Appendix L). The importance of using zirconia raw materials having a low Si content has been discussed earlier on page 129.

Characterization of Sintered Materials A to F

Because of the different methods of preparation of the six batches of raw material it was anticipated that quite different

microstructures would be developed during the final firing process. Consequently, a large quantity of oxygen-probe membranes was frabricated from the six raw materials and the green and fired densities and microstructures of selected samples were examined prior to the remainder being assembled into complete probes and tested under steel-making conditions.

The density data confirmed the earlier results that the highest green density does not necessarily produce the highest fired density. All the membranes were formed under a pressure of 10 ksi and the green densities ranged from a low of 1.77 g/cc for B to a high of 2.63 g/cc for F. However, on firing in air to 1500°C with no soak, the difference between the spray-dried and freeze-dried materials became apparent: the spray-dried materials had considerably lower fired densities, especially when the original material had been unwashed and contained a considerable quantity of NH_4Cl. The data, given in Appendix M, show that the freeze-dried materials develop a relative density between 90 and 95% on firing to 1500°C whereas the spray-dried Materials C and F are between 70% and 80% under the same conditions. For reasons, which are discussed later under Failure Analysis of Zirconia Membranes section (page 167), the spray-dried materials were subsequently fired in air to 1600°C for 1 hour and under these conditions the fired density of C was increased to approximately 5.7 g/cc, i.e., the density was comparable to that of the freeze-dried materials fired at 1500°C, whereas F was increased to only 5.4 g/cc (Appendix M).

These considerable differences between the relative

densities of the fired materials were reflected in their differing microstructures. Samples were sectioned and polished along their longitudinal axis so that they could be examined perpendicular to the pressing direction and any variations in the porosity distribution (due to die-wall effects) could be seen. However, no such effects were observed in any of the materials, which indicates the effectiveness of the Carbowax lubricant added to the six different materials.

Typical microstructures developed in each material after fabricating under 10 ksi and subsequently firing in air to 1500°C without any soaking period are shown in Figures 59 to 61. The random distribution of fine porosity is seen in the dense materials produced using freeze-dried materials. Comparison of the microstructures of Materials A, B and D with that of C shows that a much more porous product results from the use of spray-dried powders. This porosity is further increased if the NH_4Cl is not removed from the precipitate during the washing stages, as shown in F.

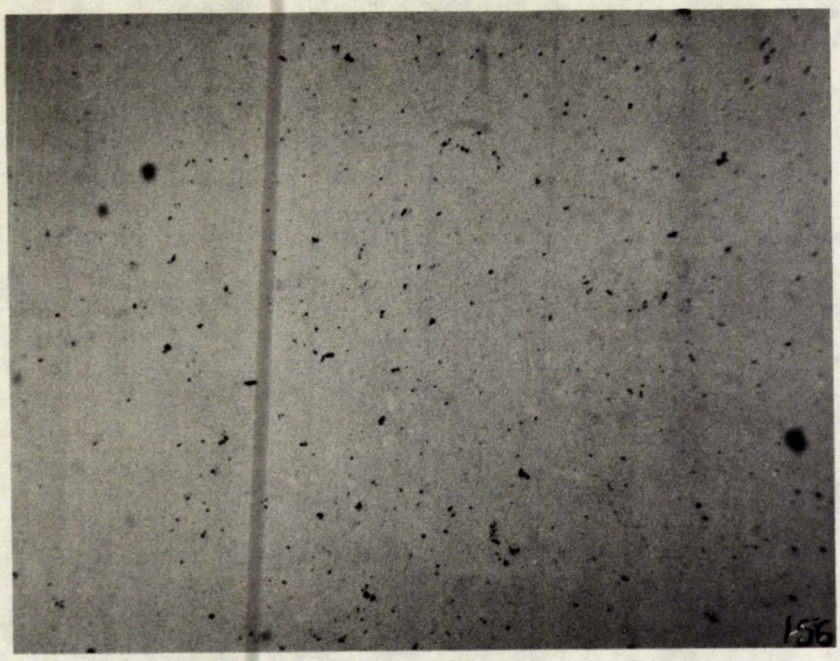

(a) 400 μm

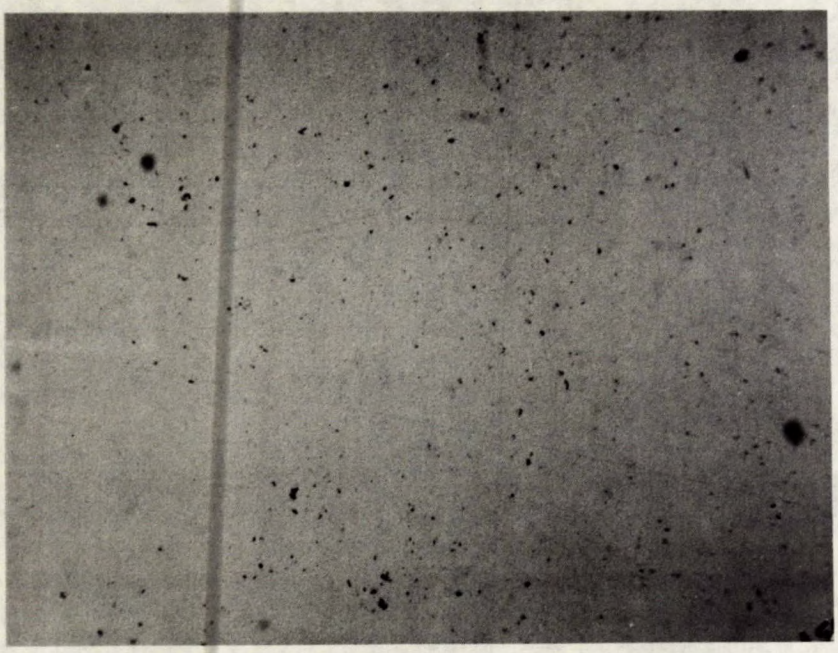

(b) 400 μm

Figure 59. Polished surface of PSZ after firing to 1500°C in air without any soaking period.

(a) Material A
(b) Material B

(a) 400 μm

(b) 400 μm

Figure 60. Polished surface of PSZ after firing to 1500°C in air without any soaking period.

(a) Material C
(b) Material D

(a) 400 μm

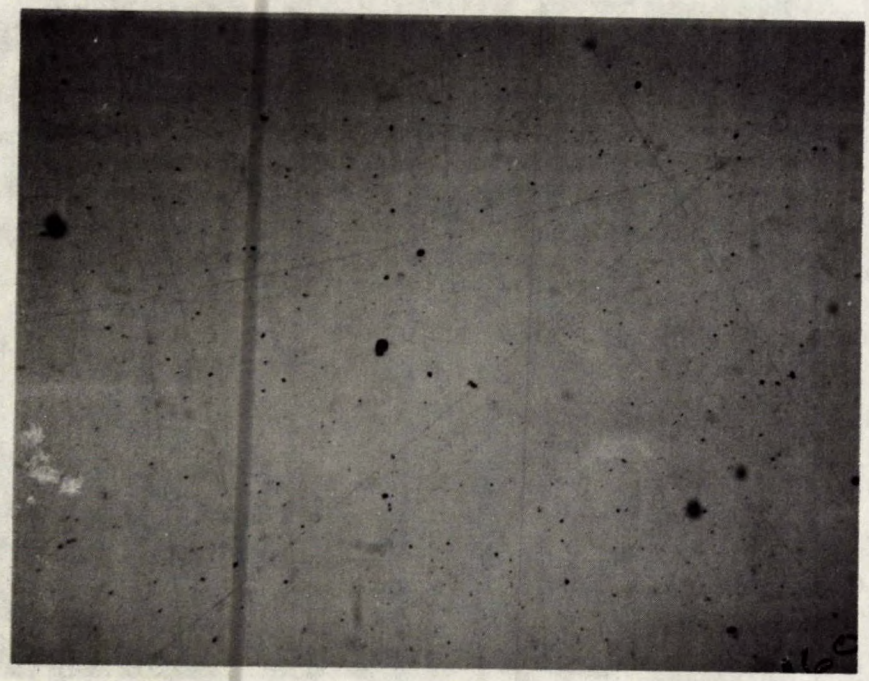

(b) 400 μm

Figure 61. Polished surface of PSZ after firing to 1500°C in air without any soaking period.

(a) Material E
(b) Material F

The detailed differences between the microstructures of the six materials are more clearly seen in the SEM micrographs of the fractured surfaces (Figure 62). In general, the freeze-dried materials have a much finer microstructure than their spray-dried counterparts. In addition, it can be seen that Materials A and B tend to develop a bimodal grain-size distribution whereas D and E appear to have a uniform grain size. No reason for this slight difference between the microstructures of these two groups of freeze-dried materials can be given - other than the possibility that the result is due to sampling and further examination of other surfaces would show that the four freeze-dried microstructures are in fact indistinguishable. It should be noted that because this bimodal distribution is observed on a fracture surface it is a genuine effect rather than a relic of a high-temperature state as discussed on page 117.

The SEM micrographs also show not only the considerable porosity present in the spray-dried materials but also the differences between the two Materials C and F. For example, F is essentially unsintered and shows only the development of very limited neck growth whereas C shows much more extensive neck growth such that the form of the spheres is essentially eliminated. Close examination of the microstructure of C and F also shows the development of a grain structure on the surface of the spheres, i.e., intra-agglomerate sintering is occurring well before any inter-agglomerate sintering.

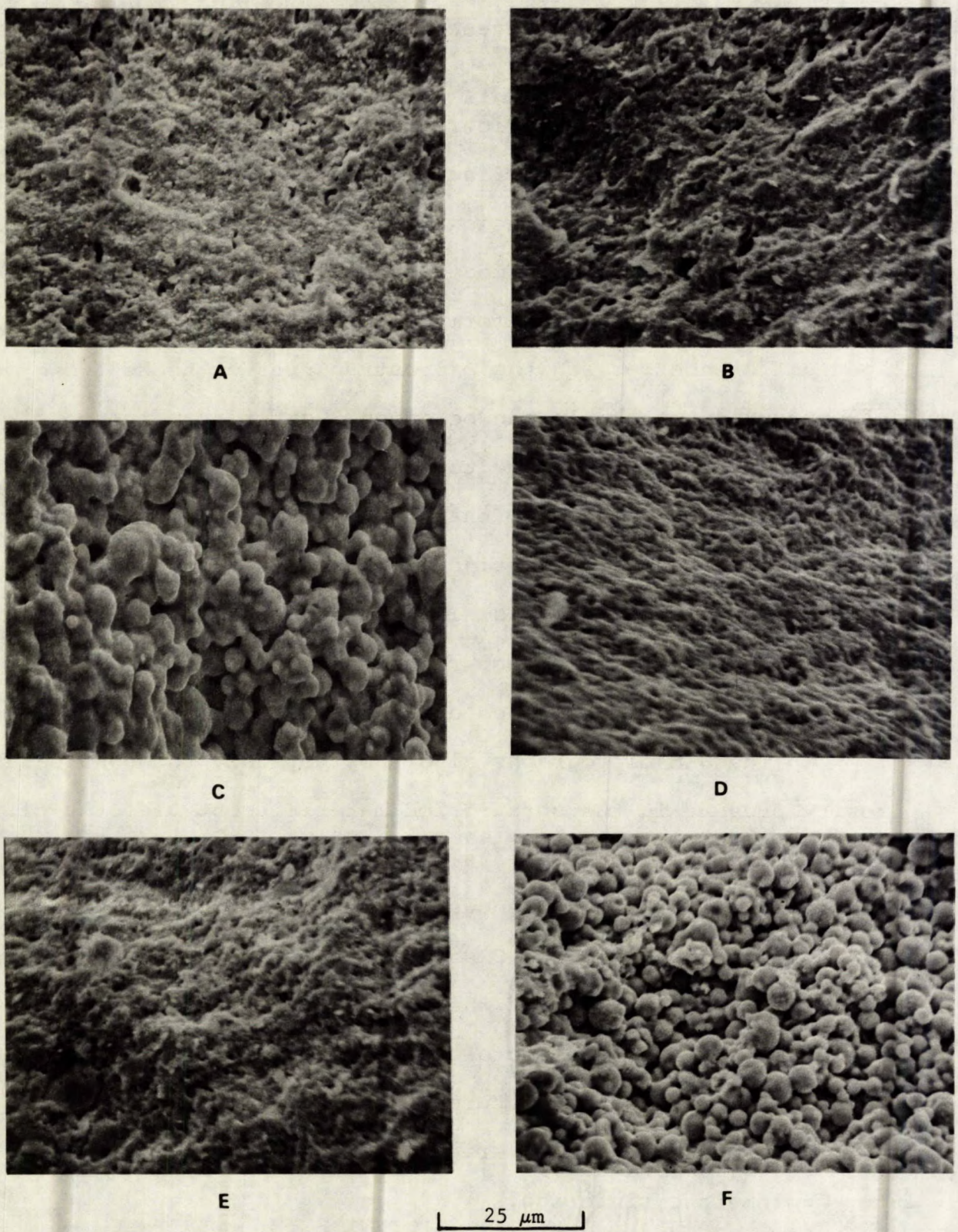

Figure 62. SEM micrographs of the fracture surfaces of Materials A to F after firing to 1500°C in air with no soaking period.

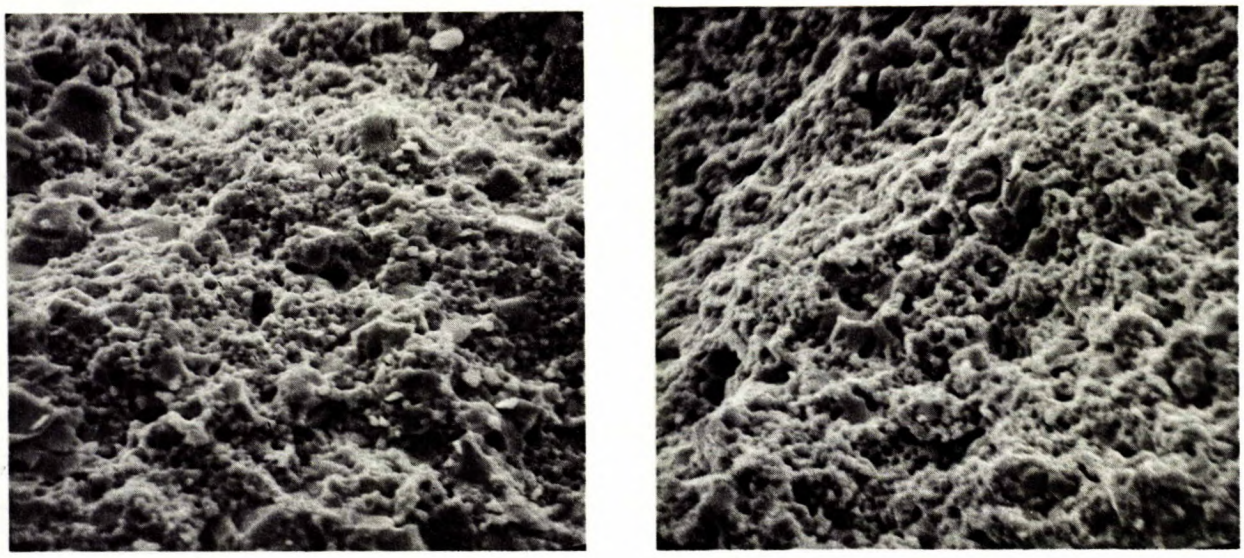

C F

25 μm

Figure 63. SEM micrographs of the fracture surfaces of Materials C and F after firing to 1600°C in air for 1 hour.

A considerable change in the microstructure of Materials C and F is developed on firing to 1600°C and soaking at that temperature for one hour (Figure 63). Discontinuous grain growth occurs in both materials resulting in the development of a bimodal grain size distribution. Comparison with the micrographs of material fired at 1500°C shows that a considerable reduction in the amount of open porosity occurs at the higher firing temperature. However, despite this extensive densification, which occurs between 1500 and 1600°C, F still has a lower relative density than C.

Pilot-Plant Trials of Oxygen Probe Assemblies

After firing, the zirconia membranes are small cylinders having a diameter of approximately 0.1-in. and a length of 0.25-in. A small hole measuring approximately 0.018-in. in diameter and 0.018-in in depth (depending on the firing shrinkage) is centrally situated at one end and this acts as the site for a platinum bead of the reference electrode. The actual assembly of the zirconia into complete oxygen probes was conducted by Quality Hermetics Ltd., Toronto, a division of Leigh Instruments Ltd. In essence, the zirconia is flame sealed into the end of a Vycor tube and the bead of the platinum reference electrode is force fitted into the small hole in the zirconia prior to the Vycor being cemented into a steatite plug (Figure 64). Subsequently, an annulus of material (which on decomposition produces a known P_{O_2} at a given temperature) and a gas vent (which ensures that the reference gas mixture passes over the platinum electrode-zirconia junction) are inserted into the Vycor and cemented in place. The Pt wire is connected to a metal ring which acts as one of the main contacts linking the disposable cell assembly to a long lance for use in a steel-making furnace. The other contact necessary for an emf readout is formed by sliding wipers that connect to a thin-walled steel tube into which the steatite plug is cemented. This tube, which is approximately 4 ft long in the industrial probe assemblies, is finally covered with a layer of fibrous thermal insulation.

In use, the probe is inserted into the molten steel. A sacrificial cover prevents the probe itself from contacting

the slag layer which would otherwise give rise to mixed potentials and an unreliable emf output. Within a few seconds, the cover (not shown in Figure 64) melts away and exposes the zirconia to the steel. This generates a considerable thermal gradient down the length of the zirconia and consequently a considerable thermoelectric potential is developed (between 0.7 and 0.8 volts). After approximately 6 seconds, the system achieves a uniform temperature and the thermoelectric potential is reduced to zero. However, during this short interval, the oxygen concentration gradient across the zirconia has been increasing as the annulus material starts to decompose and establish a reference P_{O_2} adjacent to the platinum bead. Consequently, a progressively increasing electrochemical potential is established which eventually becomes stable after approximately 5 seconds. The overall effect of these two sources of potential is shown in Figure 65, in which it can be seen that the cell output first rises to a maximum after approximately 1 second; thereafter it decreases to the final equilibrium value after a total of 6 seconds.

Because of the wide range of emf developed by the cell and the need to measure the output to the nearest millivolt in the range 0.75 volts to 1.25 volts, it is convenient to use a 0.75-volt 'bucking' voltage to oppose the cell output. This allows a 500 mv full-scale chart recorder to monitor all voltages between 0.75 volts and 1.25 volts with a resolution of one millivolt. As an additional convenience, a trigger is also used which detects the initial development of the cell emf and after a given period sounds a horn to inform the operator that the probe should be removed from the melt.

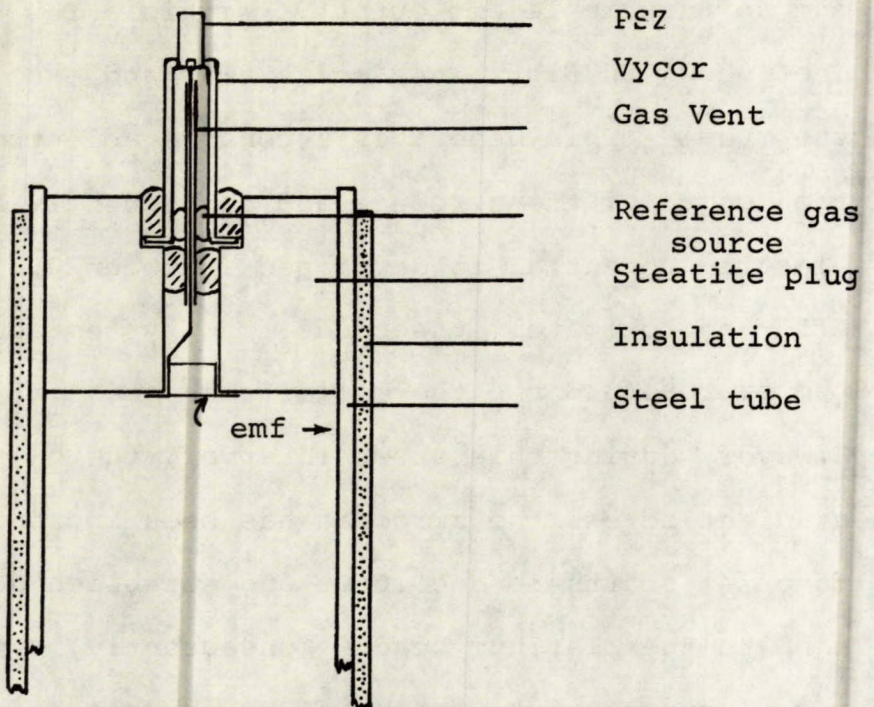

(a) Schematic of Oxygen Cell

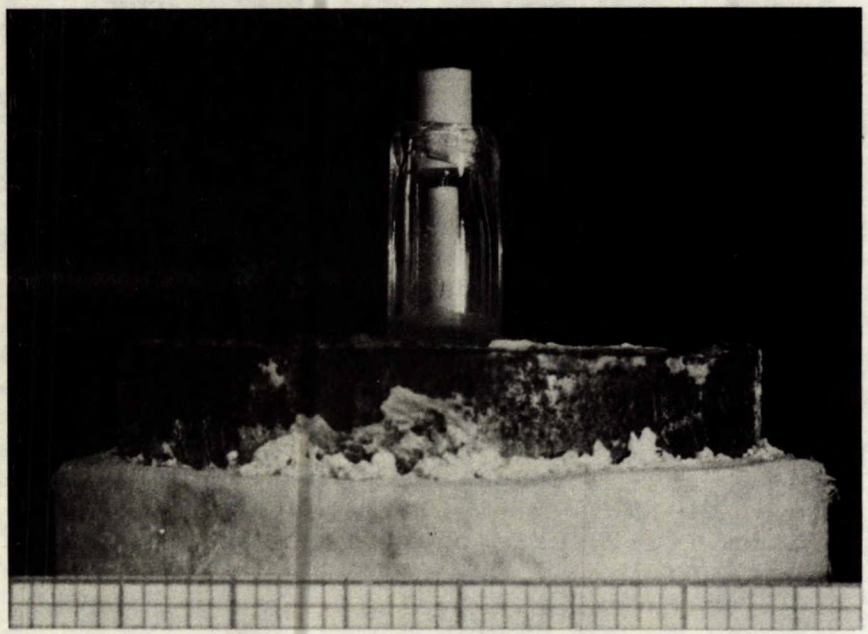

(b) Oxygen Probe Assembly with metric scale below - each small square represents one millimeter.

Figure 64. Detail of cell arrangement used in probes fabricated from PSZ produced in the present work.

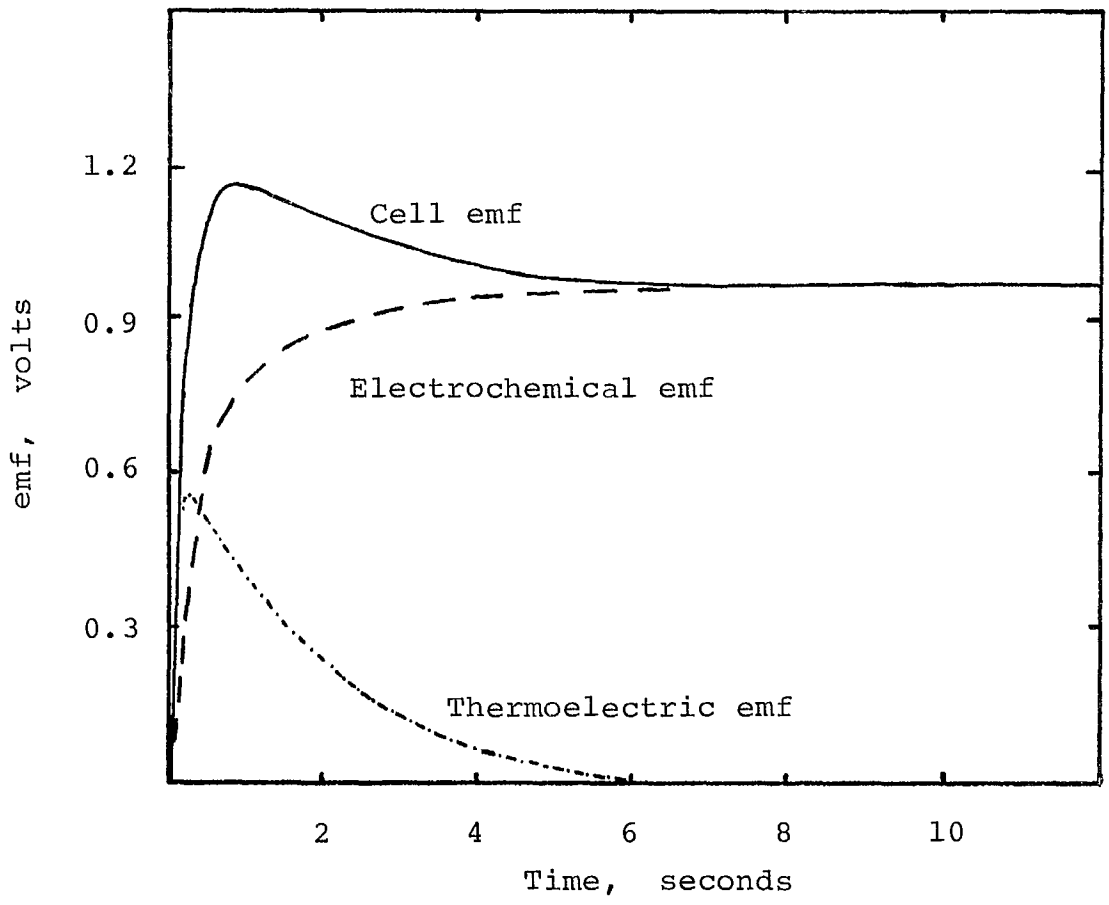

Figure 65. Typical oxygen probe output due to the combined effects of the thermoelectric and electrochemical potentials developed after insertion of the cell into liquid steel.

The actual testing of the probes was conducted by members of the Physical Metallurgy Research Laboratories of CANMET under the direct supervision of Mr. C.S. Monier-Williams, P. Eng., of Quality Hermetics Ltd., Components Division, Leigh Instruments Ltd., the only supplier of commercially available Canadian-made zirconia probes. The probes were tested in a 100-lb induction furnace operated at approximately 1600°C. The furnace was charged with a Stelco billet and 1 lb of Fe_2Si to give an oxygen concentration of approximately 50 ppm at that

temperature. The melt was covered with an argon blanket to maintain this oxygen level throughout the testing period. Where practicable, the probes were tested every minute, each probe being held in the steel for a total of 30 seconds to give approximately a 25-second readout.

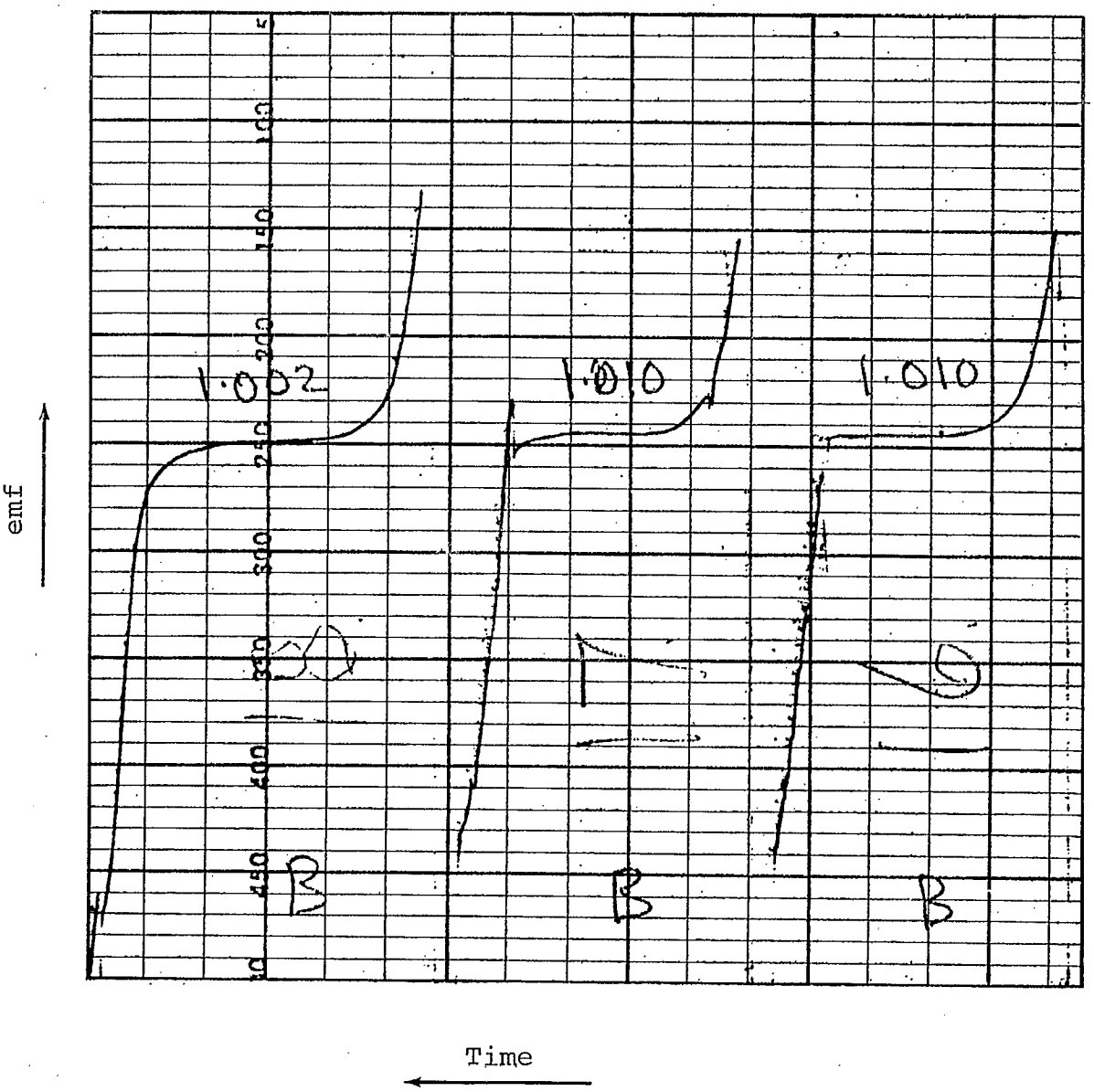

Figure 66. Actual emf-time curves for oxygen probes made from Material B and tested in steel at 1600°C.

Part of the actual results obtained from the first batch of Material B is shown in Figure 66. An ideal emf-time curve for a probe operating under these conditions would be similar to that of Curve 16 in Figure 66, i.e., a stable emf is generated after the initial peak and this emf is constant until the probe is withdrawn from the melt. Curve 17 shows a slight decrease in emf towards the end of the run; this effect is even more pronounced in Curve 18 and is probably due to the premature expiration of the reference gas source and the gradual lowering of the reference P_{O_2}.

A summary of the results obtained from the field trials is given in Appendix N. In general, it would be expected that Materials A, B and D would give satisfactory results as they were fired to a fairly low porosity and had a low concentration of impurities in them, i.e., they should not suffer from steel penetration nor give rise to any mixed potentials. This was found to be the case in practice.

The original assumption that the zirconia membranes must be fired to zero open porosity was shown to be erroneous. In the first batch of membranes tested, C and F had relative densities of 81.8% and 73.0% respectively (Table 1, Appendix M) yet even some of these cells developed a nearly normal signal. The erratic nature of the output in these cases was due to loose platinum beads - see under Failure Analysis of Zirconia Membranes section (page 167). However, despite this unexpected result, the data do show that satisfactory cells can only be fabricated from materials having a relative density >90%.

Comparison of the results from Materials A and E which were precipitated under similar pH conditions (Table 1, page 140) shows that the presence of a high Cl^- concentration does not lead to a deterioration in the performance of the zirconia. Presumably the last traces of Cl^- are lost from the material before it sinters significantly otherwise the membranes made from Material E, which contains nearly 2 wt % Cl^- in the calcined state (Table 4, Appendix L), would not fire to a relative density of 93 to 94% at 1500°C (Tables 3 and 4, Appendix M).

The effect of different pH conditions during the precipitation stage is not clear. On the one hand, Materials A and B do not show any appreciable differences in the scatter of their data and hence it might be concluded that pH is an unimportant parameter in the processing of reliable and consistent probe membranes. On the other hand, comparison of D and E suggests that the much lower standard deviation of the data for D is due to the use of a higher pH during the precipitation stage - if the different Cl^- concentration between D and E is indeed unimportant as suggested above.

It is difficult to believe that a <u>higher</u> pH would lead to the production of superior material because, although it would aid in the washing stage by assisting in the removal of adsorbed ions from the surface of the precipitate (Figure 3), it would also promote the growth of large flocs in solution that would not be broken down in subsequent processing. The stability of these flocs is demonstrated by the fact that the mean particle size of ball-milled material (Figure 58) is approximately two

orders of magnitude greater than that calculated from the surface area (Table 7, Appendix L). Consequently, it can only be suggested that some unknown synergistic effect is operating in favour of D among the three low Cl^- materials which were initially freeze-dried.

Despite the use of a lubricant in the materials, the spray-dried Materials C and F still retained their original spherical agglomerate form after all the fabrication stages (Figure 62) and consequently the membranes fired to 1500°C retained a considerable amount of open porosity. This, in turn, allowed liquid metal to penetrate the membrane and short out the cell. This again indicates the remarkable stability of the agglomerates which are developed during the initial drying process and retained throughout the subsequent wet ball-milling, drying, and pressing operations.

It would be expected that the degree of metal penetration through a membrane would be directly related to the open porosity and that the ratio between the amount of open and closed porosity would be constant for the spray-dried materials fired to the same temperature, i.e., a good correlation would be expected between the amount of penetration and the relative density. In general, this was found to be true. However, it was found that this assumption did not always hold. For example, in the first batch of membranes tested, F had a relative density of 73.0% and in the second Batch C had a density of 73.8%, yet only 14% of the F cells showed any sign of metal penetration whereas all the C cells were penetrated and shorted out. This could be

due to either a change in the amount of open porosity between the two materials despite the development of the same total porosity or, alternatively, it could result from the differences in the amount of adsorbed ions on the surface of the dried precipitate which may significantly alter the contact angle of liquid Fe on the membrane surface and hence effectively control the penetration of the metal. Unfortunately, it was not possible to measure accurately the amount of open porosity developed in these membranes due to their small size and hence the reason for the difference in the performance of high porosity membranes made from C and F could not be determined.

Increasing the firing temperature to 1600°C in the case of Materials C and F considerably increased the final density and dramatically reduced the amount of open porosity. Dye penetration tests showed that the membranes were essentially impervious and the actual testing of oxygen probes made from these higher density membranes failed to show any gross metal penetration typical of the lower density 1500°C membranes. The cell output from these 1600°C membranes was comparable to that from the cells made from the more reactive freeze-dried raw materials. In addition, the standard deviation of data from Cells C and F was comparable to that obtained from the other materials again showing that the presence of a high Cl^- concentration is unimportant to the present application.

Unfortunately, it is not valid to pool the data from the various pilot tests in order to increase the population of one set of data and hence improve the statistics because it was

impossible to guarantee that the same oxygen concentration was being measured in the different steel batches used to test the probes. In addition, the data for the commercial probes show that the observed difference between the sample means (0.013 volts) of data from the first two field trials is approximately five times the standard error of the difference (0.0027 volts) which also indicates that the two groups of data should be treated separately.

It will be recalled that initially each batch of material was to be assessed by fabricating twenty probes and testing them in molten steel. Unfortunately, however, a considerable overall loss was incurred either during the assembly stages or during the actual testing itself such that an average of only seven probes out of the original twenty were shown to be completely satisfactory in the first two pilot-plant tests. There were several reasons for this high failure rate but only one can be directly attributable to the zirconia itself and that was due to insufficient firing of Materials C and F. The remainder were due to defects which were developed in the assembly process itself and which either allowed the cell to short out or to develop an intermittent open circuit during its operation.

Failure Analysis of Zirconia Membranes

One of the most obvious reasons for cell failure was found in the first two batches of Materials C and F, which had an excessive amount of open porosity and allowed the metal to penetrate the pores and short circuit the potential initially

developed across the membrane. Typical cell output waveforms and appearance of the used membranes are shown in Figures 67 and 68. In both cases, the zirconia was ground away to a surface slightly above the lip of the Vycor tube, (Figure 64) so that the platinum electrode would be situated approximately 3 mm below the surface shown. The micrographs show qualitatively the difference in the amount of open porosity developed by these two materials on firing to 1500°C. In addition, the development of a skin of dense material around the edge of each section can be seen. This is due to secondary sintering occurring during both the flame assembly of the membrane into the Vycor and also during the immersion of the probe into the steel during testing. Examination of a longitudinal section through the probes showed that this skin was only developed in the exposed part of the membrane. Consequently, a relatively porous region existed just at the junction of the membrane with the Vycor and this was the region through which a considerable quantity of metal penetrated. As mentioned earlier, increasing the firing temperature to 1600°C and soaking at that temperature for one hour reduces the amount of open porosity retained in the Materials C and F to eliminate the gross penetration of metal through the zirconia membranes.

One of the penetration effects which is not always easy to observe is the penetration of Fe and FeO_x into hair-line cracks which are created by the stresses developed during the assembly stages. During assembly, the zirconia probe tip is sealed into a Vycor tube (Figure 64) using a series of high temperature gas flames. During the cooling cycle, the zirconia

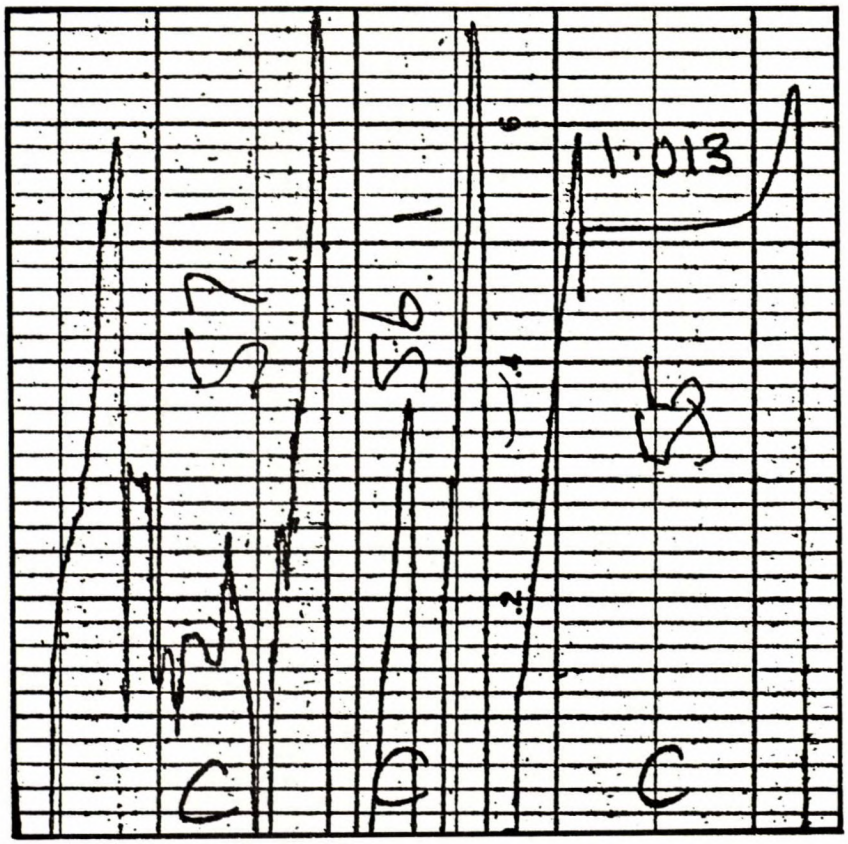

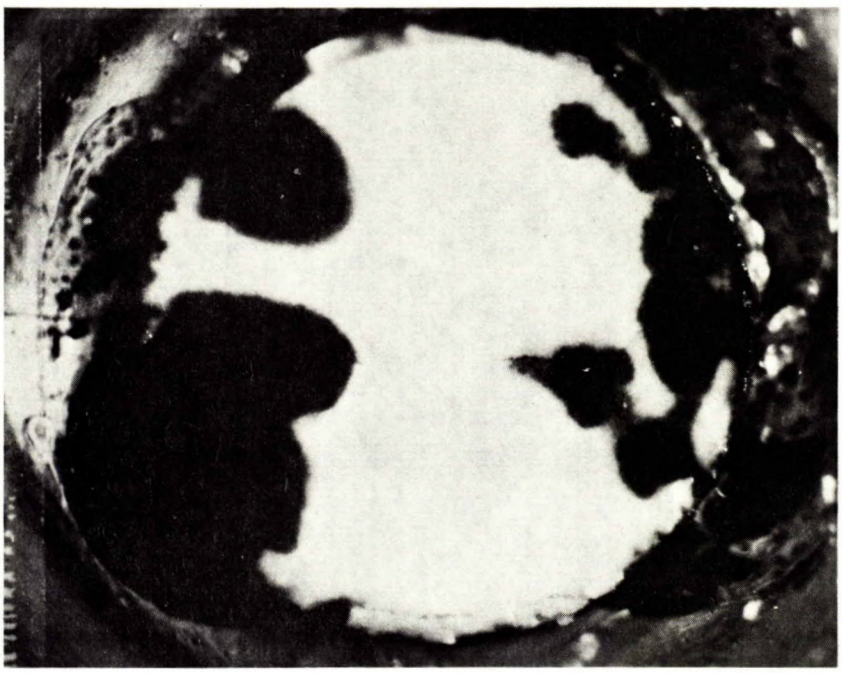

x 30

Figure 67. Output waveform and optical micrograph of probe # 57, heat 9420 (Material C).

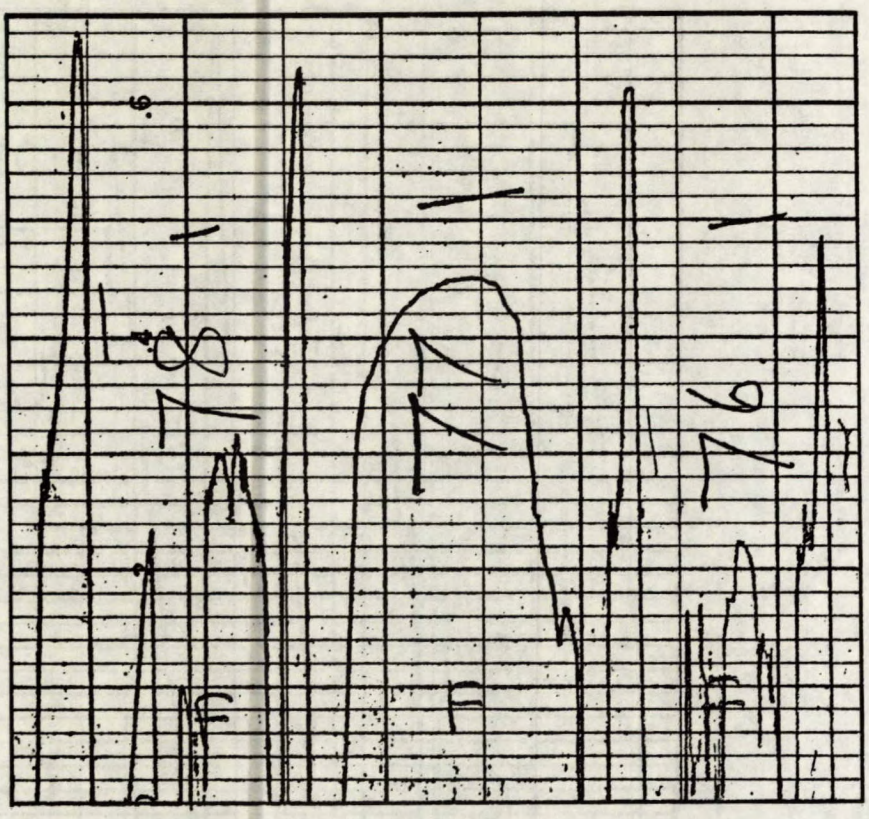

x 30

Figure 68. Output waveform and optical micrograph of probe # 76, heat 9420 (Material F).

will tend to shrink more than the Vycor (contraction coefficient of Vycor is $\sim 10^{-6}/°C$, ZrO_2: cubic $\sim 10 \times 10^{-6}/°C$ and monoclinic $\sim 4 \times 10^{-6}/°C$) and hence the membrane will suffer both radial and circumferential tensile forces. Consequently, both radial and circumferential cracks develop at the base of the membrane. This crack network can only be observed in the unused probe tips by dye impregnating polished sections (Figure 69); the cracks are too fine to be seen in undyed assemblies.

After use in liquid steel, some of these probes display a crack network similar to that revealed by dye impregnation of the unused probes. X-ray fluorescence examination of SEM-mounted samples confirmed that the cracks had been enriched with an Fe-containing material (Figure 70). From their appearance and the typical waveform developed by such probes (Figure 71), it is probable that either Fe or FeO_x vapour penetrated the cracks and rapidly increased in concentration to develop an electronically conducting network. Consequently, the cell emf output is progressively reduced and becomes zero as the cell ultimately develops a short circuit.

Despite the evidence presented in Figure 69, not all the cracked membranes develop a crack system which can expose the platinum bead to direct contact with Fe or FeO_x. Because only one end of the zirconia is held by the Vycor glass, an uneven stress distribution is formed which results in cracks being formed only at the Vycor end of the membrane. In many cases, these cracks are beneath the Vycor itself and hence do not contact the liquid metal. Under these circumstances, a normal waveform is obtained (Figure 72).

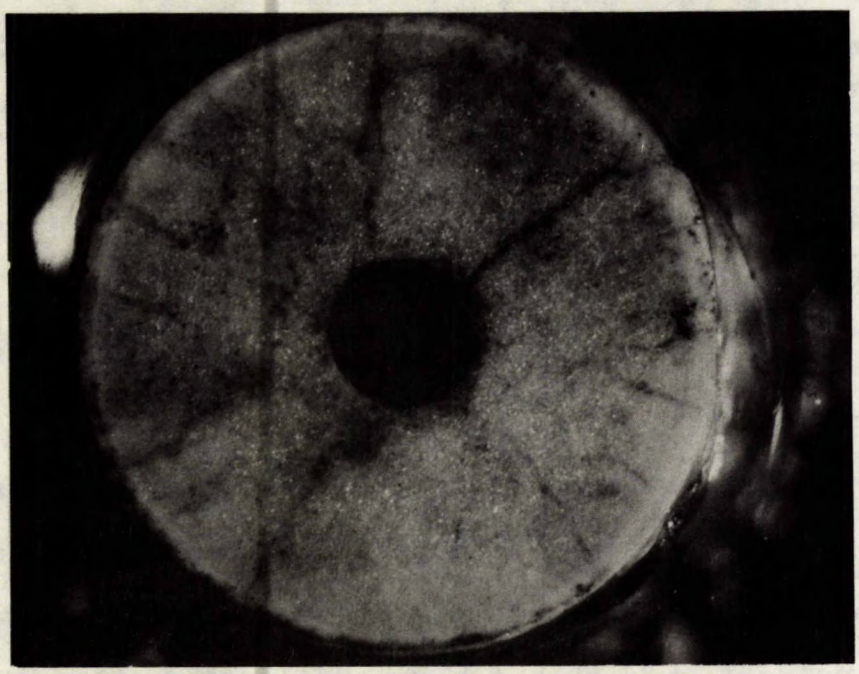

(a) Transverse section x30

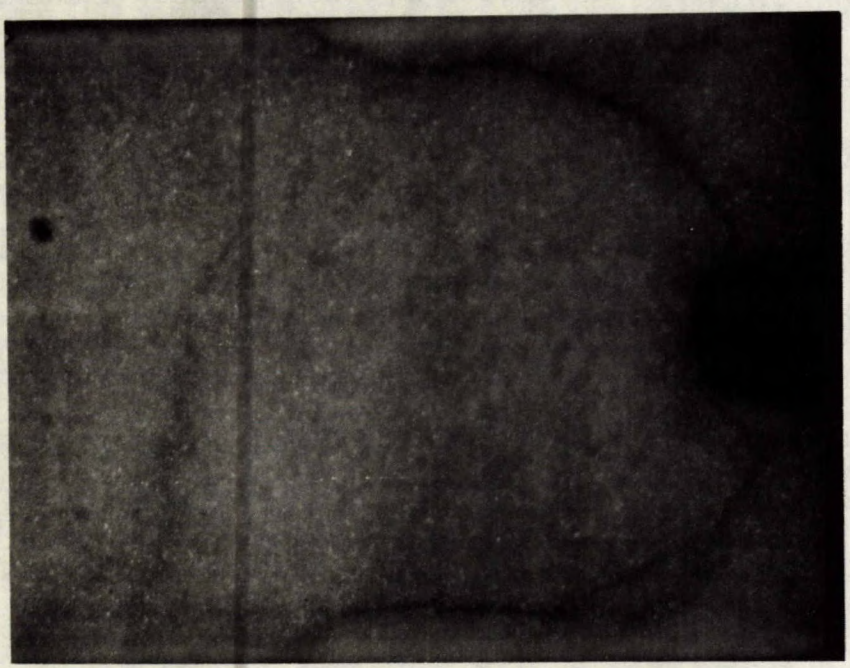

(b) Longitudinal section x30

Figure 69. Dye-impregnated polished sections of membranes taken from assembled but unused oxygen probes showing the development of radial and circumferential cracks.

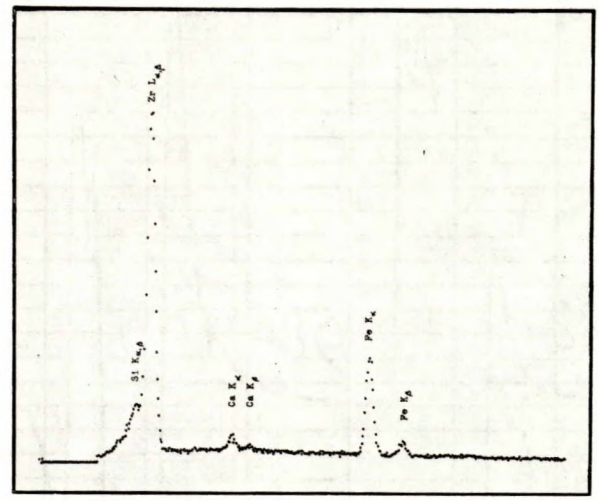

Point A

x 200

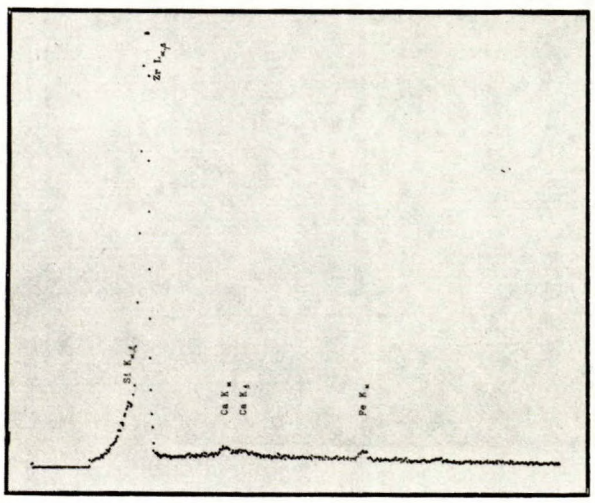

Point B

Figure 70. X-ray emission spectra of the back of probe # 58, heat 9162, showing the high concentration of iron adjacent to a crack.

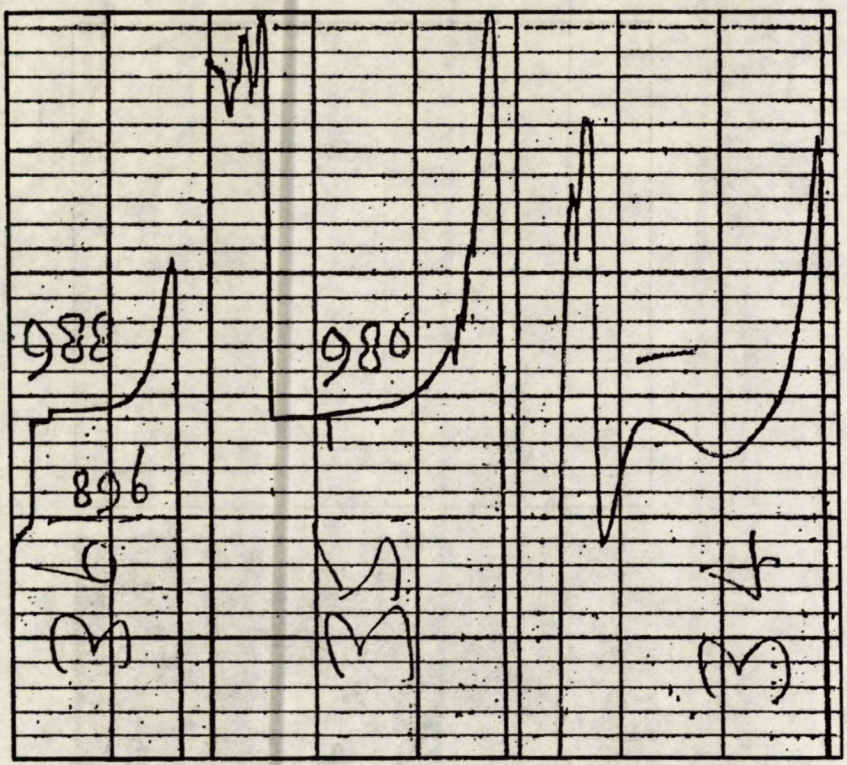

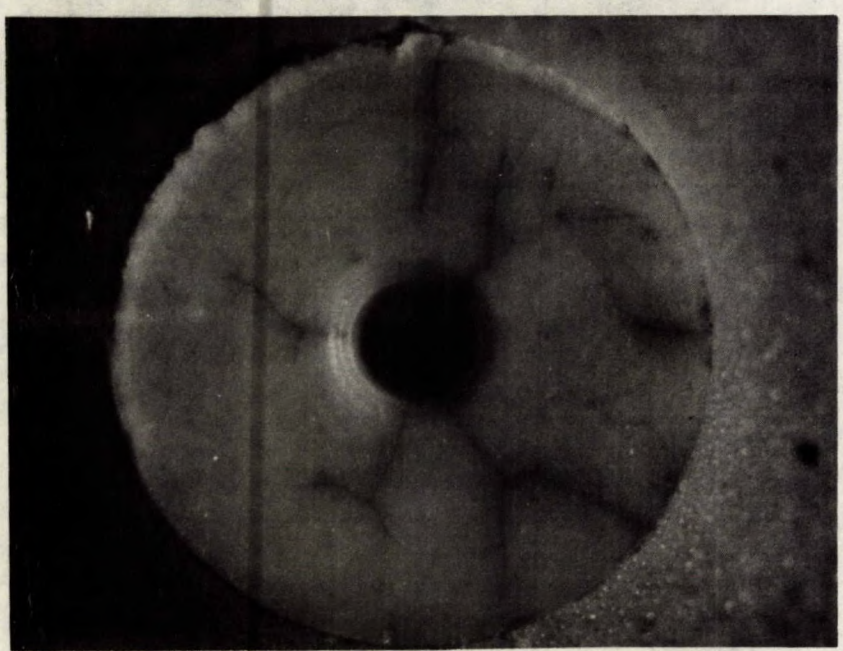

x 30

Figure 71. Output waveform and optical micrograph of probe # 34, heat 9420 (Material A). Note the unsteady output and iron penetration in the cracks.

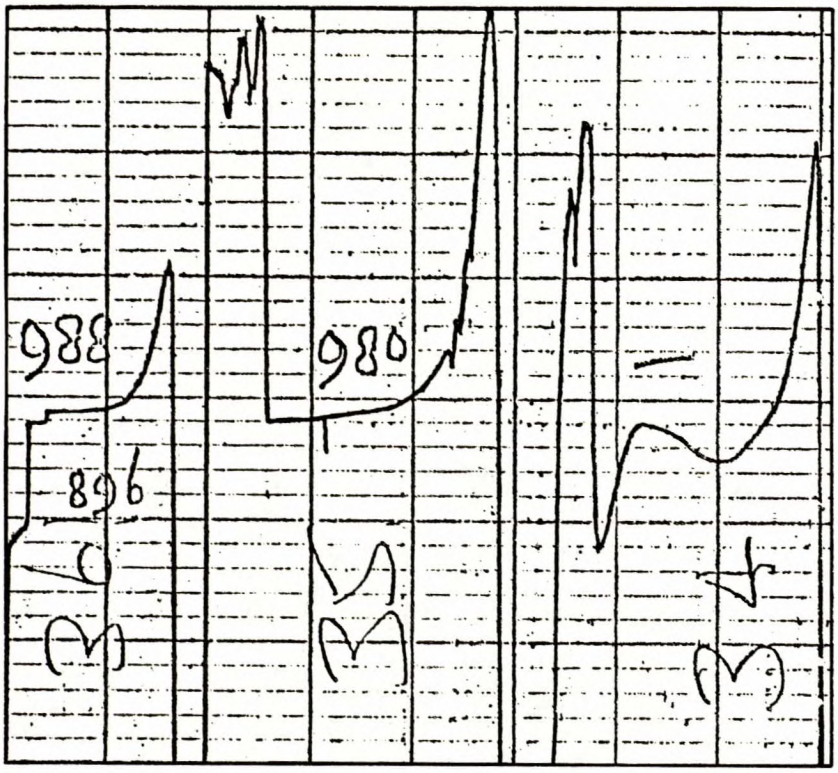

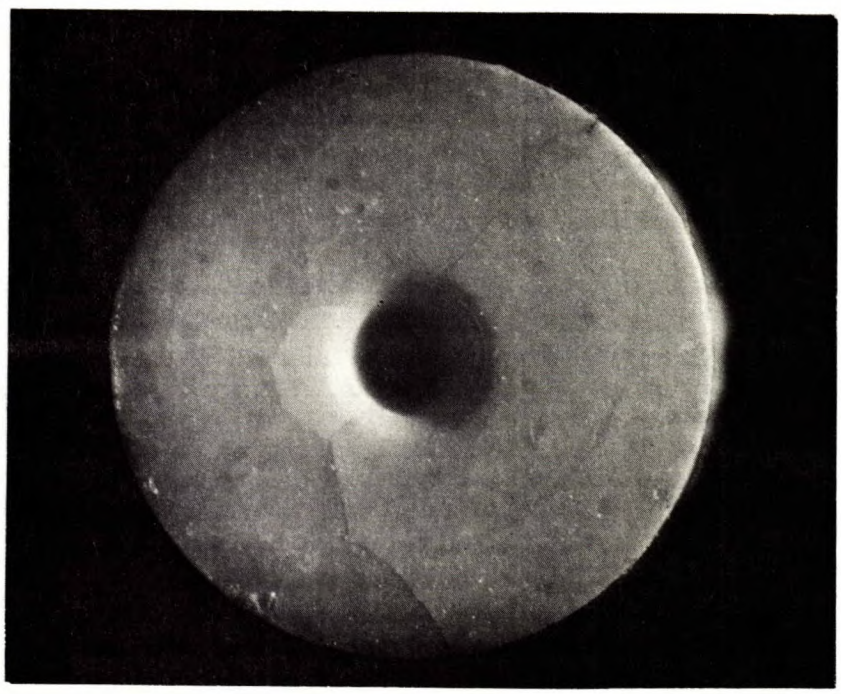

x 30

x 30

Figure 72. Output waveform and optical micrograph of probe # 35, heat 9420 (Material A). Note the steady output and the absence of contamination in the cracks.

From the foregoing, it will be realised that the probes fail for one of two reasons: either a poor electrical contact is formed (typically a loose platinum bead in the zirconia) or the membrane is permeable to Fe or FeO_x (due to either an underfired material being used or due to a crack network developing during assembly). The problems of a loose bead and underfired material are readily eliminated by routine quality control procedures but the potential for cracking the membranes is intrinsic to the current design of the probe. The introduction of an annealing cycle to allow the glass-zirconia assembly to slowly cool to room temperature did reduce the failure rate in the tested probes as shown in Figure 73, but it would be misleading to assume that this annealing step completely eliminated the cracking difficulties. In the probes made from contaminated commercial material, this problem does not arise - the cracks which are formed during the assembly stages appear to be sealed by the migration of liquid $CaSiO_3$ that is formed during the subsequent use of the probe in liquid steel (c.f. Figure 52).

Although the flame-sealing technique lends itself to automation on an assembly line, it nonetheless can completely ruin the performance of an assembled device. A more appropriate assembly procedure could be the use of a high-temperature cement to hold the electrolyte in the Vycor tubing. This would require a minimum of change in the overall processing procedures. In essence, if a single-ended pressing technique were used to form the electrolyte initially, then the cylindrical body produced would have a density gradient down the length of the sample.

On firing, this gradient would lead to a differential shrinkage and hence a conical body would be developed. This form could then be located in a pre-gauged Vycor tube so that approximately 3 mm of the ZrO_2 protrudes from the glass. An effective seal could then be made with an air-setting $NaSiO_3$-based refractory cement placed between the ZrO_2 and the glass. The conical form would hold the electrolyte in place while the cement developed an adequate green strength for subsequent handling. During use in a steel-making furnace, the cement would melt and form a glazed seal between the ZrO_2 and the Vycor - the configuration of the probe would then be maintained solely by ferrostatic pressure.

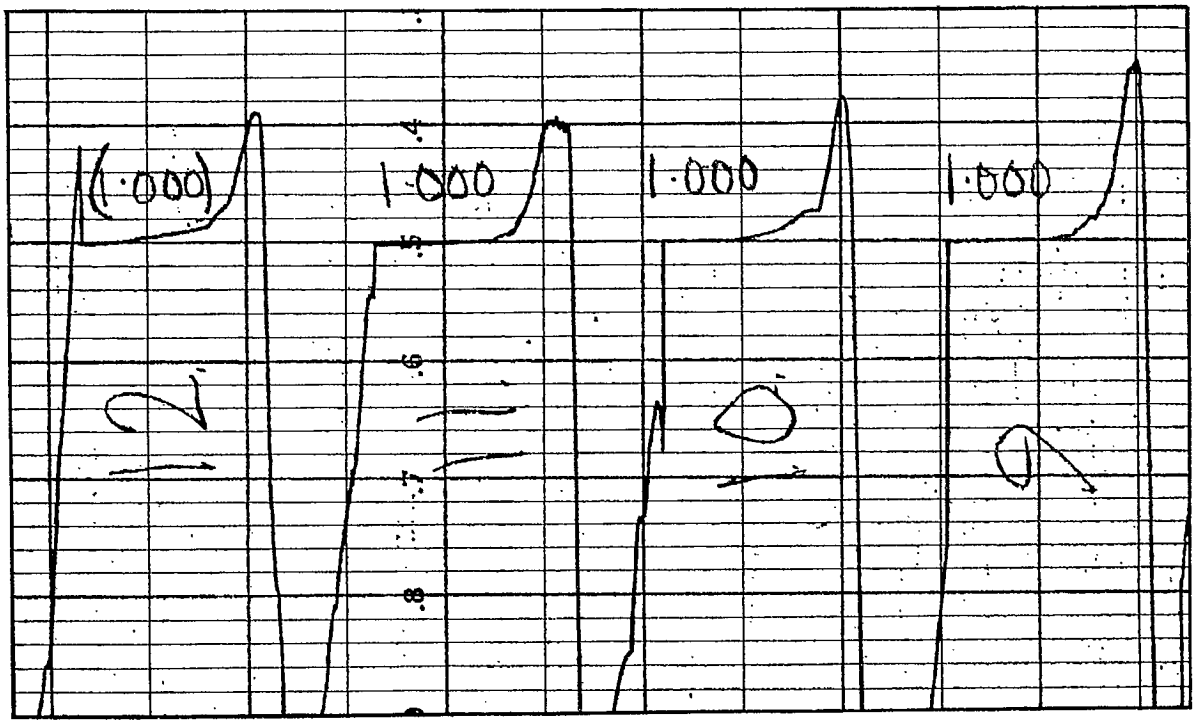

Figure 73. Output waveforms obtained from probes which were annealed immediately after flame sealing the zirconia into the Vycor.

Although the use of such a relatively low-melting cement would normally be avoided for any application at steel-making temperatures, as the eutectic in the Na_2O-Al_2O_3-SiO_2 system is approximately 732°C, it has been found satisfactory in cementing the base of the Vycor tube into the steatite plug of the assembly (Figure 64a). Consequently, the use of this cement to hold the electrolyte in the Vycor would avoid the development of any significant stress in the zirconia and thus avoid the development of cracks in the zirconia. In addition, any cracks which may be formed in the cement due to air drying too rapidly or any subsequent mishandling would be automatically sealed as a progressively thicker layer of liquid phase is formed on the surface of the cement.

CONCLUSIONS

Highly reactive, homogeneous, lime-stabilized zirconia powders can be prepared using a wet chemical procedure in which freshly precipitated $Zr(OH)_4$ is doped with a calcium formate solution. As a result, approximately 60% of the total amount of formate added is adsorbed by the precipitate - the degree of adsorption being pH dependent.

The method of drying the doped slurry strongly dictates the characteristics of the powder and these, in turn, essentially control the nature of the microstructure which is developed in fabricated and fired material. Conventional oven drying produces a hard glassy material which is unsuitable for processing by the

usual cold pressing and firing techniques. Spray drying and freeze drying produce nearly free-flowing powders, however, the spray-dried material retains a 'memory' effect through all the subsequent processing so that the original spray-dried agglomerates produce a non-uniform microstructure in the final fired body despite the use of a ball-milling step in an attempt to break up and disperse the powders prior to pressing. On the other hand, the spray-frozen and freeze-dried materials produced a much more uniform microstructure and consequently fired to a much higher density at a given temperature than the spray-dried materials of the same original composition, pH, chloride content and method of preparation.

It has been shown that the single most important parameter that controls the development of a high-density body on firing is the degree of dispersion of the raw material prior to the initial fabrication stage; the rate of intra-agglomerate sintering was found to be much greater than that for inter-agglomerate sintering. Other processing variables such as fabrication pressure, rate of binder burnout, heating rate, sintering atmosphere, firing temperature and the time at maximum temperature were found to have only a minor influence on the fired density. Provided the powders were dispersed by wet ball-milling in alcohol and treated with polyvinyl acetate and polyethylene glycol (powder binder and lubricant), spray-dried, formed at a pressure of not greater than 35 ksi and subsequently fired at a rate of not greater than 30°C/hr between 1200°C and 1500°C, bodies of 99% theoretical density would be produced on firing

to 1500°C with no soak.

The thermal-shock resistance of the fired material is strongly dependent on the composition. Maximum shock resistance was developed by material containing 7.6 mole % CaO; samples made using this composition survived continuous rapid cycling from room temperature to 1575°C and back without spalling or cracking. This behaviour was in contrast to that exhibited by either the pure or fully stabilized materials which usually shattered after the first cycle.

The mechanism responsible for this enhanced thermal-shock resistance is that proposed by Garvie and Nicholson[24]. The initially cubic material that is formed at the firing temperature becomes supersaturated during cooling and zones of approximately 2000 Å of pure tetragonal zirconia are precipitated. During further cooling, the tetragonal phase inverts to the monoclinic form at approximately 1100°C with an accompanying 3 volume % expansion which occurs against the progressively contracting cubic matrix. As a result, microcracks are formed throughout the body. This extensive network of microcracks intercepts any propagating macrocrack and thus increases the crack-tip radius. For the cracks to propagate further the stress level (degree of thermal shock) must be increased.

No correlation was found between the various precipitation conditions such as the method of mixing, pH, chloride concentration, and the method of drying, on the emf generated by subsequently produced concentration cells. Provided an impermeable electrolyte is used, the same signal is generated. However,

the permeability of the zirconia was found to be dependent on the original chloride content of the slurry despite the relatively high-temperature calcination stage prior to fabrication (T ∿1000°C, well above the sublimation temperature of NH_4Cl).

Partially stabilized zirconia will perform satisfactorily as an ionic conductor in oxygen concentration cells using metal-metal oxide reference electrodes provided the materials do not react and the equilibrium P_{O_2} is not too low. $Cr-Cr_2O_3$ electrodes give unreliable emf data due to the P_{O_2} being too low, allowing electronic conduction to occur in the electrolyte. Fe-FeO can only be used satisfactorily below 1050°C; at higher temperatures degredation of the electrolyte occurs and ill-defined emf values are generated. Ni-NiO and Co-CoO mixtures performed well in the temperature range 750°C to 1250°C. The slight diffusion of nickel into the zirconia did not affect the cell potential.

The partially stabilized 7.6 mole % CaO material performed well as the electrolyte in oxygen probes tested in liquid steel. The material successfully survived the thermal shock developed when rapidly inserted into steel at approximately 1625°C; under these conditions the heating rate was greater than 400°C/sec. After testing, none of the cells showed any degredation due to thermal shock.

Oxygen probes which used this chemically prepared electrolyte were found to be consistent in their emf readout during trials in a steel-making furnace. Provided impermeable material was used, all the batches of material produced probes

for which the standard deviation was less than the original target of 8 mv in a one-volt signal. In the case where the material was well dispersed during precipitation, washed free of chloride and freeze-dried (Material D), the standard deviation was lowered to 3 mv in a one-volt signal.

ACKNOWLEDGEMENTS

The author wishes to express his appreciation to all the members of the Industrial Minerals Laboratory and those members of the CANMET staff who have contributed to the various aspects of this report.

Thanks are particularly due to A.J. Hanson who conducted much of the technical and processing aspects of this project and to D.A. Job who conducted the experimental work on the oxygen concentration cells in the laboratory. Special thanks are also due to I.F. Wright for his comments and discussions throughout the duration of this work and to C.S. Monier-Williams, P. Eng., for his assistance in assembling the electrolyte into complete oxygen probes and testing them under steel-making conditions.

REFERENCES

1. K. Kiukkola and C. Wagner, "Measurements on Galvanic Cells Involving Solid Electrolytes", Jour. Electrochem. Soc., 104 (6), 379-387 (1957).

2. N. M. Beckmans and L. Heyne, "An Instrument for Monitoring Low Oxygen Pressures", Philips Tech. Rev., 31, 112-116 (1970).

3. K. A. Klinedinst and D. A. Stevenson, "A Solid Electrolyte Oxygen Gauge for Monitoring Trace Quantities of Water Vapour in Hydrogen Gas", Rev. Sci. Instr., 43 (3), 417-419 (1972).

4. A. D. Kulkarni et al., "Stability of Solid Electrolyte Concentration Sensors for Automatic Oxygen Control in Liquid Copper", Jour. Inst. Metals, 99, 15-18 (1971).

5. R. Baker and J. M. West, "Solid Electrolytes for Use at Steelmaking Temperatures", Jour. Iron and Steel Inst., 204 (March), 212-216 (1966).

6. K. Schwerdtfeger, "Measurement of Oxygen Activity in Iron, Iron-Silicon, Manganese, and Iron-Manganese Melts Using Solid Electrolyte Galvanic Cells", Trans. Met. Soc. AIME, 239 (Sept.), 1276-1281 (1967).

7. J. K. Pargeter, "A Method for Direct Oxygen Determination in Molten Metals", Jour. Metals, (Oct.), 27-31 (1968).

8. E. T. Turkdogan and R. E. Fruehan, "Rapid Oxygen Determination in Liquid Steel", Amer. Iron and Steel Inst. Year Book, 279-301 (1968).

9. J. K. Pargeter and D. K. Fourschou, "Direct Oxygen Determination in Commercial Steelmaking Practice", Jour. Metals, (March), 46-48 (1969).

10. G. R. Fitterer et al., "Oxygen in Steel Refining as Determined by Solid Electrolyte Technique", Jour. Metals, (August), 46-52 (1969).

11. B. Korousic, "Electrochemical Determination of Oxygen in Molten Steel. II Review of Electrolytic Properties of Solid Electrolytes", Translated by NOLIT Pub. House, Belgrade and published by U.S. Dept. of the Interior and Nat. Sci. Foundation, Washington, D.C. TT70-56005/1.
Rudarsko-Metalurski Zbornik (1), 43-57 (1970).

12. S. R. Richards et al., "An Electrochemical Probe for the Determination of Oxygen Activity in Liquid Steel", Paper from the Central Research Laboratories, The Broken Hill Proprietary Co. Ltd., Shortland, N.S.W. 2307, Australia, presented to the International Conference on the Science and Technology of Iron and Steel, Tokyo, Japan, (Sept. 7-11, 1970).

13. N. McKinnon, Private communication (1972).

14. F. J. Schnettler et al., "A Cryochemical Method for Preparing Ceramic Materials", Science of Ceramics, Vol. IV 79-90 (1968). Ed. G. H. Stewart, Published by The British Ceramic Society, Stoke-on-Trent, England.

15. V. M. McNamara, "A Wet Chemical Method for Preparation of Oxide Mixtures Applicable to Electronic Ceramics", Jour. Can. Ceram. Soc. 34, 103-120 (1965).

16. K. S. Mazdiyasni et al., "Preparation of High-Purity Submicron Barium Titanate Powders", Jour. Amer. Ceram. Soc. 52, 523-526 (1969).

17. T. A. Wheat and V. V. Mirkovich, Unpublished data (1970).

18. V. V. Mirkovich and T. A. Wheat, "Use of Liquid Nitrogen in Spray Freezing", Amer. Ceram. Soc. Bull. 49 (8), 724-725 (1970).

19. Handbook of Chemistry and Physics, Published by The Chemical Rubber Company, Cleveland, Ohio (1964).

20. W. L. Bragg, "The Crystalline State. Vol. I A General Survey", Published by Bell & Sons, London (1933).

21. Pol Duwez et al.,"Stabilization of Zirconia with Calcia and Magnesia", Jour. Amer. Ceram. Soc. 35 (5), 107-113 (1952).

22. R. C. Garvie, "The Occurrence of Metastable Tetragonal Zirconia as a Crystallite Size Effect", Jour. Phys. Chem. 69 (4), 1238-1243 (1965).

23. R. C. Garvie, "The Cubic Field in the System Cao-ZrO_2", Jour. Amer. Ceram. Soc. 51 (10), 553-556 (1968).

24. R. C. Garvie and P. S. Nicholson, "Structure and Thermomechanical Properties of Partially Stabilized Zirconia in the CaO-ZrO_2 System", Jour. Amer. Ceram. Soc. 55 (3), 152-157 (1972).

25. H. P. Klug and L. E. Alexander, "X-Ray Diffraction Procedures", p 478, Published by John Wiley & Sons Inc., N.Y. (1967).

26. J. B. Nelson and D. P. Riley, "An Experimental Investigation of Extrapolation Methods in the Derivation of Accurate Unit-Cell Dimensions of Crystals", Proc. Phys. Soc. (London) 57, 160-177 (1945).

27. N.F.M. Henry et al., "The Interpretation of X-Ray Diffraction Photographs", p 191. Published by MacMillan and Co. Ltd., London (1961).

28. R. C. Garvie, "Zirconium Dioxide and Some of Its Binary Systems", pp 117-166. In 'High Temperature Oxides, Part II: Oxide of Rare Earths, Titanium, Zirconium, Hafnium, Niobium, and Tantalum'. Edited by Allen M. Alper. Published by Academic Press (1970).

29. M. L. Hair, "Infrared Spectroscopy in Surface Chemistry", p 60. Published by Marcel Dekker Inc., N.Y. (1967).

30. C. M. Phillippi and K. S. Mazdiyasni, "Infrared and Raman Spectra of Zirconia Polymorphs", Jour. Amer. Ceram. Soc. 54 (5), 254-258 (1971).

31. N. T. McDevitt and W. L. Baun, "Infrared Absorption Spectroscopy in Zirconia Research", Jour. Amer. Ceram. Soc. 47 (12), 622-624 (1964).

32. D. S. Buist, "Investigations with the Leitz Heating-microscope Type IIA-P in the Field of Ceramics", Trans. Brit. Ceram. Soc. 69 (1), 15-20 (1970).

33. A. G. Karaulov et al., "Effect of Phase Composition of Zirconium Dioxide on Spalling Resistance", Izv. Akad. Nauk SSSR, Neorg. Mater. 3 (6), 1101-1103 (1967).

34. D.P.H. Hasselman, "Thermal Stress Crack Propagation in Severe Thermal Environments", pp 89-103, in Materials Science Research, Volume 5: Ceramics in Severe Environments. Edited by W. W. Kriegel and H. Palmour III. Published by Plenum Press, N.Y. (1971).

35. J. F. Elliot and M. Gleiser, "Thermochemistry for Steelmaking", Vol. I. Published by Addison-Wesley Pub. Co. Inc., Reading, Mass. (1960).

36. B.C.H. Steele and C. B. Alcock, "Factors Influencing the Performance of Solid Oxide Electrolytes in High-Temperature Thermodynamic Measurements", Trans. Met. Soc. AIME, 233 (7), 1359-1367 (1965).

37. D.A.J. Swinkels, "Rapid Determination of Electronic Conductivity Limits of Solid Electrolytes", Jour. Electrochem. Soc., 117 (10), 1267-1268 (1970).

38. A. Kumar et al., "Effect of Oxide Defect Structure on the Electrical Properties of ZrO_2", Jour. Amer. Ceram. Soc. 55 (9), 439-445 (1972).

39. B.C.H. Steele et al., "Anionic Conduction in Refractory Oxide Solid Solutions Possessing the Fluorite, Pyrochlore and Perovskite Structures", Proc. Brit. Ceram. Soc. #10, (March) 87-102 (1968).

40. A. V. Ramana Rao and V. B. Tare, "Electronic Conduction in Calcia-Stabilized Zirconia Between 1000-1400°C", Scripta Metallurgica 6, 141-148 (1972).

41. D. W. Strickler and W. G. Carlson, "Electrical Conductivity in the ZrO_2-Rich Region of Several M_2O_3-ZrO_2 Systems", Jour. Amer. Ceram. Soc. 48, 286-289 (1965).

42. D. Yuan and F. A. Kröger, "Stabilized Zirconia as an Oxygen Pump", Jour. Electrochem. Soc., 116 (5), 594-600 (1969).

43. H. Schmalzried, "Ionic and Electronic Conductivity in Binary Oxides and their Investigation with EMF Measurements", Zeits. Phys. Chem. Frankfurt, 38, 87-102 (1963).

44. R. W. Vest et al., "Electrical Properties and Defect Structure of Zirconia: 1. Monoclinic Phase", Jour. Amer. Ceram. Soc. 47 (12), 635-640 (1964).

45. J. F. Shackelford et al., "Role of SiO_2 in Sintering Partially Stabilized Zirconia", presented at the 75th Annual Meeting, The American Ceramic Society, Cincinnati, Ohio, 1 May 1973. (Basic Science Division, No. 15-B-73); for abstract see Amer. Ceram. Bull. 52 (4), 341 (1973).

46. B.C.H. Steele, "Electromotive Force Measurements in High-Temperature Systems", pp 3-27. Edited by C. B. Alcock. American Elsevier Co., Inc., N.Y. (1968).

47. C. J. Mogab, Private communication (1973).

48. A. Kontopoulos and P. S. Nicholson, "Ionic Conductivity of Partially Stabilized Zirconia", Jour. Amer. Ceram. Soc. 54 (6), 317 (1971).

49. M. G. Natrella, "Experimental Statistics", NBS Handbook 91, 1963. Available from The Superintendent of Documents, U.S. Government Printing Office, Washington 25, D.C.

A P P E N D I X A

APPENDIX A

Determination of the Quantity of Calcium Formate Required to Produce a Specific Concentration of Lime in Zirconia

The data presented here are for the preparation of a lime-stabilized zirconia containing 7.6 mole % CaO.

Concentration of Slurry

Samples of slurry were placed in ignited and pre-weighed platinum crucibles, dried at 110°C and ignited to constant weight at 1000°C.

		(i)	(ii)
Wt of slurry (g)	=	77.7306	93.4912
Wt ZrO_2 formed (g)	=	3.7849	4.5679
Concentration of slurry (g ZrO_2/g slurry)	=	0.04869	0.04885
Average conc of slurry (g ZrO_2/g slurry)	=	0.04877	

Concentration of Calcium Formate Solution

A solution of calcium formate (Matheson, Coleman and Bell, N.J.) was made up by dissolving 64 g in 1.75 litres of distilled water at room temperature. This solution was then clarified to remove insoluble material and the filtrate was made up to 2 litres. A concentration determination was carried out as a check against losses during the filtration stage.

		(i)	(ii)
Wt crucible + 20 ml soln (g)	=	43.7822	43.6120
Wt crucible dried 110°C (g)	=	22.5440	22.2924

		(i)	(ii)
Wt crucible (g)	=	21.9041	21.6527
Concentration of soln (g/20 ml)	=	0.6399	0.6397
Average conc of solution (g/20 ml)	=	0.6398	

Wt loss of formate on ignition to 1000°C = 56.7%

Hence average conc of formate solution = 0.3627 g CaO/20 ml

Volume of Formate Solution Required to Dope Slurry

Batch Mole %	Wt of Slurry g ZrO_2	Moles ZrO_2	Moles CaO Required	Wt CaO Required g	Wt Formate Required g	Vol Formate Required ml
7.6	101.6098	0.82462	0.06775	3.7998	6.7016	209.5

A P P E N D I X B

APPENDIX B

Adsorption of Calcium Ions Onto the Surface of $Zr(OH)_4$ Precipitate

I. Adsorption at a Low Formate Concentration

Initially the adsorption was determined in mixtures in which the molar ratio of calcium formate to zirconium hydroxide was 6.5%.

(a) Electrode calibration

Using the original standard formate solution, a series of solutions was prepared and the divalent-ion electrode potential of each was determined.

TABLE 1

Calibration of Divalent-Ion Electrode

$Ca(H.CO.O)_2$ Concentration moles/litre	Electrode Potential mV
$1.0.10^{-1}$	+45.6
$1.06.10^{-2}$ *	+23.4
$1.12.10^{-3}$	+ 6.2
$1.19.10^{-4}$	-10.0
$1.26.10^{-5}$	-26.2

*The concentration changes are not exactly an order of magnitude due to the use of a pipette which was assumed to release 20 ml but in practice delivered 21.5 ml. Consequently, in making up 250 ml of solution for the calibration, the volume of formate taken was 26.5 ml (21.5 + 5.0 ml) and hence the concentration decreases by the ratio 26.5/250, i.e., 0.106.

The emf response of the electrode was found to be essentially linear to the log (concentration) over the range 10^{-1} to 10^{-4} moles/litre - at lower concentrations the curve deviated from the theoretical Nernst relationship.

(b) Adsorption data

The determination was carried out using 21.5 ml of slurry to which 2.0 ml of 0.2462 molar $Ca(H.CO.O)_2$ solution (i.e., 32 g/litre) was added. The change of the divalent-ion electrode potential was recorded and related, using the calibration data in Part (a) above, to the change of the free Ca^{2+} ion concentration with time.

TABLE 2

Increase in Free Ca^{2+} Concentration with Time in $Zr(OH)_4$ Slurry at a Low Formate Concentration

Time seconds	$Zr(OH)_4$ Slurry pH 6		$Zr(OH)_4$ Slurry pH 8		$Zr(OH)_4$ - free Liquor	
	emf mV	$[Ca^{2+}]$ molar	emf mV	$[Ca^{2+}]$ molar	emf mV	$[Ca^{2+}]$ molar
0	-16.0	5.0×10^{-5}	-18.0	3.5×10^{-5}	-18.0	3.5×10^{-5}
6.25	-15.2	5.4×10^{-5}	-17.0	4.2×10^{-5}	+24.5	1.2×10^{-2}
12.5	-14.0	6.5×10^{-5}	- 1.5	3.7×10^{-4}	+28.0	1.8×10^{-2}
25	- 0.8	3.8×10^{-4}	+11.2	1.9×10^{-3}		
50	+ 9.0	1.4×10^{-3}	+16.1	3.5×10^{-3}		
75	+13.1	2.3×10^{-3}	+18.2	4.5×10^{-3}		
100	+15.3	3.3×10^{-3}	+18.8	5.4×10^{-3}		
150	+18.0	4.5×10^{-3}	+20.1	6.1×10^{-3}		
200	+19.4	5.7×10^{-3}	+20.9	6.8×10^{-3}		
300	+21.0	7.0×10^{-3}	+21.9	7.8×10^{-3}		
800	+24.0	1.1×10^{-2}	+24.0	1.1×10^{-2}	+31.9	2.4×10^{-2}

These data form the basis of the curves presented in Figure 6.

II. Adsorption at a High Formate Concentration

From a consideration of the law of mass action, it would be expected that more formate would be adsorbed onto the surface of the $Zr(OH)_4$ precipitate as the total concentration of formate is increased. Consequently, the experimental procedure under Part I above was repeated, using triple the volume of formate solution added to the $Zr(OH)_4$, to give a molar ratio of calcium formate to zirconium hydroxide of 19.5%.

The rate of adsorption was little different from that found at the low formate concentration and hence only the initial and final Ca^{2+} ion concentrations are presented for the $Zr(OH)_4$-free liquor and the slurry.

TABLE 3

Increase in Free Ca^{2+} Concentration in $Zr(OH)_4$ Slurry at a High Formate Concentration

Time seconds	$Zr(OH)_4$ Slurry pH 8	$Zr(OH)_4$-free Liquor
	$[Ca^{2+}]$ molar	$[Ca^{2+}]$ molar
0	3.5×10^{-5}	3.5×10^{-5}
800	2.2×10^{-2}	6.2×10^{-2}

III. Percentage of Formate Adsorbed by $Zr(OH)_4$

From the data presented in Table 2 in Part I(b) above, the quantity of formate adsorbed by the precipitate was calculated as a function of time. It is assumed that the difference between the data for the slurry and the liquor is due to adsorp-

tion by the precipitate alone. As discussed in the text, the effect of the increased viscosity of the slurry slowing down the response of the electrode was discounted.

TABLE 4

Percentage of Ca^{2+} Adsorbed onto $Zr(OH)_4$ Precipitate at a Low Formate Concentration

Time seconds	Percentage of Total Ca^{2+} adsorbed at pH 6	Percentage of Total Ca^{2+} adsorbed at pH 8
0	0	0
6.25	99.6	99.6
12.5	99.6	97.8
50	92.2	80.5
100	82.6	71.6
200	72.9	67.6
300	69.8	66.0
800	54.0	54.0

These data are presented in Figure 7.

The final equilibrium value obtained at either pH 6 or pH 8 of 54% adsorbed Ca^{2+} generated at a low formate concentration is little different from the value obtained at a high formate concentration. From the data in Table 3, the amount of adsorbed Ca^{2+} was determined to be 64.5%.

A P P E N D I X C

APPENDIX C

Determination of Free Calcium Formate in Freeze-Dried Powder

The use of a divalent-ion selective electrode to measure the concentration of Ca^{2+} in a slurry of freeze-dried zirconia powder is complicated by the additional response of the electrode to other divalent ions present such as ZrO^{2+}, $Zr(OH)_2^{2+}$ and $ZrCl_2^{2+}$. Hence, it is necessary to establish the background concentration of all divalent ions except Ca^{2+} which would be present in the freeze-dried materials. Consequently, a one-gram sample of undoped freeze-dried zirconia, which had been prepared in the same manner as the 7.6 mole % materials below, was slurried in water and the divalent-ion concentration of the liquid determined. The background divalent-ion concentration was found to be 2.2×10^{-5} moles/litre which agrees well with the value of 3.5×10^{-5} moles/litre obtained in the liquor above the fully washed precipitate that had been prepared in a different batch (see Appendix B, Table 2).

The total divalent-ion concentration developed in the slurried materials is given in Table 1. The difference between the total and the background concentrations was assumed to be the Ca^{2+} ion concentration, i.e., the concentration of the free formate which had been released from the dried powder. The percentage of free formate was then obtained from the theoretical concentration of Ca^{2+} which would be developed in these slurries assuming no adsorption had occurred, i.e., assuming a maximum concentration of 6.14×10^{-3} moles/litre.

TABLE 1

Percentage of Free Calcium Formate Released from Freeze-Dried Powder

Batch	Total [Ion^{2+}] moles/litre	Background [Ion^{2+}] moles/litre	Free [Ca^{2+}] moles/litre	Percentage of Free Ca^{2+}
A	1.7×10^{-3}	2.2×10^{-5}	1.678×10^{-3}	27.3
B	1.4×10^{-3}	2.2×10^{-5}	1.378×10^{-3}	22.4
C	1.1×10^{-3}	2.2×10^{-5}	1.078×10^{-3}	17.6
D	1.3×10^{-3}	2.2×10^{-5}	1.278×10^{-3}	20.8

The results show that the amount of free calcium formate in the powders is quite variable and ranges from approximately 17 to 27%. The average is 22%.

A P P E N D I X D

APPENDIX D

Determination of Particle Size from X-ray Diffraction and Surface Area Data

Operating Conditions for X-Ray Diffractometer

Samples were initially examined using a North American Philips Wide Angle Diffractometer operated under the following conditions:

> Fe-filtered Co K-alpha radiation; 1° scatter slits; 0.5° 2θ/min scanning speed; proportional counter with pulse height analyser; 400 counts full scale deflection; 8 sec time constant.

These conditions were not able to give sufficient sensitivity to allow low concentrations of crystalline material to be detected. Consequently, diffraction patterns were obtained with either a non-focussing Debye-Scherrer camera or a focussing Guinier-DeWolff powder camera which are more sensitive than the diffractometer. The patterns were then examined with a microdensitometer to obtain the derived diffractograms.

Operating Conditions for a Joyce Loebl Double Beam Recording Microdensitometer

A model III CS microdensitometer, produced by Joyce, Loebl and Co. Ltd., England, was used under the following conditions:

Optical Magnification	x22	Differential Control	8
Slit Width	600 μm	Forward Speed	2.5
Optical Wedge* (a)	2.90 D	Traverse ratio	1:1
(b)	0.36 D		

Resolution of Back-Reflection Doublets as a Function of Domain Size

The property of resolving or just failing to resolve the back-reflection doublets of an X-ray powder diffraction pattern has been used as an index of crystal size[20]. As is the case with an optical grating, the two lines will be resolved if the condition $nN>\lambda/\Delta\lambda$ is met, where N is the number of planes, n the order of the spectrum and λ and $\lambda + \Delta\lambda$ the wave length of the $K_{\alpha 1}$ and $K_{\alpha 2}$ doublets. The doublet is most conveniently observed in the region where $2\theta \simeq 180°$, because it is here that the components have the maximum dispersion. As $\sin\theta \simeq 1$ at high angles, $n\lambda = 2d$ ($n\lambda = 2d\sin\theta$) and hence resolution will occur if:

$$nN = 2Nd/\lambda = 2t/\lambda > \lambda/\Delta\lambda$$

As $\lambda/\Delta\lambda = 460$ for Co K_α radiation, resolution can only occur when $2t/\lambda > 460$, i.e., when $t > 230\lambda$. Hence the crystal size must be greater than 230λ i.e., 412 Å in order to resolve the doublet in the back-reflection region.

*A wedge having a useful range of 2.90 D and a slope of 0.16 D/cm was used to give maximum attenuation of the recorded peaks, whereas a wedge with a range of 0.36 D and a slope of 0.02 D/cm was used to give maximum sensitivity.

A P P E N D I X E

APPENDIX E

Surface Area Data for Calcined Zirconia Materials

Each sample (approximately 2 to 4 cc) was outgassed overnight at 125°C in an atmosphere of flowing helium. The surface area was determined using the flowing nitrogen technique. The quantity of nitrogen desorbed from the surface of a sample during warming from -189°C (boiling point of liquid nitrogen) to room temperature was measured using a Perkin-Elmer Shell sorptometer model 212C. The surface area was determined using the single point method in which the gas used was helium containing 25% nitrogen. The precision of the data was determined to be ± 7%.

TABLE 1

Variation of Surface Area with Calcination Temperature for Undoped and Doped Zirconia

Temp °C	Composition mole % CaO				
	Undoped	7.6	11.5	13.8	16.0
600	59.77	84.03	83.00	103.53	94.92 m^2/g
700	45.98	66.63	71.97	94.19	89.93
750	28.92	51.68	54.72	67.35	64.21
800	21.59	38.69	40.07	49.01	50.07
850	18.52	34.49	35.04	45.91	44.80
900	17.16	30.25	27.40	38.63	35.19
950	15.62	23.91	23.89	31.52	33.39
1000	14.42	16.06	13.81	20.21	18.23
1050	11.29	15.76	12.78	17.35	18.79

....Table Continued

TABLE 1 (Continued)

Temp °C	Composition mole % CaO				
	Undoped	7.6	11.5	13.8	16.0
1100	8.82	12.97	13.07	18.15	17.86 m^2/g
1150	6.93	11.17	12.90	14.18	15.13
1200	4.00	6.70	6.59	9.15	10.35
1250	2.11	4.38	3.87	5.37	5.29
1300	1.32	1.65	1.49	1.64	1.77

Having determined the general form of the surface area-temperature curve from the above data, the remaining compositions were calcined only between 800 and 1200°C in order to determine the plateau in the area-temperature curve for each composition.

TABLE 2

Variation of Surface Area with Calcination Temperature for Partially Stabilized Zirconia

Temp °C	Composition mole % CaO			
	2.0	4.0	6.0	9.0
800	30.77	41.15	32.50	37.06 m^2/g
850	21.00	25.84	25.94	29.20
900	22.52	19.68	20.46	21.07
1000	13.75	17.44	18.64	21.85
1100	6.44	9.69	10.09	12.76
1200	2.94	4.01	4.25	5.94

Derivation of Particle Size from Surface Area Data

If it is assumed that a powder consists of particles which have perfect cubic morphology and hence are theoretically dense, then, if the edge length is given by x, the surface area of each cube will be $6x^2$ and the volume will be x^3. Hence, if the density of the material is given by d, the specific surface (surface area per unit weight) will be $6x^2/d.x^3$ cm^2/g.

For zirconia, d is assumed to be 6 g/cc (page 37) and hence the specific surface is $1/x$ cm^2/g or $10^{-4}/x$ m^2/g when x is in centimetres. For fine powders, the micrometre or Ångström is a more convenient unit for x and hence the specific surface will be given by $1/x$ m^2/g when x is in micrometres and by $10^4/x$ m^2/g when x is given in Ångströms.

Hence, calcination of the zirconia materials to a specific surface of 20 m^2/g will produce a powder having crystallites of approximately 500 Å.

A P P E N D I X F

APPENDIX F

Variation of Bulk Density with Firing Conditions

The density of the fired samples was determined from the weight and measured volume. The precision was ±0.03 g/cc for samples with a density of 5.00 g/cc.

TABLE 1

Bulk Density of Doped Zirconia Samples Fired to 1600°C for 1 hour

Mole % CaO	7.6	11.5	13.8	16.0
As-prepared	4.64	5.38	5.30	5.21 g/cc
Calcined 850°C 1 hr	4.71	4.74	5.01	4.90
Calcined 1000°C 1 hr	4.89	4.77	5.04	4.99

TABLE 2

Bulk Density of Doped Zirconia Samples Fired to 1550°C for 4 hours

Mole % CaO	7.6		11.5		13.8		16.0	
	a	b	a	b	a	b	a	b
As-prepared	1.61	4.59	1.66	5.12	1.60	5.12	1.69	5.30 g/cc
Calcined 700°C 1 hr	1.59	5.16	1.53	5.07	1.42*	4.63	1.41*	4.97
Calcined 850°C 1 hr	1.85	4.89	1.64	5.02	1.64	5.06	1.64	5.01
Calcined 1000°C 1 hr	1.99	4.84	1.67	4.92	1.73	5.07	1.73	4.98

a - green density b - fired density * - cracked sample

A P P E N D I X G

APPENDIX G

Change in the Intensity of Major Peaks Recorded in X-ray Diffractograms of Thermally Shocked Partially Stabilized Zirconia

The intensities of the main peaks in the diffractograms of Figure 41 were determined by their height in millimetres above the extrapolated background. The traces were obtained using the microdensitometer operating under the conditions given in Appendix D.

TABLE 1

Intensity of Major Diffraction Peaks of PSZ Material

Diffraction Line		Material			
		As-fired	Shocked 1x	Shocked 35x	Powder
Cubic	(111)	87	113	134	187
	(200)	32	40	46	68
	(220)	44	50	59	79
	(311)	19	19	33	26
Monoclinic	(011)	14	14	15	18
	(110)	11	10	11	12
	(111)	71	71	79	90
	(200)	16	16	15	15
	(022)	13	12	11	12

A P P E N D I X H

APPENDIX H

Calculation of the Oxygen Partial Pressure in Equilibrium with a Metal-Metal Oxide System at Elevated Temperature*

In a general reaction in which equilibrium is established between gaseous reactants and products:

$$aA + bB + cC + \ldots \leftrightharpoons lL + mM + nN + \ldots$$

the Law of Mass Action allows the equilibrium constant K_p to be defined in terms of the partial pressure of the component phases:

$$K_p = \frac{P_L^l \quad P_M^m \quad P_N^n \quad \ldots}{P_A^a \quad P_B^b \quad P_C^c \quad \ldots}$$

However, in cases where a solid phase is present in a reversible reaction its 'active mass' should be regarded as constant irrespective of the actual amount present. Consequently, the expression for K_p will only depend on the partial pressure of the gaseous phases present. For example, if the above equilibrium reaction involved both gaseous and solid phases in a reaction of the type:

$$aA_{(g)} + bB_{(s)} + cC_{(s)} + \ldots \leftrightharpoons lL_{(g)} + mM_{(g)} + nN_{(s)} + \ldots$$

$$K_p' = \frac{P_L^l \cdot P_M^m}{P_A^a}$$

In thermodynamic terms, the chemical potential (μ) and activity of a pure solid are constant at constant temperature and external pressure. Consider a pure solid in equilibrium with its vapour; the chemical potential of the vapour is given

---

*For general information see: 'Textbook of Physical Chemistry', S. Glasstone, published by MacMillan and Co. Ltd., London (1956).

by $\mu^\circ + RT\ln P$, where P is the vapour pressure (strictly fugacity). Because the solid and vapour are in equilibrium, this will also represent the chemical potential of the solid phase. At constant temperature and external pressure, P is constant and under these conditions the chemical potential of the pure solid will be constant and hence its activity must also be constant.

Strictly, the vapour pressure and chemical potential of a solid are constant only if the total pressure, as well as temperature, is fixed. Consequently, the omission of terms for solid phases is only justifiable provided the pressure of the system is unchanged. Unless extremely high pressures are involved, the change in vapour pressure is negligible and so the slight error incurred may be ignored, i.e., the equilibrium constant with terms for the gaseous phases only can be taken as being independent of the total pressure.

From the foregoing, it will be appreciated that the equilibrium established over the surface of a metal-metal oxide mixture can be defined by the partial pressure of the oxygen alone:

$$M_{(s)} + \tfrac{1}{2}O_{2(g)} = MO_{(s)} \qquad K_p' = P_{O_2}^{-\frac{1}{2}} \qquad (1)$$

$$2M_{(s)} + \tfrac{3}{2}O_{2(g)} = M_2O_{3(s)} \qquad K_p' = P_{O_2}^{-\frac{3}{4}} \qquad (2)$$

In any reaction, the overall free energy change (ΔG) is given by $\Delta G_f^\circ + RT\ln K_p$. At equilibrium, however, ΔG is zero and hence:

$$\Delta G_f^\circ = -RT\ln K_p \qquad (3)$$

where ΔG_f° is the free energy of formation of the oxide in its standard state, i.e., at 25°C and under 1 atmosphere pressure.

From the tabulated values[35] of ΔG_f° for the formation of the oxides: FeO, CoO, NiO and Cr_2O_3, the following equations were derived for the variation of free energy with temperature in the range 600°K to 2000°K:

$$\text{FeO} \quad \Delta G_f^\circ = 14.57T - 62{,}102$$

$$\text{CoO} \quad \Delta G_f^\circ = 17.22T - 56{,}297$$

$$\text{NiO} \quad \Delta G_f^\circ = 20.46T - 56{,}416$$

$$Cr_2O_3 \quad \Delta G_f^\circ = 61.28T - 270{,}495 \quad \text{cal/mole}$$

For oxides of the type MO, combination of equations (1) and (3) gives:

$$\Delta G_f^\circ = -RT \ln P_{O_2}^{-\frac{1}{2}}$$

$$\text{hence} \qquad \log P_{O_2} = \frac{2\,\Delta G_f^\circ}{2.3026\ RT} \qquad (4)$$

similarly, for oxides of the type M_2O_3 combination of equations (2) and (3) gives:

$$\log P_{O_2} = \frac{2\,\Delta G_f^\circ}{3 \times 2.3026\ RT} \qquad (5)$$

where P_{O_2} is the equilibrium oxygen pressure in atmospheres, ΔG_f° is the free energy of formation of the oxide in its standard state in cal/mole, R (=1.98718 cal/mole °K) is the gas constant and T (°K) is the temperature.

Substitution of the equations for ΔG_f° into equations (4) and (5) above gives the following expressions for the variation of oxygen partial pressure with temperature in the range 600°K to 2000°K:

$$FeO \quad \log P_{O_2} = 6.369 - 27{,}144/T$$

$$CoO \quad \log P_{O_2} = 7.527 - 24{,}607/T$$

$$NiO \quad \log P_{O_2} = 8.942 - 24{,}659/T$$

$$Cr_2O_3 \quad \log P_{O_2} = 8.928 - 39{,}410/T$$

The solution to these equations is given graphically in Figure 48. Note that the temperature in this Figure is in °C whereas for the solution of the above equations it is in °K.

A P P E N D I X I

APPENDIX I

Calculation of the Ionic Transport Number of Zirconia as a Function of Oxygen Partial Pressure

The total electrical conductivity of a material is given by the sum of the ionic (σ_i) and electronic (σ_e) components:

$$\Sigma\sigma = \sigma_i + \sigma_e$$

and the ratio of each component conductivity to the total gives the transport number for that species, i.e., $t_i = \sigma_i/\Sigma\sigma$ and $t_e = \sigma_e/\Sigma\sigma$, hence

$$\frac{t_i}{t_e} = \frac{\sigma_i}{\sigma_e}$$

Assuming that the ionic conductivity is independent of P_{O_2} and that the electronic conductivity is proportional to $P_{O_2}^{-\frac{1}{4}}$ [1,5,37,40] then

$$\frac{ti}{te} = \frac{k}{k' P_{O_2}^{-\frac{1}{4}}} = K \times P_{O_2}^{\frac{1}{4}} \qquad (1)$$

where K, k and k' are constants.

Zirconia at 1600°C

From the data given in Figure 49, the oxygen partial pressure at which the ionic and electronic conductivities are equal at 1600°C is approximately 10^{-16} atmospheres. Under these conditions $t_i = t_e = 0.5$ and hence,

$$K\ (10^{-16})^{\frac{1}{4}} = 1$$

i.e., $$K = 10^4$$

Substitution of this value for K and of $t_e = 1 - t_i$ into equation (1) gives the expression for the variation of t_i with P_{O_2}:

$$\frac{t_i}{(1 - t_i)} = 10^4 \times P_{O_2}^{\frac{1}{4}} \qquad (2)$$

Zirconia at 1000°C

From Figure 49, $(P_{O_2})_{0.5}$ is approximately 10^{-23} atmospheres at 1000°C and hence K may be shown to be 5.62×10^5. Consequently, the expression relating t_i and P_{O_2} is given by:

$$\frac{t_i}{(1 - t_i)} = 5.62\ 10^5 \times P_{O_2}^{\frac{1}{4}} \qquad (3)$$

The solutions for equations (2) and (3) are given below for selected values of t_i. The data is presented graphically in Figure 50.

TABLE 1

Variation of t_i with P_{O_2} for Zirconia at 1000°C and 1600°C

t_i	- Log P_{O_2} (1000°C)	- Log P_{O_2} (1600°C)
0.99	15.02	8.02
0.95	17.88	10.88
0.90	19.18	12.18
0.80	20.59	13.59
0.70	21.53	14.53
0.60	22.29	15.29
0.50	23.00	16.00
0.40	23.70	16.70
0.30	24.47	17.47
0.20	25.41	18.41
0.10	26.82	19.82
0.05	28.11	21.11
0.01	30.98	23.98

A P P E N D I X J

APPENDIX J

Calculation of Concentration Cell emf from Thermodynamic Data

Both the cell emf and the oxygen gradient across the electrolyte may be calculated from the Nernst equation:

$$\Delta G = -nFE = -RT \ln P_1/P_2$$

where ΔG (cal/mole) is the free energy of the cell reaction in which an emf E (volts) is developed by the passage of n faradays through an electrolyte at a temperature T°K having an oxygen concentration gradient given by (P_1/P_2) atmospheres. F is the Faraday constant (23,066 cal/V/mole) and R is the gas constant (1.9865 cal/mole/°K).

(i) The Ni,NiO-Fe,FeO concentration cell

The cell emf E is the result of the difference between the two half-cell potentials E°:

$$E = E^\circ_{FeO} - E^\circ_{NiO}$$

which may be obtained from the tabulated standard free energies of formation[35] (ΔG°), hence

$$E = (\Delta G^\circ_{FeO} - \Delta G^\circ_{NiO})/\ nF$$

where ΔG°_f for FeO and NiO at 600°C and 1200°C are as shown below:

		600°C	1200°C
ΔG°_f	(FeO)	-49,380	-40,638
	(NiO)	-38,552	-26,278 cal/mole

Hence, the emf given by a cell operating at 1200°C is given by:

$$E = -(-40,638 - -26,278)/2(23,066) \text{ volts}$$

$$= + 311.2 \text{ mv}$$

Similarly, it may be shown that the cell will develop an emf of 234.7 mv at 600°C.

(ii) The air-liquid Fe,FeO concentration cell

From the data given in Appendix H and Figure 48 it has been shown that the equilibrium partial pressure of oxygen in liquid Fe-FeO is approximately 10^{-8} atmospheres at 1600°C. Hence, a concentration cell established between an air reference electrode and this liquid metal-metal oxide system would develop an emf given by:

$$E = \frac{RT}{nF} \ln\left(\frac{P_{air}}{P_{Fe}}\right) = \frac{1.987 \times 1873.16}{4 \times 23{,}066} \ln\left(\frac{0.21}{10^{-8}}\right)$$

$$= 680.1 \text{ mv.}$$

However, in practice, voltages of approximately one volt are developed in cells operating at 1600°C in commercial steel using an air reference electrode. This corresponds to an oxygen partial pressure in the steel given by P_{Fe}:

$$\ln \frac{P_{air}}{P_{Fe}} = \frac{1.0 \times 4 \times 23{,}066}{1.987 \times 1873.16} = 24.789$$

$$\frac{P_{air}}{P_{Fe}} = 5.8 \times 10^{10} \qquad P_{Fe} = 3.6 \times 10^{-12} \text{ atm.}$$

which indicates how far from the Fe-FeO equilibrium that commercial steel-making furnaces are operated.

A P P E N D I X K

APPENDIX K

Emf Versus Temperature Data Obtained from a Concentration Cell Operating Between 650°C and 1150°C

(i) The Fe,FeO-Ni,NiO Cell

The data below were obtained using as-fired reference electrodes which were replaced after each run. Each datum point was recorded only after the system had attained thermal and electrical equilibrium.

TABLE 1

Experimental Results

Run No.	emf mv	Temp °C	Run No.	emf mv	Temp °C
1	272	963	9	238	797
	259	882		231	741
	246	792		226	731
	233	738			
			10	263	1015
2	240	814		256	979
	256	912		244	932
	269	978		228	870
				211	786
3	268	972		201	734
	243	828			
	236	775	11	284	1029
				280	996
7	254	897		274	948
	243	860		267	900
	234	820		257	842
	227	790		243	783
	211	725		219	710
	203	685			
			12	292	1064
8	271	909		285	1017
	260	855		278	983
	252	816		265	909
	241	771		252	849
	230	681		236	791
9	276	1003	13	204	698
	260	915		220	741
	255	892		241	803
	247	838		255	869

....Table Continued

TABLE 1 (continued)

Run No.	emf mv	Temp °C	Run No.	emf mv	Temp °C
13	267	917	14*	268	946
	274	960		258	907
	283	1011		249	858
				241	846
14*	240	757			
	235	744			
	252	826			
	265	936			
	273	973			

* Data for Figure 54.

A least squares analysis of the above data gave the equation:

$$\text{emf (mv)} = 0.1974\ T^{\circ}C + 79.48$$

as the straight line of best fit with a correlation coefficient of 0.91. From this equation, values of emf were derived for given values of temperature in the range 600°C to 1200°C and data for a 95% confidence band were obtained for the line as a whole[49]. These data, which are given in Table 2 below, together with the data from Table 1, are presented in Figure 55.

TABLE 2

Confidence Interval Estimates for the Line as a Whole

Given Temp °C	Calculated emf	95% Limits of emf
600	197.9	189.7 - 206.1
650	207.8	200.9 - 214.6
700	217.7	212.1 - 223.2
750	227.5	223.9 - 231.9
800	237.4	234.0 - 240.8
850	247.3	244.4 - 250.2
900	257.1	254.0 - 260.3
950	267.0	263.1 - 270.9
1000	276.9	271.9 - 281.9
1050	286.8	280.5 - 293.0
1100	296.6	289.0 - 304.2
1150	306.5	297.5 - 315.5
1200	316.4	306.0 - 326.8

(ii) The Co,CoO-Ni,NiO Cell

The same experimental arrangement was used as in (i) above, only the Fe, FeO electrodes were replaced by the Co, CoO electrodes.

TABLE 3

Experimental Results

Run No.	emf mv	Temp °C	Run No.	emf mv	Temp °C
21	68.0	691	25	92.1	964
	79.5	823		90.8	946
	90.2	970		86.9	893
	95.0	1042		86.0	878
	99.3	1100		77.9	781
	87.5	928		71.6	703
	86.0	906		71.0	700
	83.8	884		69.0	673
	80.8	856		67.5	656
	79.5	832		66.8	650
	76.9	798			
	74.6	773	26	89.2	935
	72.9	749		84.8	884
	70.5	730		84.3	882
	69.9	717		82.0	843
	68.0	708		81.0	835
	67.4	684		79.6	821
	75.0	672		78.0	807
				77.3	806
23	87.6	930		71.4	741
	80.0	836		69.9	707
	73.8	817			
			27	76.4	773
24	102.4	1110		83.3	855
	99.3	1081		85.5	880
	95.8	1045		88.0	901
	90.2	993		93.4	970
	86.0	949			
			28	86.3	935
25	100.7	1071		85.0	920
	96.8	1019		84.0	905
	96.3	1012		83.1	893
	93.0	979		82.5	891

TABLE 3 (continued)

Run No.	emf mv	Temp °C	Run No.	emf mv	Temp °C
28	82.0	885	30	79.2	807
	81.5	879		78.0	795
	80.0	870		76.8	788
	79.0	849		76.5	782
	78.0	837		74.9	761
	76.0	828		74.1	759
	75.1	823		73.1	752
	80.6	889			
	88.8	967	31	101.6	1092
	89.0	968		99.9	1059
	90.0	977		99.1	1049
	95.4	1047		96.4	1021
	98.1	1080		92.2	960
	99.2	1090		91.2	952
	99.9	1097		89.2	926
	101.1	1105		87.5	903
	101.9	1117		85.9	883
				83.0	841
29	104.3	1142		81.2	825
	105.0	1154		79.0	791
	103.0	1118		74.2	740
	102.0	1108		72.5	721
	100.8	1087			
	98.7	1075	32	99.6	1081
	96.0	1027		96.7	1058
	95.0	1015		93.5	1011
	94.1	1004		90.8	960
	91.2	989		85.0	896
	84.6	906		83.0	872
	78.6	834		82.1	861
	74.9	786		80.6	846
				79.9	835
30	100.9	1080		78.5	817
	98.6	1035		77.1	794
	96.2	1016		76.4	786
	93.2	983		74.6	774
	89.1	925			
	87.7	911			
	83.9	860			
	82.1	846			
	81.2	833			
	80.2	823			

A least squares analysis of the above data gave the equation:

$$\text{emf (mv)} = 0.0795\ T^{\circ}C + 13.79$$

as the line of best fit with a correlation coefficient of 0.98. As in part (i) above, this equation was used to obtain the mean value of the emf for a given temperature in the range 600°C to 1200°C and data for a 95% confidence band for the line as a whole were derived.[49].

TABLE 4

Confidence Interval Estimates for the Line as a Whole

Given Temp °C	Calculated emf	95% Limits of emf
600	61.49	60.60 - 62.49
650	65.47	64.70 - 66.23
700	69.44	68.80 - 70.08
750	73.42	72.89 - 73.95
800	77.39	76.96 - 77.82
850	81.37	81.00 - 81.73
900	85.34	85.00 - 85.68
950	89.32	88.95 - 89.68
1000	93.29	92.85 - 93.73
1050	97.27	96.73 - 97.80
1100	101.24	100.59 - 101.89
1150	105.22	104.45 - 105.89
1200	109.19	108.30 - 110.08

These results are presented in Figure 56.

A P P E N D I X L

APPENDIX L

Properties of Partially Stabilized Zirconia Materials A to F

(i) Tap Density

A sample of powder from each batch was placed in a 100 ml measuring cylinder and vibrated to the minimum volume. From the sample weight and tap volume, the tap density was determined.

TABLE 1

Tap Density of Materials A to F

Material	Weight g	Volume ml	Tap Density g/ml	Drying* Process
A	13.6	72	0.19	FD
B	11.2	77	0.15	FD
C	82.7	85	0.97	SD
D	10.0	70	0.14	FD
E	15.0	80	0.19	FD
F	53.8	80	0.67	SD

* FD freeze-dried, SD spray-dried

(ii) Weight Loss on Ignition

Small batches of powder (approximately 3 g) were calcined in platinum crucibles in air for one hour prior to determining the surface area of the samples. The weight loss incurred during this heating is recorded in Table 2.

The data show the basic division of the different materials into the two groups which were either well-washed or unwashed during the wet processing stages. The additional loss shown by materials E and F is due to the retention of NH_4Cl in the unwashed powders.

TABLE 2

Percentage Weight Loss on Ignition of Materials A to F

Material	Temperature					
	850°C	900°C	950°C	1000°C	1050°C	1100°C
A		20.3	20.4	20.4	20.5	
B	16.5	16.7	17.3	17.6	20.1	21.0
C	24.0	24.0	24.1	24.2	24.3	24.4
D		13.5	13.6	13.8	14.0	
E		36.4	37.5	37.5	37.6	
F		38.5	39.0	39.1	39.2	

(iii) Concentration of Soluble Cl^- and M^{2+} in As-Prepared and Calcined Materials A to F

A 1.000-g sample of each material was reslurried in distilled water to give a total volume of 100 ml. The concentration of Cl^- and M^{2+} ions in the solution was determined using a calibrated specific ion electrode.

TABLE 3

Concentration of Cl^- in Dried As-Prepared Materials

Material	$[Cl^-]$ mole/litre	$[Cl^-]$ g/litre	Wt % Cl^- in Powder
A	3.7×10^{-3}	0.1314	1.3
B	3.4×10^{-3}	0.1207	1.2
C	4.0×10^{-3}	0.1420	1.4
D	3.0×10^{-3}	0.1065	1.1
E	6.4×10^{-2}	2.2720	22.7
F	6.0×10^{-2}	2.1300	21.3

TABLE 4

Concentration of Cl^- in Dried Calcined Materials

Material	$[Cl^-]$ mole/litre	$[Cl^-]$ g/litre	Wt of Cl^- in Powder
A 1000°C	8.6×10^{-4}	0.0305	0.31
B 975°C	5.0×10^{-4}	0.0178	0.18
C 975°C	1.3×10^{-3}	0.0462	0.46
D 1000°C	6.8×10^{-4}	0.0241	0.24
E 935°C	5.4×10^{-3}	0.192	1.92
F 935°C	5.4×10^{-3}	0.192	1.92

TABLE 5

Concentration of Divalent Ions in Dried As-Prepared Materials

Material	$[M^{2+}]$ mole/litre	$[M^{2+}]$ g/litre*	Wt of M^{2+} in Powder
A	1.8×10^{-3}	0.0720	0.72
B	1.4×10^{-3}	0.0560	0.56
C	1.1×10^{-3}	0.0440	0.44
D	1.3×10^{-3}	0.0520	0.52
E	1.3×10^{-2}	1.7514	17.51
F	2.7×10^{-2}	3.6509	36.51

*In the conversion of the concentration of M^{2+} ions from mole/litre to g/litre, it was assumed that only Ca^{2+} ions were present in materials A to D and hence the term for concentration in g/litre was obtained by multiplying the mole/litre figure by 40 - the atomic weight of Ca. However, in the case of materials E and F, it was assumed that the electrode responded only to the presence of ZrO^{2+} and $ZrCl_2{}^{2+}$ ions - comparison with the data for materials A to D shows that the concentration of Ca^{2+} is approximately 10% of the total divalent-ion concentration in materials E and F. Consequently, it was assumed that the divalent zirconium ions were present in equal concentrations and hence the mean atomic weight of 134.72 was used as the factor to convert the concentration data from mole/litre to g/litre.

TABLE 6

Concentration of Divalent Ions in Dried Calcined Materials

Material	$[M^{2+}]$ mole/litre	$[M^{2+}]$ g/litre	Wt % M^{2+} in Powder
A 1000°C	1.8×10^{-4}	0.0072	0.072
B 975°C	1.2×10^{-4}	0.0048	0.048
C 975°C	2.3×10^{-4}	0.0092	0.092
D 1000°C	1.1×10^{-4}	0.0044	0.044
E 935°C	4.0×10^{-4}	?	?
F 935°C	1.1×10^{-3}	?	?

? Identity of residual divalent ions is unknown and hence it is impossible to estimate the mean atomic weight.

(iv) Surface Area Data for Partially Stabilized Zirconia Materials A to F

The surface areas were determined by the method given in Appendix E.

TABLE 7

Surface Area Versus Temperature Characteristics of Materials A to F

Material	Temperature °C							
	850	900	935	950	975	1000	1050	1100
A		58.12		25.98		21.27 (17.73)	20.14	
B	56.68	34.34		29.90	(26.39)	23.80	12.10	6.57
C	50.42	25.78		21.15	(19.49)	20.56	8.56	2.15
D		55.53		27.06		20.80 (19.98)	23.51	
E		36.55	(18.76)	15.75		14.99	13.78	
F		27.84	(15.51)	20.75		16.72	14.51	m^2/g

( ) - Surface area determined after calcination of the main batch of each material.

(v) Chemical Analysis

Various samples of undoped and CaO-stabilized zirconia powders were calcined at 1000°C in air for 30 minutes and subsequently submitted to the Spectrochemistry Section of the Mineral Sciences Division for an analysis of the impurity levels in each material. The data, obtained by D. P. Palombo and G. L. Mason and submitted in report number SL 149-73, is duplicated in Table 8.

Unfortunately, it is not possible to analyse for chlorine by spectrochemical methods and hence their report excluded data on the total Cl^- present in each sample.

TABLE 8

Chemical Analyses of Undoped and Doped Zirconia Raw Materials

Material					
	Mg	Ca	Zr	Si	Cu
Undoped ZrO_2	0.05	0.44	PC	0.11	0.025
7.6 mole % CaO	0.02	PC	PC	0.11	0.02
11.5 mole % CaO	0.04	PC	PC	0.1	0.025
13.8 mole % CaO	0.05	PC	PC	0.11	0.009
16.0 mole % CaO	0.05	PC	PC	0.13	0.02
A	0.015	PC	PC	0.12	0.015
B	0.01	PC	PC	0.1	0.02
C	0.02	PC	PC	0.11	0.01
D	0.02	PC	PC	0.22	0.02
E	0.03	PC	PC	0.10	0.02
F	0.03	PC	PC	0.11	0.025

PC - Principal constituent

The following elements were sought but not detected:

Li Be B Na Al P Ti V Cr Mn Fe Co Ni Zn

Ga Ge As Sr Nb Mo Ag Cd In Sn Sb Ba Ta W

Pb Bi

A P P E N D I X M

APPENDIX M

Density Data for Unfired and Fired Oxygen-Probe Membranes Formed from Materials A to F

It was found convenient to test 120 probe assemblies per day under steel-making conditions, consequently at least 20 membranes were fabricated from each of the six raw materials. Random samples were taken from each batch of membranes and the density was determined by weighing and measuring both the unfired and fired materials.

TABLE 1

Density Data for First Batch of Unfired and Fired* Oxygen-Probe Membranes

Material	Unfired Density g/cc	Fired Density g/cc	Relative Density of Fired Sample+
A	2.26	5.62	
	2.28	5.56	
	2.28	5.68	
	2.18	5.65	
	2.21	5.60	
	av 2.24	av 5.62	92.6%
B	1.76	5.62	
	1.71	5.41	
	1.71	5.40	
	1.84	5.40	
	1.79	5.39	
	av 1.76	av 5.44	89.7%
C	2.06	5.12	
	1.93	4.80	
	2.08	4.86	
	2.01	4.79	
	2.13	4.66	
	av 2.16	av 4.97	81.8%

...Table continued

TABLE 1 (continued)

Material	Unfired Density g/cc	Fired Density g/cc	Relative Density of Fired Sample
D	1.85	5.56	
	1.83	5.55	
	1.81	5.49	
	1.88	5.52	
	1.82	5.56	
	av 1.84	av 5.54	91.3%
E	2.05	5.47	
	2.02	5.48	
	2.02	5.47	
	2.05	5.55	
	1.98	5.53	
	av 2.02	av 5.50	90.6%
F	2.68	4.44	
	2.71	4.41	
	2.36	4.54	
	2.69	4.37	
	2.71	4.38	
	av 2.63	av 4.43	73.0%

* Samples fired in air at 3°C/min to 1500°C without any soaking period.

\+ Based on the average value for the single crystal density determined by X-ray diffraction (6.068 g/cc, page 37).

No attempt was made to identify the samples before or after firing, hence no conclusions can be drawn regarding any relationship between the individual green and fired density figures given above.

A second batch of membranes was fabricated under the conditions given above and the density and firing shrinkage of selected samples were determined (Table 2).

TABLE 2

Density Data for Second Batch of Unfired and Fired* Oxygen-Probe Membranes

Material	Unfired Density g/cc	Fired Density g/cc	Relative Density of Fired Sample	Firing Shrinkage
A	2.22	5.60	92.3%	26.8%
	2.18	5.60	92.3%	26.8%
	2.26	5.66	93.3%	27.5%
	2.25	5.71	93.3%	27.5%
	2.20	5.57	91.8%	27.8%
	av 2.22	av 5.63	av 92.3%	av 27.3%
B	1.85	5.58	92.0%	31.0%
	1.81	5.59	92.1%	31.0%
	1.83	5.60	92.3%	31.0%
	1.79	5.56	91.6%	30.3%
	1.82	5.58	92.0%	29.6%
	av 1.82	av 5.58	av 92.0%	av 30.6%
C	2.16	4.54	74.8%	23.9%
	2.14	4.39	72.4%	23.3%
	2.12	4.49	74.0%	23.9%
	2.12	4.47	73.7%	23.3%
	2.17	4.51	74.3%	23.9%
	av 2.14	av 4.48	av 73.8%	av 23.7%
D	1.92	5.73	94.4%	31.3%
	1.95	5.83	96.1%	31.7%
	1.90	5.78	95.3%	31.3%
	1.84	5.83	96.1%	31.3%
	1.92	5.75	94.8%	31.7%
	av 1.91	av 5.78	av 95.3%	av 31.5%
E	1.87	5.53	91.1%	31.0%
	1.92	5.49	90.5%	31.7%
	1.91	5.64	93.0%	31.7%
	1.91	5.51	90.8%	31.3%
	1.87	5.57	91.8%	31.0%
	av 1.90	av 5.55	av 91.4%	av 31.3%
F	2.49	3.96	65.3%	16.9%
	2.50	4.06	66.9%	16.9%
	2.50	4.06	66.9%	16.9%
	2.53	3.95	65.1%	16.9%
	2.57	4.03	66.4%	16.9%
	av 2.52	av 4.01	av 66.1%	av 16.9%

* Samples fired in air at 3°C/min to 1500°C without any soaking period.

The samples were fired in a tube furnace having a nominal internal diameter of two inches and a hot zone of approximately three inches. Consequently, two firings were necessary and, in each case, one of the materials lay just outside the hot zone. It is for this reason that materials C and F had an abnormally low fired density in the second batch of membranes.

TABLE 3

Density Data for Third Batch of Unfired and Fired* Oxygen-Probe Membranes

Material	Unfired Density g/cc	Fired Density g/cc	Relative Density of Fired Sample	Firing Shrinkage
A	2.03	5.62	93.6%	28.0%
	2.10	5.65	93.1%	28.7%
	2.04	5.71	94.1%	28.7%
	2.11	5.66	93.9%	28.7%
	2.09	5.63	92.8%	29.0%
	av 2.07	av 5.65	av 93.5%	av 28.6%
B	1.77	5.55	91.5%	31.5%
	1.78	5.44	89.7%	31.5%
	1.80	5.49	90.5%	31.5%
	1.69	5.53	91.1%	31.5%
	1.78	5.60	92.3%	31.5%
	av 1.76	av 5.52	av 91.0%	av 31.5%
C	2.07	4.31 (5.75)+	71.0% (94.8%)+	23.8%
	2.04	4.32 (5.72)	71.2% (94.3%)	23.8%
	2.08	4.30 (5.77)	70.9% (95.1%)	23.8%
	2.09	4.31 (5.71)	71.0% (94.1%)	23.8%
	2.09	4.31 (5.69)	71.0% (93.8%)	23.8%
	av 2.07	av 4.31 (5.73)	av 71.0% (94.4%)	av 23.8%
D	1.79	5.71	94.1%	32.9%
	1.85	5.78	95.3%	32.2%
	1.85	5.75	94.8%	32.5%
	1.86	5.81	95.8%	32.9%
	1.80	5.72	94.3%	32.2%
	av 1.83	av 5.75	av 94.9%	av 32.5%

...(Table 3 continued)

TABLE 3 (continued)

Material	Unfired Density g/cc	Fired Density g/cc	Relative Density of Fired Sample	Firing Shrinkage
E	1.78	5.72	94.3%	32.5%
	1.80	5.65	93.1%	32.5%
	1.84	5.56	91.6%	32.5%
	1.81	5.59	92.1%	32.1%
	1.79	5.70	93.9%	32.9%
	av 1.80	av 5.64	av 93.0%	av 32.5%
F	2.46	4.26 (5.35)+	70.2% (88.2%)+	19.6%
	2.46	4.30 (5.34)	70.9% (88.0%)	19.6%
	2.43	4.28 (5.42)	70.5% (89.3%)	19.6%
	2.45	4.25 (5.43)	70.0% (89.5%)	19.6%
	2.43	4.27 (5.41	70.4% (89.2%)	19.6%
	av 2.45	av 4.27 (5.39)	av 70.4% (88.8%)	av 19.6%

* Samples were initially fired in air at 3°C/min to 1500°C without any soaking period.
\+ Samples were subsequently refired to 1600°C for one hour.

TABLE 4

Density Data for Fourth Batch of Unfired and Fired* Oxygen-Probe Membranes

Material	Unfired Density g/cc	Fired Density g/cc	Relative Density of Fired Sample	Firing Shrinkage
A	2.09	5.83	96.1%	28.7%
	2.13	5.77	95.1%	28.3%
	2.18	5.73	94.4%	29.0%
	2.16	5.73	94.4%	29.4%
	2.15	5.80	95.6%	29.4%
	av 2.14	av 5.77	av 95.1%	av 29.0%
B	1.78	5.65	93.1%	32.2%
	1.76	5.63	92.8%	32.2%
	1.83	5.69	93.8%	31.8%
	1.79	5.72	94.3%	31.5%
	1.76	5.65	93.1%	33.6%
	av 1.78	av 5.67	av 93.4%	av 32.3%

(Table 4 continued)

TABLE 4 (continued)

Material	Unfired Density g/cc	Fired Density g/cc	Relative Density of Fired Sample	Firing Shrinkage
C	2.10	5.80	95.6%	30.8%
	2.08	5.80	95.6%	30.8%
	2.12	5.92	97.6%	31.1%
	2.11	5.87	96.7%	31.1%
	2.09	5.84	96.2%	30.8%
	av 2.10	av 5.85	av 96.3%	av 30.9%
D	1.86	5.89	97.1%	32.9%
	1.88	5.89	97.1%	32.9%
	1.87	5.80	95.6%	32.5%
	1.88	5.92	97.6%	33.6%
	1.86	5.88	96.9%	33.6%
	av 1.87	av 5.88	av 96.9%	av 33.1%
E	1.87	5.70	93.9%	32.9%
	1.85	5.63	92.8%	32.5%
	1.88	5.75	94.8%	32.9%
	1.87	5.72	94.3%	32.9%
	1.86	5.68	93.6%	32.9%
	av 1.87	av 5.70	av 93.9%	av 32.8%
F	2.48	5.46	90.0%	25.9%
	2.47	5.50	90.6%	25.9%
	2.49	5.59	92.1%	26.6%
	2.46	5.48	90.3%	25.9%
	2.47	5.58	92.0%	26.2%
	av 2.47	av 5.52	av 91.0%	av 26.1%

* Samples A, B, D, and E were fired in air at 3°C/min to 1500°C without any soaking period. Samples C and F were fired in air at 3°C/min to 1600°C and held at that temperature for one hour.

A P P E N D I X N

APPENDIX N

Field Trials of Oxygen Probes Assembled from Materials A to F

(a) Heat 9162

All zirconia membranes in this test were pressed at 10 ksi and fired in air at 3°C/min to 1500°C with no soaking period. The cells were assembled with a self-contained gas reference and were tested in steel at approximately 1600°C.

TABLE 1

Emf Data for Probes Tested in Liquid Steel

Sample	Test No.	Temp °C	emf volts	emf* 1600	Mean and Standard Deviation of 1600°C Data
QH**	1	1595	1.046	1.049	
	2		1.057	1.060	
	3		1.050	1.053	
	4		1.050	1.053	
	5		1.055	1.058	
	14	1602	1.045	1.044	
	23		1.043	1.041	
	24		1.043	1.041	
	25	1605	1.040	1.037	
	26		1.043	1.040	
	41		1.050	1.055	
	42		1.057	1.062	
	43		1.057	1.062	
	44		1.057	1.062	
	45	1592	1.046	1.051	
	61		1.055	1.060	m 1.052 V
	64		1.052	1.057	
	65		1.048	1.053	s 0.0084 V
A	7		0.998	1.003	
	8	1590	1.002	1.007	
	9		1.010	1.013	
	11		0.997	0.999	m 1.000 V
	12		0.993	0.993	
	13	1602	0.988	0.987	s 0.0103 V

(Table 1 continued)

TABLE 1 (continued)

Sample	Test No.	Temp °C	emf volts	emf* 1600	Mean and Standard Deviation of 1600°C
B	6		1.000	1.004	
	15		1.000	1.004	
	16		1.010	1.009	
	17		1.010	1.009	
	18	1602	1.002	1.001	
	19		1.006	1.005	
	20		1.005	1.004	m 1.002 V
	21		0.996	0.994	
	22		1.000	0.998	s 0.0050 V
C	27		-	Noise	
	28		-	Noise	
	29		-	No trigger	
	30		0.980	0.984	
	31		-	Noise	
	32		0.988	0.992	
	33		-	Noise	
	34	1592	0.985	0.989	
	35		-	Noise	Very noisy
D	36		1.007	1.011	
	37		1.007	1.011	
	38		1.005	1.009	m 1.010 V
	39		1.002	1.006	
	40		1.010	1.014	s 0.0029 V
E	46		1.002	1.006	
	47		-	Noise	
	48		1.001	1.005	
	49		0.986	0.990	
	50		1.008	1.012	
	51		0.997	1.001	m 1.002 V
	52		-	Noise	
	53		0.995	0.999	s 0.0074 V
F	54	1595	0.93	Noisy	
	55		0.90	Noisy	
	56		0.90	Noisy	
	57		0.93	Erratic	
	58		-	Noise	
	59		-	Noise	
	60		0.92	Noisy	
	66		0.93	Noisy	
	67		-	V.erratic	
	68		0.95	Noisy	
	69		-	Noise	
	70		-	V.sloping	Very noisy

* All the emf data were corrected using the Nernst relationship to a theoretical value which would be developed at 1600°C.

** QH - Commercially available probe manufactured by Quality Hermetics Ltd., Toronto.

(b) Heat 9420

All membranes were pressed at 10 ksi and fired in air to 1500°C with no soaking period. The cells were assembled with a self-contained gas reference and tested in steel at approximately 1600°C.

TABLE 2

Emf Data for Probes Tested in Liquid Steel

Sample	Test No.	Temp °C	emf volts	emf 1600	Mean and Standard Deviation of 1600°C Data
QH	1	1607	1.053	1.049	
	2		1.042	1.041	
	3	1595	1.052	1.055	
	4		1.042	1.042	
	5		-	No trig	
	24		1.045	1.037	
	25		1.039	1.031	
	26		1.040	1.032	
	27		1.039	1.031	
	28	1615	1.042	1.034	
	29		1.040	1.032	
	39		1.040	1.036	
	48		-	Fail	
	49		1.050	1.048	
	58		1.042	1.042	
	65		1.045	1.042	m 1.039 V
	73		1.045	1.040	
	81	1605	1.040	1.037	s 0.0072 V
A	30		1.000	0.993	
	31		-	Erratic	
	32		-	Erratic	
	33		1.005	0.999	
	34		-	Erratic	
	35		0.980	0.975	
	36		0.988	0.983	m 0.986 V
	37		0.980	0.975	
	38		0.995	0.990	s 0.0098 V
B	40		(0.920)	-	
	41		0.990	0.986	
	42		0.992	0.988	
	43		1.002	0.999	
	44		1.005	1.002	

(Table 2 continued)

TABLE 2 (continued)

Sample	Test No.	Temp °C	volts	emf 1600	Mean and Standard Deviation of 1600°C Data
B	45	1605	1.010	1.007	m 0.994 V
	46		1.020	1.017	
	47		1.000	0.997	s 0.0107 V
C	50 - 57	All samples shorted due to metal penetration			
D	59	1600	0.997	0.997	
	60		1.005	1.005	
	61		1.001	1.000	m 1.000 V
	62		1.002	1.001	
	63		0.998	0.996	s 0.0036 V
E	66		0.996	0.993	
	67		-	Erratic	
	68		1.020	1.016	
	69		0.997	0.993	m 0.999 V
	70		1.005	1.001	
	71		0.997	0.992	s 0.0102 V
F	74 - 80	All samples shorted due to metal penetration			

(c) Heat 9654

All the samples were formed under a pressure of 10 ksi and fired in air at 3°C/min to 1500°C without any soaking period. Because of the poor performance of membranes C and F in the earlier trials due to their considerable open porosity on firing under these conditions, these particular samples were subsequently re-fired in air at 3°C/min to 1600°C and held at that temperature for 1 hour in order to develop a relative density comparable to the other membrane materials (Table 3, Appendix M).

TABLE 3

Emf Data for Probes Tested in Liquid Steel

Sample	Test No.	Temp °C	emf volts	emf 1600	Mean and Standard Deviation of 1600°C Data
A	4	1600	1.012	1.012	
	5		1.006	1.005	
	6		1.012	1.010	m 1.011 V
	7		-	Noise	
	8		1.022	1.018	s 0.0054 V
B	9		1.000	0.995	
	10		1.000	0.994	
	11		1.000	0.993	
	12		1.000	0.992	m 0.989 V
	13	1618	0.975	0.966	
	14		1.001	0.992	s 0.0112 V
C	15		1.019	1.010	
	16		1.014	1.006	m 1.010 V
	17		1.020	1.012	
	18		1.017	1.010	s 0.0025 V
D	22		0.986	0.981	
	23		1.019	1.014	
	24		0.987	0.982	m 0.996 V
	25		1.010	1.005	
	26		-	Noise	s 0.0166 V
E	27		1.000	0.997	
	28		1.001	0.999	
	29		0.996	0.995	m 0.998 V
	30		0.985	0.986	
	31		1.012	1.014	s 0.0101 V
F	32		1.018	1.021	
	33		1.008	1.012	
	34		1.016	1.021	m 1.024 V
	35	1590	1.036	1.042	
	36		1.018	1.023	s 0.0110 V

Also tested in heat 9654 was the fourth batch of materials in which the raw materials A, B, D, and E were fired at 3°C/min to 1500°C with no soak, whereas materials C and F were fired at the same heating rate to 1600°C and held at that temperature for one hour (Table 4, Appendix M). The results obtained with these membranes are given in Table 4. (Note: Materials C and F

had only a single firing in this batch compared to the refired material used in the third batch, Table 3).

TABLE 4

Emf Data for Probes Tested in Liquid Steel

Sample	Test No.	Temp °C	emf volts	emf 1600	Mean and Standard Deviation of 1600°C Data
A	38	1593	1.015	1.019	
	39		1.015	1.018	m 1.017 V
	40		1.013	1.015	
	41		-	No trig	s 0.0021 V
B	42	1600	-	Fail	
	43		-	Fail	
	44		-	Fail	
	45		0.999	0.996	
	46		-	Fail	
C	47		1.001	0.996	
	48	1610	1.016	1.011	m 1.000 V
	49		1.010	1.004	
	50		0.995	0.989	s 0.0096 V
D	52		0.995	0.990	
	53		1.006	1.001	m 0.994 V
	54		0.995	0.990	
	55	1610	1.000	0.995	s 0.0052 V
E	56		1.006	1.001	
	57		1.001	0.996	
	58		0.980	0.974	
	59		-	Noise	m 0.985 V
	60		0.997	0.991	
	61		0.970	0.964	s 0.0156 V
F	62		1.014	1.008	
	63		1.019	1.013	
	64		1.020	1.014	m 1.013 V
	65		1.021	1.015	
	66		1.021	1.015	s 0.0029 V

CANMET PUBLICATIONS

Recent CANMET publications presently available or soon to be released through Printing and Publishing, Supply and Services, Canada (addresses on inside front cover), or from CANMET Publication Office, 555 Booth Street, Ottawa, Ontario K1A 0G1

CANMET Reports:

76-1 Metals and Alloys for Arctic Use; by R. C. A. Thurston;
Catalogue No. M38-13/76-1; Price: $0.75 Canada, $0.90 other countries.

76-2 Mineral Waste Source Report No. 1 - Mining Wastes in Ontario;
by R. K. Collings;
Catalogue No. M38-13/76-2; Price: $0.75 Canada, $0.90 other countries.

76-3 Certified and Provisional Reference Materials Available from CANMET;
by G. H. Faye;
Catalogue No. M38-13/76-3; Price: $1.00 Canada, $1.20 other countries.

76-4 The Preparation of Mica Cylinders for the Measurement of Thermal Conductivity;
by F. G. McDonald and V. V. Mirkovich;
Catalogue No. M38-13/76-4; Price: $0.50 Canada, $0.60 other countries.

76-5 Tungsten Ores CT-1, BH-1, and TLG-1: Their Characterization and Preparation for Use as Certified Reference Materials; by G. H. Faye, W. S. Bowman and R. Sutarno;
Catalogue No. M38-13/76-5; Price: $1.00 Canada, $1.20 other countries.

76-6 On the Determination of the Lattice Type and Unit Cell Parameters of a Crystal Using Electron Diffraction; by K. S. Milliken;
Catalogue No. M38-13/76-7; Price: $0.50 Canada, $0.60 other countries.

76-7 Catalogue and Index of CANMET Scientific and Technical Papers Published in or Submitted to Periodicals and Presentations, 1967-1973; by Technology Information Division;
Catalogue No. M38-13/76-7; Price: $2.00 Canada, $2.40 other countries.

76-8 Comparison of Pull-Out Strength of Concrete with Compressive Strength of Cylinders and Cores, Pulse Velocity and Rebound Number; by V. M. Machotra and G. Carette;
Catalogue No. M38-13/76-8; Price: $1.00 Canada, $1.20 other countries.

76-9 Catalysts for Hydrocracking and Refining Heavy Oils and Tars Part 3: The Effect of Presulphiding Conditions on Catalyst Performance; by M. Ternan and M. J. Whalley;
Catalogue No. M38-13/76-9; Price: $4.00 Canada, $4.80 other countries.

76-10 Recent Advances in Copper Electrowinning; by D. J. MacKinnon and V.I. Lakshman;
Catalogue No. M38-13/76-10; Price: $1.50 Canada, $1.80 other countries.

76-11 The Determination of Radium 226 in Uranium Ores and Mill Products by Alpha Energy Spectrometry; by J. B. Zimmerman and V. C. Armstrong;
Catalogue No. M38-13/76-11; Price: $1.00 Canada, $1.20 other countries.

76-12 Lightweight Aggregates for Structural Concrete; by H. S. Wilson;
Catalogue No. M38-13/76-12; Price: $3.75 Canada, $4.50 other countries.

76-13 Development of a Zirconia Electrolyte for Use in a Steel-Making Oxygen Probe; by T. A. Wheat;
Catalogue No. M38-13/76-13; Price: $5.00 Canada, $6.00 other countries.